PB84-155837

EPA (Environmental Protection Agency) Complex Terrain Model Development Third Milestone Report 1983

Environmental Research and Technology, Inc.
Concord, MA

Prepared for

Environmental Sciences Research Lab.
Research Triangle Park, NC

Nov 83

U.S. Department of Commerce
National Technical Information Service
NTIS

United States
Environmental Protection
Agency

Environmental Sciences Research
Laboratory
Research Triangle Park NC 27711

EPA-600/3-83-101
November 1983

Research and Development

PB84-155837

EPA

EPA Complex Terrain Model Development:

Third Milestone Report—1983

REPRODUCED BY
NATIONAL TECHNICAL
INFORMATION SERVICE
U.S. DEPARTMENT OF COMMERCE
SPRINGFIELD, VA. 22161

TECHNICAL REPORT DATA
(Please read Instructions on the reverse before completing)

1. REPORT NO.
EPA-600/3-83-101

2.

3. RECIPIENT'S ACCESSION NO.
PB84 155837

4. TITLE AND SUBTITLE
EPA COMPLEX TERRAIN MODEL DEVELOPMENT
Third Milestone Report - 1983

5. REPORT DATE
November 1983

6. PERFORMING ORGANIZATION CODE

7. AUTHOR(S)
T. F. Lavery, D. G. Strimaitis, A. Venkatram,
B. R. Greene, S. Hanna, D. C. DiChristofaro, B. A. Egan

8. PERFORMING ORGANIZATION REPORT NO.

9. PERFORMING ORGANIZATION NAME AND ADDRESS
Environmental Research & Technology, Inc.
696 Virginia Road
Concord, Massachusetts 01742

10. PROGRAM ELEMENT NO.
CDTA1D/09-0566 (FY-83)

11. CONTRACT/GRANT NO.
68-02-3421

12. SPONSORING AGENCY NAME AND ADDRESS
Environmental Sciences Research Laboratory - RTP, NC
Office of Research and Development
U.S. Environmental Protection Agency
Research Triangle Park, North Carolina 27711

13. TYPE OF REPORT AND PERIOD COVERED
Interim 06/82-06/83

14. SPONSORING AGENCY CODE
EPA/600/09

15. SUPPLEMENTARY NOTES

16. ABSTRACT

The U.S. Environmental Protection Agency is sponsoring the Complex Terrain Model Development program, a multi-year integrated program to develop and validate practical plume dispersion models of known reliability and accuracy for simulating one-hour-average ground-level concentrations downwind of elevated sources during stable atmospheric conditions in complex terrain. The first major component of the Complex Terrain Model Development program was a field study conducted during the fall of 1980 at Cinder Cone Butte, a roughly axisymmetric, isolated 100-meter-tall hill located in the broad Snake River Basin near Boise, Idaho. The second field study was performed during 1982 at Hogback Ridge, an 85-meter-tall two-dimensional ridge located west of Farmington, New Mexico.

This report documents work performed subsequent to the Second Milestone Report to combine two preliminary complex terrain models developed from the Cinder Cone Butte data base into the Complex Terrain Dispersion Model (CTDM), and to contrast the performance of CTDM with three existing complex terrain models using measurement data from both the Cinder Cone Butte and the Hogback Ridge field experiments. A description of the Hogback Ridge field study is also included

17. KEY WORDS AND DOCUMENT ANALYSIS

a. DESCRIPTORS	b. IDENTIFIERS/OPEN ENDED TERMS	c. COSATI Field/Group

18. DISTRIBUTION STATEMENT
RELEASE TO PUBLIC

19. SECURITY CLASS *(This Report)*
UNCLASSIFIED

20. SECURITY CLASS *(This page)*
UNCLASSIFIED

21. NO. OF PAGES
292

22. PRICE

EPA Form 2220-1 (9-73)

EPA-600/3-83-101
November 1983

EPA COMPLEX TERRAIN MODEL DEVELOPMENT:
Third Milestone Report - 1983

by

Thomas F. Lavery
David G. Strimaitis
Akula Venkatram
Benjamin R. Greene
Donald C. DiCristofaro
Bruce A. Egan

ENVIRONMENTAL RESEARCH & TECHNOLOGY, INC.
696 Virginia Road, Concord, Massachusetts 01742

Contract No. 68-02-3421

Project Officer

Francis A. Schiermeier
Meteorology and Assessment Division
Environmental Sciences Research Laboratory
Research Triangle Park, North Carolina 22771

ENVIRONMENTAL SCIENCES RESEARCH LABORATORY
OFFICE OF RESEARCH AND DEVELOPMENT
U.S. ENVIRONMENTAL PROTECTION AGENCY
RESEARCH TRIANGLE PARK, NORTH CAROLINA 22771

NOTICE

This document has been reviewed in accordance with U.S. Environmental Protection Agency policy and approved for publication. Mention of trade names or commercial products does not constitute endorsement or recommendation for use.

FOREWORD

The Environmental Sciences Research Laboratory (ESRL) conducts intramural and extramural research programs in the physical sciences to detect, define, and quantify air pollution and its effects on urban, regional, and global atmospheres and the subsequent impact on water quality and land use. The Laboratory is responsible for planning, implementing, and managing research and development programs designed to quantify the relationships between emissions of pollutants from all types of sources with air quality and atmospheric effects, and to uncover and characterize hitherto unidentified air pollution problems. Information from ESRL programs and from the programs of other government agencies, private industry, and the academic community are integrated by the Laboratory to develop the technical basis for air pollution control strategies for various pollutants.

The Complex Terrain Model Development (CTMD) program is designed to develop reliable atmospheric dispersion models that are applicable to large pollutant sources located in complex terrain. The first two major field studies of this five-year program were conducted during 1980 at Cinder Cone Butte near Boise, Idaho, and during 1982 at Hogback Ridge near Farmington, New Mexico. Data from these field studies along with measurements of scaled physical simulations performed in the EPA Fluid Modeling Facility are being used to quantify the effects of terrain obstacles on stable plume dispersion. The First Milestone Report presented the performance evaluations of four existing complex terrain dispersion models and described the initial development of two proposed models. The Second Milestone Report documented subsequent improvements to the two new models and presented detailed case studies to illustrate and contrast various flow situations and ranges of model performance. This Third Milestone Report describes the evolution of the two new models into the Complex Terrain Dispersion Model (CTDM), and contrasts the performance of CTDM and three existing complex terrain models using measurement data from both field studies.

A.H. Ellison
Director
Environmental Sciences Research Laboratory

ABSTRACT

The U.S. Environmental Protection Agency is sponsoring the Complex Terrain Model Development (CTMD) program, a multi-year, integrated program to develop, evaluate, and refine practical plume models for calculating ground-level air pollutant concentrations that result from large emission sources located in mountainous terrain. The principal objective of the CTMD program is to develop models with known accuracy and limitations for simulating 1-hour average concentrations during stable atmospheric conditions, i.e., to handle the stable plume impaction problem. This Third Milestone Report describes CTDM activities performed from June 1982 through May 1983.

A Modelers Data Archive (MDA) for Small Hill Impaction Study #1 (SHIS #1) conducted at Cinder Cone Butte, Idaho in 1980 is described. This archive contains hourly average tracer gas concentrations, and hourly and 5-minute average meteorological data estimated for the height of release on the basis of meteorological data measured at the 150-m tall tower approximately 2 km north of the hill. A total of 153 tracer experiment hours are contained in the archive.

The Wrap and Lift modeling components described in the CTMD Second Milestone Report are modified and combined into the Complex Terrain Dispersion Model (CTDM). Performance statistics for two versions of CTDM are generated with the 153-hour MDA, and these are compared with performance statistics for COMPLEX I, COMPLEX II, and Valley for the same data. Sensitivity of CTDM performance to the input data is partially evaluated by modeling a total of 14 hours from two experiments with a revised MDA which reflects the best estimates of release-height meteorology determined after studying all available information from those two experiments. Model performance sensitivity of CTDM to variations in the meteorology within a 1-hour averaging period is similarly evaluated by modeling concentrations for 5-minute intervals with both versions of the MDA for the 14 hours. Modifications to CTDM that are suggested by the performance of CTDM with the 153-hour MDA as well as with the 14-hour modified MDA are described, implemented and tested.

An overview of Small Hill Impaction Study #2 (SHIS #2), conducted during October 1982 at the Hogback Ridge near Farmington, N.M., is presented. It includes a description of the climatology of the area, a description of the experiment design, and a discussion of the phenomena observed, illustrated by a descriptive account of two hours from the study.

A preliminary meteorological data set for 17 hours (34 tracer experiment hours) is presented. Observed concentrations, scaled by the emission rate, are sorted by several meteorological parameters for these 17 hours, and the resulting patterns are discussed and compared with the results from SHIS #1. A comparison of Valley, Complex I, Complex II, and CTDM performance statistics for these 17 hours is also presented and discussed.

An EPA Fluid Modeling Facility report describing a laboratory simulation of neutral flow and dispersion over Cinder Cone Butte is included as an Appendix. A second Appendix contains a discussion of an initial analysis of SHIS #2 acoustic sounder data and sonic anemometer data.

This report was submitted in partial fulfillment of contract 68-02-3421 by Environmental Research & Technology, Inc. under the sponsorship of the U.S. Environmental Protection Agency. This report covers the period June 2, 1982 to June 1, 1983.

CONTENTS

Foreword iii
Abstract iv
Figures viii
Tables xiv
Symbols and Abbreviations xvi
Acknowledgements xx
1. Introduction 1
2. Evaluation of Complex Terrain Models with the CCB Data Base 5
  2.1 SHIS #1 Modelers' Data Archive 5
  2.2 Complex Terrain Models Evaluated 10
  2.3 Model Performance Statistics 14
  2.4 Analysis of Model Performance 16
3. Development of the Complex Terrain Dispersion Model 36
  3.1 Introduction 36
  3.2 Description of CTDM(11083) 37
  3.3 Case Study Results - Experiments 201 and 210 45
  3.4 CTDM Upgrades: CTDM (14083) 93
4. The Hogback Ridge Experiment 106
  4.1 Geographic and Meteorological Setting 106
  4.2 Preliminary Flow Visualization Experiment 112
  4.3 Fluid Modeling in Support of the SHIS #2 Experimental Design 117
  4.4 Experimental Design 123
  4.5 Preliminary Field Study Results 140
5. Preliminary Modeling of the HBR Data Base 184
  5.1 Initial 17-Hour Data Base 184
  5.2 Complex Terrain Models Evaluated 193
  5.3 Overall Performance Statistics 193
6. Summary, Conclusions, and Recommendations for Further Study 203
  6.1 Principal Accomplishments and Conclusions 203
  6.2 Recommendations for Further Study 203
References 209
Appendix A: Laboratory Simulation of Neutral Plume Dispersion over Cinder Cone Butte 212
Appendix B: Supporting Meteorological Measurements - Acoustic Sounder and Sonic Anemometers 252

Preceding page blank

FIGURES

Number		Page
1	Performance statistics based on residuals of peak observed and peak modeled concentrations for Valley, COMPLEX I, COMPLEX II, CTDM(11083), and CTDM (11083-E) applied to SHIS #1 data	19
2	Scatterplots of observed and modeled peak concentrations for 153 hours of SHIS #1 data	21
3	Cumulative frequency plot of C_o/C_p for Valley applied to SHIS #1 data	23
4	Cumulative frequency plot of C_o/C_p for COMPLEX I applied to SHIS #1 data	24
5	Cumulative frequency plot of C_o/C_p for COMPLEX II applied to SHIS #1 data	25
6	Cumulative frequency plot of C_o/C_p for CTDM (11083) applied to SHIS #1 data	26
7	Cumulative frequency plot of C_o/C_p for CTDM (11083-E) applied to SHIS #1 data	27
8	Variation of observed-to-modeled ratios of SHIS #1 peak hourly tracer concentrations with peak modeled concentrations	28
9	Variation of observed-to-modeled ratios of SHIS #1 maximum hourly tracer concentrations with wind speed.	29
10	Variation of observed-to-modeled ratios of SHIS #1 maximum hourly tracer concentrations with u/N . . .	31
11	Variation of observed-to-modeled ratios of SHIS #1 maximum hourly tracer concentrations with $1-H_c/z_r$	32
12	Variation of observed-to-modeled ratios of SHIS #1 maximum hourly tracer concentrations with $1-H_c/z_r$	33
13	Variation of observed-to-modeled ratios of SHIS #1 peak hourly tracer concentrations with the product of the turbulence intensities i_y and i_z	34
14	Plume dispersion in the region of horizontal flow . .	38

FIGURES (Continued)

Number		Page
15	Geometry used to derive the effective radius of curvature R_e for the portion of the hill above H_c, and to incorporate the wind direction probability distribution function $P(\theta)$ in the Lift model	41
16	Dispersion and flow regions for stratified flow around hills	43
17	Intercomparison of wind direction time-series data for Experiment 201, derived from photographs, wind measurements at 10 m from Tower B, and interpolated wind measurements from Tower A	47
18	Intercomparison of wind direction time-series data for Experiment 201, derived from photographs, wind measurements at 10 m and 30 m from Tower B, and interpolated wind measurements from Tower A . .	48
19	Definition sketch for computing distance along the wind trajectory from the source	50
20	Intercomparison of vertical turbulence intensity time-series data for Experiment 201, derived from photographs by Methods 1 and 3, and interpolated from Tower A	53
21	Intercomparison of vertical turbulence intensity time-series data for two hours of Experiment 201, derived from photographs by Methods 1 and 3, and interpolated from Tower A. The "photo" estimates are shifted by - 10 minutes	54
22	Intercomparison of vertical turbulence intensity time-series data for Experiment 201, derived from photographs by Method 4, and interpolated from Tower A	55
23	Average distribution of lidar-inferred oil-fog droplet concentrations 800 m downwind of the source for Experiment 210, hour 3	58
24	Intercomparison of vertical turbulence intensity time-series data for Experiment 210, derived from photographs and interpolated from Tower A	60

FIGURES (Continued)

Number Page

25 Comparison of Pasquill-Gifford σ_z growth curves with σ_z data from Experiment 201 photographs 63

26 Comparison of σ_z growth curves with σ_{z1} data derived from Experiment 201 photographs 64

27 Comparison of σ_z growth curves with σ_{z2} data derived from Experiment 201 photographs 65

28 Scatterplots used in computing best-fit p for Experiment 201 66

29 Growth of σ_z with distance from the source for Experiment 201, hour 3 68

30 Comparison of vertical turbulence intensity data contained in the Modelers' Data Archive with estimates made by fitting σ_z to the σ_z data estimated from the photographs from Experiment 210 73

31 Comparison of vertical turbulence intensity data contained in the Modelers' Data Archive with estimates made by fitting σ_z to the observed σ_{z2} data for Experiment 201 74

32 Comparison of photo-derived σ_z data and calculated σ_z utilizing best-fit i_z data in Equation 41 with $\gamma = 0.525$ and $\sigma_{zo} = 0.5$ 76

33 Time-series plots of σ_w and i_z data from Towers B, C, D, E, and F on CCB compared with data from Tower A for Experiment 201 77

34 Time-series plots of σ_w and i_z data from Tower B, C, D, E, and F on CCB compared with data from Tower A interpolated to release height for Experiment 210 82

35 CTDM(11083-E) performance, as measured by peak concentrations unpaired in space, using the Modelers' Data Archive and the modified Modelers' Data Archive for Experiments 201 and 210 92

36 Illustration of the plume deformation expected over an isolated "3-D" hill and the deformation by CTDM(11083) 96

FIGURES (Continued)

Number — Page

37 Illustration of the geometry used to calculate the horizontal distribution of plume material above H_c. 97

38 CTDM(11083-E) and CTDM(14083) C_o(peak)/C_p(peak) residuals for Experiments 201 and 210 with the modified MDA 104

39 Region around the SHIS #2 at the Hogback Ridge 107

40 The SHIS #2 site 108

41 View of Hogback south of the San Juan River. 109

42 View of the Hogback experiment site from the east . . 110

43 View toward the south-east from the Hogback 111

44(a) Climatological annual wind rose for Farmington, NM . . 113

44(b) October-December stability E Farmington wind rose . . 113

45 October hourly wind roses for four nighttime hours: 2000, 0000, 0200, and 0400 MST 114

46 Summer morning downslope drainage flow 115

47 Upper air soundings at Four Corners Power Plant during turnaround meteorological conditions 116

48 FMF tow-tank flow visualization experiment - Hogback Ridge 122

49 SHIS #2 field experiment layout 125

50 PNM air quality and meteorological monitoring sites . 130

51 Meteorological data acquisition system 132

52 SHIS #2 tracer sampler locations and optical anemometer paths A, B, and C 134

53 Gas chromatography data acquisition system 138

54 Tracer gas analysis system 139

55 Raw tower ΔT from 10 m to 150 m 144

56 Hourly CF_3Br concentrations 10/12/82, 0500-0600 MDT 148

FIGURES (Continued)

Number		Page
57	Hourly CF_3Br concentrations 10/29/82, 0200-0300 MDT	149
58	Maximum hourly χ/Q ($\mu sec/m^3$) vs. $1-H_c/z_r$	152
59	Observed SF_6 concentrations for CCB Experiment 206, hour 8	153
60	χ/Q ($\mu sec/m^3$) vs. $\Delta\theta/i_y$	154
61	Five-minute exposure from Tower A, Experiment 4, 10/11/82, 0315 MDT	156
62	Five-minute exposure from HBR south of target area, Experiment 4, 10/11/82, 0315 MDT	157
63	Five-minute exposure from Tower A, Experiment 4, 10/11/82, 0340 MDT	158
64	Vertical profiles of hourly meteorological data, Tower A, 10/11/82, 0300-0400 MDT	160
65	Time-series of 5-minute wind directions from Tower A and Tower C, Experiment 4, 10/11/82	161
66	Time-series of 5-minute wind directions from Tower A and Tower B, Experiment 4, 10/11/82	162
67	Hourly SF_6 concentrations, Experiment 4, 10/11/82, 0300-0400 MDT	163
68	Along-hill profiles of hourly SF_6 concentrations, 10/11/82, 0300-0400 MDT	164
69	Hogback samplers by rows	165
70	Hourly CF_3Br concentrations, 10/11/82, 0300-0400 MDT	167
71	Along-hill profiles of hourly CF_3Br concentrations, 10/11/82, 0300-0400 MDT	168
72	Five-minute exposure from Tower A, Experiment 10, 10/22/82, 0330 MDT	169
73	Five-minute exposure from HBR south of target area, Experiment 10, 10/22/82, 0330 MDT	170

FIGURES (Continued)

Number		Page
74	Vertical profiles of hourly meteorological data, Tower A, Experiment 10, 10/22/82, 0300-0400 MDT	171
75	Time-series of 5-minute wind directions from Tower A and Tower C, Experiment 10, 10/22/82	172
76	Time-series of 5-minute wind directions from Tower A and Tower B, Experiment 10, 10/22/82	173
77	Hourly SF_6 concentrations, 10/22/82, Experiment 10, 0300-0400 MDT	175
78	Along-hill profiles of hourly SF_6 concentrations, 10/22/82, 0300-0400 MDT	176
79	Hourly CF_3Br concentrations, Experiment 10, 10/22/82, 0300-0400 MDT	177
80	Along-hill profiles hourly CF_3Br concentrations, 10/22/82, 0300-0400 MDT	178
81	Five-minute exposure from HBR south of the target area, Experiment 10, 10/22/82, 0425 MDT	179
82	Hourly SF_6 concentrations, Experiment 10, 10/22/82, 0400-0500 MDT	180
83	Vertical profiles of hourly meteorological data, Tower A, 10/22/82, 0500 MDT	181
84	Time-series of 5-minute wind directions, Experiment 10, 10/22/82	182
85	Hourly CF_3Br concentrations, Experiment 10, 10/22/82, 0400-0500 MDT	183
86	Height section and orientation of idealized HBR relative to Tower A as represented in CTDM	194

TABLES

Number Page

1 Descriptive Statistics and Associated Analyses of Model Performance 17

2 Summary of Residual Statistics for SHIS #1 18

3 Summary of Areas for Improving CTDM(11083) Based on Analyses of Experiments 201 and 210 94

4 Comparison of Model Performance Statistics for CTDM(14083) and CTDM(11083-E) Using the SHIS #1 MDA 105

5 Preliminary Visualization Experiment Examples of H_c Analyses 118

6 FMF Tow-Tank Experiments 120

7 Measured Heights of 10-cm High Streamer at the Upwind Base and Crest of the HBR Model 121

8 Instruments, Heights and Direct and Derived Measures at the Four Towers 127

9 Definitions of the Measures 129

10 Primary Sampler Locations 135

11 Additional Samplers 136

12 Number of SHIS #2 Experimental Hours with Tracer Gas Releases and Concentrations 142

13 Summary of Tracer Concentration Data 143

14 Five Highest χ/Q Observed at HBR and CCB 151

15 Hogback Samplers by Row 166

16 SHIS #2 Tracer Data Withheld for Model Validation Purposes 185

17 SHIS #2 Hours Selected for Initial Modeling 187

TABLES (Continued)

Number Page

18 17-Hour Data Base Summary Statistics 188

19 Comparison of Wind Measurements at 40 m for 17 Hogback Study Hours 190

20 Summary of Model Input Data for SF_6 and CF_3Br Releases 191

21 Model Performance Statistics, 17-Hour Data Base . . . 195

22 Results of Hourly CTDM(E) Simulations 197

23 Results of Hourly CTDM Simulations 198

24 Results of Hourly COMPLEX I Simulations 199

25 Results of Hourly COMPLEX II Simulations 200

26 Experiment 11 Five-Minute Average Winds 201

LIST OF SYMBOLS AND ABBREVIATIONS

SYMBOL	
$a(z)$	Radius of an ideal circular hill in horizontal cross-section
α	Product of $T_u \cdot T_h$
α_m	Angular horizontal plume spread, including meander
α_s	Angular horizontal plume spread, without meander
b_{scat}	Scattering coefficient
C	Concentration
χ	Concentration
C_i	Instantaneous concentration
C_{max}	Maximum hourly averaged concentration
C_o	Observed concentration
$C_o(s_o, z)$	Vertical profile of concentration modeled at $s = s_o$
C_p	Modeled concentration
d	Distance of the source from the stagnation point
D	Effective radius of curvature minus the dividing-streamline height
D'	D modified to simulate stability-dependent horizontal plume distortion
$\Delta\theta$	Angle between mean plume trajectory and the trajectory over the hill center
E	Plume spread angle in the vertical
ϵ	Error or residual
Fr_H	Froude number based upon hill height
Fr_L	Froude number based upon hill length
γ	Molecular exchange coefficient
h	Terrain elevation above a "zero plane"
H	Hill height (crest)
H_c	Critical dividing-streamline height
H_m	Elevation of the peak observed concentration
H_s	Plume centerline height over terrain (stand-off distance)
H_*	$H-H_c$

θ	Wind direction
θ_d	Direction of the stagnation streamline
θ_o	Mean wind direction of approach flow
i_x, i_y, i_z	Turbulence intensities alongwind, crosswind, and vertical
L	Distance beyond s_o to the point where $T = T_{min}$
L_o	Distance beyond s_o to the peak terrain elevation along the plume trajectory
$L_{1/2}(H_c)$	Half-length (horizontal alongwind scale) of the hill midway between H and H_c
m_a	Arithmetic mean
m_g	Geometric mean
N	Number (in a summation)
N	Brunt-Vaisala frequency
p	Parameter equivalent to $2\gamma^2$
$P(\theta)$	Wind direction probability distribution function
Q	Tracer emission rate
$Q(s,z)$	Vertical profile of mass flux
r_a	Measure of resolution (arithmetic)
r_g	Measure of resolution (geometric)
r, θ, z	Polar coordinate system
R_e	Effective radius of curvature
Ri	Richardson number
s	Distance along plume trajectory
s	Distance from source to receptor
s_a	Distance along terrain from impingement point to receptor
s_a	Arithmetic standard deviation
s_g	Geometric standard deviation
s_o	Distance along wind direction from source to terrain at H_c elevation
s_v	Virtual source distance (vertical plume spread)
s'_v	Virtual source distance (horizontal plume spread)
σ	Standard deviation
σ_θ	Standard deviation of horizontal wind direction
σ_u	Standard deviation of alongwind velocity fluctuations of the mean wind

σ_v	Standard deviation of crosswind velocity fluctuations of the mean wind
σ_w	Standard deviation of vertical velocity fluctuations
σ_y,σ_z	Crosswind horizontal and vertical standard deviation of tracer concentrations
σ_{zo}	Value of σ_z at $s = s_o$
T	σ_z enhancement factor (terrain factor)
T_h	Terrain factor for plume streamline height above ground
T_{min}	Minimum value of T along plume trajectory
T_o	Minimum value of T near center of hill
T_σ	Terrain factor for vertical plume spread
T_u	Terrain factor for plume transport speed
u	Generic wind speed
U_o	Approach flow wind speed profile
x	Generic distance downwind from source
x_v	Virtual source distance
y	Generic crosswind distance from plume centerline
x_r,y_r,z_r	Tracer release coordinates
x_R,y_R,z_R	Receptor coordinates
z_r	Plume release height

ABBREVIATIONS

ARLFRO	Air Resources Laboratory Field Research Office
APS	Arizona Public Service Company
ATDL	Atmospheric Turbulence and Diffusion Laboratory
BAO	Boulder Atmospheric Observatory
BFM	Butte Field Model
CCB	Cinder Cone Butte
CTDM	Complex Terrain Dispersion Model
CTMD	Complex Terrain Model Development
EPA	U.S. Environmental Protection Agency
ERT	Environmental Research & Technology
ESRL	Environmental Sciences Research Laboratory
FMF	Fluid Modeling Facility
FMN	Farmington Airport
GC	Gas chromatograph

GLC	Ground-level concentration
HBR	Hogback Ridge
Hz	Hertz
LASL	Los Alamos Scientific Laboratory
LMF	Linear mass flow meter
MDA	Modelers' Data Archive
MDS	Meteorological Data System
MDT	Mountain Daylight Time
MRI	Meteorology Research, Inc.
MSL	Mean Sea Level
$\mu s/m^3$	Micro-seconds per cubic meter
NAAQS	National Ambient Air Quality Standard
NAWC	North American Weather Consultants
NOAA	National Oceanic and Atmospheric Administration
ns/m^3	Nano-seconds per cubic meter
ppb	Parts per billion by volume
ppt	Parts per trillion by volume
PDF	Probability distribution function
PFM	Potential Flow Model
PNM	Public Service Company of New Mexico
PPC	Plume path coefficient
PSD	Prevention of Significant Deterioration
RTD	Resistance Thermometric Device
SHIS	Small Hill Impaction Study
TRC	TRC Environmental Consultants, Inc.
WPL	Wave Propagation Laboratory
WSSI	Western Scientific Services, Inc.

ACKNOWLEDGEMENTS

Continuing progress in the EPA CTMD program reflects the dedicated efforts of many people. In particular, we gratefully acknowledge the special contributions of the following individuals to the Hogback Ridge field program:

- Ray Dickson, Gene Start, Jerry Sagendorf and Russ Ackerman (NOAA ARLFRO) for flow visualization, tracer experiments, tracer analysis, 10-m and 30-m towers, and the meteorological data acquisition, communications and analysis system;
- Wynn Eberhard (NOAA WPL) for operation of the lidar system, and Bill Neff (NOAA WPL) for the Doppler acoustic sounder;
- Clark King (NOAA WPL) and colleagues at NOAA ATDL for operation of the tethersonde systems;
- Norm Ricks (Morrison/Knudsen) for the photography program--and especially for his unfailingly good spirits during cold and lonely vigils high on the 150-m tower;
- Bob Lehman, Steve Anderson and John Faust, for site logistics and operation of the 150-m tower; and
- Dan Godden, for command center coordination and real time data analysis.

Finally, we give special thanks to Frank Schiermeier, Bill Snyder and George Holzworth (EPA) for their unflagging support and encouragement. Throughout, they have willingly shared with us the difficult times, and should share in our successes as well.

SECTION 1

INTRODUCTION

The U.S. Environmental Protection Agency is sponsoring the Complex Terrain Model Development (CTMD) program, a multi-year, integrated program to develop, evaluate, and refine practical plume models for calculating ground-level air pollutant concentrations that result from large emission sources located in mountainous terrain. The principal objective of the CTMD program is to develop models with known accuracy and limitations for simulating 1-hour average concentrations during stable atmospheric conditions, i.e., to handle the stable plume impaction problem.

The objectives of the program were described by Holzworth (1980) and generally follow the recommendations of the participants of the EPA sponsored workshop to consider the issues and problems of simulating air pollutant dispersion in complex terrain (Hovind et al. 1979). The program was subsequently designed with a perspective toward modeling and included model development efforts based on physical modeling, field experiments and theoretical work. The CTMD was designed to proceed from field experiments and physical modeling for isolated simple terrain features to field measurements/experiments centered on an operational full-scale power plant.

The program was begun in June 1980. The first major component was the Small Hill Impaction Study #1 (SHIS #1), a field experiment* conducted during the fall of 1980 at Cinder Cone Butte (CCB), Idaho. CCB is a roughly axisymmetric, isolated 100-meter tall hill located in the broad Snake River Basin near Boise, Idaho. The field program consisted of ten flow visualization (oil-fog) experiments and 18 multi-hour tracer gas experiments conducted during stable flow conditions with supporting meteorological, lidar and photographic measurements.

---

*The prime contractor for the CTMD is Environmental Research & Technology, Inc. (ERT). The principal subcontractors for the CCB experiments were Western Scientific Services, Inc. (WSSI), responsible for fixed meteorological data (towers, instrumentation and data communication) and North American Weather Consultants (NAWC), responsible for the experimental field program (tracer and smoke releases, tracer data collection, photography, mobile meteorology, and field logistics). In allied activities, the EPA Fluid Modeling Facility (FMF) has provided laboratory fluid modeling support; the NOAA Wave Propagation Laboratory (WPL) supported the field program with a manned lidar system; and TRC Environmental Consultants, Inc. provided independent data audits.

The CCB data were used to develop and evaluate two new, preliminary modeling algorithms (called the Impingement and Neutral models) and to evaluate the performance of current EPA complex terrain plume dispersion models (Valley, COMPLEX I, COMPLEX II, and Potential Flow Model (PFM)). The Impingement model simulates dispersion during strongly stable flows in which plumes remain approximately horizontal and impinge on and travel around the sides of CCB. The Neutral model simulates dispersion during slightly stable and neutral flows in which plumes rise over CCB. For the model evaluations, 45 hours were selected from the 18 tracer experiment days. The meteorological and tracer data were used in a "hands-off" mode: no modifications were made to the models to improve their predictions.

The EPA CTMD First Milestone Report - 1981 (Lavery et al. 1982) describes the air quality models that were evaluated, the evaluation methods, and overall model performance. The CCB field experiments and associated quality assurance activities are described, and a series of experiments conducted in the EPA Fluid Modeling Facility (FMF) towing tank to simulate the field studies are presented in an appendix.

The SHIS #1 tracer gas source data (emission rates, locations and heights of SF_6, CF_3Br, and oil-fog releases), concentration data and meteorological data (from six towers, a tethersonde and free balloons) were subsequently delivered to EPA and are available from the EPA Project Officer. A CCB Modelers' Data Archive (MDA) has also been prepared and is available from the Project Officer. It includes winds and other meteorological parameters derived specifically for the SF_6 and CF_3Br release heights as well as hourly average tracer gas emission rates and ground-level concentration data.

The EPA CTMD Second Milestone Report - 1982 (Strimaitis et al. 1983) documents work accomplished from fall 1981 through April 1982 to improve the Impingement and Neutral modeling approaches, to refine the meteorological and tracer gas data bases, and further analyze the data to relate plume behavior and observed meteorological conditions. Unlike the hands-off evaluations described in the First Milestone Report, the approach taken in this report was a case-study analysis. From the 45 hours used in the first report, 14 hours were selected for detailed individual case-study to illustrate and contrast various flow situations and ranges of model performance.

The second report describes improvements to the Impingement and Neutral models and the subsequent evolution to the Wrap and Lift models. It also describes several analyses of the CCB data base, including a comparison of turbulence statistics from tower measurements with those derived from lidar data and photographs, time-series and spectral analyses of wind data, and streamline deflection estimates based on temperature data.

The Second Milestone Report also contains, as an appendix, a report prepared by the EPA FMF. The report describes a series of wind tunnel and tow-tank experiments designed to study various aspects of stratified, sheared flow over a variety of simple obstacles, as well as flow over a model of CCB. In particular, the dividing-streamline concept is evaluated and shown to be appropriate for obstacles of differing aspect ratio embedded in stably stratified flows, both with and without wind shear.

This Third Milestone Report documents work accomplished from June 1982 through May 1983. It describes the further evolution of the Lift and Wrap models into one model, the Complex Terrain Dispersion Model (CTDM). Two versions of CTDM and three existing complex terrain plume models (Valley, COMPLEX I and COMPLEX II) have been evaluated with the entire 153-hour CCB MDA. An assessment of the performance of the models shows that a version of CTDM that simulates enhanced turbulence near the crest and lee of CCB is significantly better than the other models.

The various case-study and systematic analyses that have been performed in support of the model development efforts, as reported here and in the Second Milestone Report, and the physical modeling studies have led to a more complete understanding of the dynamics of flows and of plume dispersion around CCB. The concept of a dividing-streamline (H_c) has been shown to be useful in discriminating between essentially horizontal flows and flows that go over CCB. A tracer plume released above H_c tended to travel over the hill, and its plume path was consistent with streamlines in weakly stratified flow. The highest ground-level tracer concentrations during this latter sort of event were observed near the crest or on the lee side of CCB.

When a plume was released well below H_c, it tended to travel around the side of CCB, generally preferring one side. During this situation, the highest concentrations were measured on the upwind face of the hill or along the hill sides, depending on how often the plume lay along the stagnation streamline. A release at a height near H_c and close to the stagnation streamline produced the highest concentrations measured during the CCB experiments. These higher concentrations were generally observed at elevations near or below the release height.

An examination of turbulence intensity measurements, photographs and lidar data has shown that the vertical plume growth is related to the vertical turbulence intensity and Brunt-Vaisala frequency and is proportional to the square root of downwind distance to distances of about 1 km. For distances farther downwind, the growth rate is uncertain although physical modeling studies suggest that the growth rate goes to zero after a certain travel time. The data measured on the towers located on CCB indicate that turbulence is enhanced near the crest and on the lee side. Plume growth in the horizontal is controlled by high frequency turbulence and by low frequency meanders with time scales of about two hours.

This Third Milestone Report also provides an overview of the second Small Hill Impaction Study (SHIS #2)* conducted during October 1982 at

---

*ERT is continuing to provide overall CTMD project management and is responsible for the model development. During SHIS #2, ERT was responsible for field management, the 150-m and 60-m towers, site logistics, and quality assurance. Through an Interagency Agreement with EPA, NOAA Air Resources Laboratory Field Research Office (ARLFRO) conducted the flow visualization and tracer experiments, was responsible for the 10-m and 30-m towers, and operated a real-time data acquisition and analysis system. NOAA WPL provided lidar, acoustic sounders, a tethersonde, and optical and sonic anemometers. TRC provided independent performance audits.

Hogback Ridge (HBR) near Farmington, New Mexico. The HBR experimental design was similar to the CCB design. It included tracer and flow visualization experiments with concurrent meteorological, lidar and photographic measurements. The experiment produced approximately 179 tracer hours and has effectively extended the modeling data base to include flow and dispersion around a two-dimensional ridge.

An initial analysis of the HBR tracer concentrations and the unedited meteorological data suggests that the dividing-streamline concept is applicable to ridge settings. H_c distinguishes between flows that surmount the ridge and highly variable flows below. The highest concentrations were measured on the windward side of HBR when tracer gas was released below H_c.

The next field experiment in the CTMD program will be conducted at an electric generating power plant located in mountainous terrain. The site selection process is underway. Feasibility studies will be conducted at one or more prospective sites during the fall of 1983. The full-scale study is scheduled for the fall of 1984.

This report consists of five major sections and two appendices. Section 2 presents the results of the evaluation of the complex terrain models with the SHIS #1 MDA. The current version of CTDM and suggested model upgrades are described and evaluated in Section 3. Section 3 also describes case-study analyses of CCB Experiments 201 and 210. The Hogback Ridge experiment and its initial findings are presented in Section 4. The preliminary modeling of a 17-hour subset of the HBR data base with CTDM, Valley, COMPLEX I and COMPLEX II is discussed in Section 5. Section 6 presents the summary, conclusions, and recommendations for future work. Appendix A describes a laboratory simulation of neutral plume dispersion over Cinder Cone Butte. Appendix B discusses an initial analysis of the SHIS #2 monostatic acoustic sounder and sonic anemometer data.

SECTION 2

EVALUATION OF COMPLEX TERRAIN MODELS WITH THE CCB DATA BASE

An initial comparison of modeled and observed SF_6 concentrations from SHIS #1 was summarized in the CTMD First Milestone Report. COMPLEX I and II, PFM, Valley, and two new algorithms, Neutral and Impingement, were evaluated by means of SF_6 concentrations from up to 45 CCB experiment hours. Model performance statistics similar to those recommended by Fox (1981) were used to assess relative model performance.

During the preparation of the First Milestone Report, the Valley model was the only EPA complex terrain screening model recommended for regulatory use. Since then, EPA (Rhoads 1982), in an addendum to the "Regional Workshop on Air Quality Modeling: A Summary Report" (April 1981), has recommended a new regulatory approach--a two-tiered screening approach for complex terrain applications. Valley model calculations provide the initial screening. If these calculations suggest violation of any NAAQS or PSD increment, then a second-level screening technique may be used. EPA recommends COMPLEX I as the second-level screening technique.

The Second Milestone Report described the evolution of the Neutral and Impingement models to the Lift and Wrap models. Since that time, the Wrap and Lift algorithms have evolved into the Complex Terrain Dispersion Model (CTDM); the meteorological and tracer gas concentration data bases have been refined; and a Modelers' Data Archive (MDA) has been prepared for all available SF_6 and CF_3Br tracer gas release periods. In all, 153 modelable tracer-hours of data are now available from SHIS #1.

This section contains the results of comparing modeled and observed concentrations using this expanded data base. A description of the methods used to prepare the SHIS #1 MDA is followed by a brief explanation of how Valley, COMPLEX I, COMPLEX II, and CTDM are run with this archive data. Model performance statistics are then presented, and an analysis of model performance follows.

2.1 SHIS #1 Modelers' Data Archive

The MDA developed from the SHIS #1 contains observed 1-hour average tracer gas concentration data, tracer release information, and observed and derived meteorological parameters estimated at release height for each of the hours during SHIS #1 in which either SF_6 or CF_3Br tracer gas was released. The method of estimating meteorological data representative of tracer gas release heights relies on a few central assumptions and is objectively applied to all the data with few exceptions. Those assumptions and a description of the procedures are presented in the following sections.

Because the meteorological data contained in the archive are estimates of the meteorological conditions affecting the transport and diffusion of the tracer gases, they should be viewed as approximate. This is particularly evident in the estimated wind direction. For example, the wind set at the 40-m level on Tower A was partially operational during experiments 205, 206, 210, and 211. Some data from this instrument are recoverable, but winds are estimated at this level only by making an assumption about the difference in wind directions between 40 m and 80 m. At times, the assumption may not represent the real situation. With the scale of Cinder Cone Butte, a resulting wind direction error of less than 10° could at times cause the modeled plume to miss the hill entirely during a period when the actual plume produced significant concentrations on the hill.

Subjective estimates of the most appropriate wind directions as derived from evidence of actual plume transport directions are in preparation and will be included in a second version of the MDA when available.

2.1.1 Tracer Concentration Data

Tracer gas concentration data from the SHIS #1 data base (available through EPA) include data from 1-hour samplers, co-located 1-hour samplers, 10-minute samplers, and reflection mast samplers (a subset of the 10-minute samplers), and they include "recount" concentration data resulting from re-analyzing a subset of all bag samples as part of the quality assurance program. The data base also provides additional information on the sampler location and the quality of each individual sample.

Tracer gas data contained in the MDA have been assembled from the SHIS #1 data base. All values are reported as 1-hour averages. These averages include concentrations from all 1-hour sampling bags labeled as good, the average of good concentrations obtained from the two samples collected at co-located sampler sites, the average of the two concentrations obtained from samples included in the recount analyses, the average of good 10-minute concentrations at standard 10-minute sampler sites, and the average of good 10-minute concentrations obtained at the foot of the sampling mast locations. In the case of the 10-minute samples, hourly concentration averages are included only if not more than one 10-minute period was missing from the hour.

The position of each sampler is included in the archive along with the 1-hour average tracer gas concentration. The coordinate system is a Cartesian system with origin at the center of CCB, x-axis oriented toward true east, and y-axis oriented toward true north. The sampler position identification code for each concentration is also included. A map of CCB with each sampler position is contained in the First Milestone Report.

2.1.2 Tracer Release Information

The MDA contains the average emission rate of the tracer gas, the polar coordinates of the position of the source, the elevation of the base of the source crane, the height of the source above the ground, and the times at which the tracer gas was turned on and turned off.

The emission rate is an average mass release rate (g/s) from the time at which the release valve was opened to the time at which it was shut off. In some cases, this period of time was less than 1 hour, but in most cases it was several hours. The start and stop times for the release are referenced to the beginning and ending times of each experiment hour, respectively. A start time of -10 (minutes) indicates that the tracer was released ten minutes before the start of the sampling hour. An end time of -5 (minutes) indicates that the release ended 5 minutes before the end of the hour.

Coordinates of the source position are expressed in the hill coordinate system, a polar grid centered on Cinder Cone Butte. The zero height contour in this system corresponds to the 3100-ft elevation MSL (944.9 m). Release elevations are presented in meters above the ground, and the elevation of the ground at the release position is given as the difference in meters from 944.9 m MSL. A topographic map of Cinder Cone Butte can be found in the First Milestone Report.

2.1.3 Meteorological Data

Meteorological data contained in the MDA differ from those contained in the SHIS #1 data base in that: all quantities apply to the release height of the tracer gas rather than to the height of fixed instrument levels; derived parameters computed from the meteorological data base are included; and 1-hour averages are constructed.

A "spline under tension" method (Cline 1974) was used to interpolate meteorological variables between instrument levels on Tower A. This method produces a linear interpolation when a tension factor of 50 is specified, and it produces a cubic spline curve through the data when a tension factor of zero is specified. The suggested nominal tension factor of 1.0 produces a smooth curve through all data points in a profile. It does not invent the cusps and regions of high curvature between data points that are common with the cubic spline. After inspecting a number of profiles produced with tension factors between 0.5 and 3.0, the factor 1.2 was selected. This factor produces slightly greater curvature near instrument levels than does a factor of 1.0, but it also reduces the magnitude of local maxima/minima between data points in regions where the vertical gradient of the profile quantity must change sign.

Meteorological conditions representative of release height are assumed to be equivalent to data taken from the Tower A vertical profile at the same height above the surface as the height of release, even though the surface elevation at the release point generally differs from the surface elevation at Tower A. This approximation is consistent with the spatial resolution of the meteorological instrumentation because the release locations lie between

1 and 2.5 km from Tower A, because differences in surface elevations between the base of Tower A and release locations vary between -6.1 m and 1.5 m with a mean difference of -3.7 m, and because the vertical resolution of wind measurements above 10 m on Tower A is 30 m or greater. (Wind sets were located at 2, 10, 40, 80, and 150 m.)

The sequence of 5-minute data in the MDA was constructed as follows:

- Tower A wind speeds, wind directions, and temperatures contained in the refined data base were scanned for missing data. When missing 5-minute values were encountered, they were replaced with values estimated by linear interpolation in time. Only UVW prop wind data were used to develop wind information because the F460 cup and vane instruments were placed only at the 2-, 10-, and 150-m levels, while most release heights were between 20 m and 60 m.

- The temperature, the vertical component of the wind speed, and the horizontal wind speed and direction were estimated at release height by "spline under tension" interpolation with a tension factor of 1.2. Horizontal speeds and directions were first broken into wind components, and the components were interpolated to obtain the wind speed and direction at release height. The 40-m level wind data were incomplete in four of the experiments (205, 206, 210, 211), so that interpolation of the winds between 10 m and 80 m was necessary. However, the u-component (east-west) of the wind data from 40 m was available, and the mean winds were approximately SE during each of these experiments rather than nearly N or S. By assuming that the directional wind shear was small between 40 m and 80 m at Tower A during these four experiments, estimates of the wind speed at 40 m were made with the 40-m u-component and the 80-m wind direction measurements. The resulting wind speed profiles indicated that the speeds estimated at 40 m are generally reasonable, and so these speed and direction estimates of 40-m level winds were used in the interpolation procedure for nearly all 5-minute periods during which the 40-m v-prop was inoperative. However, because the wind directions near 40 m appear to differ substantially from those at 80 m during the last hour of experiment 211, the spline interpolation between 10 m and 80 m was used for this period of time.

- Turbulence data were estimated at release height by employing a linear interpolation rather than the spline interpolation. The turbulence velocity scales σ_u, σ_v, and σ_w were obtained from the turbulence intensity values contained in the refined data base by multiplying by the wind speed. Unlike wind and temperature data, missing turbulence data were not filled in by interpolating in time. However, estimates of σ_w were prepared for those experiments in which one of the horizontal wind speed props malfunctioned at the 40-m level. In these experiments (205, 206, 210, and 211), reported values of i_z in the refined data base are flagged as bad because the reported wind speed is incorrect. But because the w-prop was working, the σ_w values are not necessarily deficient. σ_w was recovered by multiplying the original value of i_z by the original value of the wind speed. The value of σ_w was then interpolated to source height. A prop response correction derived from the work of Horst (1973) was applied. More information on its application to the Cinder Cone Butte data can be found in the Second Milestone Report. No prop response corrections were applied to σ_u or σ_v.

- The Brunt-Vaisala frequency, N, was estimated at source height by interpolating the temperature profile in the immediate vicinity of the release height to obtain the local temperature gradient.
- The dividing-streamline height, H_c, was obtained from the splined profiles of temperature and wind speed by means of the integral formula presented in the First Milestone Report. A bulk hill Froude number was calculated for the layer between H_c and the top of the tower, 150 m, and also for the layer between 2 m and 150 m. The hill height in both calculations is the difference between 95 m and the height of the bottom of the layer (either H_c or zero).
- The Pasquill-Gifford stability class was calculated from net radiation and wind speed data by means of the method of Williamson and Krenmayer (1980). Wind speeds measured by the cups at the 10-m level on Tower A (reported as scalar averages) and the net radiation data were interpolated in time whenever missing values were encountered. The stability class was calculated as a number between 1 and 6, where 1 denotes stability class A. Both the stability class and the 10-m wind speed are included in the data archive.

Most 1-hour average data in the MDA were obtained from this sequence of 5-minute average data interpolated to release height. Only stability class data were not obtained in this way. The 1-hour stability class was found from the 1-hour averages of net radiation and 10-m wind speed.

The remaining 1-hour average data in the MDA were constructed as follows:

- The wind speed and direction were calculated as both vector and "scalar" averages. Two versions of the "scalar" wind direction were calculated. One is a scalar average of the 5-minute vector resultant wind directions. The second is a vector average of unit vectors along each 5-minute vector resultant wind direction so that all directions have equal weighting, as in a scalar average, but the averaging is performed with vector arithmetic.
- Temperatures and parameters calculated from the splined profiles of the 5-minute temperature and wind data--N, H_c, Fr--were simply averaged to provide 1-hour average values.

- Horizontal turbulence data σ_u and σ_v were computed for 1-hour periods by adding the contribution due to the 5-minute turbulence values to the contribution due to the variability of the 5-minute average winds. Let $(\sigma)_{60,0}$ denote the total 1-hour value of the standard deviation; let $(\sigma)_{5,0}$ denote the total 5-minute standard deviation; and let $(\sigma)_{60,5}$ denote the standard deviation of the 5-minute average winds over a 1-hour period. Then

  $$(\sigma)^2_{60,0} = (\sigma)^2_{60,5} + \overline{(\sigma)^2_{5,0}} \quad . \qquad (1)$$

  Note that although prop response corrections were not applied to the $(\sigma)_{5,0}$ values, they were implicitly contained in $(\sigma)_{60,5}$ because the 5-minute wind data in the refined data base include corrections for prop response and wake effects. Also, because no time interpolation was performed on the 5-minute turbulence data, less than a full set of 12 values may be available during some hours. In these cases the average of the $(\sigma)^2_{5,0}$ values will be incomplete. The number of $(\sigma)_{5,0}$ values contained in each hour are denoted by N(su), N(sv), and N(sw) in the archive.

- The vertical turbulence σ_w was computed for 1-hour averaging periods in the same way as σ_u and σ_v, except that the prop response correction suggested by Horst (1973) was also applied. Neither the $(\sigma_w)_{5,0}$ nor the $(\sigma_w)_{60,5}$ data used in the formula for $(\sigma_w)_{60,0}$ have the correction already applied. Rather, the correction was applied directly to $(\sigma_w)_{60,0}$. Note that the construction of $(\sigma)_{60,0}$ by the above formula is exact in the case of σ_w, but only approximate in the case of σ_u and σ_v.

2.2 Complex Terrain Models Evaluated

2.2.1 Valley Model

The Valley model (Burt 1977) is recommended by EPA as the initial screen in a two-tiered screening approach for complex terrain analyses in support of regulatory decisions. Valley is designed to provide an estimate of the maximum 24-hour pollutant concentration expected to occur on elevated terrain near a point source of air pollution in any 1-year period. This concentration is computed with a steady-state, univariate Gaussian plume dispersion equation, modified to provide a uniform crosswind distribution over a 22.5° sector and using assumed worst-case meteorological conditions.

The model assumes that the plume travels toward nearby terrain with no vertical deflection until the centerline of the plume comes to within 10 m of the local terrain surface. Thereafter, the centerline is deflected to maintain a stand-off distance of 10 m from the terrain surface. The plume is considered to impinge upon the terrain at points where terrain height equals the plume height, and the impingement point used in the calculation of maximum plume impact is the nearest such topographic point as viewed from the source.

Worst-case meteorological conditions are defined by that combination of wind speed and Pasquill-Gifford (PG) dispersion stability class that produces the highest possible concentration at the impingement point. For large sources of air pollution, a stack-top wind speed of 2.5 m/sec and PG stability class F are recommended as those conditions that will produce the highest concentrations during stable conditions when plume impingement is most likely.

The model estimate is implied to be a 1-hour average concentration. The 24-hour average concentration is estimated by dividing this 1-hour average concentration by four, on the premise that the impinging plume may affect a specific point for no more than [illegible] hours in any 24-hour period. It should be stressed that because neither the tracer source release heights, crane locations, nor meteorological conditions were equivalently "persistent" from hour to hour during the actual experiments, the CCB data base is not appropriate for testing the Valley model as it is used in regulatory applications.

The longest steady averaging period for tracer releases and concentrations in the CCB field study was four hours. Most steady averaging periods were between one and two hours. Consequently, only 1-hour Valley estimates have been compared with maximum observed hourly tracer concentrations.

The hourly emission rate has been reduced for those hours in which tracer gas was released for less than a full hour. On and off times are taken from the MDA, and a transit time shift has been included that has been calculated from the mean hourly scalar wind speed at source height and the distance to the center of the hill.

Release crane positions during the experiments range from a distance of 540 m to a distance of 1,424 m from the center of the hill. The local release heights of the nonbuoyant tracer gas vary from 15 m to 60 m. The distance to the nearest point of impingement is taken to be the difference between the distance from the source to the center of the hill and the radius of a representative circle fit to the hill at the height of the source. This representative radius is given by (CTMD First Milestone Report)

$$a(z_r) = 970\, z_r^{-0.38} \tag{2}$$

for elevations between 10 and 60 m above 944 m MSL.

Concentration estimates scaled by the emission rate are computed by:

$$\frac{C}{Q} = \frac{(2.03)(10^6)}{\sigma_z u x} \exp(-0.5\,(H_s/\sigma_z)^2), \tag{3}$$

which is derived from Equation 2-1 of the Valley Model User's Guide (Burt 1977). C is in units of $\mu g/m^3$, and Q is in units of g/sec. H_s is the altitude of the plume centerline above local terrain (stand-off distance).

The wind speed is set to 2.5 m/sec, and the stand-off distance is fixed at 10 m to be consistent with the regulatory applications of Valley. However, because the 10-m value is not based on any theoretical analysis, it may not be an appropriate scale for the narrow plume configuration of the tracer experiments (compared to plume sizes encountered with large pollutant sources).

The standard deviation of the vertical pollutant distribution (σ_z) is calculated from the Pasquill-Gifford-Turner (PGT) formula:

$$\sigma_z = 0.362\, x^{0.55} - 2.7 \tag{4}$$

The constants in this equation are taken from Table 2-1 of the Valley Model User's Guide. They are applicable for PG stability class F over a range of x between 100 and 1,000 m, which includes all of the impingement distances in the CCB archive.

2.2.2 COMPLEX I and COMPLEX II Models

COMPLEX I and COMPLEX II are sequential complex terrain models designed to estimate 1-hour, 3-hour, 24-hour, and annual pollutant concentrations resulting from point-source emissions. Concentrations are estimated at many receptors using hour-by-hour meteorological data. COMPLEX I is the EPA-preferred second-level screening technique. COMPLEX II has been issued by EPA for public testing and evaluation.

Several terrain treatment options (formulated by the Complex Terrain Team at the February 1980 Chicago Workshop on Air Quality Models) are available in the COMPLEX models. The standard option for PG stability classes E and F is based on the plume behavior simulated by the Valley model. This was the option selected for evaluation with those stable hours in SHIS #1. (The COMPLEX models also contain a buoyancy-induced dispersion option, but this feature has not been used in this modeling because the tracer releases are nonbuoyant.)

COMPLEX I is a univariate Gaussian plume model with 22.5° sector averaging in the horizontal. It uses the PG stability class system. COMPLEX II differs from COMPLEX I only in its representation of crosswind plume spread. Whereas COMPLEX I assumes a 22.5° horizontal sector averaging, COMPLEX II assumes the familiar crosswind Gaussian profile. (In all other respects, the two models are identical.)

COMPLEX I for stable (class E, F) conditions is essentially an extension of the direct-impingement Valley model to hourly averaged wind speed, wind direction, and stability class instead of the assumed worst-case meteorology; COMPLEX II replaces Valley's 22.5° horizontal sector averaging with a Gaussian crosswind profile. For neutral or unstable conditions, COMPLEX I and COMPLEX II permit different (nonimpingement) terrain assumptions. For stability classes A through D, the terrain treatment allows the plume centerline to rise over terrain features, but at a height less than its initial height over flat terrain. Its actual height at any point is computed from its initial height, the local terrain height, and a plume path coefficient. The resultant simulated plume height above the local elevated terrain height is always at least half its initial height when the recommended plume path coefficient is used.

The evaluation of COMPLEX I and COMPLEX II with the CCB data base was performed by embedding the essential computational algorithms of these two models within a computer code called the Butte Field Model (BFM). The COMPLEX algorithms were invoked by selecting specific options for plume path coefficients, dispersion parameters, sector averaging, and surface reflection treatment.

Input data for the models were taken from the MDA. They consisted of hourly scalar average wind speed and unit-vector average wind direction at source height, source location, hourly stability class, receptor locations, and receptor heights. Receptor information was provided for all potential (93) sampling locations. Although the samplers were designed to measure tracer concentrations no closer to the surface than 1 m, no receptor height offset was used in the modeling because the model resolution is no more accurate than 1 m.

In addition, the BFM code has been modified to accommodate those experiment hours that contain fewer than 60 minutes of tracer gas release. Start and stop times have been computed from data contained in the MDA, and transport time delays have been estimated from the mean wind speed for the hour and the distance from the release point to the hill center. The mean hourly speed is used rather than the local 5-minute average speed because the variability of the 5-minute average speeds is greatest at low wind speed. The travel time is likely to extend beyond a single 5-minute period when the wind speed is low, and therefore some speed averaging occurs over the time of travel. The hourly tracer gas release rate is reduced by multiplying by the ratio of the net period of tracer gas relese to 60 minutes.

2.2.3 Complex Terrain Dispersion Model (CTDM)

CTDM is the result of combining the Lift and Wrap algorithms described in The Second Milestone Report into one model for use in analyzing the data from SHIS #1. Unlike the other models evaluated, CTDM has the ability to utilize onsite measurements of turbulence and flow parameters beyond the mean wind speed and the inferred surface layer stability class. Version 11083 of CTDM is described in detail in Section 3.2.

The Probability Distribution Function (PDF) form of CTDM(11083) and that of CTDM(11083-E) have been chosen for evaluation in this section. Note that version 11083-E includes a terrain enhanced σ_z. The probability distribution of wind directions was constructed from the 5-minute wind direction and i_y data contained in the MDA. Other input meteorological data included hourly values of H_c, i_z (Horst-corrected), scalar wind speed, unit-vector average wind direction, and local Brunt-Vaisala frequency. Receptor data were provided for all 93 potential sampling locations, and model estimates of tracer gas concentrations were computed at the surface of the hill.

The model also contains an adjustment for those hours that contain fewer than 60 minutes of tracer gas release. As in the BFM simulation of

COMPLEX I and COMPLEX II, start and stop times and a transport time shift are computed, but the PDF form of CTDM (11083) adjusts the PDF rather than the hourly emission rate. All 5-minute periods that contain fewer than 2.5 minutes of tracer material (after accounting for transport time) are removed from the PDF computation.

2.3 Model Performance Statistics

The evaluation of the several complex terrain models is based primarily on the analysis of residuals

$$\epsilon = C_o - C_p \tag{5}$$

where C_o is the observed concentration and C_p is the corresponding predicted concentration. Both C_o and C_p have been normalized by dividing by the tracer gas emission rate. The specific evaluation measures and methods follow from the methods discussed in the First Milestone Report, from the results of the AMS/EPA workshop on model validation and model uncertainty (Fox 1981), from the EPRI workshop on validation of plume models (Londergan 1980), and from the work of Venkatram (1982).

Two kinds of residual statistics are used, arithmetic and geometric. Arithmetic means and standard deviations are particularly useful if the residuals are normally distributed. For residuals that are more nearly log-normally distributed, geometric statistics are more useful. Log-normal residuals are transformed into normally distributed residuals by the transformation

$$C' = \ln C. \tag{6}$$

The arithmetic mean and standard deviation of the residuals are computed as

$$m_a = \frac{1}{N}\sum_i \epsilon_i = \frac{1}{N}\sum_i (C_0 - C_p)_i \tag{7}$$

$$s_a = \left[\frac{1}{N}\sum (\epsilon_i - m_a)^2\right]^{1/2} \quad .$$

Because of the transformation in Equation 6, the mean and standard deviation of transformed, log-normally distributed residuals become

$$m_g = \exp \frac{1}{N}\sum_i \ln (C_o/C_p)_i \tag{8}$$

$$s_g = \exp\left[\frac{1}{N}\sum_i (\ln (C_o/C_p)_i - \ln m_g)^2\right]^{1/2}$$

The above equations are numerically well-behaved if neither C_o nor C_p is zero. However, there are times when even the peak hourly C_p is estimated to be zero. Because different models may produce different numbers of "zero" hours, intercomparison of m_g and s_g statistics for these models becomes somewhat imprecise if these zeros are simply removed from the statistics.

A second approach is also used in this report. When plotted on log-probability paper, a log-normally distributed set of residuals should produce a straight line. If we assume that the residuals for a particular model applied to the CCB data base represent one sample of the "true" residual distribution for that model, then small variations from a straight line plot may be neglected compared to the overall trend contained in the sample. The geometric mean residual (m_g), or bias, is the intersection of the trend line with the 50th percentile, and the geometric standard deviation (s_g), or noise, is found from the slope of the trend line. Let m denote the value of C_o/C_p along the trend line for the nth percentile, and let p denote the number of standard deviations from the center of a normal distribution to the point at which the area under the curve equals n/100. Then

$$s_g = \left(\frac{m}{m_g}\right)^{1/p} \quad . \tag{9}$$

Note that because n may vary between 0 and 100, while the area under half of the normal curve is at most 0.5, the sign of p will depend on whether m is less than or greater than m_g.

This method for estimating m_g and s_g does not suffer from numerical problems of vanishingly small values of C_o or C_p, because C_o/C_p ratios for these values occur in the tails of the distribution which are neglected. Their influence is accounted for in the position and slope of the trend line.

A general discussion of the interpretation of model performance residuals is contained in the First Milestone Report, in the EPRI workshop report (Londergan 1980) and in the paper by Venkatram (1982). The characteristics of an ideal model are easily stated. The modeled concentrations will nearly match observed concentrations at all points. Consequently, m_a and s_a will be nearly zero, or m_g and s_g will be nearly one. Furthermore, a plot of the residuals versus C_p, or any other combination of the observed or input meteorological parameters, would show the residuals to be normally distributed in a narrow band, and therefore uncorrelated with C_p (or other modeling parameters). The degree to which the mean residual for a particular model differs from the ideal mean and the degree to which the standard deviation of the residuals differs from the ideal standard deviation are measures of the overall accuracy and precision of the model.

Beyond these measures, a desirable attribute of a model is its ability to distinguish among predictions corresponding to different dispersion and flow conditions. This "resolution" depends on the relationship between the precision of the model and the separation between individual model predictions. Because the precision, as measured by the standard deviation of the residuals ($\sigma(\epsilon)$), represents the uncertainty of the model estimates, a model will exhibit better resolution if the "distance" between individual model estimates exceeds the uncertainty. The average "distance" among a set of model estimates is the standard deviation of the modeled concentrations $\sigma(C_p)$. Therefore, the ratio of the standard deviation of the residuals to the standard deviation of the model estimates should be as small as possible to maximize the resolution:

$$r = \sigma\ (\epsilon)/\sigma\ (C_p) << 1. \qquad (10)$$

If the residuals are normally distributed, then

$$r_a = s_a\ /\ \sigma\ (C_p). \qquad (11)$$

If the residuals more nearly follow a log-normal distribution, then

$$r_g = \ln s_g\ /\ \sigma\ (\ln C_p). \qquad (12)$$

The analysis of residuals is based on the residuals of (1) peak concentrations paired in time, but unpaired in space, and (2) all concentrations on CCB paired in time and space. The emphasis on these two sets of residuals is based on the necessity of the model to predict the highest concentrations* and to simulate properly the dynamics of the flows and turbulence that determine the ground-level concentrations on CCB. In addition to the statistics of the residuals, the residuals are plotted against various meteorological parameters to help ascertain biases or uncertainties in the model input or formulation. Table 1 summarizes the residual statistics and graphical displays used in the next subsection.

2.4 Analysis of Model Performance

Overall residual statistics developed by comparing model calculations with tracer gas concentrations sampled at CCB are given in Table 2 and plotted in Figure 1. Results are presented for five models,

- CTDM (11083-E)
- CTDM (11083)
- Valley
- COMPLEX I
- COMPLEX II

The columns labeled "Peak Concentrations" in Table 2 summarize the errors in estimating 1-hour maximum concentrations, regardless of location, over the 153 tracer hours. The columns titled "All Concentrations" summarize the mean errors in estimating concentrations observed at all sampling points (paired in space and time).

---

*For example, compliance with air quality standards is most often estimated in terms of the highest, second-highest modeled concentration at a receptor location.

TABLE 1. DESCRIPTIVE STATISTICS AND ASSOCIATED ANALYSES OF MODEL PERFORMANCE

	Means	Variances	Distributions	Scatter Plots
C_o	$\overline{C_o}$	$\sigma(C_o)$	–	vs. C_p
C_p	$\overline{C_p}$	$\sigma(C_p)$	Cumulative frequency	vs. C_o
C_o-C_p	m_a	s_a, r_a	–	
C_o/C_p	m_g	s_g, r_g	–	
$C_{o_{max}} - C_{P_{max}}$	m_a	s_a, r_a	–	vs. met
$C_{o_{max}}/C_{P_{max}}$	m_g	s_g, r_g	Cumulative frequency	vs. met

met: u, u/N, $i_y * i_z$, $1-H_m/z_r$, $1-H_c/z_r$ where H_m is the elevation on CCB of the maximum C_o, and z_r is the relese height of the plume.

TABLE 2. SUMMARY* OF RESIDUAL STATISTICS FOR SHIS #1

	Peak Concentrations (unpaired in space)						All Concentrations		
	m_a	s_a	r_a	m_g	s_g	r_g	m_a	s_a	r_a
CTDM(11083-E)	3.3	27.4	0.90	1.37 (1.23)	3.2 (3.3)	0.99	0.50	12.7	1.13
CTDM(11083)	2.8	33.7	0.88	2.08 (1.70)	6.9 (5.2)	1.18	-0.51	15.4	1.01
Valley	-41.0	25.5	1.63	0.24	3.0	5.52	--	--	--
COMPLEX I	-15.0	37.9	0.93	0.65 (0.53)	3.8 (3.2)	1.29	-6.04	21.9	0.99
COMPLEX II	-60.1	99.7	0.94	0.38 (0.32)	5.0 (4.6)	1.09	-5.61	36.9	0.99

Note: ( ) values of m_g, s_g are calculated directly from the C_o/C_p ratios, with the $C_p = 0$ values removed.

---

*Based on the 153 tracer hours from the CCB data base. Arithmetic m_a and s_a statistics carry units of 10^{-6}sec/m^3 or μs/m^3.

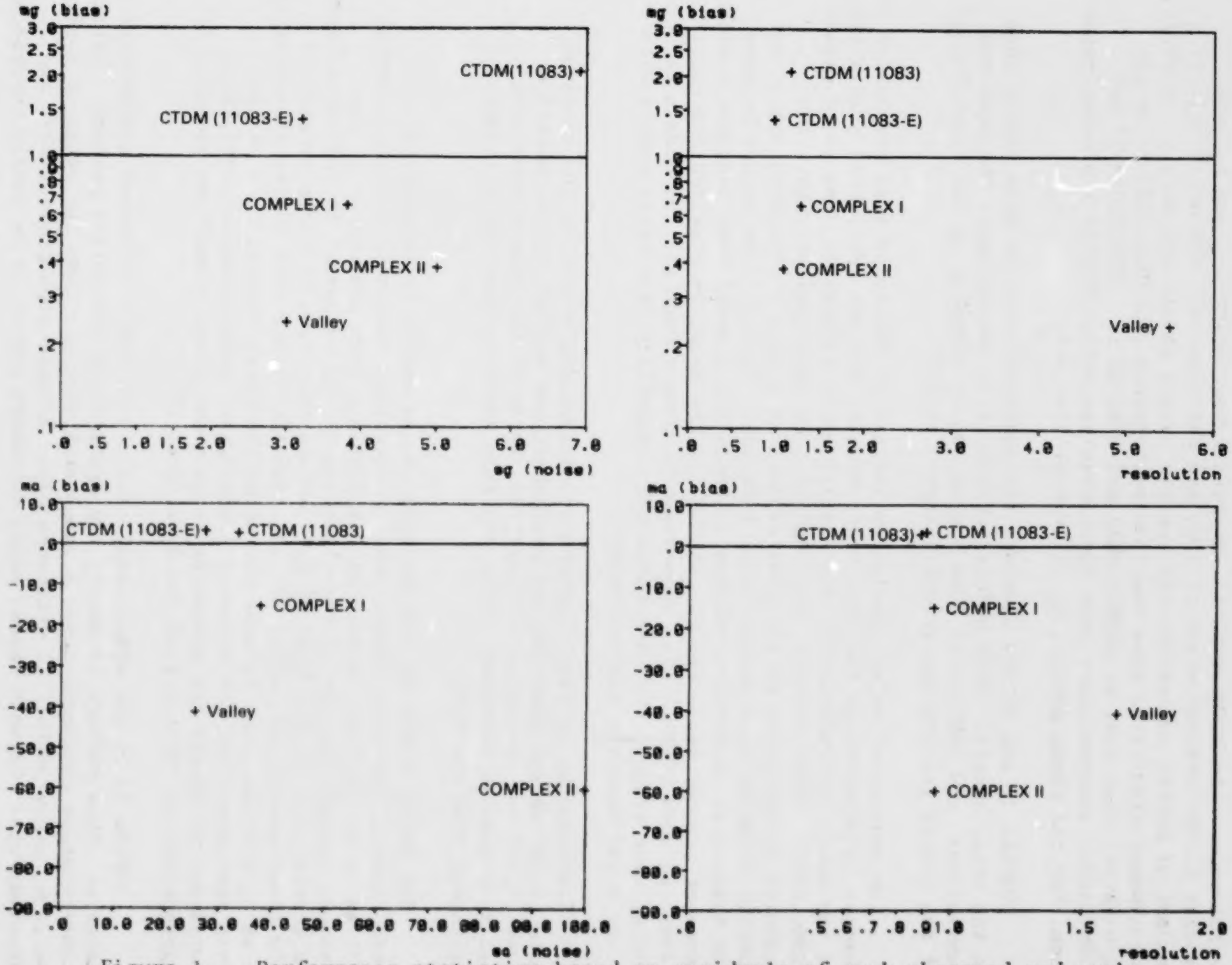

Figure 1. Performance statistics based on residuals of peak observed and peak modeled concentrations for Valley, COMPLEX I, COMPLEX II, CTDM (11083), and CTDM (11083-E) applied to SHIS #1 data (153 hours).

The residual statistics suggest that CTDM(11083-E) has the best overall performance. The CTDM(11083-E) log-normal statistics (m_g and s_g) are closest to the desired value of 1.0, and the bias (m_a) and noise (s_a) of the set of paired concentrations are the lowest of all the models. However, the summary statistics show that the performance of CTDM(11083-E) is not much better than that of CTDM(11083) and COMPLEX I. CTDM(11083-E) and CTDM(11083) underestimate peak concentrations while COMPLEX I overestimates them. For the three models, s_g is greater than 3.0.

COMPLEX II and Valley simulate the observations much more poorly than do the other models. Both models substantially overestimate the peak concentrations, and COMPLEX II does a poor job in reproducing the distribution of the tracer gas concentrations observed on CCB.

The measure of model resolution identifies Valley as less responsive to changes in meteorology than the other models, but the resolution statistics of the other four models are not significantly different. One would expect CTDM(11083), CTDM(11083-E), and COMPLEX I to have similar resolution measures on the basis of the scatterplots of Figure 2 discussed below, but COMPLEX II would be expected to be inferior. This dilemma occurs because the measure of resolution reduces to unity for a model that produces a wide range of concentration values compared to the range in observed concentrations, as does COMPLEX II. Consequently, even though all the models except Valley have roughly the same resolution capability, the three models with lower noise measures perform better.

Scatterplots of peak observed concentrations scaled by the emission rate (C_o/Q) versus peak modeled concentrations scaled by the emission rate (C_p/Q) are presented in Figure 2. Three of the models show qualitatively similar patterns, while two show patterns that are distinctly different from the rest.

The Valley model is not designed to use onsite meteorological measurements, but uses "worst-case" meteorology instead. Therefore, model estimates of C_p/Q only depend on the distance from the source to the nearest terrain feature at the elevation of the release. At CCB, this leads to a relatively narrow band of C_p/Q values that is unlike the pattern of the other models evaluated. We see from the figure that Valley overestimates most C_o/Q values, but it underestimates the seven largest C_o/Q values. This indicates that the standard "worst-case" meteorological conditions contained in Valley for screening large power plant plumes are probably not appropriate on the scale of the SHIS #1 at CCB.

COMPLEX II is the other model with a distinctly different scatterplot pattern. This pattern is nearly the opposite of the Valley pattern. Valley concentration estimates cover a range much narrower than the range of observations, while COMPLEX II estimates cover a range much greater than the observations. In both cases, model estimates appear to be poorly correlated with the observations.

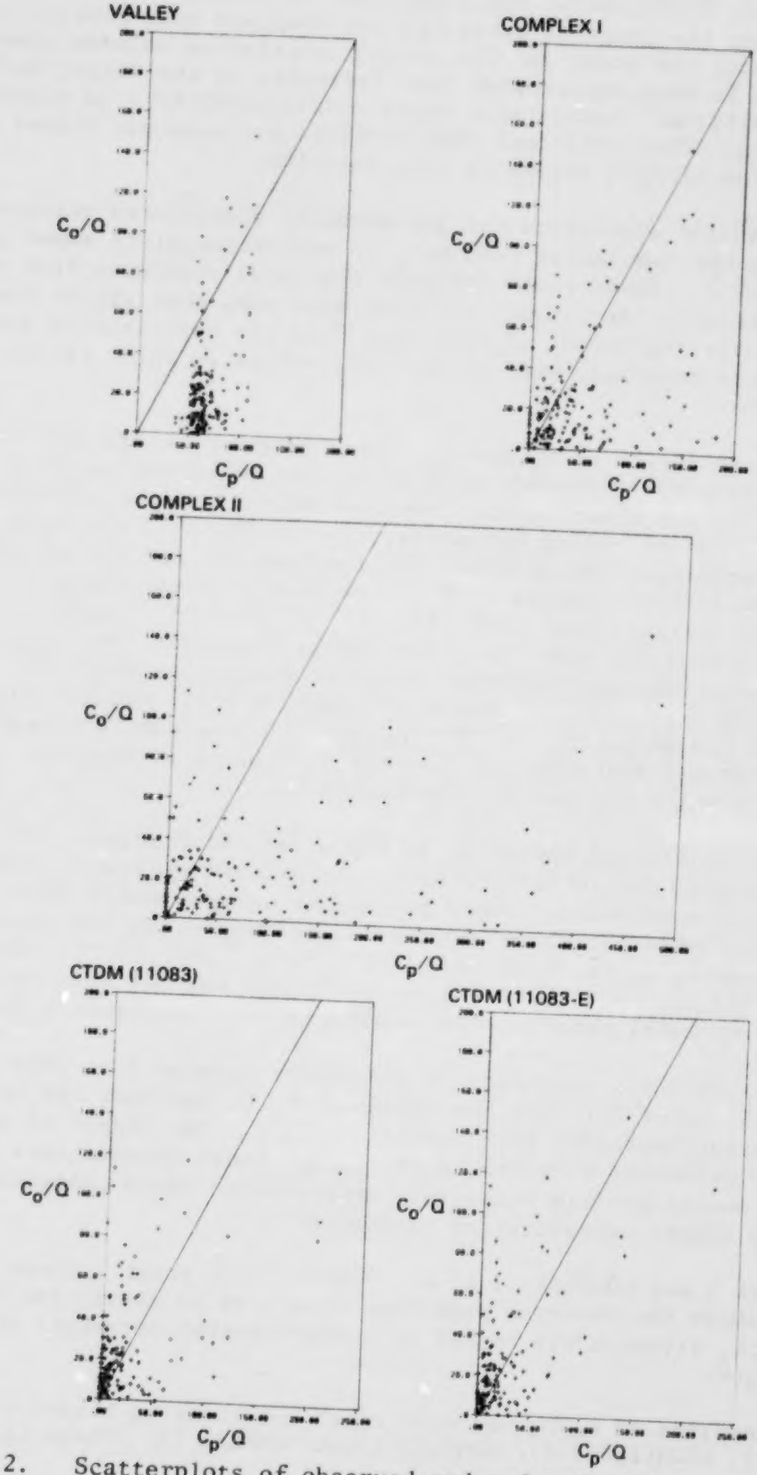

Figure 2. Scatterplots of observed and modeled peak concentrations (C/Q, μs/m^3) for 153 hours of SHIS #1 data.

COMPLEX I, CTDM(11083), and CTDM(11083-E) display similar patterns of scatter in that the range of estimated and observed peak hourly concentrations are nearly the same, and the visual correlation between observations and estimates is much better than that indicated by the Valley and COMPLEX II patterns. Among these three models, COMPLEX I is biased toward overestimation; CTDM(11083) and CTDM(11083-E) are somewhat biased toward underestimation of C_o/Q values of less than 100.

The geometric statistics for log-normally distributed residuals were obtained from the cumulative frequency of occurrence plots shown in Figures 3 through 7. These plots indicate that peak residuals from none of the models are strictly log-normal, but they also show that all of the distributions are nearly log-normal if the "tails" of the distribution are ignored. These tails are generally made up of C_o/C_p values in which either C_o or C_p is nearly zero.

Besides estimates of m_g and s_g, these frequency plots may also be used to estimate the frequency with which peak model estimates are within a factor of 2 (or any other factor, for that matter) of the peak observed concentrations. 22% of Valley estimates, 41% of COMPLEX I estimates, 21% of COMPLEX II estimates, 28% of CTDM(11083) estimates, and 44% of CTDM(11083-E) estimates are within a factor of 2 of the peak observed concentrations. These figures indicate that CTDM(11083-E) and COMPLEX I ought to have better performance statistics than the other models. However, the cumulative frequency distributions and the other residual statistics show that all the models produce a substantial amount of noise in their simulations. There is clearly room for improving the reliability of these models intended for use in complex terrain settings. There is a discussion of suggested improvements to CTDM and their basis in Section 3.

To help understand the noise in the model calculations, the residuals based on the peak concentrations have been plotted against C_p and several meteorological parameters. These plots show where a model might be doing comparatively better or worse, thereby indicating areas for improvement. Figure 8 shows C_o/C_p vs. C_p/Q for CTDM(11083), CTDM(11083-E), COMPLEX I, and COMPLEX II. A similar figure for Valley has not been presented because Valley model concentration estimates fall into such a narrow range.

The figure shows that many of the underestimates from CTDM(11083) and CTDM(11083-E) occur for very low values of C_p/Q, and that the tendency for underestimation decreases with increasing C_p/Q. The degree of overestimation also decreases with increasing C_p/Q. These observations indicate that these models perform relatively better under those conditions that produce the higher concentration estimates.

COMPLEX I and COMPLEX II do not display this trait. These models tend to overestimate the observed peak concentrations to nearly the same degree for all C_p/Q, although the number of underestimates decreases with increasing C_p/Q.

Scatterplots of C_o/C_p vs. wind speed are given in Figure 9 for CTDM(11083), CTDM(11083-E), COMPLEX I and COMPLEX II. There is considerable

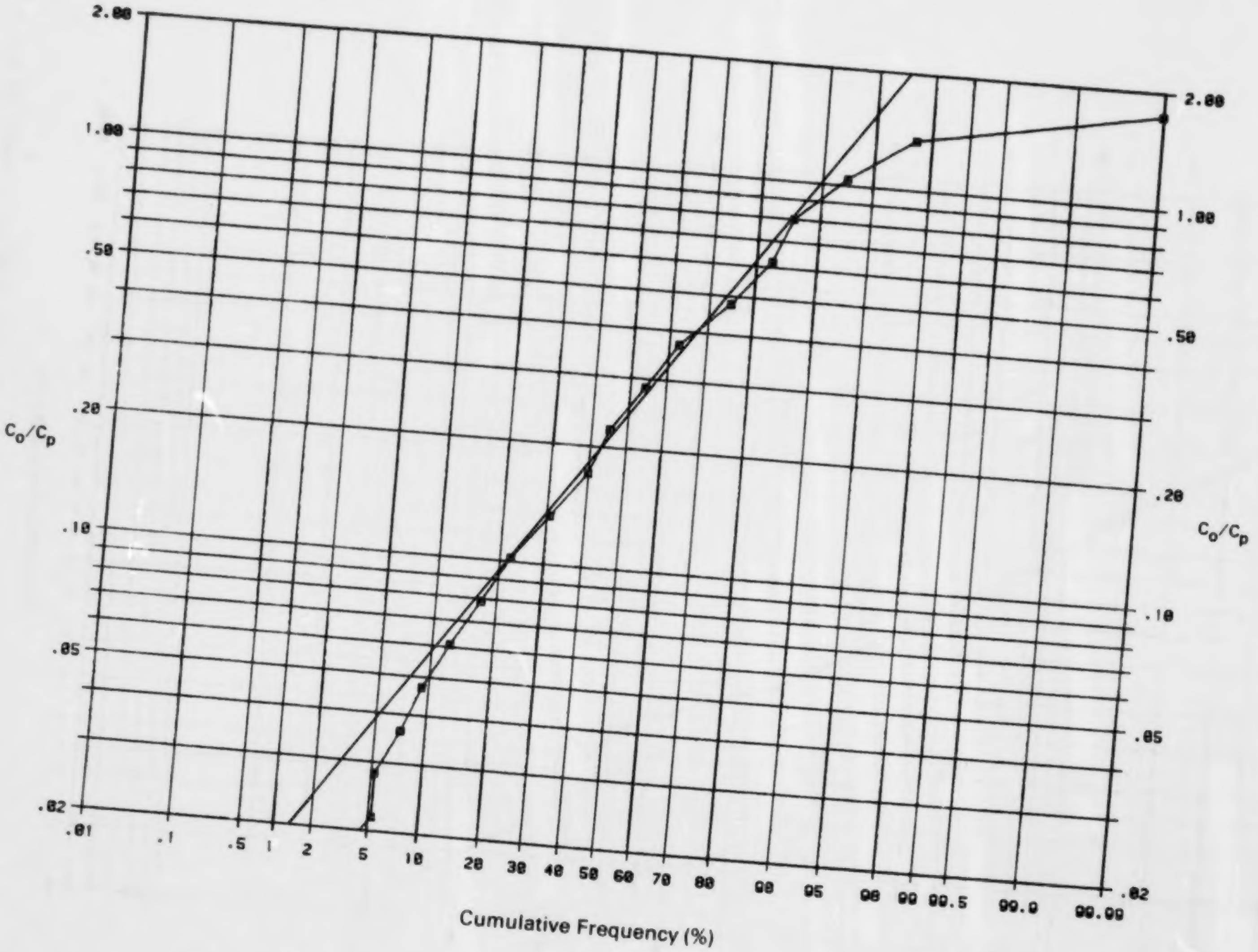

Figure 3. Cumulative frequency plot of C_o/C_p for Valley applied to SHIS #1 data (153 hours).

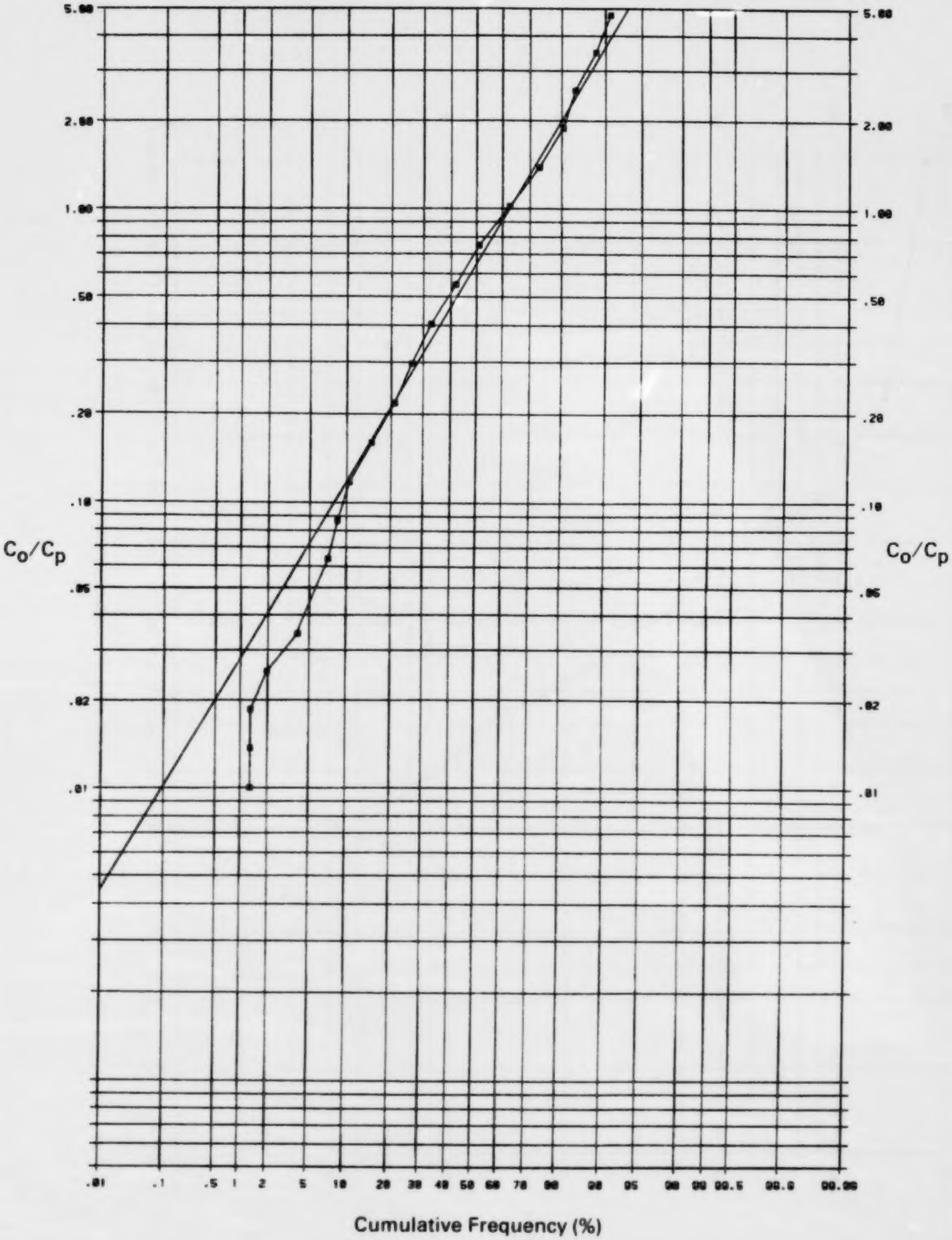

Figure 4. Cumulative frequency plot of C_o/C_p for COMPLEX I applied to SHIS #1 data (153 hours).

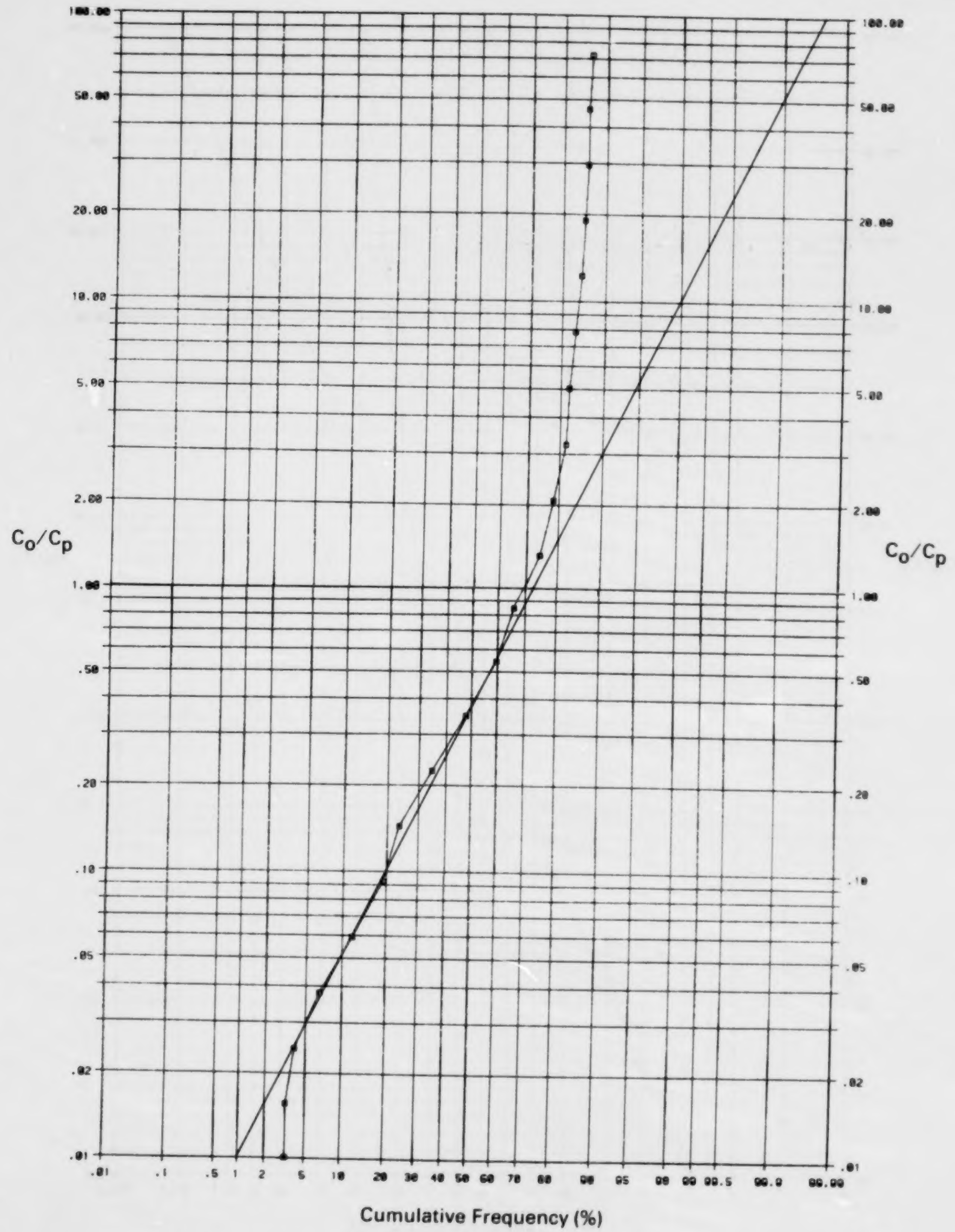

Figure 5. Cumulative frequency plot of C_o/C_p for COMPLEX II applied to SHIS #1 data (153 hours).

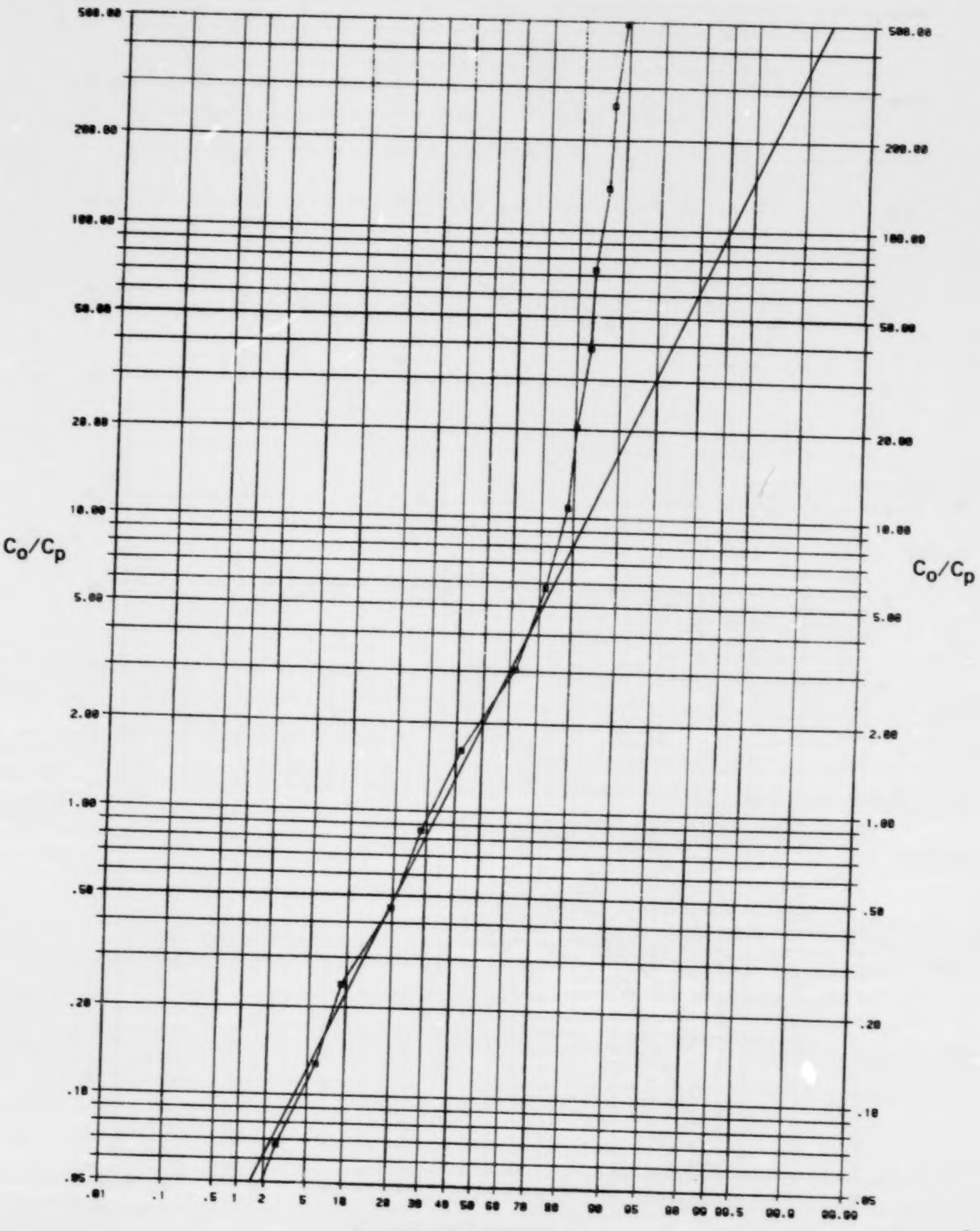

Figure 6. Cumulative frequency plot of C_o/C_p for CTDM (11083) applied to SHIS #1 data (153 hours).

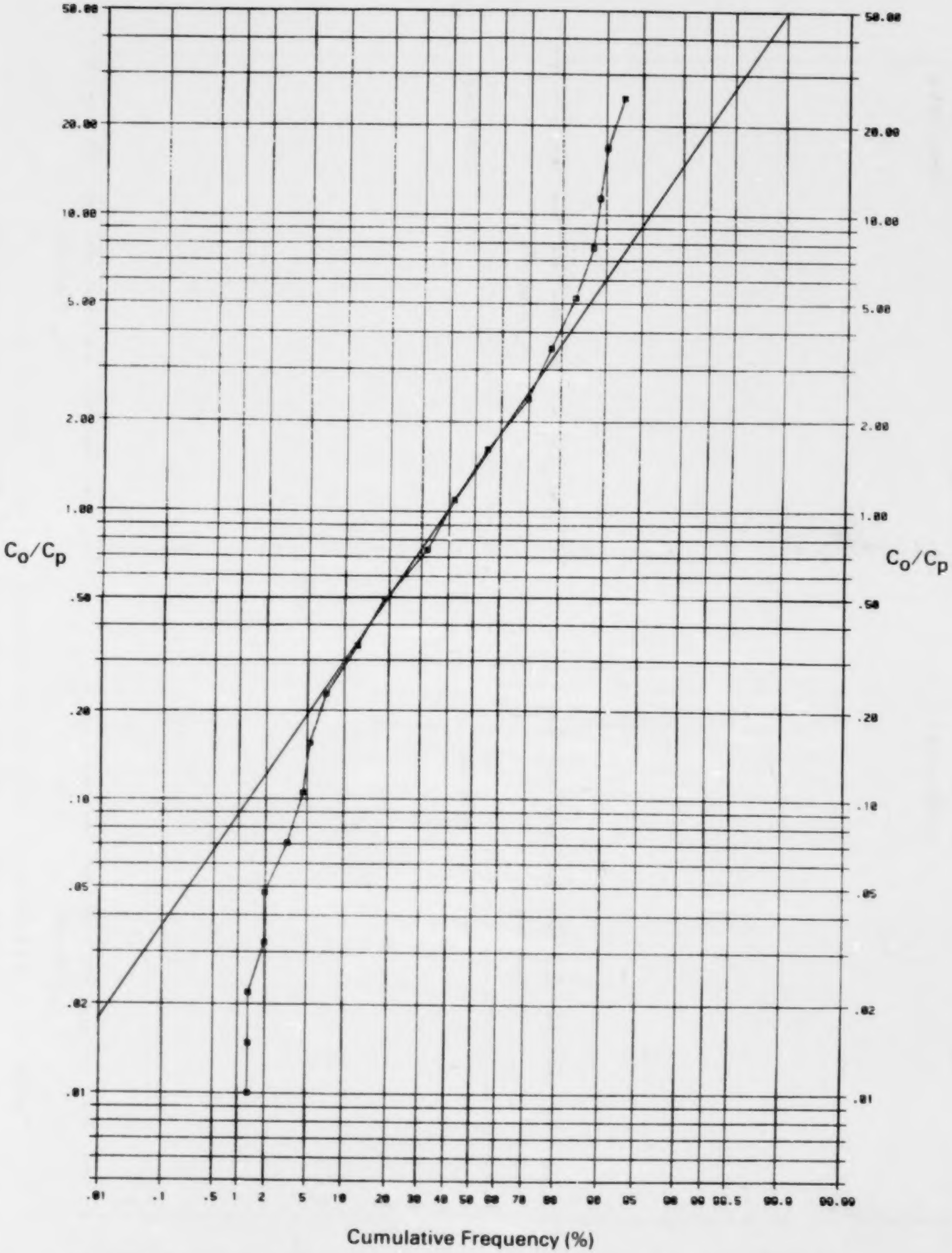

Figure 7. Cumulative frequency plot of C_o/C_p for CTDM (11083-E) applied to SHIS #1 data (153 hours).

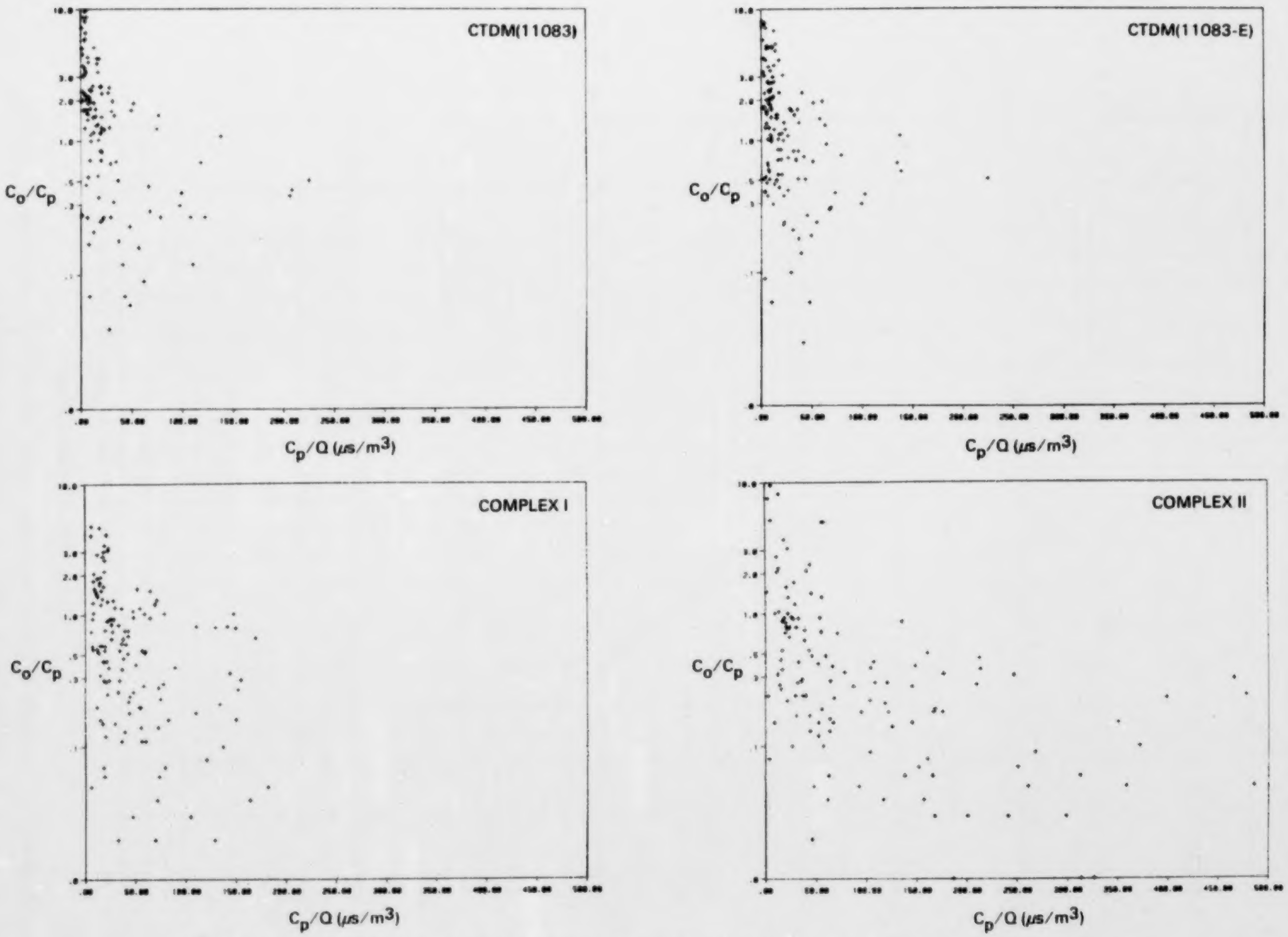

Figure 8. Variation of observed-to-modeled ratios of SHIS #1 peak hourly tracer concentrations with peak modeled concentrations.

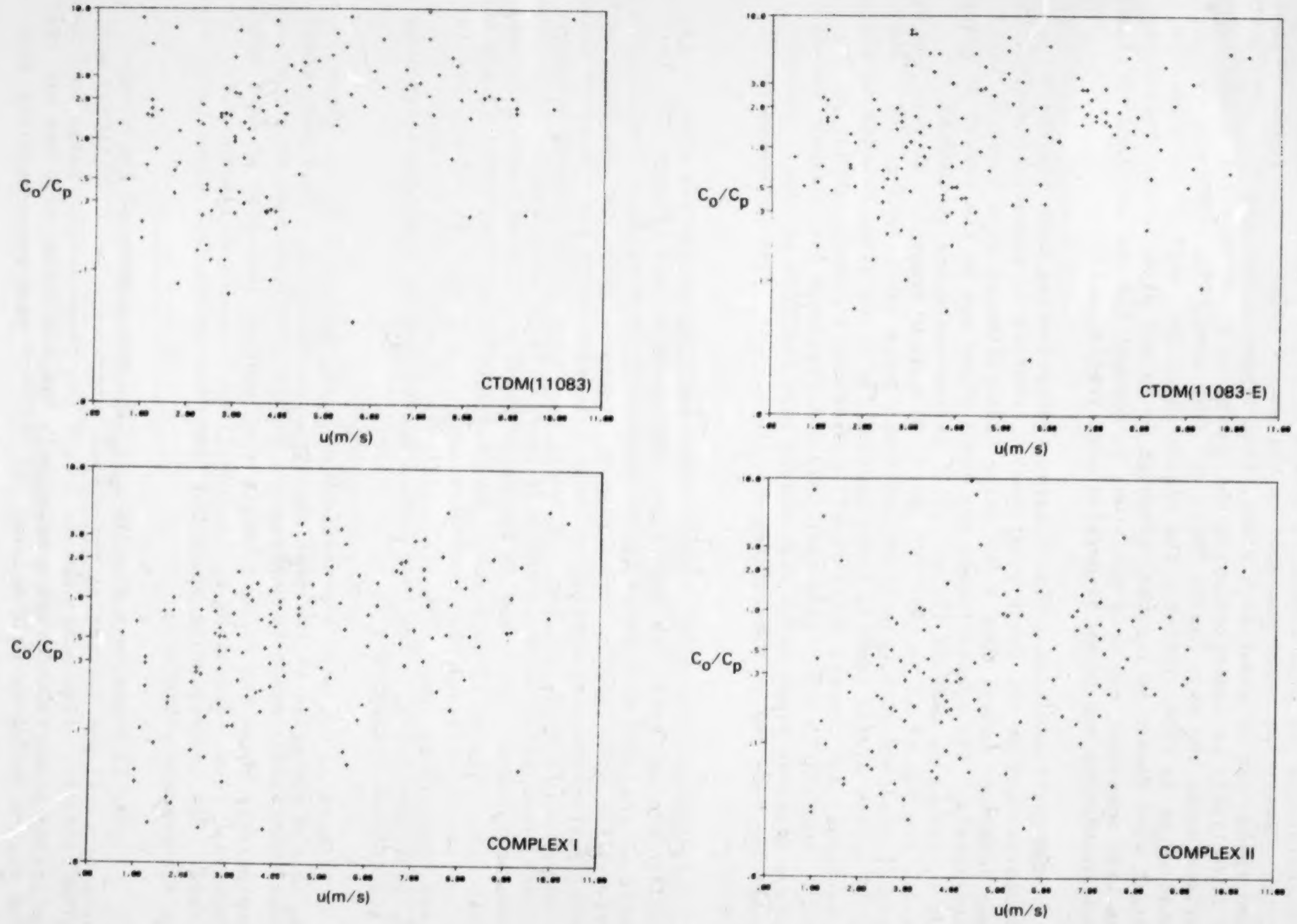

Figure 9. Variation of observed-to-modeled ratios of SHIS #1 maximum hourly tracer concentrations with wind speed (u).

scatter in all of the plots, but some trend can be seen in the patterns. CTDM(11083) exhibits a distinct bias toward underestimating observed peak concentrations for wind speeds in excess of about 5 m/sec. Because H_c is probably small (or zero) compared to the source heights when source-height wind speeds are as great as 5 m/sec, this suggests that the Lift component of CTDM(11083) is underestimating the amount of plume material on the surface under the more nearly "neutral" flow conditions. When σ_z is enhanced as in CTDM(11083-E), the figure shows that much of this bias at larger wind speeds is reduced, although it is not eliminated. Therefore, the Lift component may need revisions to account for the combined effects of flow distortion and plume dispersion more realistically.

COMPLEX I exhibits a bias towards overestimating peak observed concentrations at the lower wind speeds. COMPLEX II appears to exhibit the same behavior, except that a few large underestimates also occur at light wind speeds. The overestimates for light winds may be the result of using PGT σ_y values in COMPLEX II, and 22.5° sector-averaging in COMPLEX I (e.g., see Figure 12 in the CTMD Second Milestone Report). At very low wind speeds, the wind direction often underwent large variations at CCB. The 22.5° sector within COMPLEX I may underestimate the plume meander in these conditions, and thereby consistently overestimate concentrations on the hill. COMPLEX II would also certainly underestimate the meander, but its narrow Gaussian plume might also nearly miss the hill at times, thereby producing both the underestimates and the overestimates indicated in Figure 9.

Scatterplots of C_o/C_p against other modeling parameters also reflect the patterns just described. For example, u/N (Figure 10), the ratio of the mean wind speed to the Brunt-Vaisala frequency, distinguishes between the more "stable" and the more "neutral" hours, and the patterns of model performance are similar to those discussed above for the plots against wind speed. $1-Hc/z_r$ (Figure 11), where z_r is the plume release height, orders model performance in the near-neutral limit when $1-Hc/z_r$ is greater than approximately 0.5, and in the very stable limit when $1-Hc/z_r$ is less than zero. Figure 11 indicates that CTDM(11083) and CTDM(11083-E) are most prone to overestimate peak concentrations when H_c exceeds 0.5 z_r, but is less than 1.5 z_r, and CTDM(11083) generally produces underestimates for H_c less than 0.5 z_r. The bias toward overestimating peak concentrations with COMPLEX I increases as H_c increases.

Figure 12 contains scatterplots of C_o/C_p against $1-H_m/z_r$, where H_m is the elevation of the peak observed concentration. This plot shows that CTDM(11083) tends to underestimate peak concentrations when they occur appreciably above the release height--yet another indicator of more nearly "neutral" flow. Enhancing σ_z in CTDM(11083-E) tends to lessen this trend. The corresponding plots for COMPLEX I and II (not shown here) show no discernible pattern.

Figure 13 contains a plot of C_o/C_p vs. the product of the cross-wind vertical and horizontal turbulence intensities for CTDM(11083) and CTDM(11083-E). (The other models do not use these data). Large turbulence intensity products indicate a relatively large dilution of plume material. The figure indicates that modeled and observed peak concentrations most

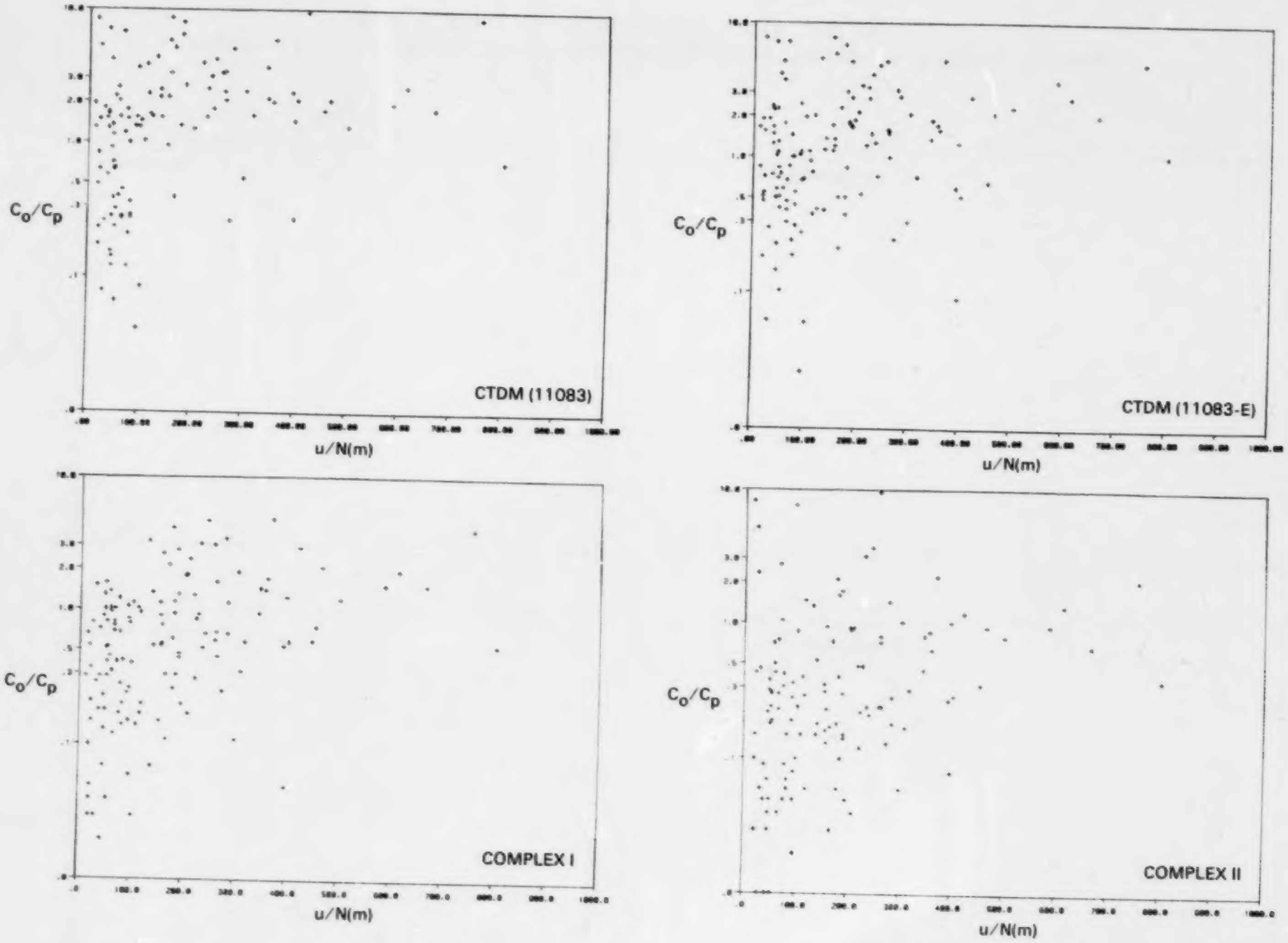

Figure 10. Variation of observed-to-modeled ratios of SHIS #1 maximum hourly tracer concentrations with u/N.

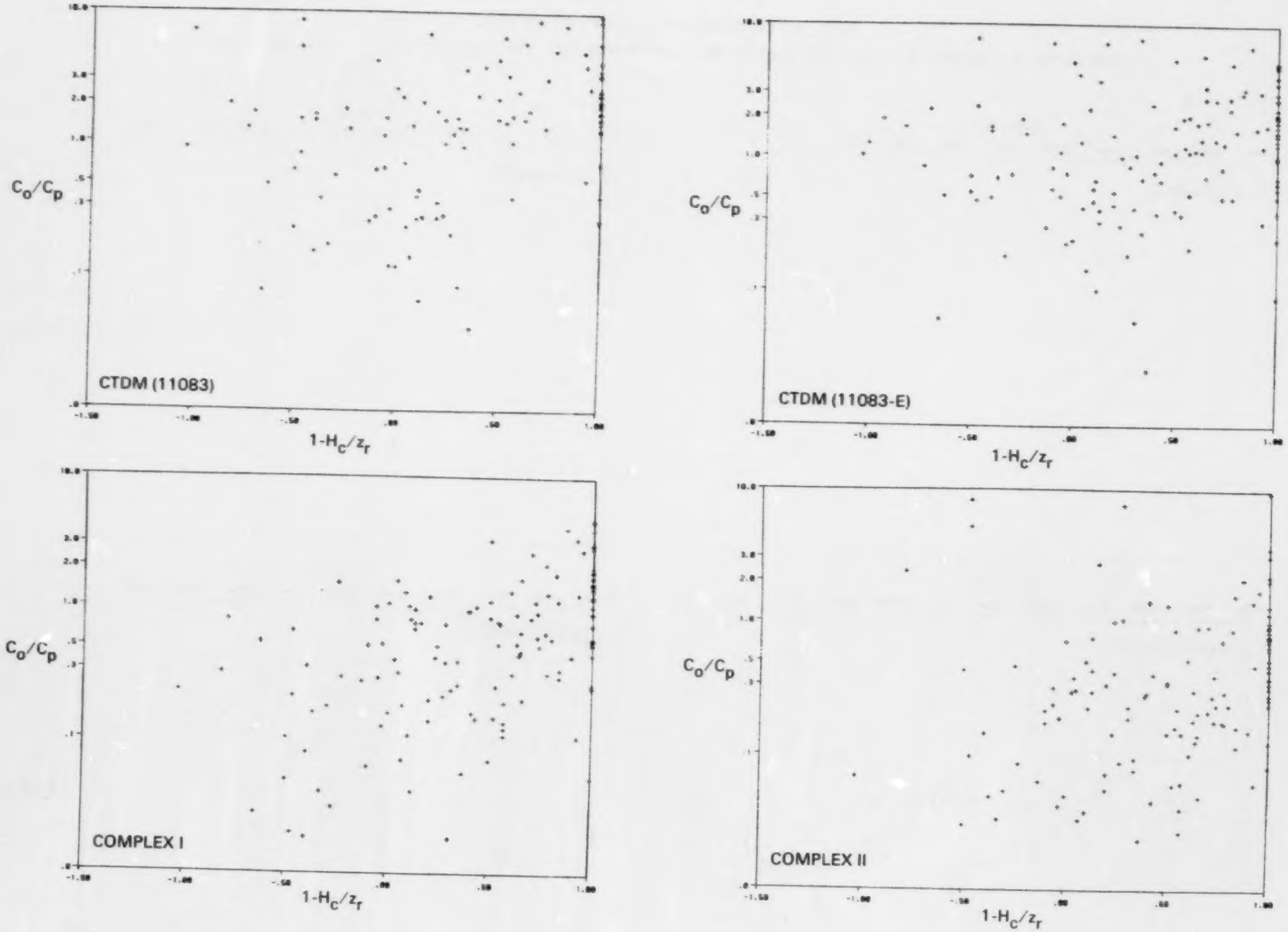

Figure 11. Variation of observed-to-modeled ratios of SHIS #1 maximum hourly tracer concentrations with $1-H_c/z_r$.

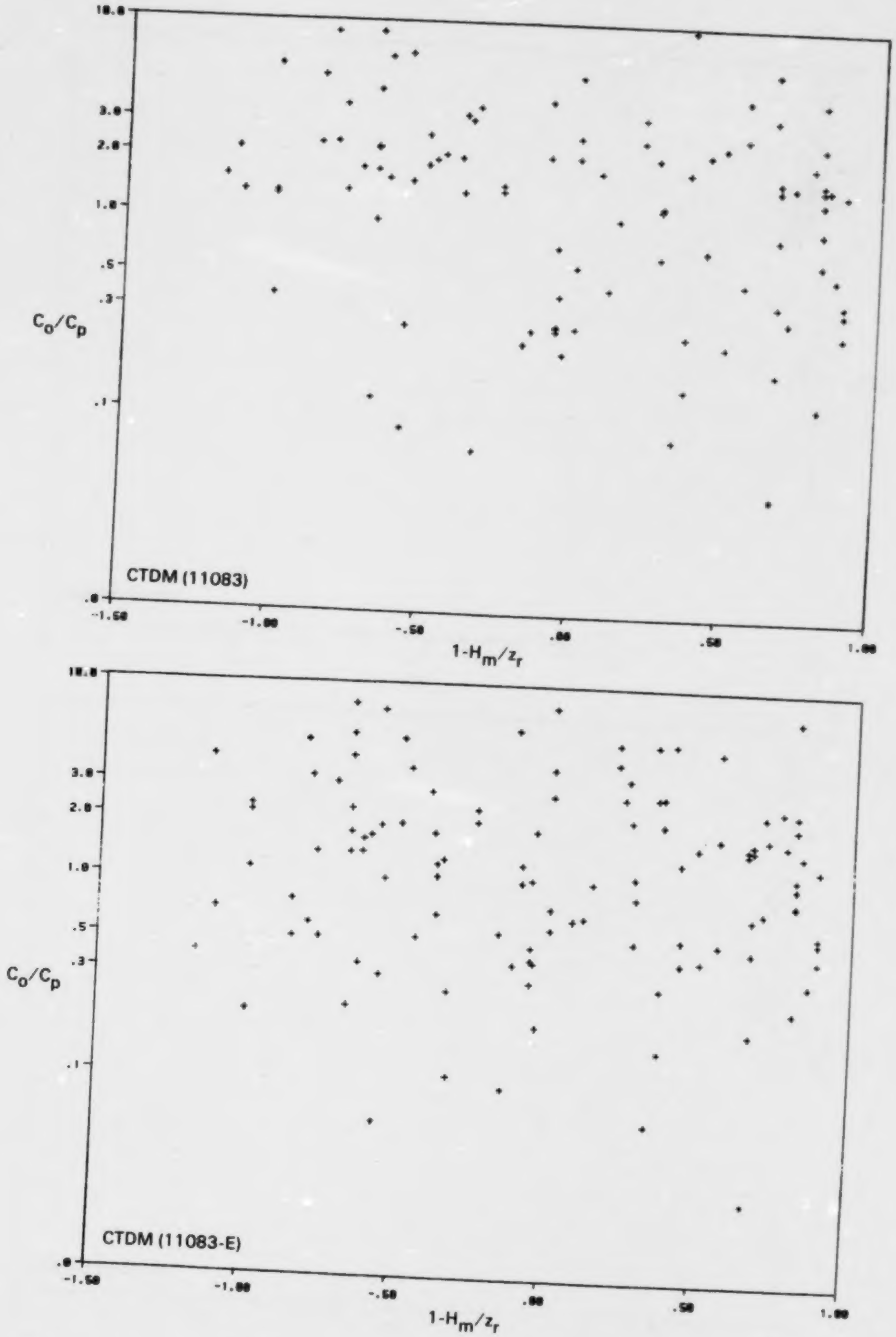

Figure 12. Variation of observed-to-modeled ratios of SHIS #1 maximum hourly tracer concentrations with $1-H_m/z_r$. (H_m is the height of the observed concentration.)

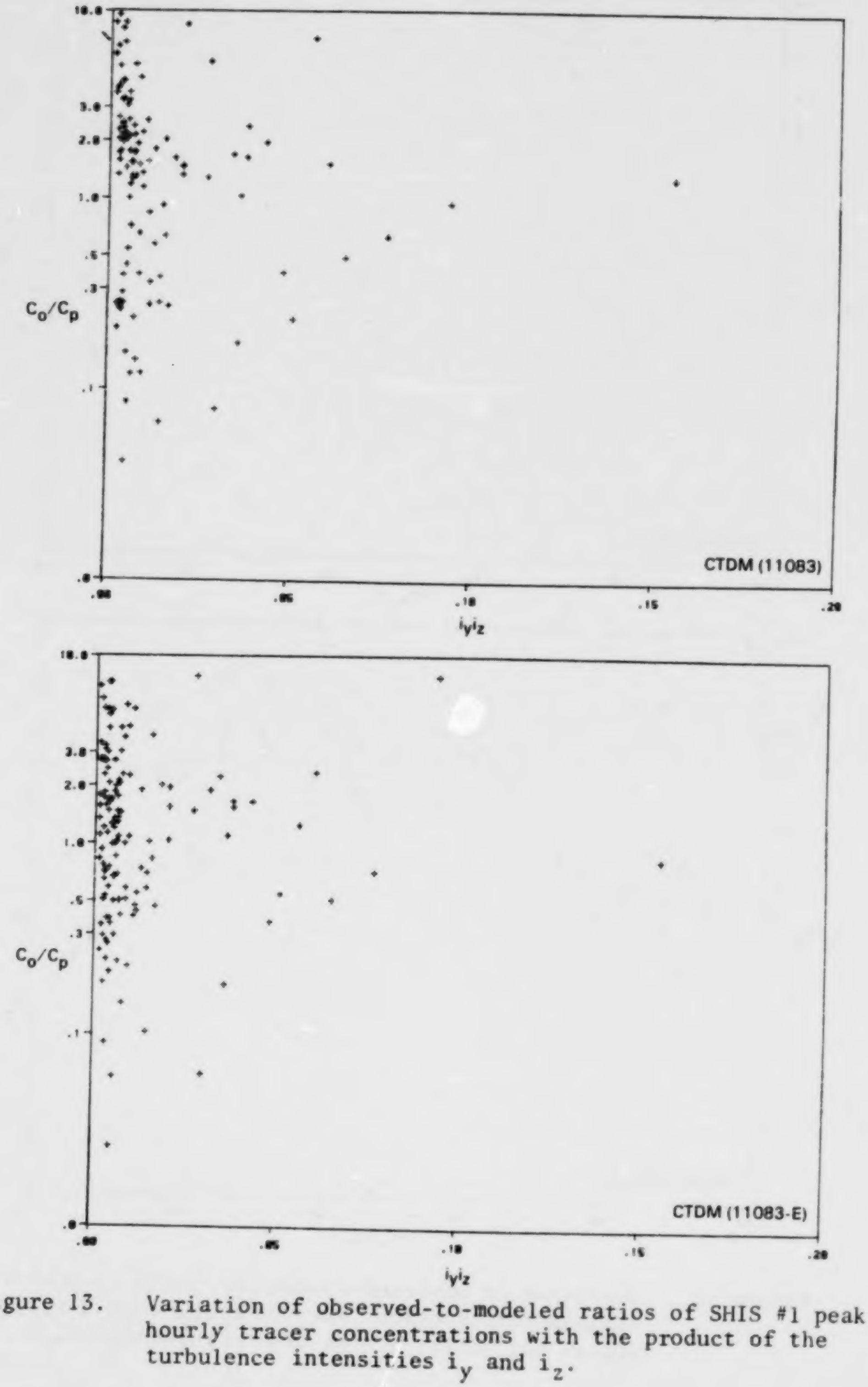

Figure 13. Variation of observed-to-modeled ratios of SHIS #1 peak hourly tracer concentrations with the product of the turbulence intensities i_y and i_z.

nearly agree when the plume is well-diluted. When the dilution is much weaker, the plume is more compact, exhibiting considerably less meander. Under these conditions, the peak modeled concentration is very sensitive to plume path assumptions, wind direction, and postulated flow distortion/plume dispersion effects. This sensitivity is illustrated in the figure by the large scatter for low values of $i_y i_z$. The figure also shows that the bulk of the CCB data falls into this category.

SECTION 3

DEVELOPMENT OF THE COMPLEX TERRAIN DISPERSION MODEL (CTDM)

3.1 Introduction

CTDM is a point source plume model that incorporates several concepts about stratified flow and dispersion over an isolated hill. The emphasis to date has been on including those phenomena that are thought to be important in controlling the magnitude and distribution of plume concentrations across the windward portion of CCB. However, although the formulation of modeling concepts contained in CTDM has general inherent applicability, certain details make explicit use of the geometry of CCB to simplify the code. Consequently, CTDM should be viewed as a research code at this time rather than a code suitable for regulatory applications.

We expect CTDM to evolve during the CTMD project. As more data are analyzed from SHIS #1, and as data from SHIS #2 are analyzed, the specific formulations will change as will the range of phenomena contained in the model. These changes will be treated as updates to CTDM rather than the basis for new model nomenclature.

CTDM evolved from model codes described in the first two Complex Terrain Model Development (CTMD) milestone reports.

Two preliminary models were described in the First CTMD Milestone Report. The Impingement model corresponds to low Froude-number flows in which a plume remains horizontal as it impinges on and flows around the hill. The Neutral model corresponds to moderate or large Froude-number flows in which a plume goes over the top of the hill. A number of refinements were made to these two models, and these were described in the CTMD Second Milestone Report. These refined versions of the Neutral and Impingement models are referred to as the Lift and Wrap models.

Since then the Lift and Wrap models have undergone additional refinements and have been combined into one model; now CTDM performs both kinds of computations whenever the dividing-streamline height, H_c, is non-zero. This section of the report provides a description of how Lift and Wrap were modified and combined to form version 11083 of CTDM. The description is followed by a detailed study of the data from two SHIS #1 experiment days. CTDM upgrades suggested by the analysis of these data are presented, and the performance of this latest version of CTDM is evaluated.

3.2 Description of CTDM(11083)

CTDM treats the flow around an isolated hill as though the flow takes place in two discrete layers. Flow below the critical dividing streamline (H_c) is restricted to travel in horizontal planes around the hill. Flow above H_c is allowed to rise over the top while undergoing some degree of distortion consistent with weakly stratified flow over a sphere. That is, Lift modeling assumptions are employed for plume material which is released or which diffuses above H_c, and Wrap modeling assumptions are employed for plume material which is released or which diffuses below H_c. Because streamline patterns above and below H_c are markedly different, the plume is assumed to separate into two independent segments where the H_c surface intersects the windward face of the terrain.

The segment initially below H_c spreads around the sides of the terrain. As the plume grows with distance beyond the point of separation, however, its vertical profile is no longer Gaussian (or reflected Gaussian) in shape. This is because the material above H_c at the point of separation is no longer available to mix below H_c.

The segment initially above H_c continues to travel up and over the hill, but the plume material that had been below H_c at the point of separation has been displaced by the solid terrain surface. The vertical profile of the upper plume segment therefore is no longer a simple reflected Gaussian distribution; rather, it is a reflected segment of a Gaussian distribution profile.

3.2.1 The Wrap Component of CTDM(11083)

Because observations indicate considerable meander of the horizontal wind during a typical hour, we assume that the hour can be divided into several quasi-steady periods. We also assume that the average angular spread of the plume, α_s, corresponding to these periods is small compared to the total meander, α_m, during the hour. Concentrations are assumed to occur on the hill's surface only when a portion of the plume is directed along the stagnation streamline; therefore, the maximum concentration occurs at the stagnation point.

During any single quasi-steady period, denoted by the subscript i, the concentration at the stagnation point A (see Figure 14) will be non-zero only if the mean wind direction during the period lies within $\alpha_{si}/2$ of the stagnation streamline ($\theta_i = \theta_d \pm \alpha_{si}/2$). If this concentration is denoted by $C_i(\theta,\theta_d)$, then the average concentration, C_{max}, at A over an hour is given by

$$C_{max} = \int_{\theta} C_i(\theta, \theta_d) P(\theta) d\theta \qquad (13)$$

where $P(\theta)$ is the hourly probability density function of wind directions. If the wind speed, vertical plume spread, and horizontal plume spread angle are nearly constant among quasi-steady periods during the hour, then the only non-zero contributions to the integral in Equation 13 arise for wind directions within $\pm \alpha_s/2$ of the stagnation wind direction. Furthermore, if

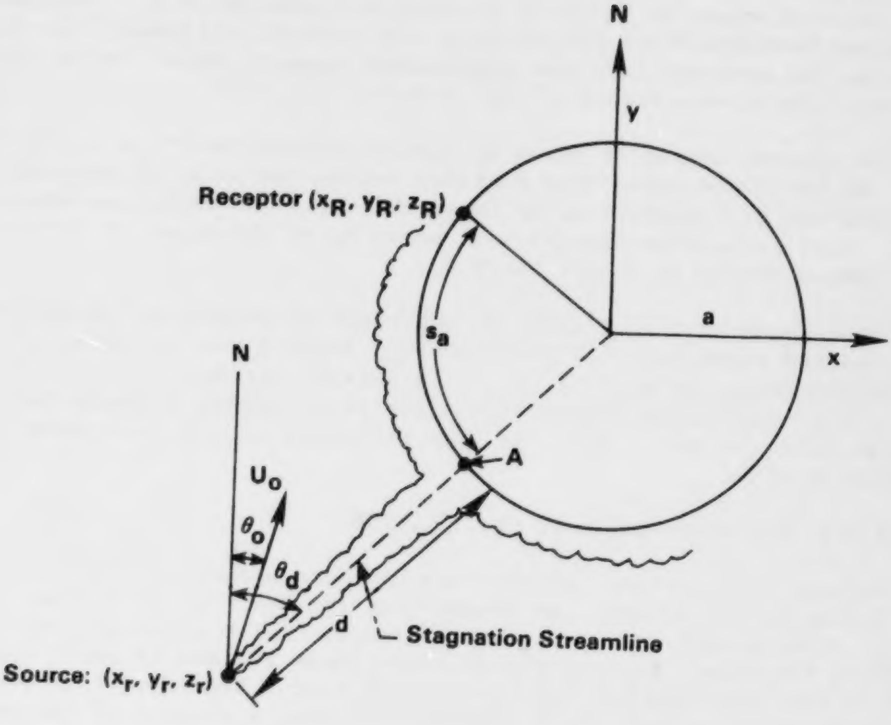
N
y
Receptor (x_R, y_R, z_R)
a
x
s_a
N
U_o
θ_o
θ_d
A
d
Stagnation Streamline
Source: (x_r, y_r, z_r)

Figure 14. Plume dispersion in the region of horizontal flow.

the concentration distribution within the plume during each quasi-steady period is assumed to be uniform, and if the spread due to plume meander during the hour is much greater than α_s, so that $P(\theta)$ is nearly constant within the interval α_s, then

$$C_{max} = \bar{C}_i \int_{\theta_d-\alpha_s/2}^{\theta_d+\alpha_s/2} P(\theta)d\theta = \bar{C}_i P(\theta_d)\alpha_s \tag{14}$$

where

$$\bar{C}_i = \frac{Q}{\sqrt{2\pi}\sigma_z U_o \alpha_s d} . \tag{15}$$

In Equation 15, σ_z, U_o, and α_s represent averages for the relevant hour.

From the CCB experiments we do not have a continuous record of $\theta(t)$ as a function of t; only 5-minute averages of θ and i_y are available. To use this information, we assume that θ is uniformly distributed in the interval $2\sqrt{3}\sigma_\theta$ about the 5-minute averaged value θ, and we set σ_θ equal to i_y. We then use linear interpolation to estimate values of θ and σ_θ between measured values (see the CTMD Second Milestone Report).

Equation 15 presumes that the centerline of the plume lies below H_c. However, the form of Equation 14 applies equally well to all streamlines and hence, to all segments of the plume below H_c. By making the assumption that the flow beneath H_c is purely two-dimensional, each point below H_c in the plane of the stagnation wind direction is a stagnation point. Consequently, concentrations at receptors along the leading face of the hill are given by

$$C(d,z_R) = \frac{P(\theta_d)}{d} C_o(d,z_R) = \frac{Q\,P(\theta_d)}{\sqrt{2\pi}\sigma_z(d)U_o d}\left(e^{-0.5((z_R-z_r)/\sigma_z)^2} + e^{-0.5((z_R+z_r)/\sigma_z)^2}\right) \tag{16}$$

where d is the distance to the receptor, and z_R is the elevation of the receptor.

Beyond the point at which plume material impinges on the hill at the elevation of a receptor, the distance to the receptor is taken to be the sum $d + s_a$ (see Figure 14), and the vertical distribution of plume material below H_c just before impingement is assumed to map onto the surface of the hill. That is, the probability factor $P(\theta_d)$ is the same for all receptors, so that the modeled concentration at any point changes only as that point moves farther downwind along the hill, changing s and σ_z, or as its elevation changes, changing z_R. We model these changes in concentration by treating the vertical distribution of plume material below H_c at the impingement point of the dividing-streamline as a series of point sources, and integrate the response function or Green's function from the level surface to H_c. Consequently, the "vertical" distribution of plume material lies along the surface of the hill, and reflection occurs only along the plane z = 0.

$$C(d+s_a, z_R) = \frac{P(\theta_d)}{d+s_a} \int_o^{H_c} \frac{C_o(d,z)}{\sqrt{2\pi}\sigma_z'} \left(e^{-0.5((z_R - z)/\sigma_z')^2} + e^{-0.5((z_R + z)/\sigma_z')^2}\right) dz. \quad (17)$$

Note that $C_o(d,z)$ is evaluated using Equation 16, and that

$$(\sigma_z')^2 = (\sigma_z(d + s_a))^2 - (\sigma_z(d))^2. \quad (18)$$

3.2.2. The Lift Component of CTDM(11083)

Several features of the Lift model differ from conventional bivariate Gaussian plume modeling techniques: the horizontal distribution of plume material can be defined by the distribution of 5-minute average winds rather than the Gaussian distribution function; the overall curvature of the hill in the crosswind direction is allowed to distort the horizontal plume distribution over the hill; and plume material below H_c at the point of impingement is not allowed to affect concentrations estimated by Lift.

The probability density function for the wind direction, $P(\theta)$, can be incorporated by replacing the exponential term for the crosswind distribution as follows:

$$\frac{1}{\sqrt{2\pi}\,\sigma_y} e^{-0.5(y/\sigma_y)^2} \rightarrow \frac{P(\theta)}{s}, \quad (19)$$

where s is the distance to the receptor, and $P(\theta)$ is derived in the same way as that described in subsection 3.2.1. The user is given the option of using either the Gaussian form or the PDF form.

Plume distortion in the horizontal direction (along the surface of the hill in the crosswind direction) tends to cause the plume to spread over a wider area when over the hill than when over flat ground because streamlines do not follow straight lines as they pass over the hill. Consequently, the wind direction that places plume material at a particular receptor is not the direction defined by the positions of the source and receptor alone, and it is therefore not the correct angle for specifying the probability factor $P(\theta)$. To estimate the correct angle, we assume that the crosswind profile of the hill above H_c is characterized by a section of arc specified by the height of the hill above H_c ($H_* \equiv H - H_c$)), and the approximate radius of the hill at H_c, $a(H_c)$. (See Figure 15 and Equation 2.) The offset distance D is

$$D = (a^2 - H_*^2)/2H_* \quad . \quad (20)$$

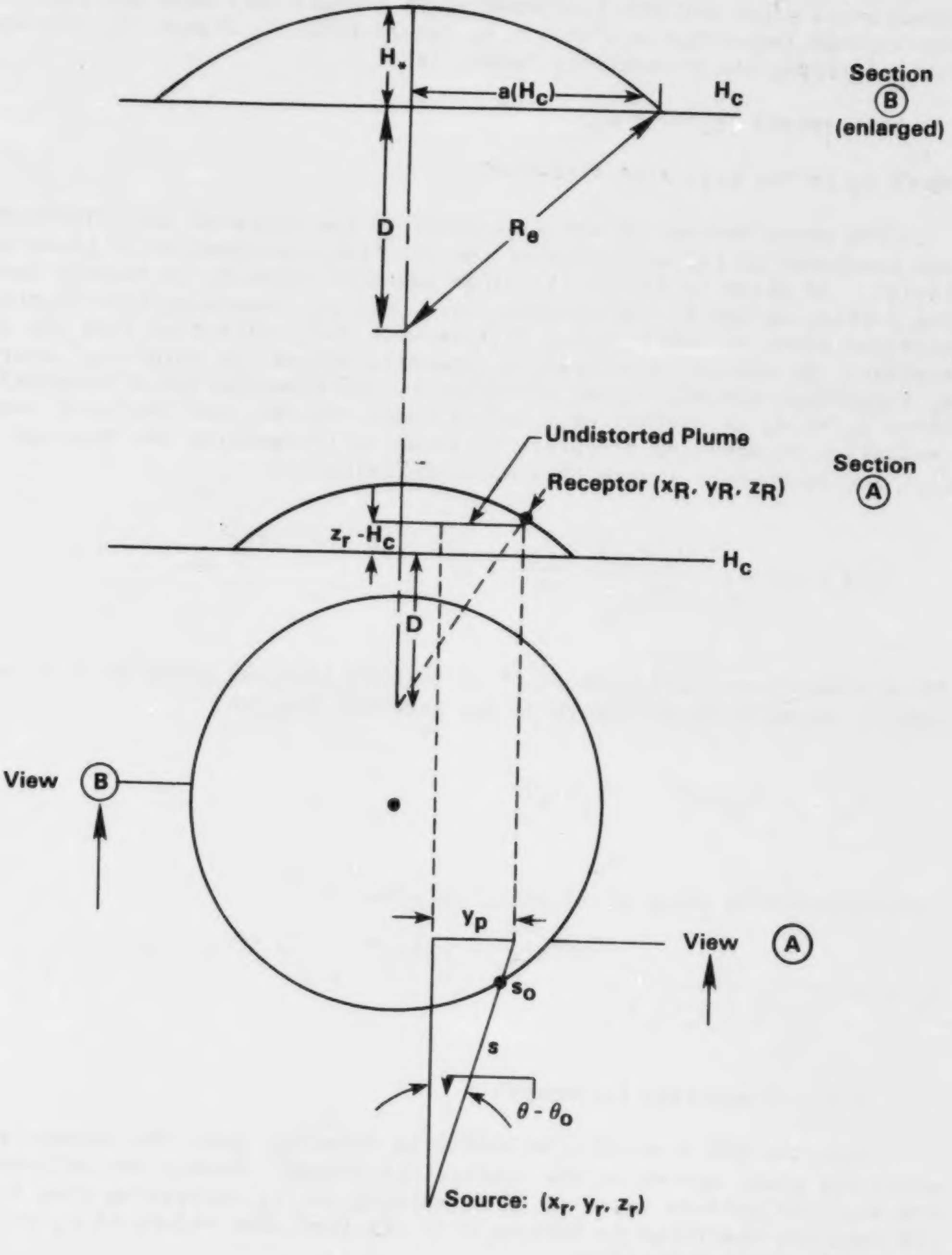
H*
a(Hc)
Hc
Section B (enlarged)
D
Re
Undistorted Plume
Receptor (xR, yR, zR)
Section A
zr - Hc
Hc
D
View B
yp
View A
so
s
θ - θo
Source: (xr, yr, zr)

Figure 15. Geometry used to derive the effective radius of curvature R_e for the portion of the hill above H_c, and to incorporate the wind direction probability distribution function $P(\theta)$ in the Lift model.

By assuming that the flow is axisymmetric, the relationship between the undistorted plume and the distorted plume depends only upon the section of arc through the receptor (Section A, Figure 15). In Figure 15, the angle for specifying the probability factor is

$$\theta = \arcsin (y_p/s) + \theta_o \tag{21}$$

where θ_o is the mean wind direction.

The third feature of the Lift model as incorporated into CTDM(11083) is the treatment of the evolution of the vertical distribution of plume material. As drawn in Figure 16, plume material below H_c is removed from the profile at the H_c impingement level, and the remaining distribution of material above H_c continues to diffuse with full reflection from the hill surface. To obtain concentration estimates beyond the point (s_o) where H_c intercepts the hill along direction θ, the distribution of material above H_c at s_o is treated as a set of point sources, and the total concentration at downwind receptors is found by integrating the response function for each point source from H_c to infinity.

$$C(s,\theta,0) = \int_{H_c}^{\infty} \frac{C_o(s_o,z)}{\sqrt{2\pi}\,\sigma'_z} \frac{P(\theta)}{s}\, 2\, e^{-0.5((z - H_c)/\sigma'_z)^2} dz. \tag{22}$$

As in subsection 3.2.1, the solution to this integral produces a series of product terms of error functions and exponentials, and

$$(\sigma'_z)^2 = (\sigma_z(s))^2 - (\sigma_z(s_o))^2 . \tag{23}$$

The distribution of material at s_o is given by

$$C_o(s_o,z) = \frac{Q}{\sqrt{2\pi}\, U_o \sigma_z(s_o)} \left(e^{-0.5((z_r - z)/\sigma_z)^2} + e^{-0.5((z_r + z)/\sigma_z)^2}\right). \tag{24}$$

3.2.3 Dispersion Parameters

When the PDF form of CTDM(11083) is selected, only the dispersion parameter for plume spread in the vertical is needed. Background information and analysis methods employed in developing the σ_z expression used for CCB data are described in Section 3.3. We find that values of σ_z calculated from the expression

$$\sigma_z = i_z(s + s_v)/(1 + N(s + s_v)/(U_o 2\gamma^2))^{0.5}, \tag{25}$$

with $2\gamma^2 = 0.55$, fit the CCB data quite well. N is the Brunt-Vaisala frequency and s_v is the virtual source distance associated with source-

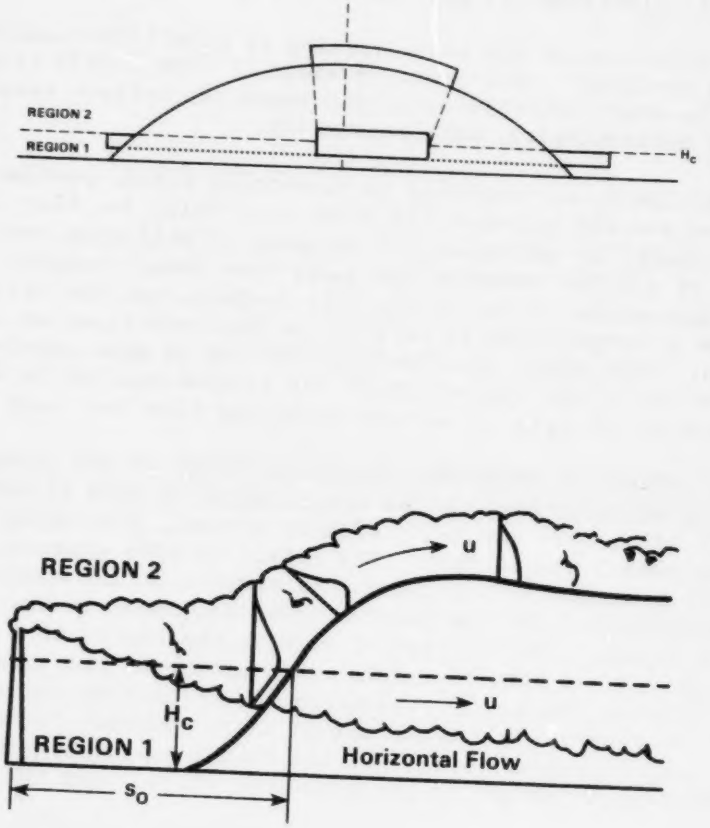
REGION 2
REGION 1
H_c
REGION 2
u
u
H_c
REGION 1
Horizontal Flow
s_o

Figure 16. Dispersion and flow regions for stratified flow around hills.

induced plume spread. If the PDF form is not selected, the dispersion parameter for horizontal plume spread is assumed to be given by

$$\sigma_y = i_y(s + s'_v) \tag{26}$$

where s'_v is the virtual source distance based on the rate of plume growth in the horizontal.

3.2.4 CTDM(11083-E) and CTDM(11083-E)-5

The structure of the basic version of CTDM(11083) was discussed in the preceding sections. Additional versions of CTDM(11083) have been developed to test the model sensitivity to alternate hill-effect assumptions and alternate meteorological data resolution.

CTDM(11083), as described in subsection 3.2.2, presumes that streamline distortion and the accompanying plume distortion for flow over the top of the hill (Lift) do not cause any increase in diffusion over that which is expected at similar downwind distances over level terrain. The plume centerline approaches closer to the hill surface, but the vertical extent of the plume is proportionally reduced, so concentrations at the surface remain unchanged. This model for flow over the top is most appropriate if enhanced diffusion due to the distortion of the streamlines can be neglected, and if the flow over the hill is no more turbulent than that away from the hill.

The effects of increased diffusion (aided by the plume's approaching nearer the hill surface) can be approximated in CTDM by enhancing the rate of growth of σ_z over the hill, without explicitly bringing the centerline of the plume nearer the surface. The effect of this approach on the vertical distribution factor is similar to the terrain factor approach contained in the COMPLEX models and the Neutral model evaluated in the CTMD First Milestone Report. But instead of viewing the factor as a change in the centerline height, we view the factor as a change in the relative size of the plume. However, because σ_z increases, dilution also increases, which reduces the centerline concentrations in the plume. Therefore, this treatment is not equivalent to the terrain factor approach, particularly as σ_z approaches the height of the plume centerline over the terrain.

The σ_z-enhancement approximation is made by altering Equation 23:

$$(\sigma'_z)^2 = \frac{(\sigma_z(s))^2}{T^2} - (\sigma_z(s_o))^2 \tag{27}$$

where

$$T = PPC \quad \text{for} \quad z_R \geq z_r$$

$$T = 1 - (1 - PPC)\,(z_R - H_c)/(z_r - H_c) \qquad \text{for} \quad z_R < z_r \tag{28}$$

PPC is the "plume path coefficient." This definition for the factor T is the same as that used to define terrain factors in the COMPLEX models. This enhanced-σ_z version of CTDM(11083) (denoted as CTDM(11083-E)) has been run on the CCB data base with PPC set equal to 0.5 in order to evaluate the importance of increased dispersion over the hill.

A second alternative CTDM(11083) utilizes the sequence of 5-minute meteorological data, rather than 1-hr average meteorology supplemented by the calculated PDF for wind directions. In this version, the 5-minute horizontal distribution of plume material is assumed to be Gaussian in form, characterized by

$$\sigma_y = i_y(5\text{-min})\ (s + s_v') \ . \tag{29}$$

All other model formulations remain the same. Because 1-hour average concentrations are constructed from calculated 5-minute average concentrations, variations in wind speed dilution, turbulence intensities, and the dividing-streamline height are explicitly modeled in addition to the distribution of 5-minute average wind directions. Running this version (denoted by appending (5)) of CTDM(11083) on the CCB data base will test the importance of including short-term variations in H_c, u, and turbulence intensity in the modeling of SHIS #1.

3.3 Case Study Results - Experiments 201 and 210

The model evaluations discussed in subsection 2.4 indicate that some improvement is gained in the performance of CTDM if σ_z is enhanced over the hill. However, much "noise" in the residuals remains. One possible source of noise is the meteorological data used to drive the model estimates. The MDA described in subsection 2.1 represents an objective best estimate of the meteorological conditions at source height derived from data measured at Tower A alone. However, alternate meteorological data for model input might be developed for some experiments if all available data are studied. Note that Tower A was located 2.3 km to the north of CCB, approximately one to three kilometers away from the tracer release locations.

We have begun an extensive case-study of the SHIS #1 data to develop all available information on the transport and diffusion of plume material at CCB. In this process, the consistency among the data will be tested, and the performance of various modeling assumptions can be better evaluated. Because the modeled concentrations are very sensitive to the trajectory of plume material and the rate of diffusion of that material to the surface, we are particularly interested in evaluating (1) the correspondence between the sequence of 5-minute average wind directions interpolated to source height on the basis of Tower A measurements and the smoke plume trajectory as recorded by observers' field notes and photographs; (2) the characteristics of the plume trajectory near the hill; (3) the correspondence between the rate of plume growth in the vertical as observed in photographs and the measured vertical turbulence intensity on Tower A; (4) the relationship among turbulence intensity measurements on the hill and those at Tower A; and (5) the form of the growth of σ_z upwind of the hill as derived from a combination of lidar data and photographs. Results of these evaluations performed on data from Experiments 201 and 210 are summarized in this section.

3.3.1 Plume Trajectories

Key views of the oil-fog plume that are important in estimating plume trajectories from photographs are those taken from behind the release crane looking along the plume trajectory and those taken from atop CCB looking back toward the release crane. For those views from behind the crane, wind directions are most easily estimated when the plume passes over some recognizeable portion of the hill. Any horizontal displacement of streamlines when the plume is close to the hill is subjectively taken into account. For views from the hilltop, wind directions are most easily estimated when the plume is seen to pass over one of the camera positions on either peak, or when the plume trajectory "passes through" a known landmark on the ground away from the hill (such as a turn in a road). On the basis of these considerations, wind direction estimates from the photographs are least accurate when the plume misses the hill to one side or the other. Fortunately, the most useful information during these periods is that the plume is off to the side of the hill, and is therefore having very little impact on tracer concentrations in the sampler array.

In Figure 17, photo-derived estimates of wind direction at the source for each available 5-minute period during Experiment 201 are compared with the MDA wind direction estimates and also with the wind direction measurements at the 10-m level of Tower B, which is located on the south peak of CCB. The first 2-hour segment of data displays good general agreement in wind direction, but the period between 2000 and 2200 displays more scatter. In particular, the various wind direction estimates would lie nearer one another if the Tower A estimates were shifted by approximately 10 minutes between 2020 and 2030. Because the plume was released 952 m northwest of CCB, the release point is nearly as close to Tower A as it is to Tower B. Furthermore, because the wind speed exceeded 3 m/sec during the interval, events at Tower A would be swept across the source area within about 5 minutes. Therefore, the discrepancy between the Tower A data and the information inferred from oil-fog plume photographs and measured at Tower B is probably due to spatial as well as temporal inhomogeneity in the flow. For modeling purposes, it is evident that Tower A wind directions do not accurately depict plume transport for this period.

Figure 18 displays the time-series of 5-minute average wind directions for Experiment 210 as estimated from photographs, as interpolated to release height on the basis of Tower A measurements, and as measured at the 10-and 30-m levels of Tower B. These results indicate that the 10-m level of Tower B is most representative of the oil-fog plume transport directions for the three hours of available data from this experiment. Tower B wind direction data from the 30-m level are generally within 5-10° of the "photo" directions for the remainder of the experiment. The wind directions inferred from Tower A data correspond well with the "photo" directions at times during the experiment but are off by up to 20° at other times. This relative lack of correspondence is probably the result of relying on 80-m level wind direction data to supplement the incomplete wind data for the 40-m

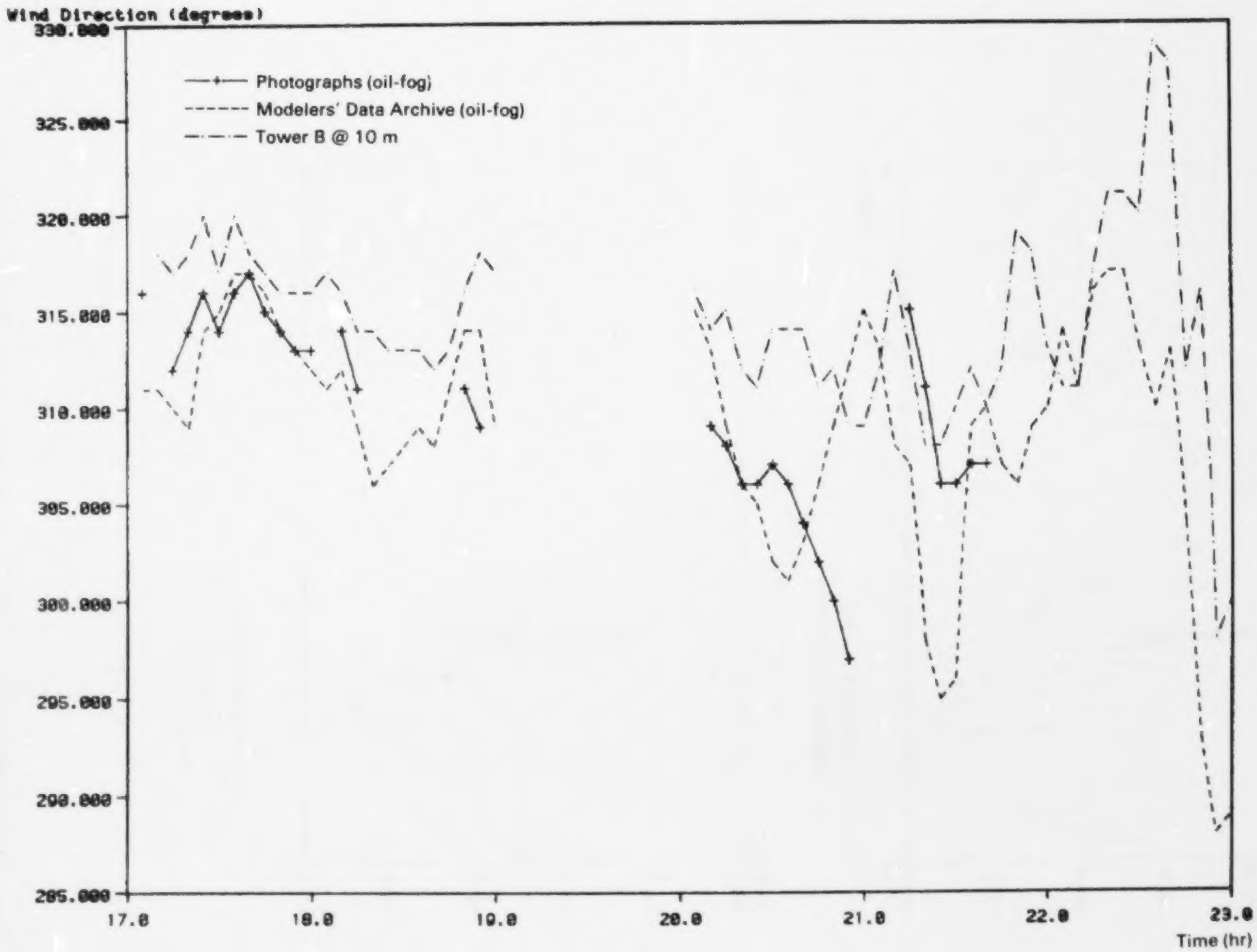

Figure 17. Intercomparison of wind direction time-series data for Experiment 201, derived from photographs, wind measurements at 10 m from Tower B, and interpolated wind measurements from Tower A.

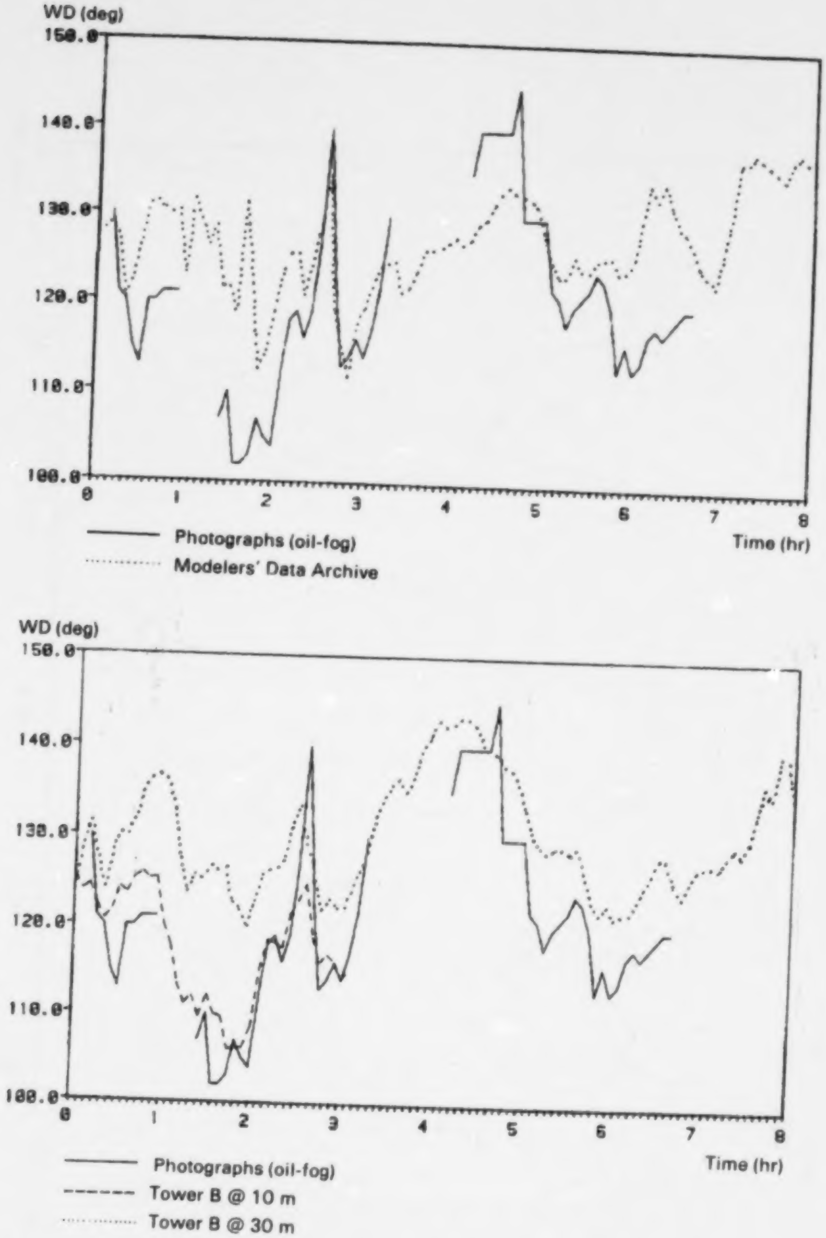

Figure 18. Intercomparison of wind direction time-series data for Experiment 210, derived from photographs, wind measurements at 10 and 30 m from Tower B, and interpolated wind measurements from Tower A.

level on Tower A. Modeling for this experiment must therefore consider the wind directions measured on Tower B and those inferred from the photographs.

3.3.2 Vertical Turbulence Intensity and Initial Plume Growth

Experiment 201

Values of the vertical component of turbulence intensity, i_z, have been estimated from available photographs by several methods and compared with i_z values measured on Tower A. Photographs used in the analysis for Experiment 201 are wallet-size enlargements from 35-mm film. Lengths measured on each photo are converted to angles by the formula:

$$\alpha = \arctan (\ell(\mathrm{mm})/113\ \mathrm{mm}) \tag{30}$$

where ℓ is the measured length, and 113 mm is the effective focal length for the enlargement (50 mm • 2.26). The enlargement factor of 2.26 was estimated by comparing the size of the dominant features on the film and the enlarged print.

These angles are converted to full-scale distances by means of the geometry depicted in Figure 19. The length C is the known distance between the camera position and the release crane; A is the distance between the release crane and any point downwind along the wind trajectory; B is the distance between this point and the camera position; and the sum $\alpha_1 + \alpha_2$ is the total angle α subtended by A as viewed from the camera position. Because this angle can be large, the small angle approximation to Equation 30 is not used, and all distances along the film plane are measured from the center of the image. Hence, two measurements are needed for α. The angle β is obtained from the wind direction and the angle from the camera position to the release crane. With these definitions, the distance downwind of the source is

$$A = \frac{C \sin (\alpha)}{\sin (180-\alpha-\beta)} \quad . \tag{31}$$

Similarly, the thickness of the visible oil-fog plume is obtained from the photograph as an angle, $\delta\theta$, and the full-scale dimension is given by $B \cdot \delta\theta$, where

$$B = \frac{C \sin (\beta)}{\sin (180-\alpha-\beta)} \quad . \tag{32}$$

The intensity of turbulence in the vertical has been estimated via three methods based on measurements of the vertical size of the plume and also via a fourth method based on a direct measurement of the angle spread. Each is described below.

Method 1. Close to the source, the growth in the vertical size of the plume is expected to be nearly linear with distance, and the rate of growth is assumed to be equal to the vertical turbulence intensity. By measuring the angle of spread, E, near the source and assuming that the distribution of plume material is shaped like a top hat, the turbulence intensity is estimated to be:

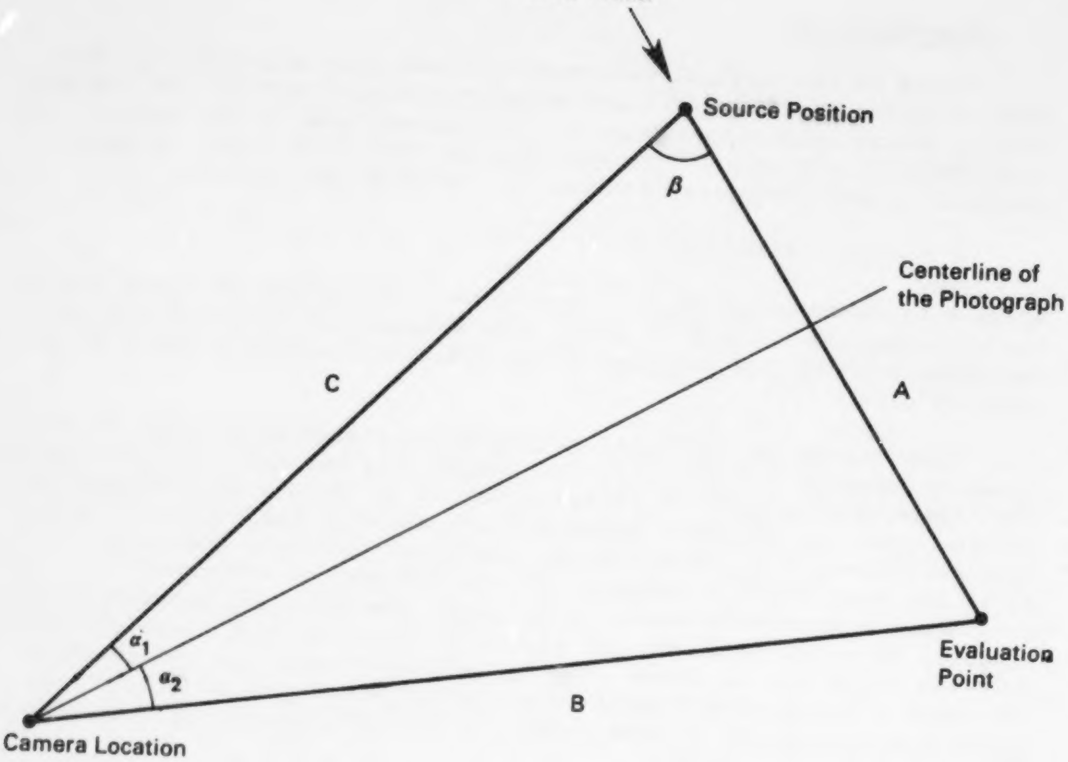
Wind Vector
Source Position
β
Centerline of the Photograph
C
A
α_1
α_2
Evaluation Point
B
Camera Location

Figure 19. Definition sketch for computing distance along the wind trajectory from the source.

$$i_{z1} = \sigma_z/x = E/2\sqrt{3} \; . \qquad (33)$$

Method 2. This approach utilizes the same principle as Method 1, but instead of measuring the spread angle at the source, we measure the plume thickness, h, at several distances along the plume and set the spread angle, E, equal to the maximum value of h/x.

Due to the uncertainties introduced in using the MDA wind directions for the respective 5-minute periods, photo-estimated directions are used to obtain h(x); and instead of assuming a top-hat distribution to relate E to i_z, we have assumed a bi-linear "triangular" distribution because the smoke density is not uniform across the plume. In this method, the vertical intensity of turbulence is given by

$$i_{z2} = \left(\frac{\sigma_z}{x}\right)_{max} = E/2\sqrt{6} \; . \qquad (34)$$

Method 3. Due to uncertainties in defining the edge of the plume and in relating the σ_z estimates to a Gaussian distribution, Method 2 was judged to be of marginal utility. Method 3, used in place of Method 2, applies the technique of Gifford (1980) to relate observed plume dimensions to equivalent σ_z estimates, assuming that the plume spread is Gaussian. This approach provides an estimate of σ_z for each observation of h when a maximum value of h is specified for each plume.

Ideally, the plume should be photographed against a uniform background. It should be uniformly illuminated, and it should be visible at distances large enough to define h_{max}. Most of the nighttime photographs from Experiment 201 were taken with a fairly uniform background, but the lighting is not uniform and h_{max} is generally not clearly established. However, most of these photographs show a slowly-growing plume at the larger distances downwind, so we have set $h_{max} = h(x_{max}) + 1$ (rounded to the nearest whole meter) for those cases in which h_{max} is not clearly attained within the field of view of the photograph.

With this assumption, each value of h measured on the photographs gives rise to an estimate of σ_z for an effective Gaussian distribution of plume material. The turbulence intensity is then calculated with

$$i_{z3} = (\sigma_z/x)_{max} . \qquad (35)$$

Equation 35 once again assumes that the vertical growth of the plume with distance (time) is linear in the initial stages over which σ_z/x should attain its maximum value. Due to the assumptions required for this method, it should provide "upper bound" estimates for i_z.

Method 4. This approach makes use of the estimates of σ_z derived by means of the Gifford technique, but it obtains i_z estimates by matching the observed values of σ_z (t) to

$$\sigma_z(t) = \sigma_w t/(1 + Nt/p)^{0.5} \qquad (36)$$

at $t = 0.5t_{max}$. Equation 36 is the model for σ_z that was used in the Second Milestone Report. In that report, p was a free parameter that was set equal to 1.5 on the basis of comparing σ_z estimates with σ_z values obtained by the WPL lidar system at CCB. However, when Equation 36 is inverted to solve for p with $\sigma_w = i_{z3} \cdot U$ and $\sigma_z(t) = \sigma_z$ (Gifford), p is found to be approximately 0.6. Consequently,

$$i_{z4} = \frac{\sigma_z \text{ (Gifford)}}{x} \left(1 + \frac{Nx}{0.6u}\right)^{0.5} \Bigg|_{x \sim 0.5 x_{max}} , \qquad (37)$$

where x_{max} is the farthest downwind distance at which a value of h can be estimated.

Figure 20 (top panel) shows the correspondence between i_{z1} and the 30-m i_z value interpolated from Tower A data. The intensities nearly agree during the first two experiment-hours and during the sixth hour, but show significant differences during the fourth and fifth experiment-hours. In these two hours, i_{z1} values appear to be either too small or too large. It should be pointed out, however, that the larger values of i_{z1} occur during periods of significant horizontal plume meander and that this horizontal "smearing" could appear as an increase in the vertical dimension of the plume in the photographs.

The 30-m interpolated i_z value from Tower A is also compared to i_{z3} in Figure 20 (bottom panel). The i_{z3} values are moderately greater than the Tower A values during hours 18, 19, and 23. But they agree better during hours 21 and 22, with the notable exception of the peak at 2100. Although the peak in the "photo" i_z's may have an artificial component as has been speculated above, it is unlikely that the peak should be entirely absent. In fact, it is tempting to shift the plots in time so that the fluctuations in the two data sets nearly coincide. Figure 21 shows the result of shifting the "photo" i_z values by -10 minutes.

Several of the peaks in hours 21 and 22 nearly line up in Figure 21. Therefore, it seems plausible that the turbulence field near the smoke plume lags the turbulence measurements on Tower A during this period of time. We saw evidence for this 10-minute phase lag in the wind direction time-series plotted in Figure 17. Plots (not shown here) of σ_w and i_z from 2, 10 and 40 m on Tower A and from 2 and 10 m on Tower B further support the interpretation that the wind shift and the vertical turbulence occur uniformly later near the hill than at Tower A. If this is correct, then the photo i_z values are roughly 2 to 3 times the Tower A i_z value during this part of Experiment 201.

The time-series of i_{z4} values is plotted in Figure 22 alongside those Tower A i_z values interpolated to the release height. It is seen that the i_{z4} estimates tend to inflate the larger values in the i_{z3} time series, but change very little otherwise. The lower part of Figure 22 compares i_{z4} with the i_z values measured at 10 m and 40 m on Tower A. The comparison suggests that "actual" i_z values at plume height could have been underestimated in the MDA during the first two hours of Experiment 201, and by similar reasoning they could also have been underestimated during those

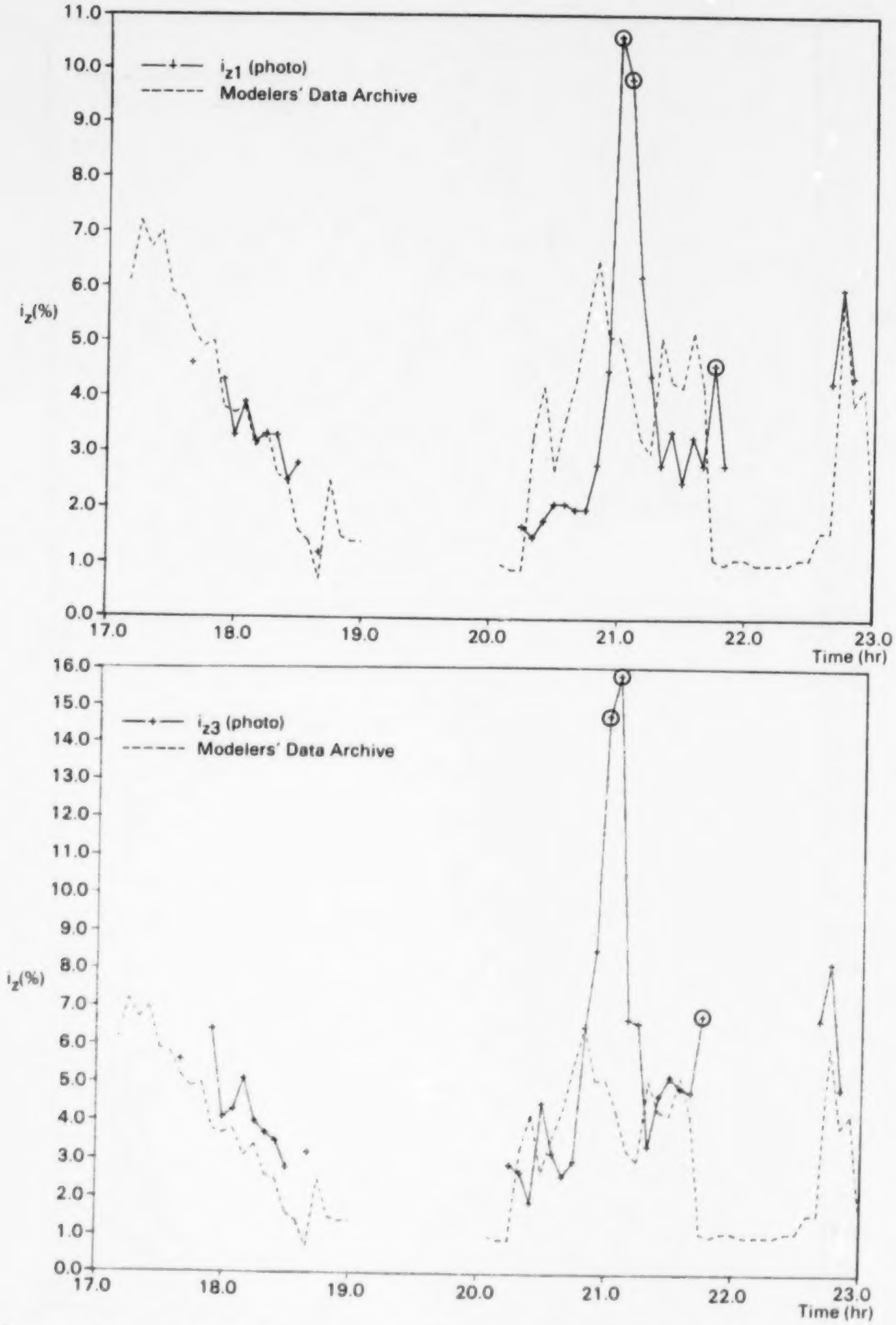

Figure 20. Intercomparison of vertical turbulence intensity (i_z) time-series data for Experiment 201, derived from photographs by Methods 1 and 3, and interpolated from Tower A. (Circles denote periods of considerable horizontal meander.)

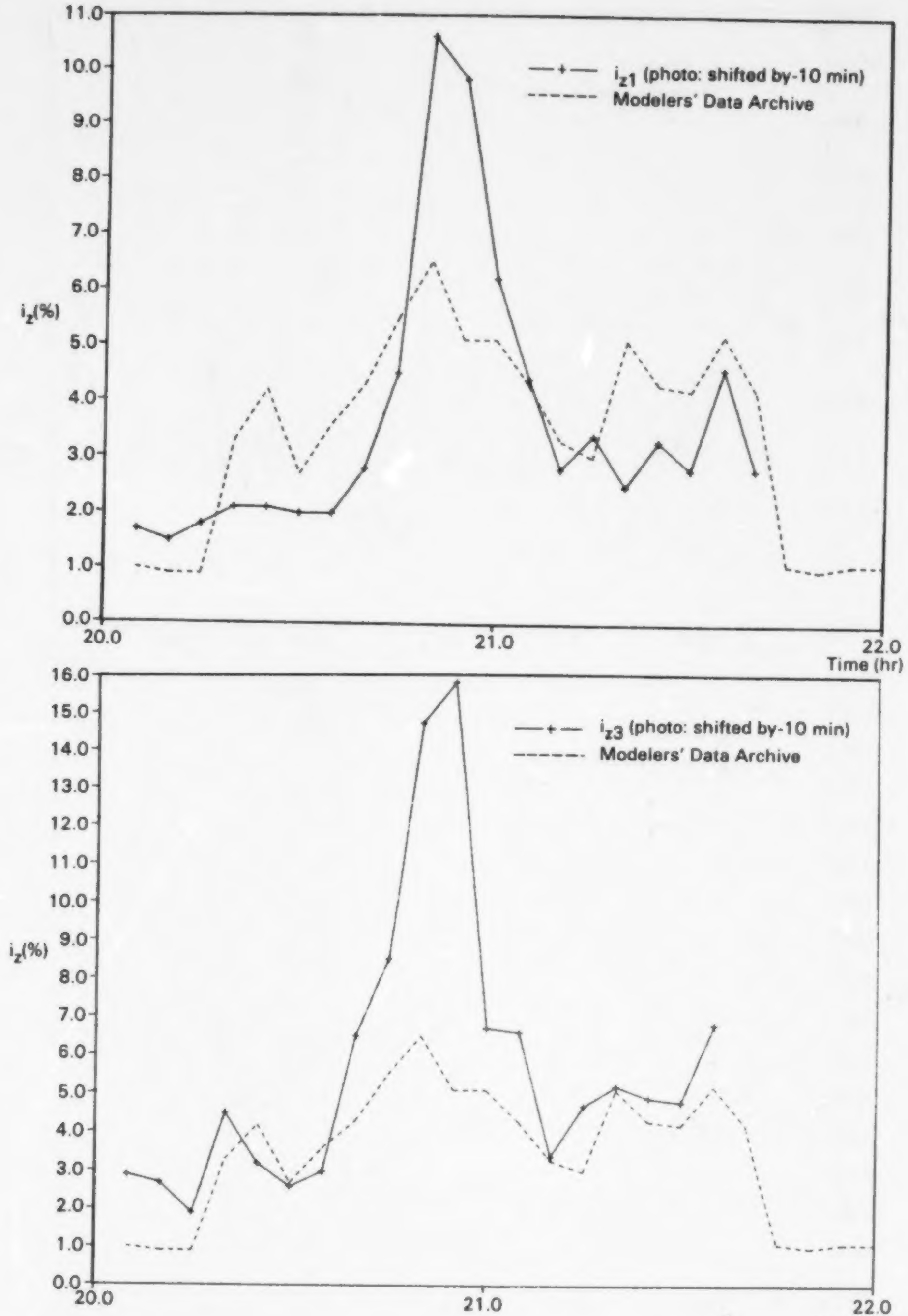

Figure 21. Intercomparison of vertical turbulence intensity (i_Z) time-series data for two hours of Experiment 201, derived from photographs by Methods 1 and 3, and interpolated from Tower A. The "photo" estimates are shifted by - 10 minutes.

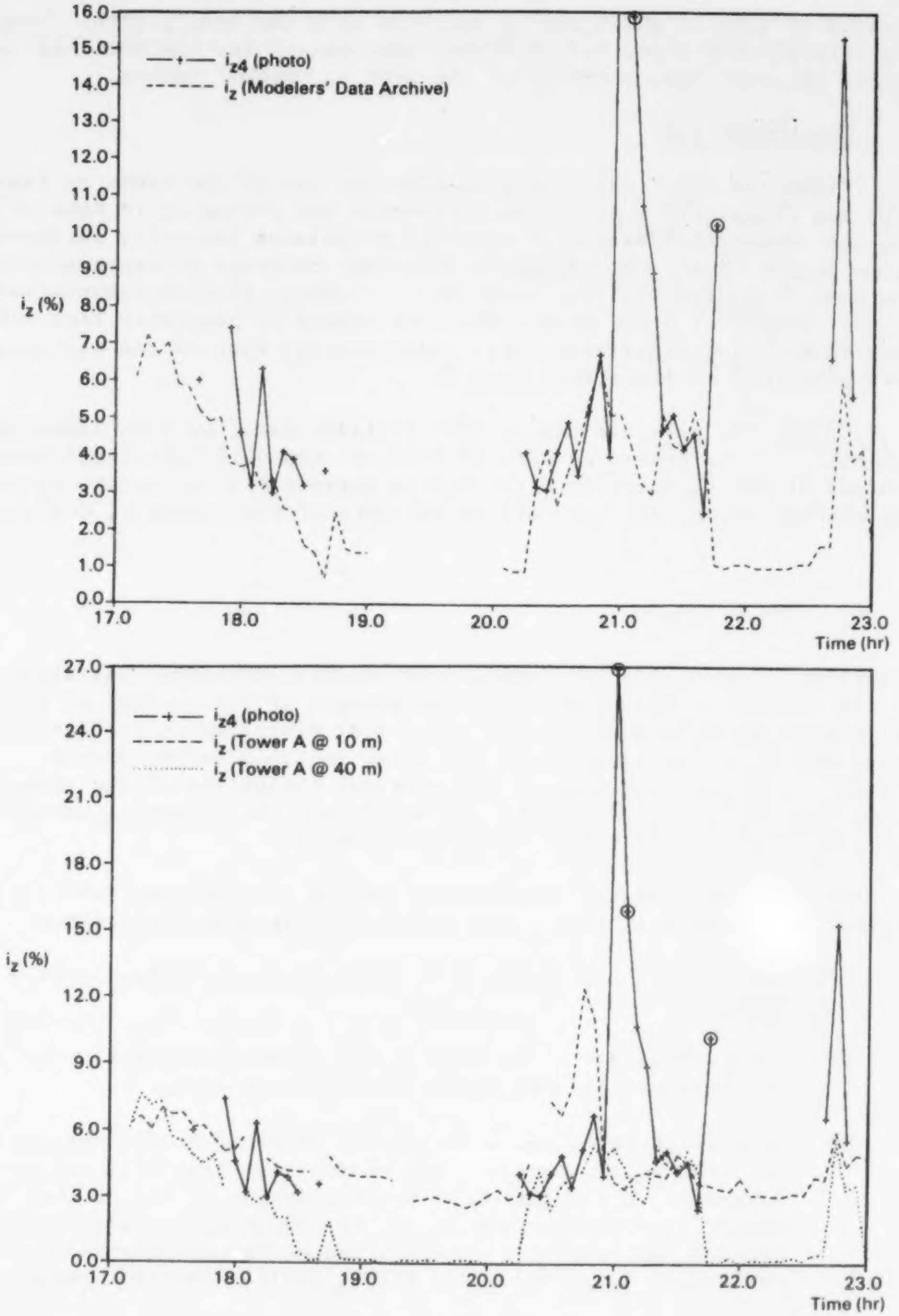

Figure 22. Intercomparison of vertical turbulence intensity (i_z) time-series data for Experiment 201, derived from photographs by Method 4, and interpolated from Tower A. (Circles denote periods of considerable horizontal meander.)

periods of time in which the i_z value at 40 m was nearly zero. However, the interpolated tower values appear appropriate for the remainder of hours 21 and 22, with the exception of the peak i_z (photo) values.

Experiment 210

Processed lidar data are available for two of the hours in Experiment 210, and these data are used to supplement the photographic data in evaluating the representativeness of vertical turbulence intensity estimates at plume height (MDA). Photographic and lidar coverage of experiment-hour 3 is the most extensive for this experiment, although photo-documentation of the initial stages of plume growth near the source is generally less extensive than that during Experiment 201. Consequently, much of the analysis has been performed on experiment-hour 3.

Unlike the previous use of SHIS #1 lidar data, we have looked more carefully at the processed data to evaluate how well calculated second moments of the backscatter distribution represent an effective σ_z for the oil-fog plume, and how well an estimate of the 1-hour σ_z calculated by

$$\sigma_{z_e}^2 = \overline{\sigma_z^2} + \sigma_H^2 \qquad (38)$$

agrees with the σ_z for a superposition of each individual distribution during the hour. Note that $\overline{\sigma_z^2}$ is the average of the squares of the calculated second moments of the individual distribution profiles during the hour, and σ_H^2 is the variance of the plume centroid height during the hour. Recall that much of our previous evaluation of the proposed σ_z growth function used in CTDM was based upon the 1-hour σ_{ze} values obtained from the lidar data using Equation 38.

In this new analysis, best-fit σ_z values are obtained from the processed individual scan lidar data arrays by following these steps:

1) Data arrays are scaled from relative b_{scat} intensity to actual b_{scat}.

2) Data arrays are integrated in the crosswind direction to yield a crosswind-integrated vertical profile of b_{scat}.

3) A Gaussian envelope is fit to the vertical profile by the method of least square errors. The envelope is that of a reflected Gaussian. The location of the centerline is set at the centroid height, and the surface is set to the height of the terrain beneath the centroid. The fitting procedure provides both the centerline b_{scat} value and the σ_z for the best-fit curve.

Step 2 takes any apparent rotation or tilt of the plume in cross-section into account.

Best-fit σ_z values for extended periods are obtained from the vertical profiles resulting from step 2 above in the following way:

- A vertical grid-point spacing is set up to match the greatest vertical resolution available in each scanning plane.
- An average surface elevation is specified for each scanning plane.
- B_{scat} values are interpolated to the vertical grid and summed over all scans within each plane.
- A Gaussian envelope is fitted to the resulting vertical distribution, and best-fit σ_z and maximum b_{scat} values are obtained.

The crosswind-integrated/time-integrated vertical profiles of the plume upwind of the hill are remarkably Gaussian. An example vertical profile is shown in Figure 23. The best-fit σ_z values for the individual means are generally not much different from the second moments of the distribution. The average ratio of the best-fit σ_z to the second moment for the individual scans for hour 3 are:

scan plane	211°	225°	236°	244°	251°	264°
ratio	.90	.92	.95	.92	.84	1.06

Those for hour 6 are:

scan plane	211°	225°	236°	244°	251°	264°
ratio	1.14	1.20	1.00	.86	1.14	1.23

In each case, the 236° plane had by far the most samples.

Focussing on the 236° scanning plane, the ratio of the best-fit 1-hour σ_z to the effective σ_z (second moment plus centroid) is found to be 0.77 in hour 3, and 0.94 in hour 6. These results tend to suggest that the effective σ_z values used in the CTMD Second Milestone Report may be overestimating the vertical size of the plume.

Photographs of the plume taken from the side of the plume trajectory are available from two locations during experiment-hour 3. Because lidar data are available for this hour, measurements of optical smoke plume thickness from these photos can be compared with the best-fit σ_z values obtained from individual lidar scans. Although the lidar data are not 5-minute averages of the plume as are the photographs, the plume appears very coherent during this hour, which suggests that a comparison of the two measurement techniques may be instructive.

Estimates of plume thickness are obtained from the photographs using methods similar to those discussed above. The major departure from that methodology involves projecting the negative image of each frame onto a sheet of graph paper to obtain the plume dimension and position data.

Lidar-σ_z data are compared with photo-h (thickness) data only at those points where the lighting is sufficient to fully illuminate the plume.

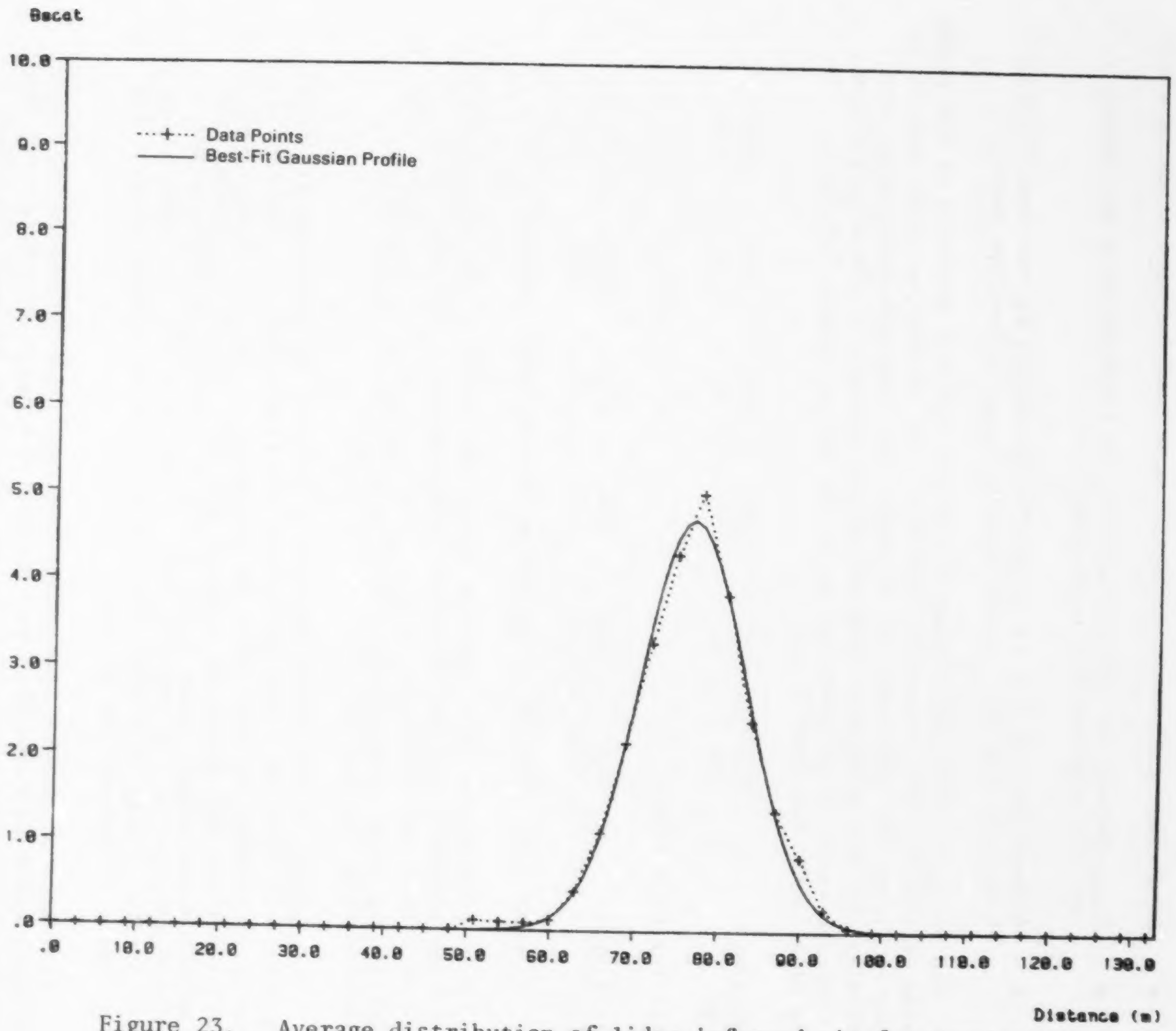

Figure 23. Average distribution of lidar-inferred oil-fog droplet concentrations 800 m downwind of the source for Experiment 210, hour 3.

For photographs taken at camera position 0-11, these points are close to the source, about 50 to 150 m downwind. For photographs taken at camera position 0-10, these points are near the base of the hill (~ 600 m downwind), and also in the col area when the plume traveled over the top of CCB and through the illumination of the draw tower lights. By taking only those lidar and photo data coincident in time, and within 50 m distance, we find that the six available ratios of h/σ_z average 3.69 with a variance of 0.24. Due to the criteria for strong illumination, the photo-h data ought to fully represent total plume thickness, and this may be why the variance is so small.

If we had assumed a top-hat distribution for the plume material, then the ratio of h/σ_z would be 3.46. If we had assumed a semi-circular distribution, h/σ_z would be 4.47. Consequently, the mean value of 3.69 obtained by comparing these photo-h and lidar-σ_z values is quite reasonable for such a coherent plume.

Vertical turbulence intensity values have been inferred from the photo-h data for experiment-hour 3. These data are converted to σ_z data by means of the factor 3.7, and we assume that i_z is equal to σ_z/x out to the first photo evaluation point downwind of the source. When those estimates are compared with the interpolated i_z values contained in the MDA, we find that the four archive values less than or equal to .002 (0.2%) are clearly inappropriate, and we also find that the remaining five values of i_z for which we have photo-derived i_z estimates are on the average 73% of those estimates. Because the linear growth law is unlikely to hold at the distance of the first evaluation point, the interpolated i_z values may represent an even greater degree of underestimation.

Photographic data from Experiment 210-hour 6 are not as extensive as those for hour 3. The regions in which the lidar sampling planes overlap the photographs are sparse, and the plume was not so steady. These factors degrade the quality of comparison between plume thickness obtained from photographs and σ_z values calculated from lidar data. An approximate conversion factor between photo-derived plume thickness and lidar-derived σ_z is on the order of 3.4. No estimates of i_z are possible because the first part of the plume in view of the camera is approximately 500 m downwind of the release.

The first section of the plume is visible in the photographs from experiment-hours 1 and 2. By assuming that a representative ratio of σ_z/h is 3.7 as obtained from the analysis of data from experiment-hour 3, estimates of i_z can be compared with i_z values contained in the MDA. A time-series of these data is presented in Figure 24.

"Photo" i_z estimates agree quite well with the i_z values interpolated to the height of the smoke plume during the first hour, but are substantially larger during the second hour. Observer notes refer to the plume's billowy appearance during a portion of experiment-hour 2 and the photographs clearly show it as well. During the third hour, the "photo" i_z estimates are generally greater than the interpolated Tower A data by about 30%, as mentioned previously.

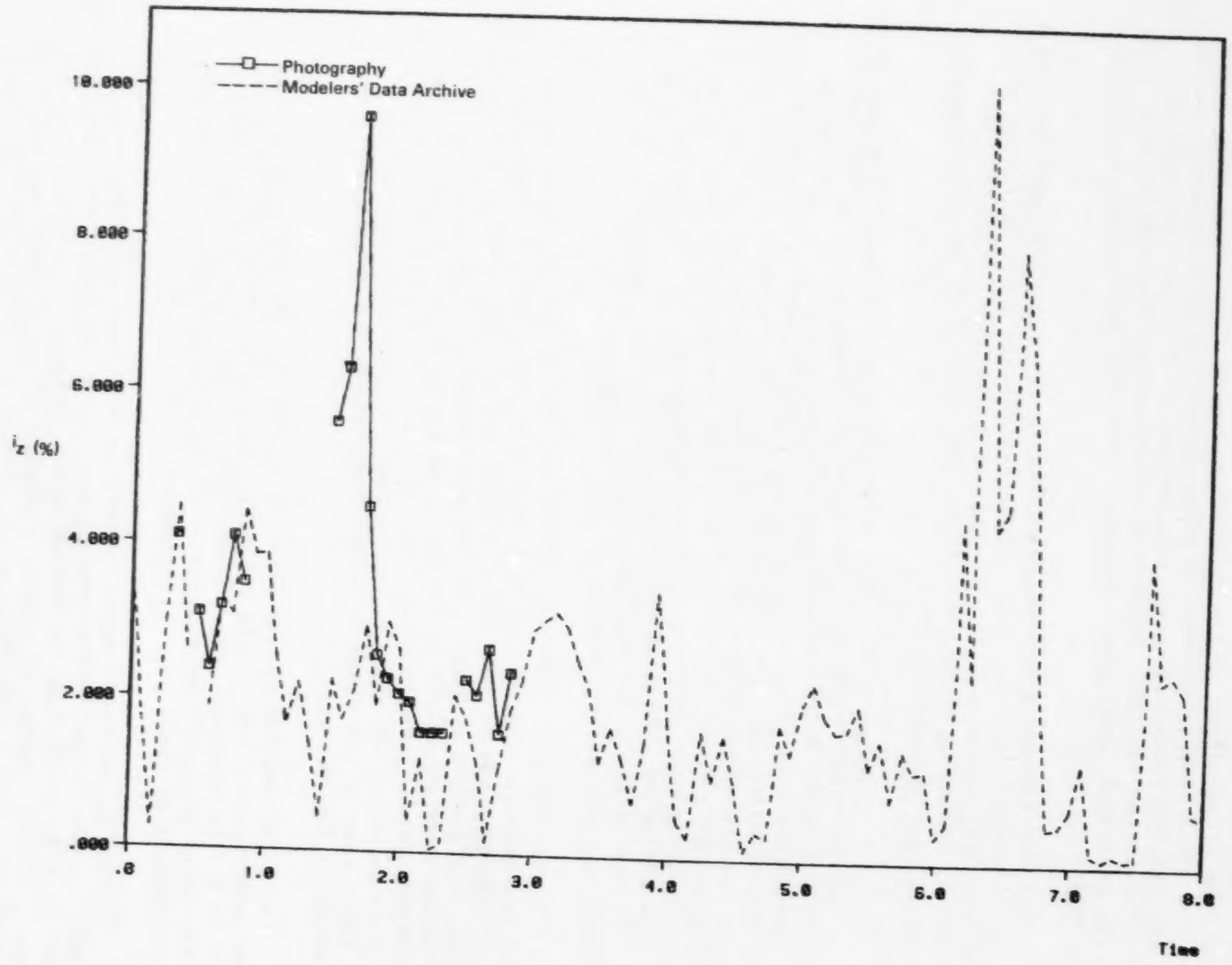

Figure 24. Intercomparison of vertical turbulence intensity (i_z) time-series data for Experiment 210, derived from photographs and interpolated from Tower A.

Conclusion

Vertical turbulence intensity data contained in the MDA generally "follow" the observed behavior of the oil-fog plume. However, there are periods in which these data do not appear to be representative of turbulence at the release site. Excluding these periods, there remains an apparent underestimation of i_z in the archive data compared to rates of initial plume growth obtained from photographs. Some of this may be due to the neglect of source-induced turbulent mixing. Results obtained after including source-induced turbulence are discussed in subsection 3.3.4.

3.3.3 Plume Growth in the Vertical

Because CCB surface concentrations can be very sensitive to the size of σ_z, the form of $\sigma_z(x)$ is an especially important topic for evaluation. In particular, we have evaluated the form of $\sigma_z(x)$ proposed in the CTMD Second Milestone Report by analyzing the growth of photo-derived and lidar-derived σ_z values with distance between the release position and the upwind base of CCB.

Experiment 201

Plume thickness values obtained from photographs are converted to estimates of σ_z by using the Gifford technique and a top-hat distribution assumption. Because processed lidar data are as yet unavailable for Experiment 201, there is no check on which of these methods is more appropriate. Also, although the analysis of lidar data from Experiment 210 showed that $\sigma_z \sim 3.7$ h, this result may not be appropriate for Experiment 201 because the lighting conditions are substantially different in these two experiments. Consequently, this analysis of the vertical growth of the plume with distance will continue to focus on both methods. Note that the top-hat method is expected to underestimate actual σ_z values with increasing distance downwind because the "edges" of the plume are lost. Also, the Gifford technique is expected to overestimate actual σ_z values with increasing distance because the true maximum in apparent plume thickness is not usually seen in the photograph, and because the plume brightness may decrease with distance due to the light scattering properties of the plume rather than due to dilution.

Vertical turbulence intensities estimated from photographs are referred to by i_{z1}, i_{z3}, and i_{z4}, and these have the same meaning as in the previous subsection. σ_{z1} values are computed from plume thickness data by assuming that the plume material exhibits a top-hat distribution:

$$\sigma_{z1} = h/2\sqrt{3} \quad . \tag{39}$$

σ_{z2} values are computed from h data by means of the Gifford technique (only σ_{z1} and σ_{z2} are used in the subsequent analyses). Vertical plume spread is also computed from the PGT dispersion parameter formulas for the most appropriate stability class as contained in the MDA. These are simply denoted by σ_z(PGT).

Figure 25 displays the ratio of σ_{z1} and σ_{z2} to σ_z(PGT) versus downwind advection time. The ratios are plotted as logs to facilitate "factor of 2" types of comparisons. It is evident that the σ_{z2} estimates follow a growth law more similar to that contained in the σ_z (PGT) curves than do the σ_{z1} estimates. The analyses also suggest that σ_z(PGT) values would match the photographic estimates better if they were based on a more refined estimate of vertical turbulence intensity than the surface stability class. ~~Even so, the PGT curves tend to overestimate~~ the rate of growth of the vertical spread with time as derived by the Gifford technique.

Figure 26 contains comparisons of σ_{z1} (top hat) against σ_z values calculated by means of Equation 36 with p set equal to 1.5. As in Figure 25, the ratio of σ_{z1} to σ_z is plotted as a log versus advection time. Two versions of σ_z (calculated) are presented: one uses i_{z1}, the other uses i_{z3}. These two estimates of i_z tend to bracket those values interpolated from Tower A data. The results of the comparison show that the functional form assumed in Equation 36 causes the plume to grow too rapidly with advection time, compared to the development of σ_z obtained with the top-hat assumption. Futhermore, i_{z1} tends to align σ_{z1} with the calculated values better than i_{z3} because the i_{z1} values are also derived from the top-hat distribution assumption.

Figure 27 indicates that Equation 36 performs better when σ_{z2} (Gifford) is viewed as the more accurate description of the plume spread. The upper portion of the figure compares σ_{z2} with σ_z calculated by means of Equation 36 with $i_z = i_{z3}$ and p set equal to 1.5. The distribution of ratios is centered at approximately 1.0, and the rate of growth of σ_{z2} beyond approximately 30 seconds travel time tends to follow that prescribed by Equation 36.

Because Equation 36 appears to simulate the overall growth trend in σ_{z2} beyond t = 30 sec during Experiment 201, we have used the σ_{z2} and i_{z3} data to re-evaluate the value of the parameter p.

By solving Equation 36 for p,

$$p = \frac{Nt}{(i_z ut/\sigma_z)^2 - 1} \qquad (40)$$

and a least squares fit to the scatterplot of $(i_{z3}ut/\sigma_{z2})^2 - 1$ versus Nt produces a value of 0.6 for p. In the notation of Pearson et al. (1981), $p = 2\gamma^2$, and so a value of 0.6 produces a γ of 0.55. The theory of Pearson et al. (1981) indicates that γ, a molecular exchange coefficient, could range from 0.1 to 0.8.

Using this new value of p, we have recalculated the i_{z4} estimates described previously. Recall that the matching actually takes place at the measurement point nearest to 0.5 t_{max}, where t_{max} is the measurement point farthest from the release crane. A re-evaluation of p was made with σ_{z2} and i_{z4} as a consistency check, and the results are displayed in Figure 28. The upper plot contains all data, and the lower contains only those data that were not used to match i_{z4} to σ_{z2}. The value of p is nearly the same in both plots; p (upper) = 0.567, p (lower) = 0.566.

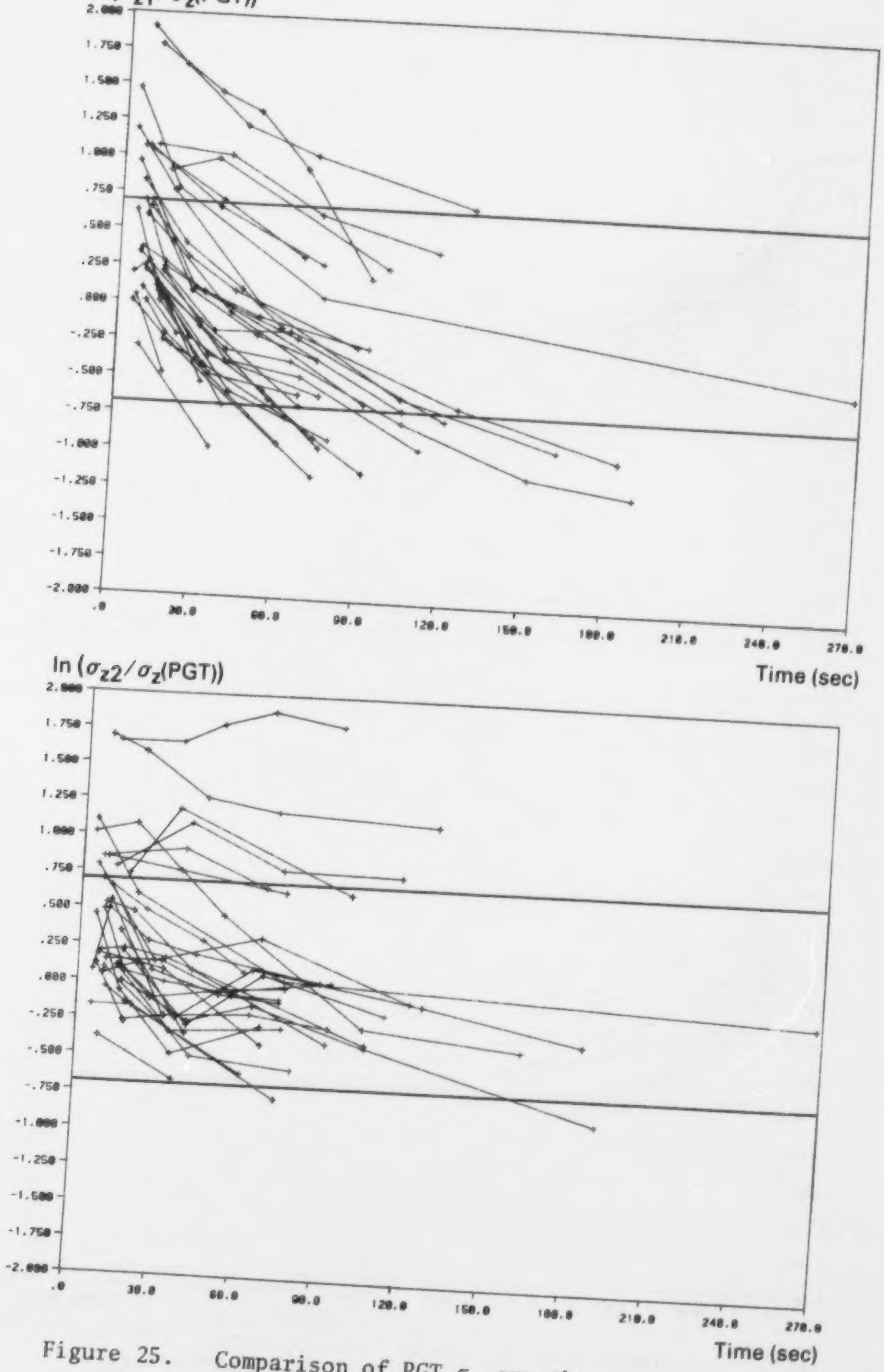

Figure 25. Comparison of PGT σ_z growth curves with σ_z data from Experiment 201 photographs.

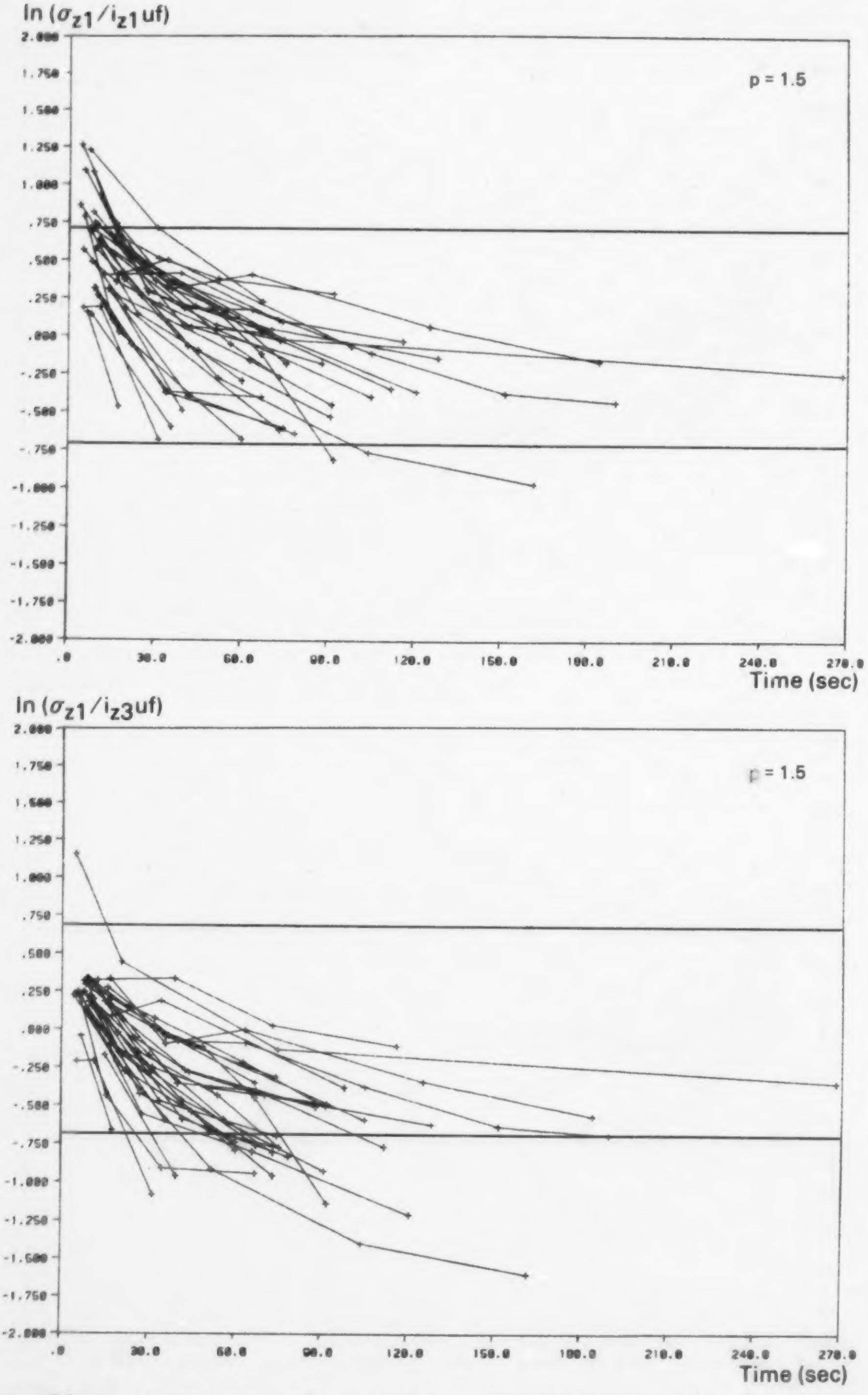

Figure 26. Comparison of σ_z (calc.) growth curves with σ_{z1} data derived from Experiment 201 photographs. (σ_z(calc.) = i_z uf, $f = t/(1 + Nt/p)^{0.5}$).

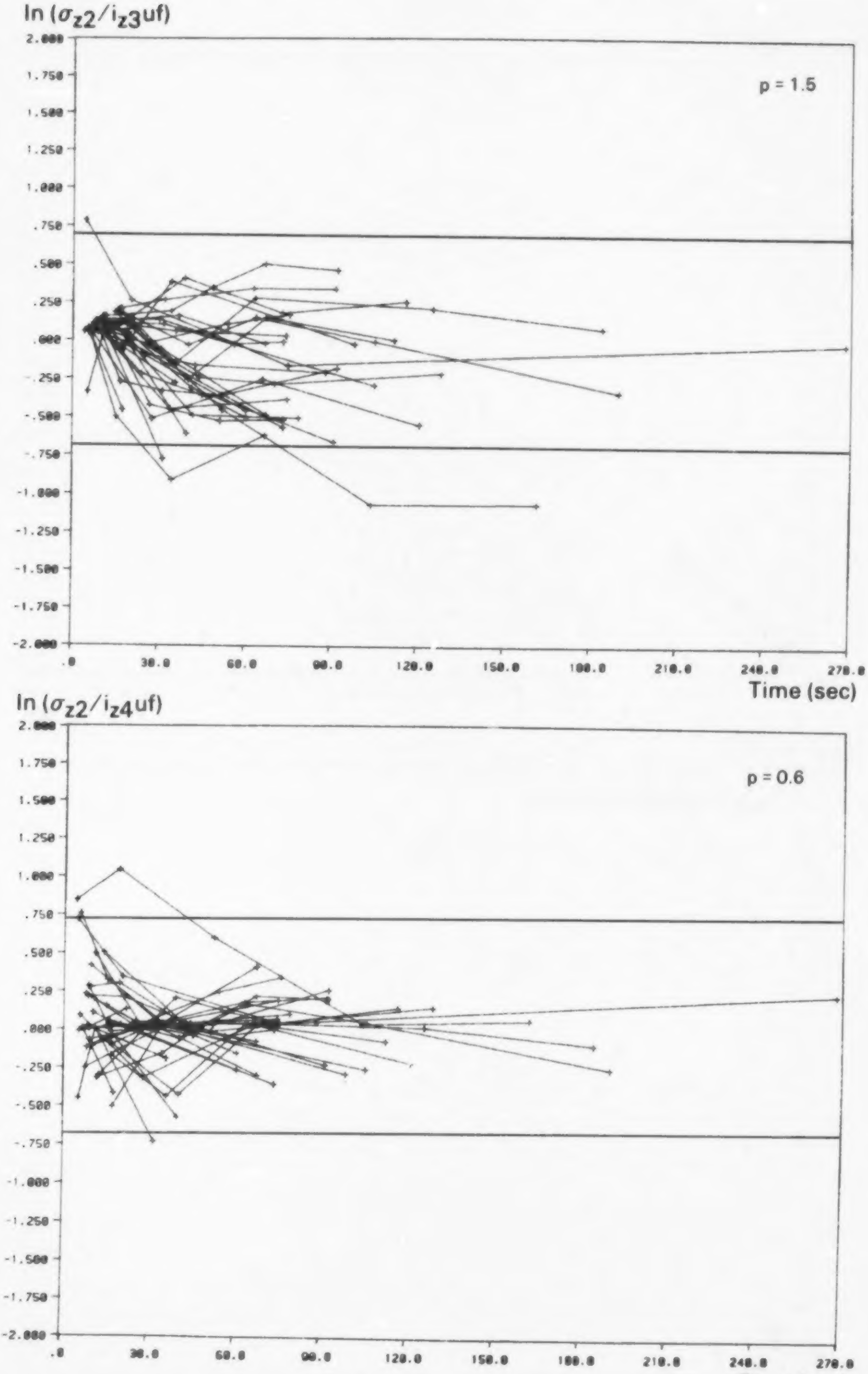

Figure 27. Comparison of σ_z(calc.) growth curves with σ_{z2} data derived from Experiment 201 photographs. (σ_z(calc.) = $i_z uf$, $f = t/(1+Nt/p)^{0.5}$).

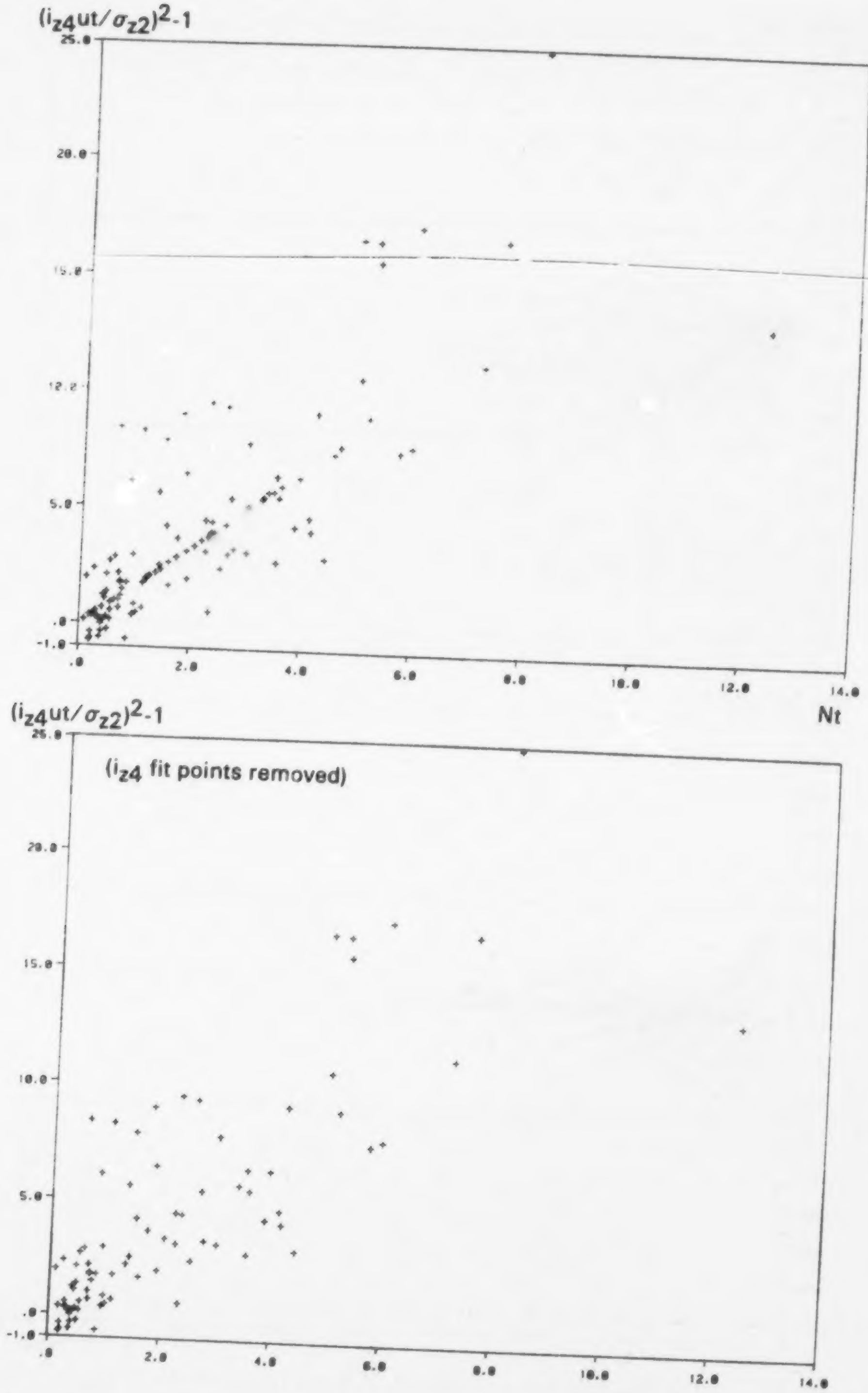

Figure 28. Scatterplots used in computing best-fit p for Experiment 201.

These analyses increase our confidence in estimating σ_z by Equation 36. We see that the growth trend is similar to those Gifford technique estimates of σ_z derived from the photographs. And we also see (Figure 22) that the i_z values inferred by matching the photo σ_z values to Equation 36, with $p = 0.6$, at the measurement point nearest 0.5 t_{max} are generally "reasonable" compared with i_z values measured on Tower A.

Experiment 210

The analysis of the growth of σ_z with distance during Experiment 210 focuses on experiment-hour 3 because the link between vertical plume thickness as measured from the photographs and σ_z as calculated from the lidar data is best for this hour.

The relationship among the photo-estimates of σ_z, the lidar estimates of σ_z, and the curve $\sigma_z(x)$ computed with Equation 36 ($p = 0.6$) and the photo-derived i_z estimates are summarized in Figure 29. In this figure, the "plus" symbols represent the photo-estimates of σ_z; the "box" symbols represent the lidar-σ_z values; and the solid line is the computed $\sigma_z(x)$ curve. The figure suggests the following:

- The computed σ_z (x) curve corresponds well with most of the data points out to 600 to 800 m from the source.
- For those periods without photo-estimates of σ_z, simply multiplying the interpolated i_z data from Tower A by 1.37 (the reciprocal of 0.73) places the calculated $\sigma_z(x)$ curve in the neighborhood of the lidar-σ_z points.
- When the plume passes through the col, the apparent size of the plume is on the order of one-half the value expected in the absence of the hill.
- Although the $\sigma_z(x)$ curve appears quite reasonable in general, the correspondence with the other data would improve somewhat if the i_z value were increased, and if the curve grew more slowly than with distance to the 1/2 power beyond 200 to 300 m.

These results indicate that the form of Equation 36 is appropriate for estimating the dispersion of elevated smoke releases during Experiments 201 and 210, at least over distances on the order of 500 m to 1000 m. Unresolved, however, is the question of whether the square-root distance growth continues well beyond 1000 m at CCB. This far-field growth law is not of critical importance for the purpose of estimating concentrations over CCB, but it will become more important in estimating concentrations for full-scale power plant situations. For the present, we shall use the formulation of Equation 36, and re-interpret our estimates of i_z by including a measure of source-generated turbulence in the analysis.

3.3.4 σ_z Tuning Parameters

The preceding discussions of the σ_z analyses assumed that i_z and p could be viewed as free parameters in fitting observed estimates of σ_z

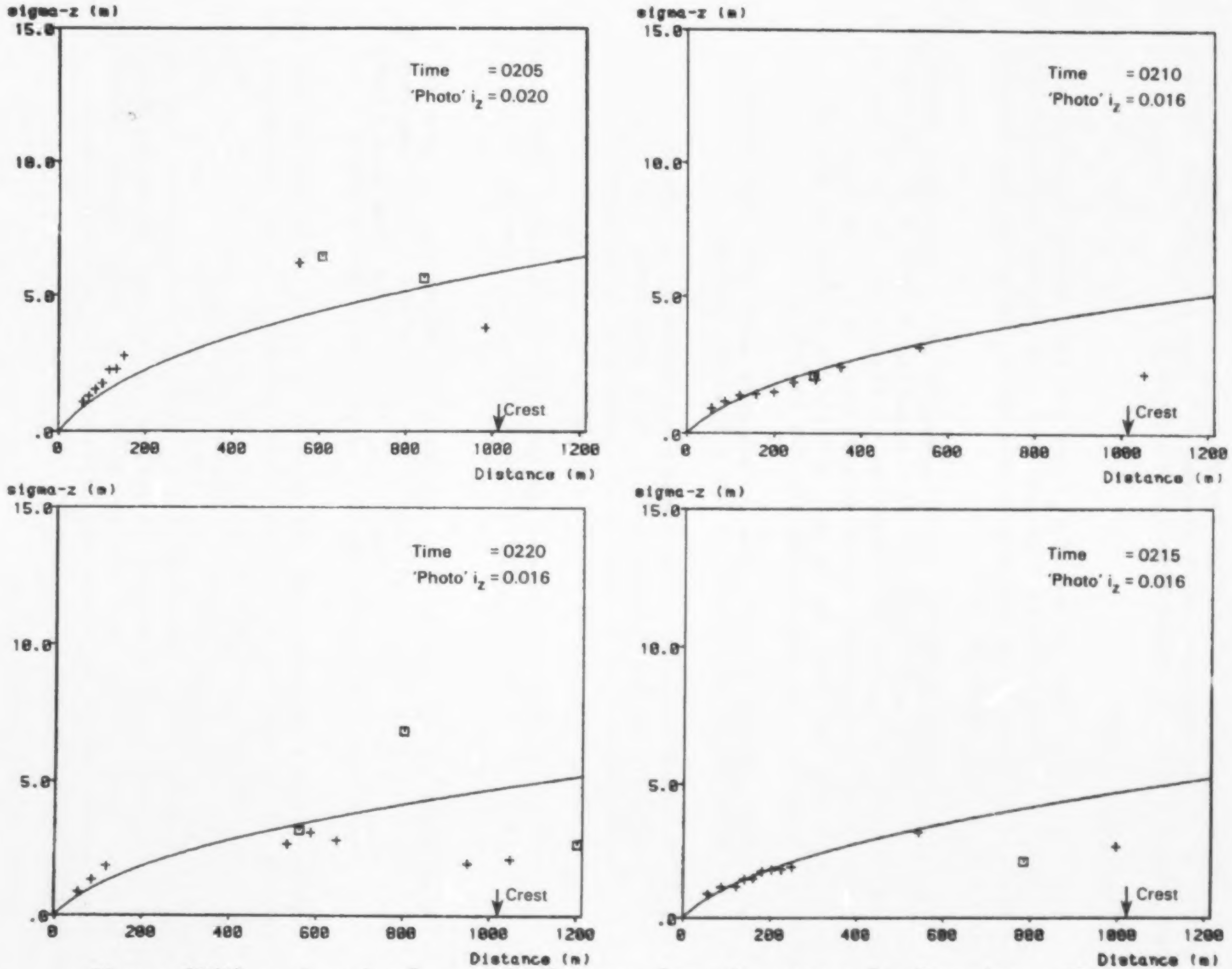

Figure 29(1). Growth of σ_Z with distance from the source for Experiment 201, hour 3. + denotes photo-derived σ_Z's; ⊡ denotes lidar-derived σ_Z's; solid curve is $i_Z x/(1+N\ x/pu)^{0.5}$, p = 0.6.

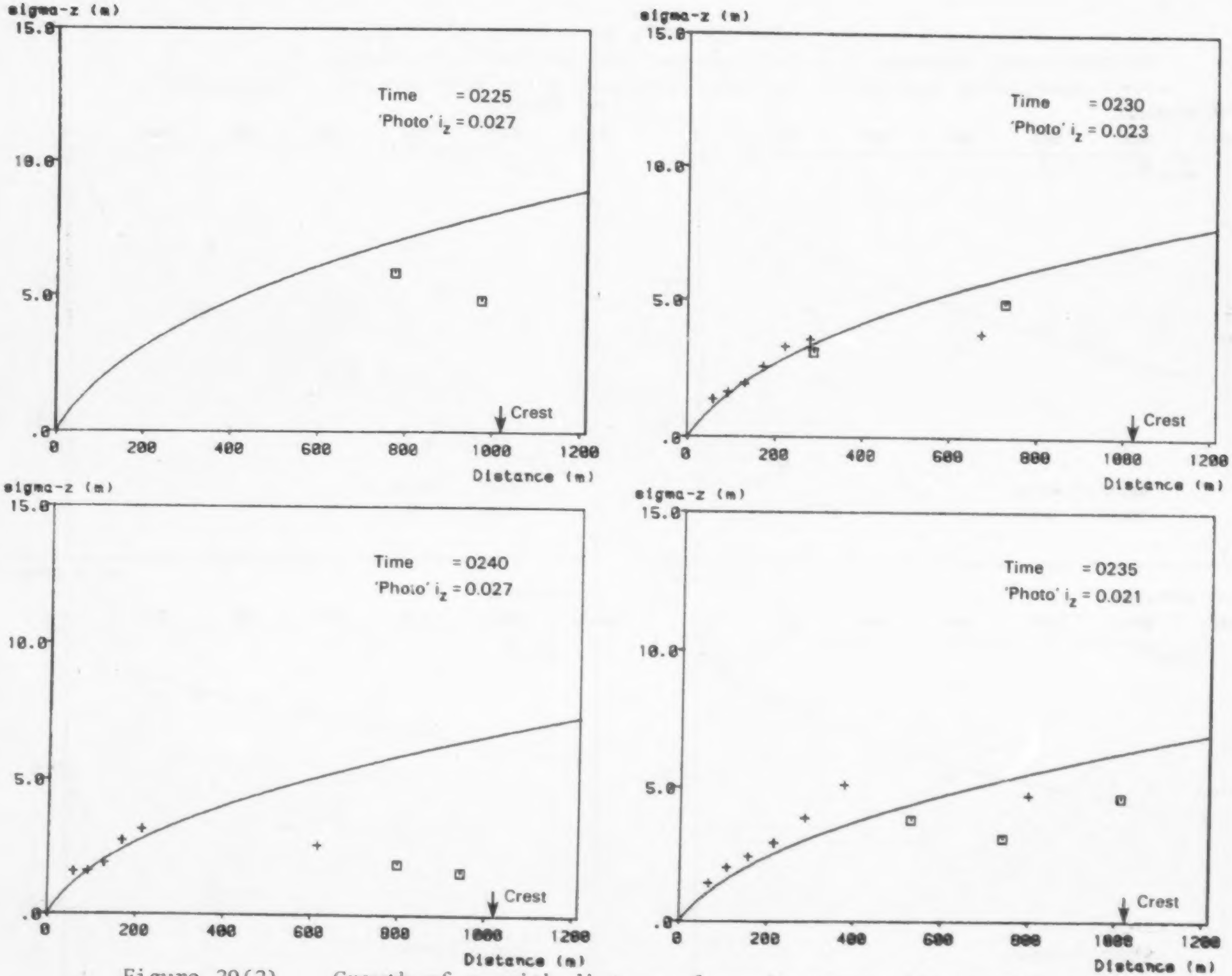

Figure 29(2). Growth of σ_z with distance from the source for Experiment 201, hour 3. + denotes photo-derived σ_z's; ⊡ denotes lidar-derived σ_z's; solid curve is $i_z x/(1+N\ x/pu)^{0.5}$, p = 0.6

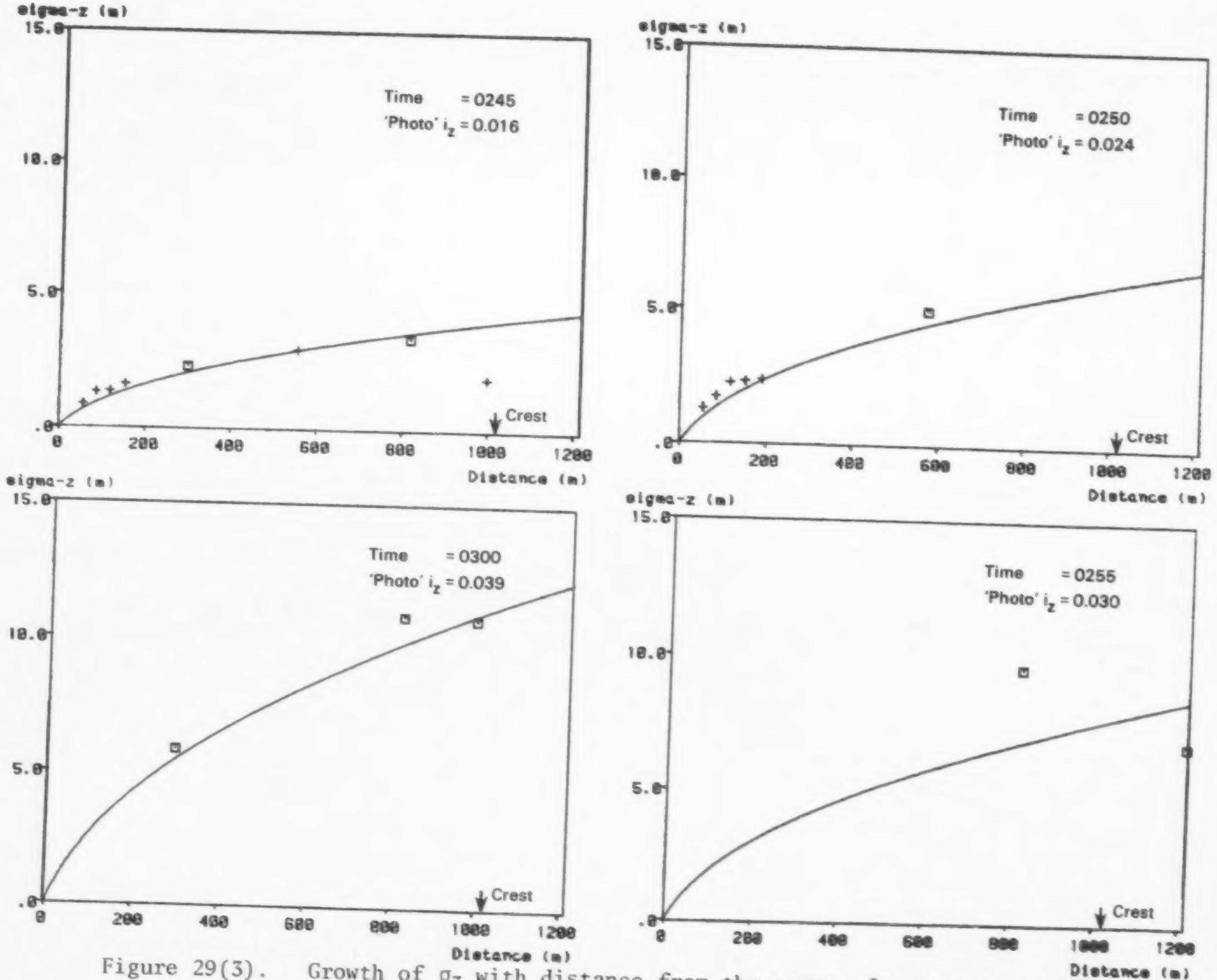

Figure 29(3). Growth of σ_z with distance from the source for Experiment 201, hour 3. + denotes photo-derived σ_z's; ⊡ denotes lidar-derived σ_z's; solid curve is $i_z x/(1+N\ x/pu)^{0.5}$, p = 0.6

to the other variables in Equation 36. But Equation 36 does not explicitly contain the effect of source-induced turbulence on the development of σ_z with distance. This omission could be responsible in part for discovering that the photo-derived i_z estimates are generally greater than i_z values contained in the MDA.

When the source-induced turbulence is included as a "virtual source distance" (x_v), Equation 36 is rewritten as

$$\sigma_z(x) = i_z(x + x_v)/(1 + N\ (x + x_v)/u\ 2\gamma^2)^{0.5} \qquad (41)$$

so that there are three free parameters. x_v is not treated as a parameter in itself, however. Instead, the initial mixing is characterized by an initial σ_{zo}, where

$$\sigma_{zo} = \sigma_z(x = 0) \qquad (42)$$

Fixing the value of σ_{zo} therefore allows one to calculate x_v by means of Equation 41.

A Monte Carlo parameter optimizing scheme is used to select the combination of σ_{zo}, i_z, and γ that provides the best fit of Equation 41 with the estimated σ_z data. When this is applied to each 5-minute period of Experiment 210-hour 3, γ is found to vary from 0.16 to 0.76, with an average value of 0.4. The range in γ reflects the range in the shape of $\sigma_z(x)$ contained in Figure 29. The smaller values of γ apply to $\sigma_z(x)$ curves that level out more at large x, and the larger values apply to $\sigma_z(x)$ curves with a greater rate of growth at large x. Due to the uncertainty in the σ_z estimates in Figure 29 and the possible influence of the hill on the plume near the upwind base of the hill, no clear trend in γ could be identified in the data to construct a model for γ. Therefore, we choose to fix γ at a representative median value. On the basis of the analyses presented in subsection 3.3.3, and the generally good agreement between the data in Figure 29 in which σ_z(calc.) is based on $p = 0.6$, γ is chosen to be 0.525 (and p is now 0.55).

Fixing the value of γ forces the optimizer to adjust the values of σ_{zo} and i_z in fitting Equation 41 to the data. Using the data for Experiment 210-hour 3 once again, σ_{zo} varies from 0.3 m to 1.7 m. Eight of the twelve values are less than 0.75, and these average 0.48 m. The best-fit value of i_z is not very sensitive to the value of σ_{zo} when σ_{zo} is in the 0.3-m to 1.7-m range. For example, if 0.5 is substituted for 1.21, the best-fit i_z value changes from 0.014 (1.4%) to 0.016. Therefore, most of the variability in σ_{zo} when σ_{zo} is appreciably different from 0.5 during this experiment-hour goes toward improving the goodness-of-fit. A representative value for σ_{zo} appears to be 0.5 m.

All of the experiment-hours of Experiment 210 produce similar ranges of γ and σ_{zo}. When γ is fixed at 0.525, and σ_{zo} is fixed at 0.5 m, the best-fit values of i_z generally follow the measured i_z data. Differences between the best-fit and measured i_z data are found to result from the following factors:

- waves - the plume had pronounced waves in it at times, and best-fit i_z's were approximately 1.3 times the measured i_z's. However, this difference is reduced considerably if we assume that the photographs show a triangular distribution rather than a top hat.

- horizontal spread - during some periods of considerable horizontal meandering or spreading of the smoke plume, the vertical size of the plume is overestimated.

However, there are periods in which the photographic data are genuinely dissimilar to the Tower A turbulence intensity estimates at the plume height. These occur when the tower i_z values are less than 0.008, or when the photos show periods of enhanced vertical spread. Figure 30 contains the time-series plots of the interpolated i_z data from the MDA and the best-fit i_z data from the preceding analysis. Those periods in which an undisputed discrepancy exists between the two i_z values are indicated by circling the best-fit i_z data points.

The analysis of plume spread data from Experiment 210 indicates that:

- the σ_z formula with $\gamma \approx 0.5$ and $\sigma_{zo} \sim 0.5$ is appropriate for moderate wind speed (3-8 m/sec) experiments such as 210, when the oil-fog is generated by the TIFA thermofogger; and

- turbulence intensities interpolated to the release height from Tower A data are generally appropriate, although the lower values (less than 0.008) appear consistently too small.

The same analysis has been applied to the data for Experiment 201. In this case, we have taken the "σ_{z2}" estimates of plume spread derived from the photographs with the Gifford technique. Preliminary tests of fitting several randomly selected 5-minute time periods with γ, σ_{zo}, and i_z as free parameters produced several estimates of γ between 0.3 and 0.6. On the basis of the overall fit of 0.57 (subsection 3.3.3) for Experiment 201 and on the results found in analyzing Experiment 210 data, γ was set at 0.55; σ_{zo} was set at 0.5; and best-fit values of i_z were obtained.

Figure 31 shows these estimates of i_z compared to the i_z data contained in the MDA. Between 2020 and 2145, the archive wind speed, Brunt-Vaisala frequency, and i_z data are shifted in an attempt to account for the apparent lag between the Tower A data and the plume and Tower B data. Data for 2020 are persisted for 10 minutes, and the remaining data in the period are shifted in time so that the 5-minute period ending at 2035 is filled with data from 2025, and so on. The photo-derived σ_z data are fit using Equation 41 with the shifted u and N data, and the resulting best-fit i_z data are compared against the shifted MDA i_z data in Figure 31.

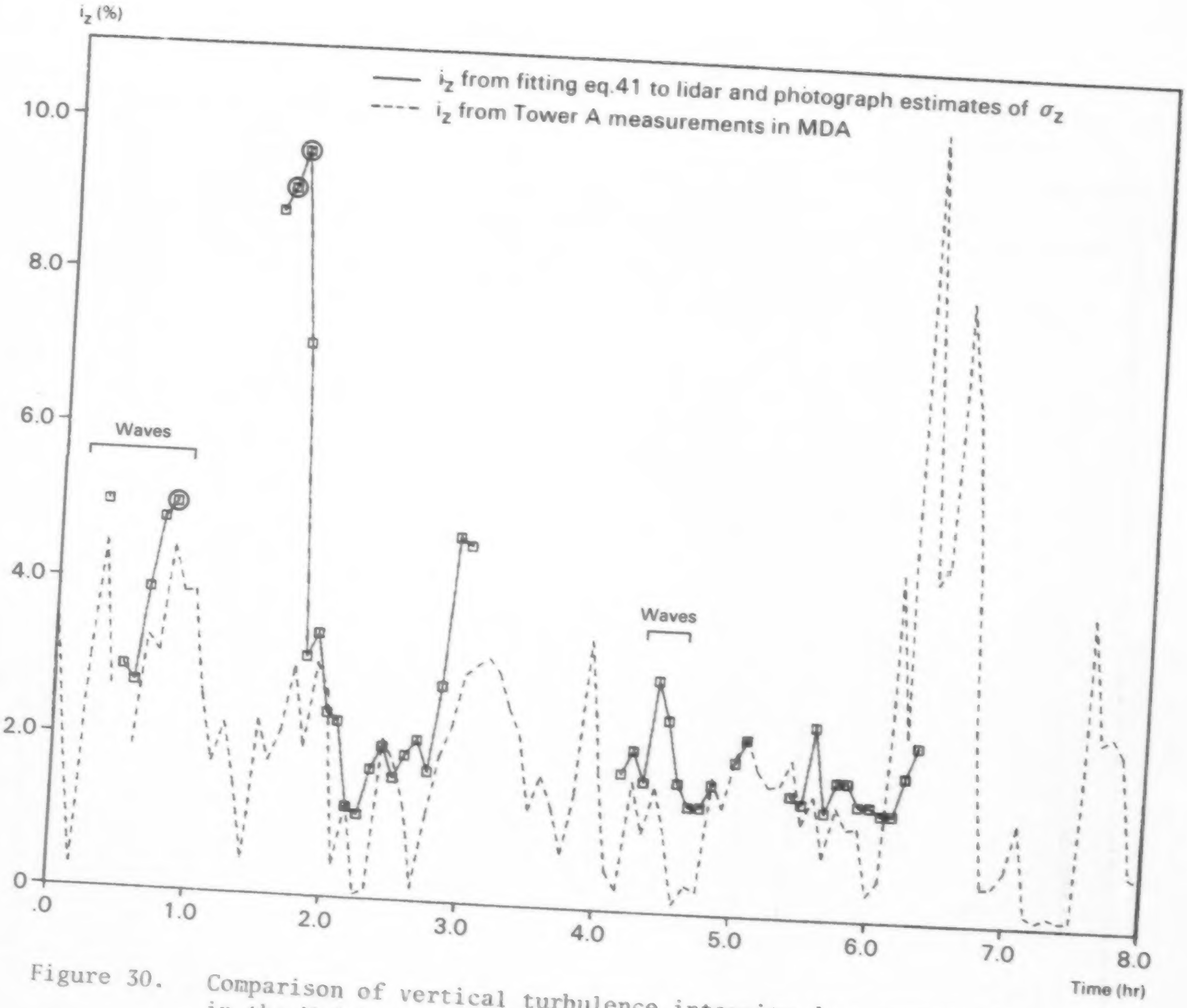

Figure 30. Comparison of vertical turbulence intensity data contained in the Modelers' Data Archive with estimates made by fitting σ_z (calc.) to the σ_z data estimated from the photographs from Experiment 210. (Circles denote periods of relatively large i_y.)

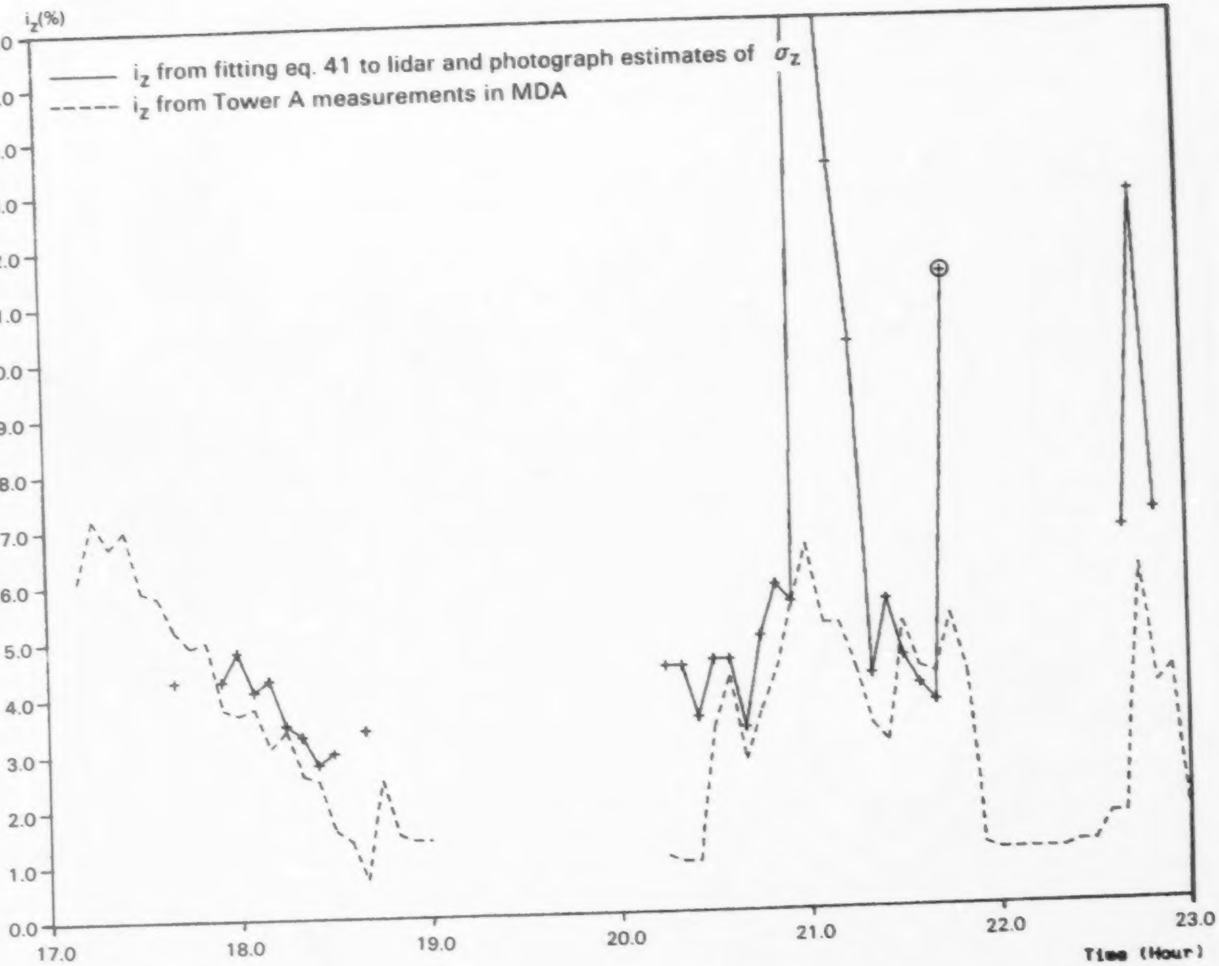

Figure 31. Comparison of vertical turbulence intensity data contained in the Modelers' Data Archive with estimates made by fitting σ_z (calc.) to the observed σ_z^2 data for Experiment 201. (Circle denotes period of relatively large i_y.)

Aside from the major isolated peaks in the best-fit i_z time-series, the best-fit estimates lie reasonably close to the MDA i_z values. This boosts our confidence in modeling σ_z at CCB with Equation 41 and the turbulence data interpolated to the release height. However, this analysis has also indicated that the Tower A data are not always representative of conditions at the release. The smoke plume undergoes considerable vertical growth at times when the archive data would indicate more modest growth and when low values of turbulence intensity are recorded, the smoke-plume growth does not reflect this.

An assessment of how well the calculated σ_z data fit the photo-derived σ_z data can be obtained by plotting the photo-derived σ_z values against the calculated σ_z values. Figure 32 shows the result of doing this for Experiments 201 and 210. The fit is uniformly best for the smaller values of σ_z because these are closer to the release point, and are therefore controlled most by the best-fit i_z value. Beyond this region, the shape of the growth curve is more strongly influenced by γ, N, and u. Here the fit is not so good, but most of the calculated values lie well within a factor of two of the photo-derived values. These figures, taken with Figures 30 and 31, indicate that $\gamma = 0.525$ and $\sigma_{zo} = 0.5$ are reasonable representative values for Experiments 201 and 210.

3.3.5 Turbulence Over CCB

Experiment 201

Five towers were operated on CCB during SHIS #1. Tower B (a 30-m tower) was placed on the south peak, and Towers C, D, E, and F (10-m towers) were placed near the 70-m height contour on the northeast, southeast, southwest, and northwest sides of CCB, respectively. Vertical turbulence data on CCB for Experiment 201 are available at the 2-m level of Towers C, E, and F, at the 2-m and 10-m level on Tower D, and at the 2-m, 10-m, and 30-m level of Tower B. The 2-m and 10-m level data from these towers, the turbulence data from Tower A at the 2-m, 10-m and 40-m levels, and the Tower A turbulence data interpolated to the smoke-release height (30 m) are plotted in Figure 33.

The data interpolated to smoke height are taken from the MDA. Other Tower A data and the Tower B data are taken from the full data base, and a prop-response correction factor is applied (as discussed in CTMD Second Milestone Report). Data from Towers C, D, E, and F are taken from the full data base, adjusted for prop response, and then adjusted for the inclination of the mean 5-minute wind to the horizontal. The latter adjustment is an approximate method to obtain the turbulence intensity in the direction perpendicular to the mean streamline of the flow:

$$\sigma_w'^2 = \frac{\overline{u}^2 + \overline{v}^2}{\overline{u}^2 + \overline{v}^2 + \overline{w}^2}\left(\sigma_w - \sigma_u\sqrt{\frac{\overline{w}^2}{\overline{u}^2 + \overline{v}^2}}\right)^2 . \qquad (43)$$

This formula is approximate in that the full expression for σ'_w contains the cross-correlation $\overline{u'w'}$, which is not measured. Because the absolute value of $\overline{u'w'}$ must be less than the product $\sigma_u\sigma_w$, two limit cases

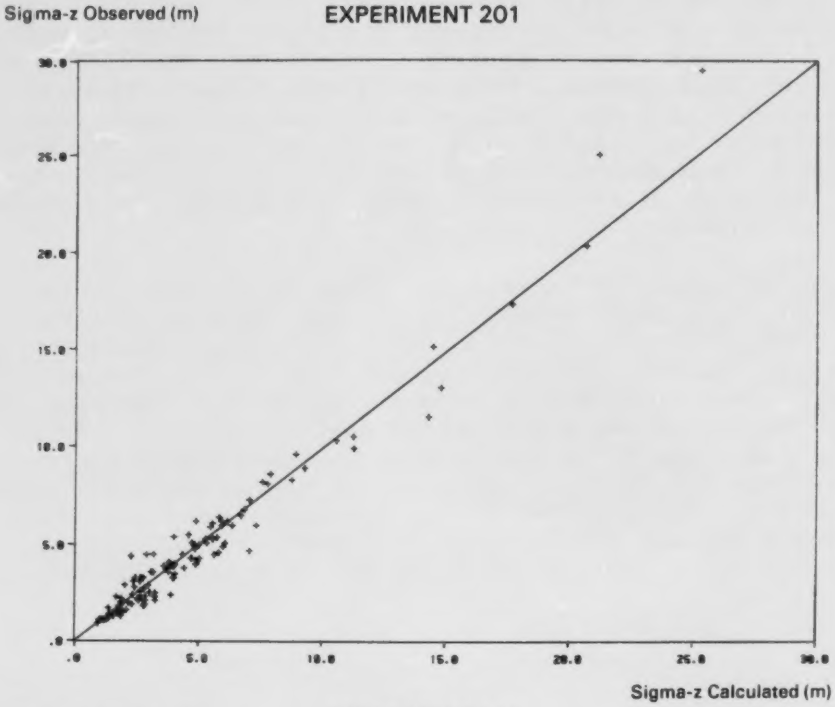

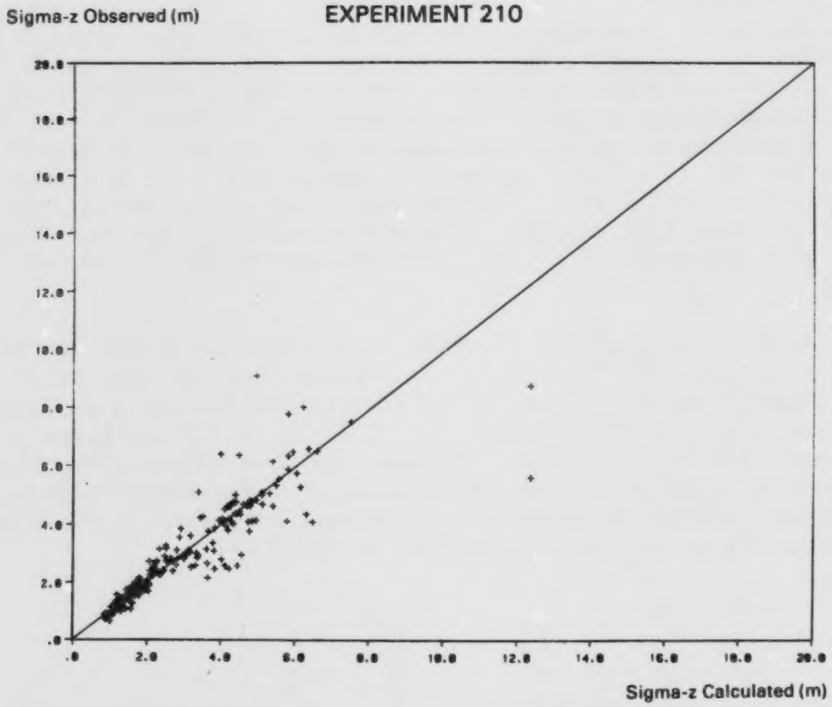

Figure 32. Comparison of photo-derived σ_z data and calculated σ_z utilizing best-fit i_z data in Equation 41 with $\gamma = 0.525$ and $\sigma_{zo} = 0.5$.

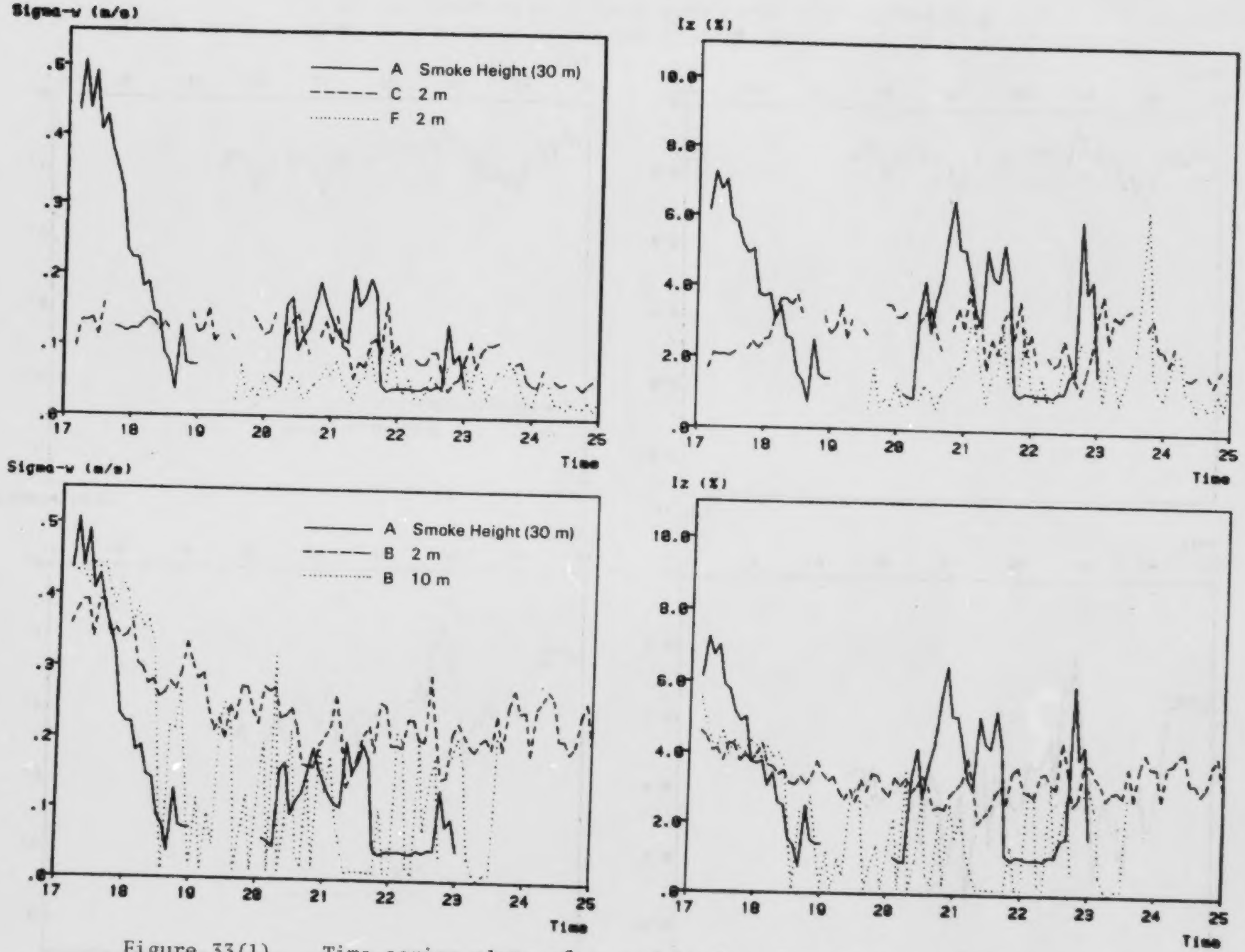

Figure 33(1). Time-series plots of σ_w and i_z data from Towers B, C, D, E, and F on CCB compared with data from Tower A for Experiment 201.

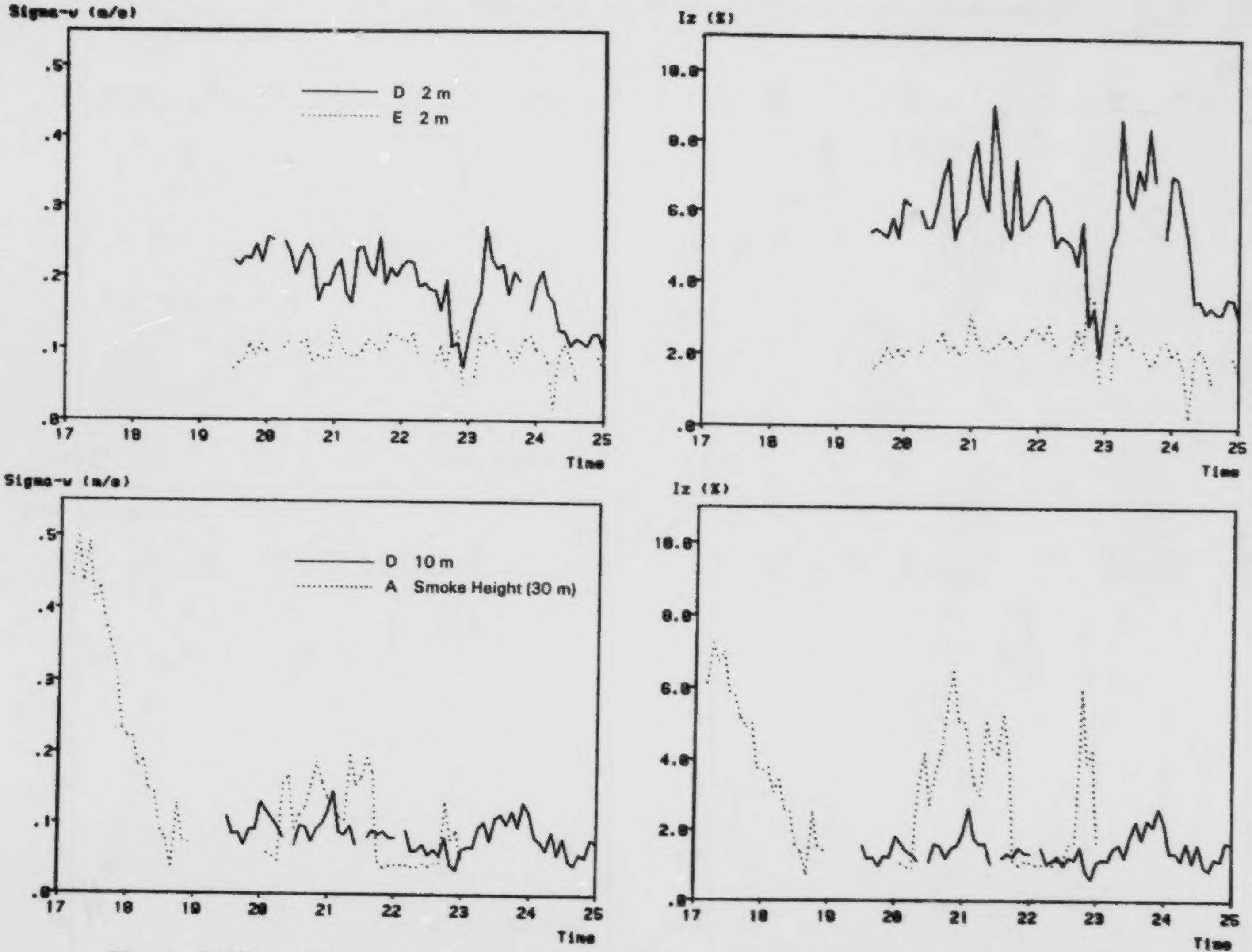

Figure 33(2). Time-series plots of σ_w and i_z data from Towers B, C, D, E, and F on CCB compared with data from Tower A for Experiment 201.

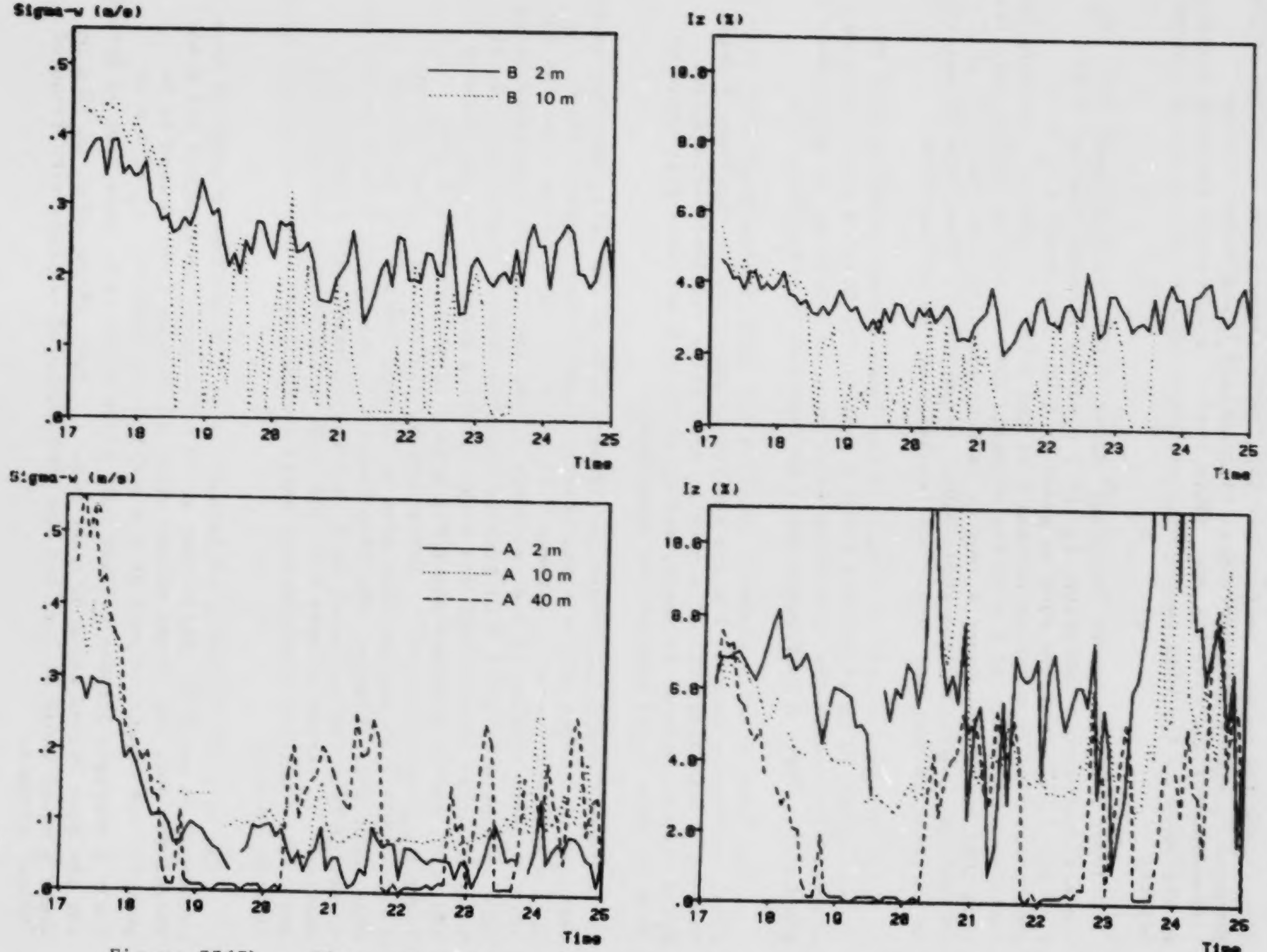

Figure 33(3). Time-series plots of σ_w and i_z data from Towers B, C, D, E, and F on CCB compared with data from Tower A for Experiment 201.

are $\overline{u'w'} = 0$, and $\overline{u'w'} = \sigma_u\sigma_w$. Because we expect $\overline{u'w'}$ to be non-zero, we have chosen the latter limit. This implicitly assumes that a portion of the measured σ_w arises from horizontal fluctuations being turned upslope (downslope) by the hill surface. Note that w is corrected for prop response on the basis of the wind tunnel data presented in the CTMD Second Milestone Report.

Tower F is the truest "windward" tower on CCB for Experiment 201. The vertical turbulence intensity, i_z, at 2 m varies between 0.01 and 0.03 (1.0 and 3.0%), with one peak as great at 0.06. The Tower A i_z data interpolated to 30 m varies between 0.01 and 0.06. In general, however, the turbulence intensity at 2 m on the windward face of CCB is considerably less than that at 30 m on Tower A, and it is substantially less than that at 2 m on Tower A, which averages about 0.06. Consequently, these data do not show an increase in vertical turbulence intensity on the upwind slope.

Of further interest is a peak in the Tower F data record at 2100 MST. This is about 10 to 15 minutes after a peak in the Tower A data. This is further evidence of the turbulence shift seen in comparing the plume photographs with Tower A turbulence data, as reported in subsection 3.3.2.

The Tower E (at a windward location for much of Experiment 201) vertical turbulence data at 2 m are similar in magnitude to the Tower F data. However, these data exhibit a greater mean value and less variability. Still, the turbulence intensity and σ_w at Tower E are less than those at 30 m on Tower A for most of the experiment.

Towers C and D lie toward the leeward side of the hill, and they record vertical turbulence levels significantly greater than Towers E and F. i_z at 2 m on Tower C remains between 0.02 and 0.04. Much of the time the pattern is quite similar to that at Tower F, and the Tower C turbulence intensity is generally about 0.01 greater than the Tower F turbulence. i_z at Tower D varies between 0.02 and 0.09, spending much of the time between 0.06 and 0.08, and σ_w averages about 0.2 m/sec, which exceeds all 30-m Tower A σ_w data after 1830. Consequently, the vertical turbulence at 2 m on Tower D is greater than that at 30 m on Tower A for nearly all of Experiment 201. However, the 10-m Tower D i_z values are about a factor of 4 smaller than the 2-m level data, and the σ_w values are a factor of 2 smaller. i_z varies between 0.01 and 0.02, and σ_w varies between 0.05 and 0.12, remaining approximately equal to the lower levels of turbulence at 30 m on Tower A.

The vertical intensity of turbulence at 2 m on Tower B tends to vary between 0.03 and 0.04, while that at 10 m "bounces" between 0.0 and 0.03. Therefore, only the larger values of i_z at 30 m on Tower A tend to be greater than the turbulence at 2 m and 10 m on Tower B. σ_w at 2 m on Tower B averages between 0.2 and 0.25 m/sec after 1830, equalling or exceeding the peak values below 40 m on Tower A. Peak values of σ_w at 10 m on Tower B equal those at 2 m, but the turbulence is unsteady with frequent "quiet" periods.

In conclusion, the vertical turbulence data over CCB during Experiment 201 indicate little, if any, increases in plume diffusion along the upwind face of CCB. Increased mixing could occur near the surface of the crest of CCB, especially during those periods when the vertical mixing away from the hill was relatively weak, and increased mixing would certainly occur in the lee close to the surface.

Experiment 210

The oil-fog plume was released on the southeast side of CCB for the duration of Experiment 210. Therefore, Tower D is primarily a windward tower; Tower F is a leeward tower; and Towers C and E are along the side of the hill. Vertical turbulence data from these towers and from Tower B atop the south peak of CCB are compared with data from Tower A, estimated for the plume release height, in Figure 34.

The vertical turbulence intensity (i_z) from the 2-m height on Tower D is generally slightly greater than that at the release height on Tower A, although there are periods when the fluctuations are out of phase. The intensity at D is approximately 2% (±1%) after 0200. Data from 10 m on Tower D are similar.

In the wake (Tower F), there is a greater difference between the 2-m and 10-m data, and also between these data and the turbulence intensity interpolated to release height with Tower A data. Vertical turbulence intensity at 2 m is 2 to 3 times that at 10 m after 0200, and both are several times the turbulence intensity at Tower A after 0200. During the first hour, however, the Tower A turbulence exceeds that at Tower F.

Over the top of the south peak of CCB, the turbulence at 2 m exceeds that at Tower A nearly all the time, and the turbulence at 10 m, although less that that at 2 m, also frequently exceeds that at Tower A during the shortened 3-hour record. This suggests that the estimates of turbulence intensity from Tower D may be underestimated by setting $\overline{u' w'} = \sigma_u \sigma_w$. Consequently, the turbulence data from Experiment 210 indicate that turbulence levels may increase over much of the hill, causing increased plume diffusion.

3.3.6 Implications for Modeling

The preceding analyses show that some degree of modeling error could arise in simulating Experiments 201 and 210 due to using inappropriate meteorological data as model input. To test the significance of this possibility, CTDM(11083), CTDM(11083)-5, CTDM(11083-E), and CTDM(11083-E)-5 have been run on a new version of the data for the SF_6 release height (at or near the oil-fog smoke release height).

The following changes have been made to the MDA in preparing a modified MDA for Experiment 201:

- 1705-1800 - All data are unchanged from the MDA.

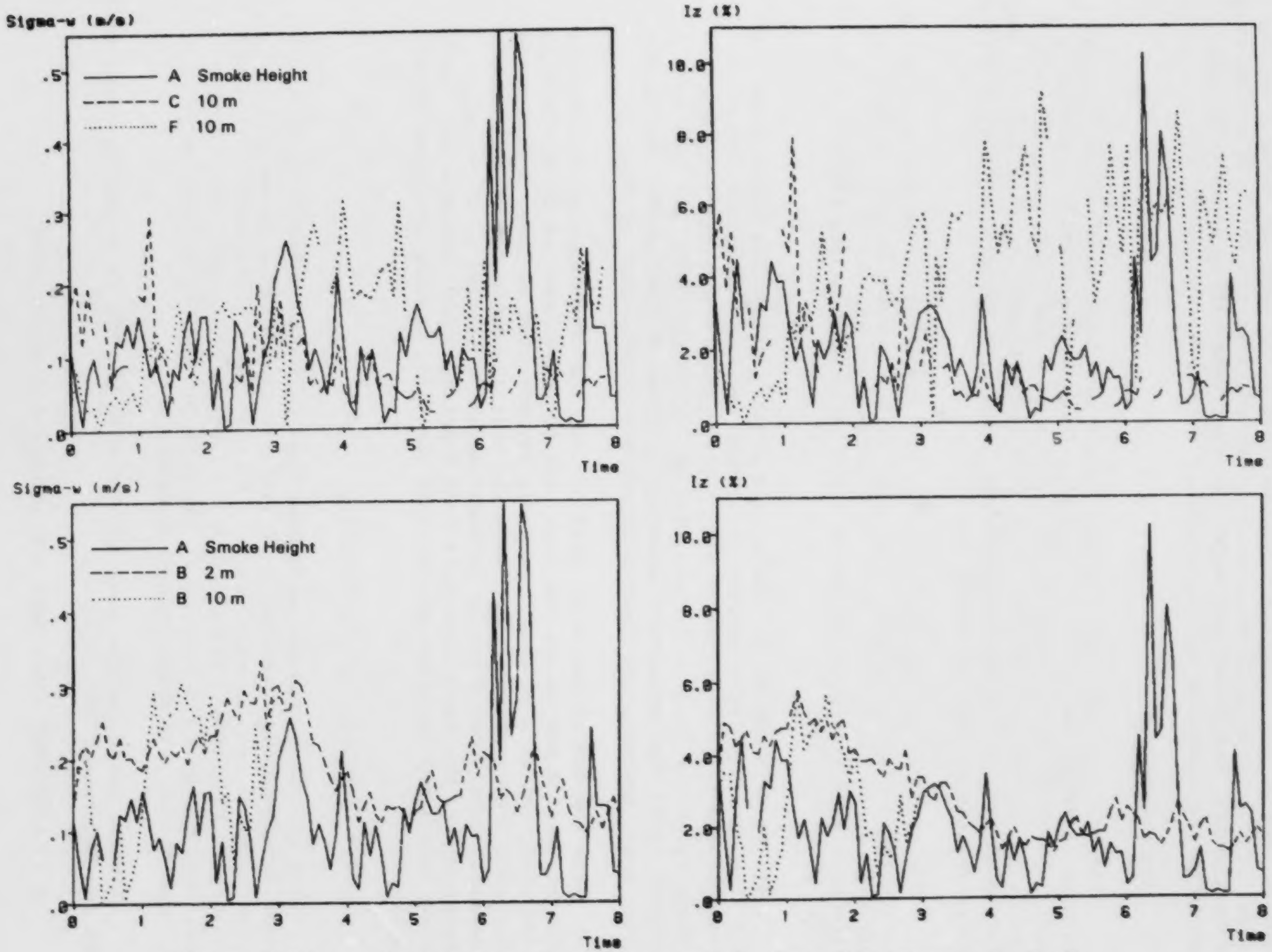

Figure 34(1). Time-series plots of σ_W and i_z data from Towers B, C, D, E, and F on CCB compared with data from Tower A interpolated to release height for Experiment 210.

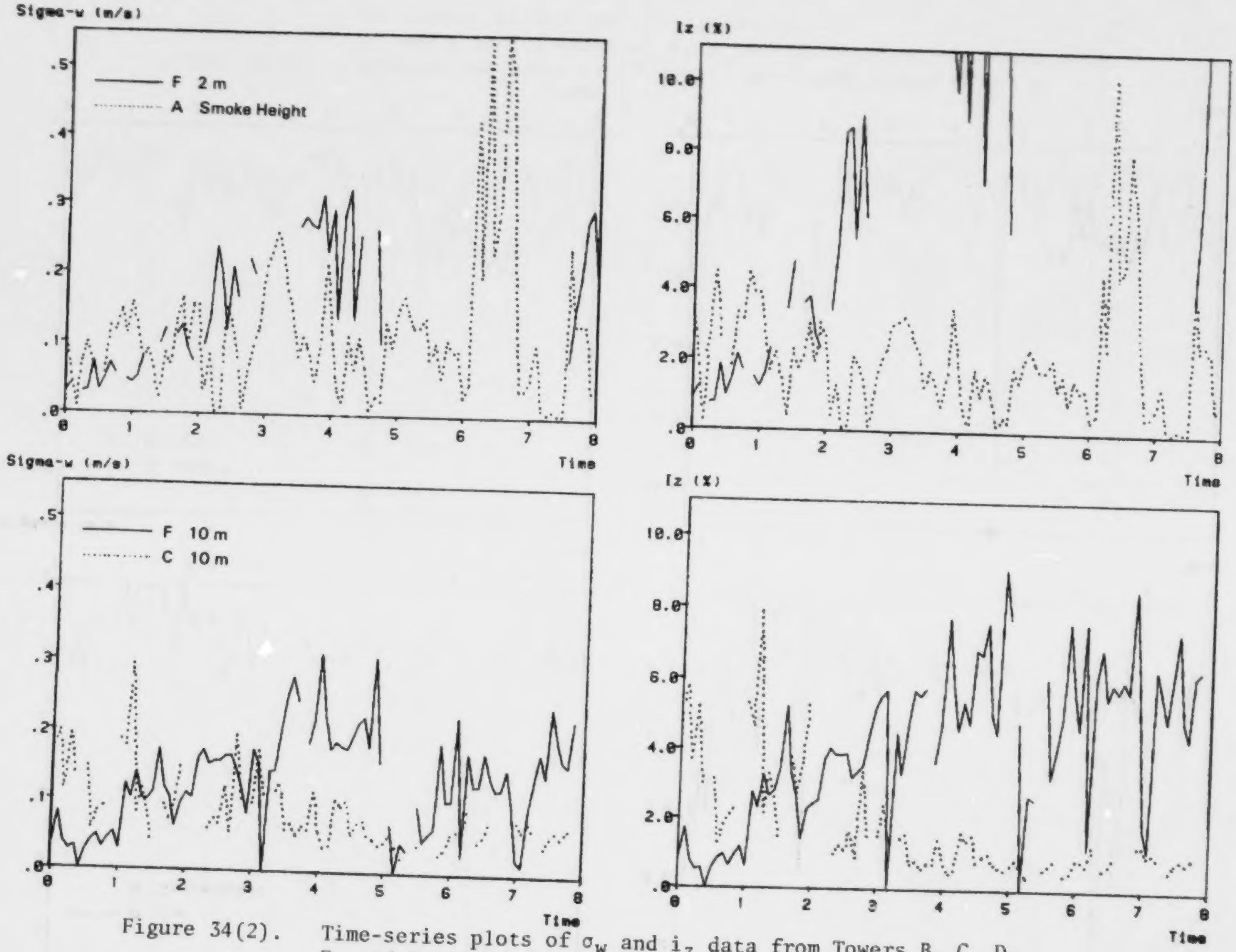

Figure 34(2). Time-series plots of σ_w and i_z data from Towers B, C, D, E, and F on CCB compared with data from Tower A interpolated to release height for Experiment 210.

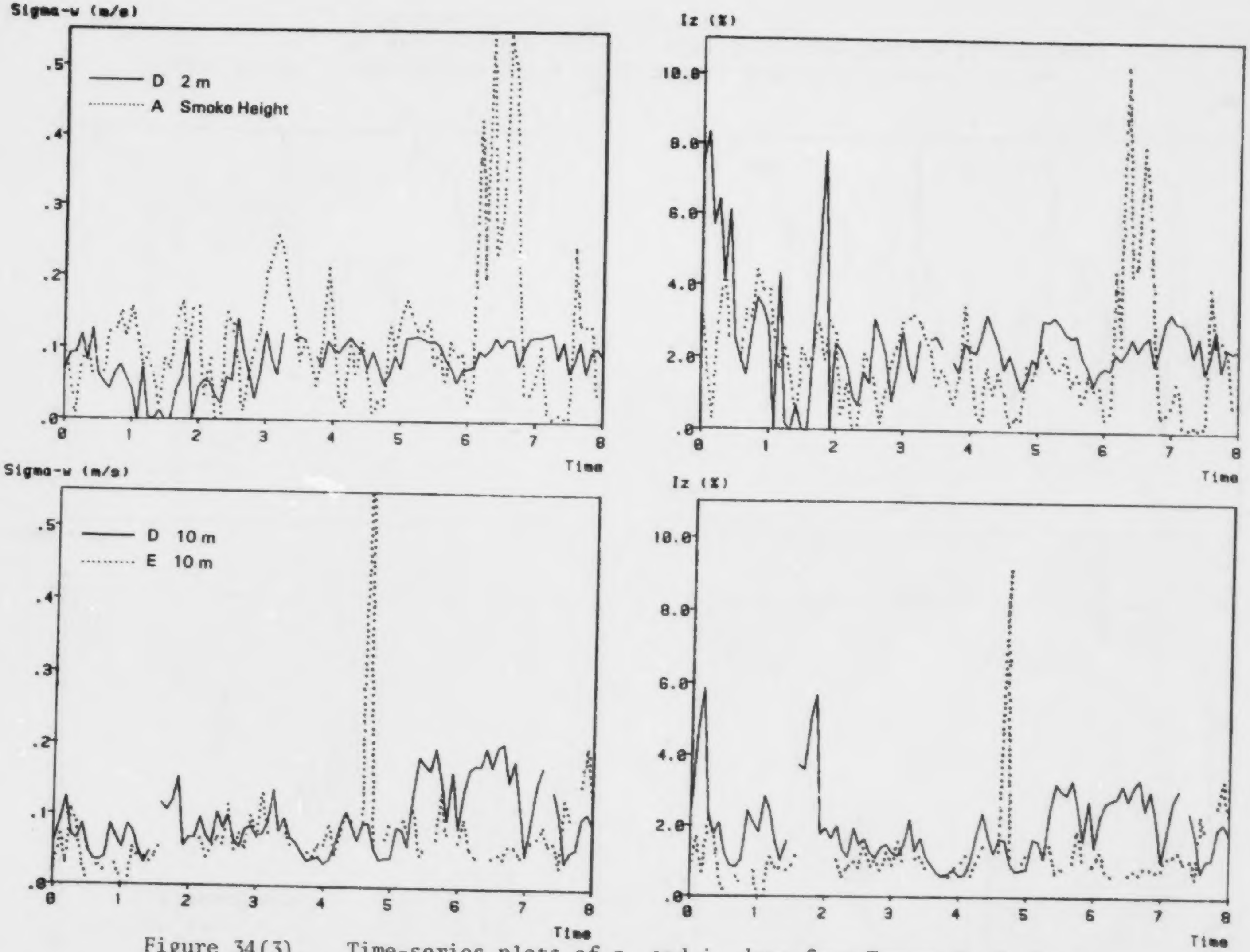

Figure 34(3). Time-series plots of σ_w and i_z data from Towers B, C, D, E, and F on CCB compared with data from Tower A interpolated to release height for Experiment 210.

- 1805-1900 - Best-fit i_z data are substituted when available, and a lower bound of 0.020 (2.0%) is placed on the MDA values, reflecting the lack of any best-fit i_z data near or below 0.020.

- 2005-2020 - Photo wind directions are substituted when available, and i_z is set equal to 0.035 as a representative lower bound.

- 2025-2030 - Photo wind directions and best-fit i_z values are substituted, and all other meteorology is persisted from 2020.

- 2035-2200 - Photo wind directions and best-fit i_z values are substituted when available, and all other meteorology is shifted by 10 minutes (e.g. 2025 data are used at 2035). i_z is restricted to be no smaller than 0.020.

- 2205-2300 - Best-fit i_z values are substituted when available, and all other meteorology is unchanged except that i_z is restricted to be no smaller than 0.020.

Note that whenever the best-fit i_z exceeds 0.080, its value is reduced by 25%. This is done because the photo-derived σ_z values at these times are thought to be overestimates, either due to horizontal meander or the approximations required to apply Gifford's technique to these data.

The following changes have been made to the MDA in preparing a modified MDA for Experiment 210:

- 0000-0020 - All data are unchanged from the MDA.

- 0025-0100 - Photo wind directions are substituted.

- 0105-0300 - Photo wind directions and best-fit i_z data are substituted when available; the missing wind direction data are filled-in with data from 10 m on Tower B, and i_z from the MDA are restricted to be no smaller than 0.015, as reflected in the lowest best-fit estimated for data from Experiment 210.

- 0305-0800 - Same as for the period 0105-0300 except that the average of the archive wind direction and the 30-m Tower B wind direction are used to fill gaps in the photo wind directions.

Experiment 201, Hour 18

The peak observed concentration is 458 ppt, and this occurred on the windward face of the hill at release height (30 m). The wind speed varied from between 6.0 and 7.4 m/sec during the hour, and the dividing-streamline height was no greater than 2 m (essentially zero).

Because the meteorology is not altered for this hour, the modeled estimates are unchanged. CTDM(11083) estimates a peak concentration of 178 ppt, and CTDM(11083-E) estimates 169 ppt. Both estimates place the peak value at the location of the observed peak concentration. The 5-minute version of CTDM(11083-E) estimates a peak concentration of 173 ppt, located high on the windward face.

The observed concentration is underestimated because the plume size is "too large," causing too great a dilution. A second calculation made on the basis of films taken from the peak of CCB and aerial photographs fares somewhat better. The size of the instantaneous core of the plume is estimated from the aerial photos; i_y is estimated by assuming a top-hat distribution; the plume core is assumed to be circular; both σ_y and σ_z are assumed to grow linearly with distance; the center of the plume is allowed to touch the surface; and the frequency of this impact at a receptor near the camera location on the north peak is estimated from the film. The resulting estimate lies between 380 ppt and 440 ppt, while the observed concentration is 465 ppt. This exercise indicates that even the best representative meteorological data measured at Tower A can lead to substantial errors in estimated concentrations.

Experiment 201, Hour 19

The peak observed concentration is 401 ppt, located near the windward peak of CCB. Peak modeled concentrations are:

- 34 ppt - CTDM(11083) with MDA, located just leeward of the crest
- 94 ppt - CTDM(11083) with modified MDA, located near the windward peak
- 94 ppt - CTDM(11083)-5 with modified MDA, located near the windward peak
- 482 ppt - CTDM(11083-E) with MDA, located on the windward face near the release elevation
- 605 ppt - CTDM(11083-E) with modified MDA, located on the windward face near the release elevation
- 389 ppt - CTDM(11083-E)-5 with modified MDA, located on the windward face near the release elevation.

Using the best-fit i_z data, which are generally greater than the MDA values, leads to greater concentrations. In the case of CTDM(11083), this improves both the location and magnitude of the peak value. For CTDM(11083-E), however, this change causes increased overestimation. When 5-minute averages of the meteorological data are used, CTDM(11083-E)-5 performs much better in estimating the peak concentration magnitude, although the placement is too low on the windward face. Note that the second highest observed concentration (363 ppt) is also located near the release elevation on the windward face of the hill, so the model estimate of the location of peak concentration is not as bad as it might first appear.

Experiment 201, Hour 21

The peak observed concentration is 246 ppt, located slightly above the release elevation. Peak modeled concentrations are:

- 900 ppt - CTDM(11083) with MDA
- 723 ppt - CTDM(11083) with modified MDA
- 689 ppt - CTDM(11083)-5 with modified MDA
- 797 ppt - CTDM(11083-E) with MDA
- 569 ppt - CTDM(11083-E) with modified MDA
- 851 ppt - CTDM(11083-E)-5 with modified MDA.

All of these estimates are located midway up the windward face of the hill. From the distribution of observed concentrations and the oil-fog plume photographs, it appears that the plume preferentially curved around one side of the hill. The band of greatest observed concentrations lies along approximately the same elevation as the peak modeled concentration. The hourly mean H_c is 23 m, or 7 m less than the release height. This suggests that the plume is undergoing a greater horizontal deflection than what is allowed by the Lift module.

The modifications made to the MDA produce a significant improvement in the model estimates, especially in CTDM(11083-E). Perhaps an altered version of the model which shifts more of the plume to the side of the hill will reduce the size of the peak modeled concentration as well as improve its location.

Experiment 201, Hour 22

The peak observed concentration is 437 ppt, located slightly above the release elevation (the same receptor as last hour). Peak modeled concentrations are:

- 1595 ppt - CTDM(11083) with MDA
- 1064 ppt - CTDM(11083) with modified MDA
- 1144 ppt - CTDM(11083)-5 with modified MDA
- 1081 ppt - CTDM(11083-E) with MDA
- 605 ppt - CTDM(11083-E) with modified MDA
- 963 ppt - CTDM(11083-E)-5 with modified MDA.

All of the modeled peak concentrations are located near the top of the windward face. The distribution of concentrations and the meteorology are quite similar to that from the preceding hour. The dividing-streamline height is now computed to be 26 m, or only 4 m below the release height.

The modified MDA again produces a substantial improvement in the peak estimated concentrations. As with hour 21 however, more horizontal deflection seems to be needed. Also, the shift in H_c closer to the release elevation has increased both the observed and the modeled concentrations. This sensitivity to H_c implies that the resolution in calculating and incorporating H_c could account for much of the remaining discrepancy in the peak concentrations.

Experiment 201, Hour 23

The peak observed concentration is 304 ppt, located at the windward base of the hill. Peak modeled concentrations are:

- 923 ppt - CTDM(11083) with MDA
- 695 ppt - CTDM(11083) with modified MDA
- 430 ppt - CTDM(11083)-5 with modified MDA, located 10 m above the observed peak
- 405 ppt - CTDM(11083-E) with MDA
- 315 ppt - CTDM(11083-E) with modified MDA
- 433 ppt - CTDM(11083-E)-5 with modified MDA.

All of these estimates, except that for CTDM (11083)-5, occur on the same face of the hill as the peak observed concentration, but at an elevation of approximately half the hill height. The mean dividing-streamline height is now 1 m above the release height, but the range in H_c over the hour extends from 24 m to 40 m. Even with such a range in an important modeling parameter, the inability of the model to produce the peak observed concentration well below H_c is probably real. It may be that the Wrap module needs to be re-evaluated, or that additional dynamics (e.g., some type of upwind vortex flow) need to be introduced to bring more material to the surface at the base of the hill.

Experiment 210, Hour 1

The peak observed concentration is 28 ppt, and few others are appreciably greater than zero. The peak occurs at the upwind base of the hill, but the second highest concentration (26 ppt) is found low, off on the side of the hill ("side" of the hill as opposed to either the leeward or windward faces of the hill). The peak modeled concentrations are:

- 163 ppt - CTDM(11083) with MDA
- 175 ppt - CTDM(11083) with modified MDA
- 145 ppt - CTDM(11083)-5 with modified MDA
- 56 ppt - CTDM(11083-E) with MDA
- 59 ppt - CTDM(11083-E) with modified MDA
- 59 ppt - CTDM(11083-E)-5 with modified MDA.

All of these occur on the side of the hill above H_c, which exceeds the 30-m release height by 12 m. It appears that the Wrap module does not project enough material along the stagnation streamline, and that the Lift module allows too much of the material away from the stagnation streamline trajectory to impact the hill. Changes to the MDA only modify the wind directions, and these appear to have a small impact on the modeled concentrations.

Experiment 210, Hour 2

The peak observed concentration is 395 ppt, located well below the release height on the south side of the hill. With a release height of 57 m and an H_c of 35 m, σ_z must be large and the frequency of winds along the stagnation streamline must be high for the Wrap Module to produce so large a concentration. Peak modeled concentrations are:

- 45 ppt - CTDM(11083) with MDA, located at the center of the hill
- 226 ppt - CTDM(11083) with modified MDA, located high on the lee side
- 146 ppt - CTDM(11083)-5 with modified MDA, located near 35 m on the windward face
- 162 ppt - CTDM(11083-E) with MDA, located high on the windward face
- 386 ppt - CTDM(11083-E) with modified MDA, located on the south peak
- 311 ppt - CTDM(11083-E)-5 with modified MDA, located near the release height on the windward face.

The new wind directions and vertical turbulence data make a substantial difference in model performance. Although the location of the peak concentration is not close to the location of the peak observed, CTDM(11083-E) comes close to the observed magnitude. With 5-minute input data, CTDM(11083-E)-5 underestimates the peak value by a larger margin, but the location is improved considerably.

Experiment 210, Hour 3

The peak observed concentration is 297 ppt, located at the base of the hill in the lee. The peak modeled concentrations are:

- 0 ppt - CTDM(11083) with MDA
- 2 ppt - CTDM(11083) with modified MDA
- 42 ppt - CTDM(11083)-5 with modified MDA, located low on the lee side
- 16 ppt - CTDM(11083-E) with MDA, located midway up on the side of CCB
- 148 ppt - CTDM(11083-E) with modified MDA, located high on the lee side
- 166 ppt - CTDM(11083-E)-5 with modified MDA, located at the crest.

Once again, the modifications to the input data are extremely important in modeling this hour, but equally important is the "enhancement" in CTDM(11083-E). Together, the observed concentration on the crest of the hill is virtually matched, and the concentrations high on the lee side are approached. What seems to be missing in CTDM(11083-E) is the observed streamline depression in the lee caused by lee waves.

Experiment 210, Hour 4

The peak observed concentration is 132 ppt, located high on the lee side of the hill. Peak modeled concentrations are:

- 1 ppt - CTDM(11083) with MDA
- 0 ppt - CTDM(11083) with modified MDA
- 3 ppt - CTDM(11083)-5 with modified MDA

- 74 ppt - CTDM(11083-E) with MDA, located high on the lee side of CCB
- 21 ppt - CTDM(11083-E) with modified MDA, located high on the lee side of CCB
- 37 ppt - CTDM(11083-E)-5 with modified MDA, located high on the windward face.

It is not at all clear from these results that the modified input data are any more representative. CTDM(11083-E) seems to work better with the MDA. However, a modified enhancement algorithm that would push the peak enhancement leeward of the crest might improve the results of CTDM(11083-E)-5. Because photo-derived wind directions are available for less than half of the hour, and because no photo-derived i_z data are available, the modifications made to the MDA are largely persistence-guided guesses.

Experiment 210, Hour 6

The peak observed concentration is 134 ppt, located midway-up on the lee side of the hill. Two samplers on this part of the hill actually recorded 134 ppt, but the next highest concentration is 67 ppt located on the south peak. Peak modeled concentrations are:

- 0 ppt - CTDM(11083) with MDA, and CTDM(11083), CTDM(11083)-5 with modified MDA
- 10 ppt - CTDM(11083-E) with MDA, located half-way up on the lee side
- 7 ppt - CTDM(11083-E) with modified MDA, located at the same receptor
- 15 ppt - CTDM(11083-E)-5 with modified MDA, located at the same receptor.

Little can be said about why the modeling is so inaccurate at this time. More study is needed to understand the evolution of the observed concentrations.

Experiment 210, Hour 7

The peak observed concentration is 212 ppt, located just leeward of the south peak. Peak modeled concentrations are:

- 69 ppt - CTDM(11083) with MDA, located at the center of CCB
- 18 ppt - CTDM(11083) with modified MDA, located at the center of CCB
- 45 ppt - CTDM(11083)-5 with modified MDA, located just leeward of the crest
- 166 ppt - CTDM(11083-E) with MDA, located high on the windward face
- 151 ppt - CTDM(11083-E) with modified MDA, located high on the windward face
- 195 ppt - CTDM(11083-E)-5 with modified MDA, located high on the windward face.

The revised input data have a relatively minor impact on the modeled concentrations compared to the enhancement of CTDM(11083-E). It appears from the distribution of concentrations that CTDM(11083-E) could do better with a modified enhancement factor algorithm that would shift the primary impact area to the lee side.

Experiment 210, Hour 8

The peak observed concentration is 384 ppt, located near the base of the hill in the lee. The peak modeled concentrations are:

- 12 ppt - CTDM(11083) with MDA, located near the observed peak
- 5 ppt - CTDM(11083) with modified MDA, located near the observed peak
- 98 ppt - CTDM(11083)-5 with modified MDA, located near the observed peak
- 114 ppt - CTDM(11083-E) with MDA, located low on the side of the hill
- 112 ppt - CTDM(11083-E) with modified MDA, located near the observed peak
- 232 ppt - CTDM(11083-E)-5 with modified MDA, located low on the side of the hill.

The modified input data have the greatest impact on the performance of CTDM(11083-E)-5. The peak is now within a factor of 2 of the peak observed concentration, but the location is shifting away from the observed location in the lee. It is difficult to judge what types of model modifications might improve these results because no photo-derived estimates of i_z or wind direction are available. Modifications made to the MDA consist of averaging the MDA wind directions with those from the 30-m level of Tower B. This is based on the correspondence of these data with photo-derived wind directions during previous hours.

Summary

Some mechanism for increasing concentrations estimated by Lift over the hill appears to be necessary. The σ_z enhancement algorithm in CTDM(11083-E) apparently improves the model performance, but a more carefully structured algorithm is needed to better resolve when and where an "enhancement" should occur. For the present, CTDM(11083-E) can be used to evaluate the impact of modifying the input data for Experiments 201 and 210.

The ratio of the peak observed concentration to the peak modeled concentration (CTDM(11083-E)) is plotted in Figure 35 to compare the two sets of input data. The results of using the actual 5-minute sequence of data (CTDM(11083-E)-5) are also included to evaluate the importance of simulating the coupled variability in wind speed, H_c, and turbulence intensity. Out of this set of 12 experiment-hours, 2 hours show no significant change (one of these had no modifications to the MDA), and 1 hour shows a worse model performance when the best of either the 1-hour or the 5-minute version of CTDM(11083-E) with the modified MDA data is compared to the 1-hour version of CTDM(11083-E) with the MDA. Therefore, the overall model performance statistics will probably improve when the detailed evaluation of the meteorological information from all available sources is complete.

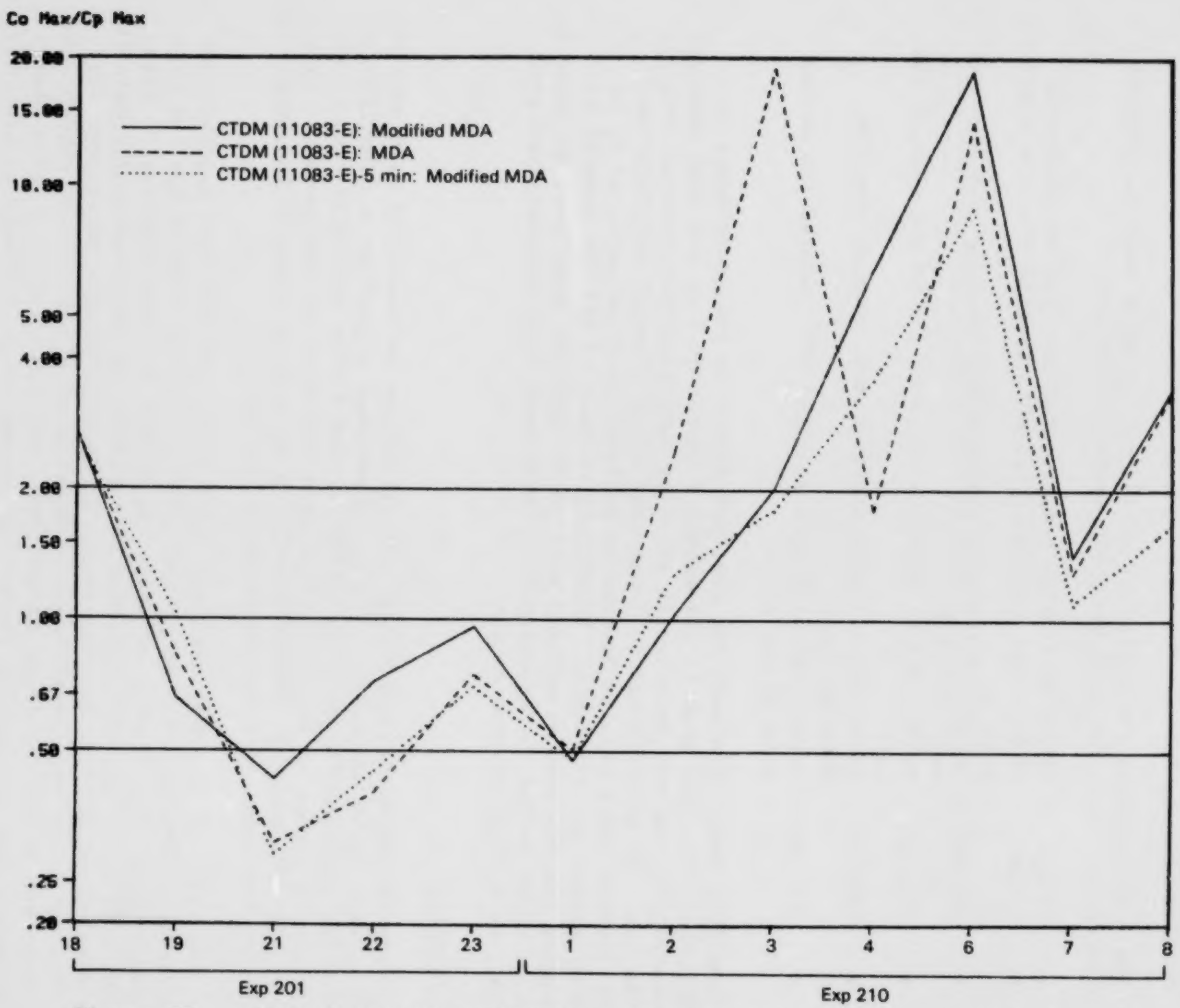

Figure 35. CTDM (11083-E) performance, as measured by peak concentrations unpaired in space, using the Modelers' Data Archive and the modified Modelers' Data Archive for Experiments 201 and 210.

Model performance is not consistently improved by simulating each 5-minute period instead of simulating hourly concentrations with hourly-averaged meteorological data. At times, the 5-minute simulation improves the distribution of concentrations even though the peak estimate is degraded This behavior may reflect an inadequacy in the model formulation, and a subsequent improvement in the model could lead to even better model performance.

Comparing modeled and observed concentrations with the two sets of input data has indicated areas in which CTDM should be changed to better reflect the observed plume behaviour. Chief among these is the use of a terrain-driven mechanism similar to that contained in CTDM(11083-E). Other areas for model improvement are summarized in Table 3. Because most of the hours studied in Experiments 201 and 210 are primarily "Lift" hours, we have focused our attention on Lift-related improvements. These are described in the next subsection.

3.4 CTDM Upgrades: CTDM(14083)

The case-study results for Experiments 201 and 210 reported above indicate that:

- Equation 41 should be used to estimate σ_z, with $\gamma \sim 0.5$, and $\sigma_{zo} \sim 0.5$ m.
- Turbulence may increase within 10 m of the hill surface.
- The transition from Wrap to Lift at H_c is too "severe," especially when the mean wind direction is not directed near the stagnation streamline.
- The effects of terrain on the path, distortion, and diffusion of the plume over the hill must be explicitly formulated within Lift.

CTDM(11083) already incorporates the first finding, but CTDM must be reformulated to incorporate the remaining three. At this stage, we will treat the increase in near-surface turbulence as an implicit factor in the plume distortion and diffusion formulation.

This section contains a description of the new formulations for the Lift module, an evaluation of the model performance characteristics for Experiments 201 and 210, and an overall evaluation of the relative model performance when CTDM(14083) is applied to the MDA.

3.4.1 Lift/Wrap Transition Upgrade

CTDM(11083) treats all flow beneath H_c as two-dimensional, horizontal flow and all flow above H_c as "neutral" flow. Because the Lift module deforms the horizontal distribution of plume material above H_c as if the flow were part of axial flow over a sphere, material just above H_c travels up and over the hill while that just below is advected round the side. This produces a zone of zero concentrations between these two plume segments.

TABLE 3. SUMMARY OF AREAS FOR IMPROVING CTDM (11083) BASED ON ANALYSES OF EXPERIMENTS 201 and 210*

Experiment-Hour	Area for Model Improvement
201-18	Non-Gaussian formulation
201-19	Unclear
201-21	More horizontal deflection in Lift near H_c
201-22	More horizontal deflection in Lift near H_c
201-23	Wrap assumptions near base of hill
210-1	More horizontal deflection in Lift, less in Wrap near H_c
210-2	More horizontal deflection in Lift, less in Wrap near H_c
210-3	Better terrain effect adjustment in Lift with lee wave and wake sensitivity
210-4	Better terrain effect adjustment in Lift with lee wave and wake sensitivity
210-6	Unclear
210-7	Better terrain effect adjustment in Lift with lee wave and wake sensitivity
210-8	Unclear

---

*The need for a terrain effect in Lift similar to that in CTDM(11083-E) is seen in all hours.

Figure 36 is a schematic illustration of how this abrupt transition between the Lift and Wrap modules differs from what one would expect on the basis of tow-tank studies (e.g., Snyder and Hunt 1983). When the bulk of the plume material is near or below H_c, we would expect a significant horizontal deflection of much of the material above H_c. This deflection would be greatest for plume segments to the side of the stagnation streamline. Material close to the stagnation streamline, but above H_c, would experience relatively little horizontal deflection. The structure of CTDM(11083) allows little horizontal deflection for all plume material above H_c because the effective radius of curvature controls the deformation. Stratification is not accounted for.

This departure of the modeled plume distribution from that which is expected not only produces a qualitatively incorrect distribution of surface concentrations, it also can lead to quantitative overestimates of the peak concentration. Below H_c, the plume is physically deflected to the side of the hill so that concentrations on the hill are solely determined by the probability that plume material lies along the stagnation streamline. If the plume spends little time near the stagnation streamline, the concentrations on the surface are considerably less than those under the "center" of the plume. Above H_c, CTDM(11083) shifts the plume very little in the horizontal so that the "center" of the plume rides over some portion of the hill. For plumes close to H_c in height but away from the stagnation streamline, the "center" of the plume would be expected to deflect mostly around the side of the hill instead, like material below H_c. Hence, CTDM(11083) would overestimate peak expected concentrations.

The effective radius of curvature can be altered in the Lift module to increase the horizontal displacement of streamlines with increasing stratification. Recall that an offset D was defined to be the difference between the effective radius of curvature, and the height of the hill above H_c. If D is nearly zero, the horizontal shift of plume material away from the stagnation streamline would approach that of the Wrap module, but material close to the stagnation streamline would still rise along the surface over the hilltop. The parameter D therefore provides a convenient mechanism within Lift to smooth the transition between the two module components when the release height is close to H_c.

Figure 37 illustrates the geometry. The example shown in the figure illustrates how the method shifts the plume material farther from the hill center as D' becomes much less than D. Vertical profiles of plume material are weighted by the fraction of time that the wind blows along the effective direction to the receptor, rather than the actual direction to the receptor from the source. Therefore the PDF for small angles from the stagnation wind direction controls the magnitude of concentrations over most of the hill.

This geometric method for shifting plume material is just a convenient mechanism to obtain the desired results. The central assumption for actually controlling the degree of redistribution is the parameter D'. Because we wish to retain the basic structure of CTDM for the time being, D' has been designed to respond to the release height of the plume relative to H_c. If the plume is released below H_c, then we set D' equal to some

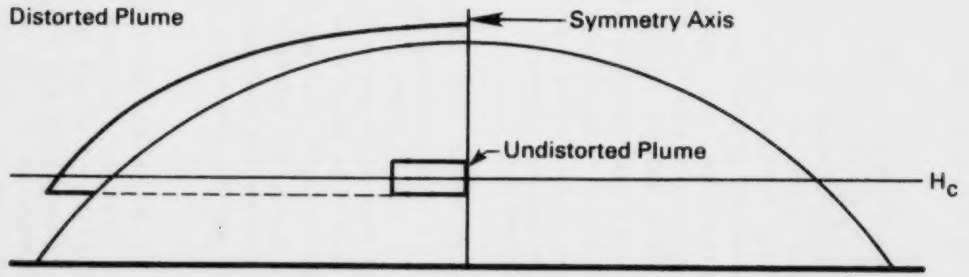
Distorted Plume
Symmetry Axis
Undistorted Plume
H_c

Expected Plume Structure

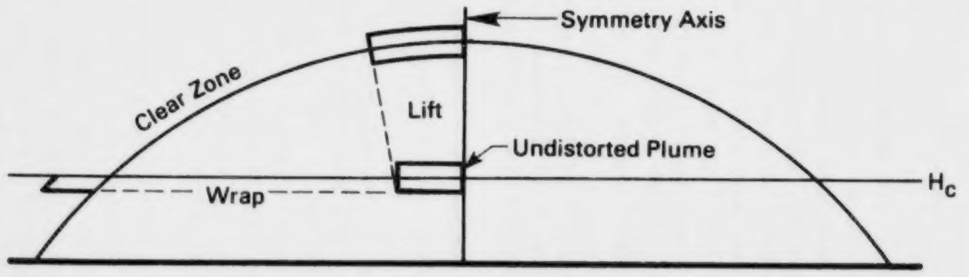
Symmetry Axis
Clear Zone
Lift
Undistorted Plume
Wrap
H_c

CTDM (11083) Plume Structure

Figure 36. Illustration of the plume deformation expected over an isolated "3-D" hill and the deformation produced by CTDM (11083).

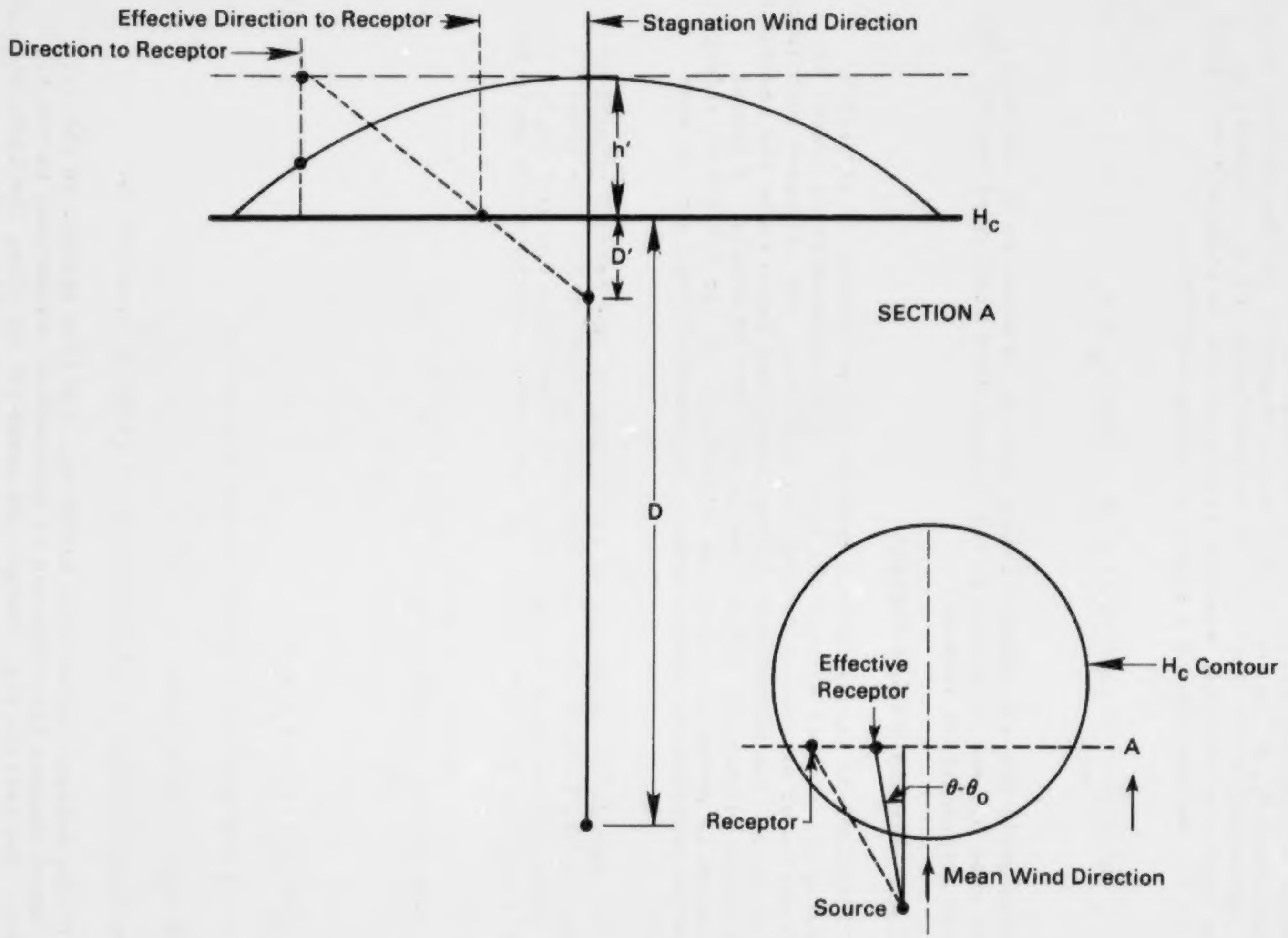
Effective Direction to Receptor
Direction to Receptor
Stagnation Wind Direction
h′
D′
D
H_C
SECTION A
Effective Receptor
H_C Contour
A
θ-θ_O
Receptor
Mean Wind Direction
Source

Figure 37. Illustration of the geometry used to calculate the horizontal distribution of plume material above H_C.

]

minimum value so that all plume material above H_c at the impingement circle is distributed over the hill surface by streamlines close to the stagnation streamline, regardless of how large σ_z is. If the plume is released above H_c, D' is set to some value between D and the minimum value of D', depending on the ratio of the release height to H_c. Because we have no theory or physical modeling results as yet to formulate an expression for D', we have chosen a simple weighting expression:

$$D' = D'_{min} + [1 - (H_c/z_r)^3]D \quad \text{for} \quad z_r > H_c \tag{44}$$

This expression has the desired limits when z_r is equal to H_c and much greater than H_c, and it shifts to the neutral flow limit more rapidly than a linear interpolation formula.

3.4.2 Terrain Effects Upgrade

CTDM(11083-E) incorporates a measure of the effects of terrain by increasing the size of σ_z over the hill. This enhancement is viewed as a combination of streamline distortion, diffusion, and increased turbulence over the hill. The enhancement factor itself was taken to be the inverse of the "terrain correction" factor used in the COMPLEX models. A better formulation is needed to relate the enhancement to the individual effects of streamtube contraction, speed changes, increased mixing, and lee wave effects.

The upgrade to the method of simulating various terrain effects is included in the Lift module. As discussed in Section 3.1, the plume is split where the dividing-streamline of the flow meets the hill (s_o). If the hill surface were flat beyond s_o, the surface concentration would be

$$C(s,\theta,0) = \int_{H_c}^{\infty} \frac{2Q(s_o,z)\,P(\theta)}{U_o\sqrt{2\pi}\,\sigma_z'\,s}\, e^{-0.5((z-H_c)/\sigma_z')^2}\,dz. \tag{45}$$

where

$$\sigma_z'^2 = \sigma_z^2(s) - \sigma_z^2(s_o) \quad . \tag{46}$$

$Q(s_o,z)$ is the vertical profile of mass flux at s_o:

$$Q(s_o,z) = C_o(s_o,z)U_o \quad . \tag{47}$$

The vertical profile of concentration is given by Equation 24.

If the terrain is not flat beyond s_o, the flow adjusts to the terrain, which changes the closeness of approach of streamlines to the hill surface. The terrain also changes the speed of the flow, the turbulence in the flow, and the trajectory of the plume over the hill surface. Assuming that the trajectory adjustments are already accounted for as in subsection 3.4.1, denote the net effect of plume height changes between s_o and s in

Equation 45 by $T_h(z-H_c)$. Denote the net effect of travel time, streamtube contraction, and turbulence changes by $T_\sigma \sigma_z{}'$, and denote the net effect of flow speed changes by $T_u U_o$. The diffusion of each elemental plume segment in the vertical profile at s_o is modeled as a point source released at a net height of $T_h(z-H_c)$, into a flow of speed $T_u u_o$, with a diffusion rate characterized by $T_\sigma \sigma_z{}'$ over the distance between s_o and s:

$$C(s,\theta,0) = 2\,\frac{P(\theta)}{s}\int_{H_c}^{\infty}\frac{C_o(s_o,z)u_o}{\sqrt{2\pi}\,T_\sigma \sigma_z{}'\,T_u U_o}\,e^{-\left(\frac{T_h(z-H_c)}{\sqrt{2}\,T_\sigma \sigma_z{}'}\right)^2}\,dz \tag{48}$$

Substituting for $C_o(s_o,z)$,

$$C(s,\theta,0) = \frac{2P(\theta)}{s}\,\frac{Q}{2\pi\sigma_{zo}U_o}\,\frac{1}{T_\sigma T_u \sigma_z{}'}\int_{H_c}^{\infty} e^{-\left(\frac{T_h(z-H_c)}{T_\sigma \sqrt{2}\sigma_z{}'}\right)^2}\left[e^{-\left(\frac{z_r-z}{\sqrt{2}\sigma_{zo}}\right)^2} + e^{-\left(\frac{z_r+z}{\sqrt{2}\sigma_{zo}}\right)^2}\right]dz \quad . \tag{49}$$

If the flow behaved as purely two-dimensional potential flow, then T_h and T_u would be inversely related: $T_u = 1/T_h$. Because the flow is unlikely to behave as purely two-dimensional potential flow, set

$$\begin{aligned} T_u &= \alpha/T_h \\ T &\equiv T_h/T_\sigma \end{aligned} \tag{50}$$

Then the solution to Equation 49 is

$$C(s,\theta,0) = \frac{P(\theta)}{s}\,\frac{QT}{\sqrt{2\pi}U_o\alpha\sigma_z{}''}\left[e^{-\left(\frac{T(z_r-H_c)}{\sqrt{2}\sigma_z{}''}\right)^2}\left(1+\text{erf}\,\frac{z_r-H_c}{\sqrt{2}\sigma_{zo}}\,\frac{\sigma_z{}'}{\sigma_z{}''}\right) + e^{-\left(\frac{T(z_r+H_c)}{\sqrt{2}\sigma_z{}''}\right)^2}\left(1-\text{erf}\,\frac{z_r+H_c}{\sqrt{2}\sigma_{zo}}\,\frac{\sigma_z{}'}{\sigma_z{}''}\right)\right] \tag{51}$$

where

$$\begin{aligned} \sigma_z{}'^2 &= \sigma_z{}^2(s) - \sigma_{zo}{}^2 \\ \sigma_z{}''^2 &= \sigma_z{}^2(s) - (1-T^2)\sigma_{zo}{}^2 \end{aligned} \tag{52}$$

$$\sigma_{zo}^{2} = \sigma_{z}^{2}(s_{o}) .$$

Equation 51 takes on a more familiar form when H_c is set to zero:

$$C(s,\theta,0) = \frac{2P(\theta)}{s} \frac{QT}{\sqrt{2\pi} U_{o} \alpha \sigma_{z}''} e^{-\left(\frac{Tz_{r}}{\sqrt{2}\sigma_{z}''}\right)^{2}} \qquad (53)$$

The terrain modifications enter through two factors: α and T. T appears only in combination with σ_z''. From Equation 52,

$$\left(\frac{\sigma_{z}''}{T}\right)^{2} = \left(\frac{\sigma_{z}'}{T}\right)^{2} + \sigma_{zo}^{2} \qquad (54)$$

so that the factor T is seen to modify the rate of growth of σ_z between s_0 and s, much like the σ_z enhancement factor of CTDM(11083-E). If α is set to 1.0 as in the two-dimensional flow limit, then the terrain effect is explicitly a relative increase in dispersion, presumably related to the combined effects of streamtube distortion (enhanced concentration gradients) and increased turbulence. If α is set to T, then the net "centerline" concentration in the plume remains unaltered by the terrain, so that the terrain effect is explicitly a displacement of the plume toward the surface.

The dependence of α and T on the parameters controlling the flow is not known for certain. Approximate expressions for the vertical deflection of streamlines in uniform weakly stratified flows ($Fr_H > 1$, but $Fr_L < 1$) have been suggested by Smith (1980) and Hunt and Richards (1982), and the structure for similar flows with wind shear and non-uniform stratification have also been explored in Hunt and Richards (1982). These studies show that streamlines can come very close to the hill surface on the leeward side of the hill, as observed in physical modeling studies (e.g. Snyder and Hunt 1983). However, the magnitude of any increase in concentration in the lee of the hill is uncertain. The role of streamline convergence on plume growth in axisymmetric flow over a sphere was formulated by Hunt and Mulhearn (1973) by means of a local analysis about the centerline of a thin plume. This theory provides estimates of surface concentrations in the neutral stratification limit, provided that surface boundary layer effects are ignored.

Because a theory for α and T that would cover the entire range of Froude number encountered in the SHIS #1 MDA is incomplete, our efforts were focused on obtaining expressions for α and T that best fit the CCB data. In this way, the data will help determine the forms for α and T that are most consistent with what we currently understand about the physics of the problem.

As a first step, we will assume that T is dependent on Fr_L in much the same way as is the streamline pattern. When Fr_L is large, T will reach a minimum value near the crest of the hill. When Fr_L is small, T will reach a minimum value on the lee side. However, once the minimum value is reached, we assume that T remains at this value due to a combination of streamline adjustments (Smith 1980) and wake turbulence.

Fr_L is defined to be

$$Fr_L = Fr_H \frac{H-H_c}{L_{1/2}(H_c)} \tag{55}$$

where $L_{1/2}(H_c)$ is the half-length of the hill midway between H_c and the top of the hill, H. Fr_H is the Froude number based on the height of the hill, calculated for the flow above H_c. The distance from the impingement point (or the base of the hill if $H_c = 0$) to the greatest terrain elevation along the wind trajectory from the source to the effective receptor is denoted as L_o. The distance from the impingement point to the point where T first attains its minimum value for this wind direction is

$$L = L_o/(1 - e^{-2.3\,Fr_L}) \quad . \tag{56}$$

When Fr_L is much greater than 1, $L = L_o$. When Fr_L is equal to 0.3, $L = 2L_o$. The coefficient of Fr_L contained in Equation 56 is chosen to place the minimum value of T at the leeward base of the hill ($H = H_c$) when Fr_L attains its minimum expected value ($Fr_L = 0.3$). For receptors at distances between s_o and L, T is obtained by linear interpolation:

$$T = T_{min} + \frac{1 - T_{min}}{L}(s_o + L - s) \tag{57}$$

$$s_o \leq s \leq s_o + L$$

where s is the distance to the receptor, and s_o is the distance to the impingement point (or the base of the hill if $H_c = 0$). T is set equal to 1.0 for receptors with s less than s_o, and T is held at T_{min} for receptors beyond $s_o + L$.

The value of T_{min} in Equation 57 should be different for a plume segment that passes toward the side of a hill than for a plume segment that passes directly over the peak of a hill. To include this effect, let T_{min} equal T_o over the peak of a hill, and

$$T_{min} = T_o + (1 - T_o)\,(y/a(H_c))^2$$
$$T_{min} = 1 \text{ if } |y| > a(H_c) \tag{58}$$

where y is the cross-wind position of the receptor in a coordinate system with x aligned with the mean wind direction, and $a(H_c)$ is the approximate radius of the hill at an elevation equal to H_c.

Because T/α is a measure of the amount of dilution experienced by the modeled plume as T becomes different from 1.0, we would expect α to be approximately equal to 1.0 when the plume is very close to the surface compared to σ_z, and we would expect α to be approximately equal to T when the plume is far from the surface compared to σ_z. When the plume is close to the surface (i.e., close to H_c), much of the decrease in T will probably result from increased diffusion because the flow distortion places much of the plume within a region of increased turbulence. When the plume is well above the surface, the convergence of streamlines towards the surface will place a good deal more of the "tail" of the plume close to the surface and within the zone of increased turbulence, but the majority of the plume will remain above and will not be subject to a marked increase in mixing.

These concepts have been tested by running the new version of the model (CTDM(14083)) on the data for Experiments 201 and 210, with α set equal to T. CTDM(14083) incorporates Equations 44 and 51, and T_o has been set to 0.5. By using a similar enhancement scale, the new formulation of the Lift model can be compared with CTDM(11083-E). Because α appears outside the exponential functions, a comparison of the observed and modeled concentration patterns will indicate how α should vary. This comparison has been made with the use of the modified MDA.

The ratio of the net release height to the size of σ_z at the impingement point ($(z_r - H_c)/\sigma_{zo}$) is found to order the behavior of α, and our expectation of how α should vary is confirmed:

- $\alpha \sim T$ when $(z_r - H_c)/\sigma_{zo} = 3.14, 3.91, 5.17, 8.50$
- $\alpha \sim 1$ when $(z_r - H_c)/\sigma_{zo} = -0.20, 0.33, 1.00, 2.00$

Note that four of the hours are not pertinent to this evaluation of α. The comparison also indicates that some plume dilution is needed immediately on the windward face of the hill when $(z_r - H_c)/\sigma_{zo}$ is less than O(1.0), that Equation 57 works well for T when $(z_r - H_c)/\sigma_{zo}$ is greater than O(1.0), and that $T_o = 0.5$ is generally of the right magnitude when $(z_r - H_c)/\sigma_{zo}$ is less than 5.0. For $(z_r - H_c)/\sigma_{zo}$ much greater than 5.0, T should be controlled exclusively by the streamline depression. If we take the minimum approach distance from potential flow theory for flow over a sphere, then the lower bound for T_o should be approximately 0.3.

These findings have been incorporated into CTDM(14083). When $(z_r - H_c)/\sigma_{zo}$ is less than 1.0, T has been set equal to T_o at all receptors and α has been set equal to 1.0 to simulate dilution of plumes very close to H_c as they are swept over the hill in a turbulent boundary layer. Whenever $(z_r - H_c)/\sigma_{zo}$ is greater than 3.0, α has been set equal to T to simulate the importance of plume displacement relative to dilution. Linear interpolation is used for α when $(z_r - H_c)/\sigma_{zo}$ is between 2.0 and 3.0. And T_o varies linearly between 0.5 and 0.3 for $(z_r - H_c)/\sigma_{zo}$ between 5.0 and 10.0. T_o is 0.5 below 5.0, and 0.3 above 10.0.

3.4.3 CTDM(14083) Performance Evaluation

CTDM(14083) was applied to the 12 hours from Experiments 201 and 210 for which modified input data were developed. The results are displayed in

Figure 38 in terms of the ratio of the peak observed concentration to the peak modeled concentration, unpaired in space.

CTDM(14083) is compared with CTDM(11083-E) with both 1-hour and 5-minute data in the figure. When the best results for either the 1-hour or 5-minute version of the two models are compared, version 14083 does better than in version 11083-E in 3 of the hours; it does about as well as version 11083-E in 5 of the hours; and does worse in the remaining 4 hours. The performance of CTDM(14083) tends to be worse than that of CTDM(11083-E) for those hours when the peak concentration occurs on the windward face of the hill not far above H_c. In these cases, the enhancement structure in version 11083-E begins to increase the dilution of the plume dramatically (see Equation 27), while the structure in version 14083 requires a significant growth in σ_z with distance before the enhancement can produce a similar effect (see Equations 52 and 54). Several hours in Experiment 201 appear to require this dilution. This deficiency in the new version of the Lift module emphasizes the need to consider the effect of the hill on the growth of σ_z upwind of the point where H_c "intersects" the hill. The tow-tank experiments of Snyder and Hunt (1983) document significant vertical motion in impinging streamlines below H_c, and observers during SHIS #1 frequently reported a more "diffuse" plume when the oil-fog plume was directed toward the hill, below H_c. For releases well above H_c, CTDM (14083) generally does better in locating the peak concentration correctly, even though the magnitude may not be estimated better.

CTDM(14083) has also been tested with all 153 hours of data in the MDA. The results are listed in Table 4 along with those from CTDM (11083-E). These results are similar to those contained in Figure 38 in that no great improvement is evident in the performance of the new version. The bias has moved marginally closer to the ideal, and the noise has increased marginally. A slight improvement in the resolution measure is also noted. These results indicate that a significant improvement in CTDM will require a careful evaluation of the structure of α and T, the inclusion of a framework for modifying flow and turbulence assumptions in the Wrap module, and detailed evaluation of the data contained in the MDA on a case-hour by case-hour basis.

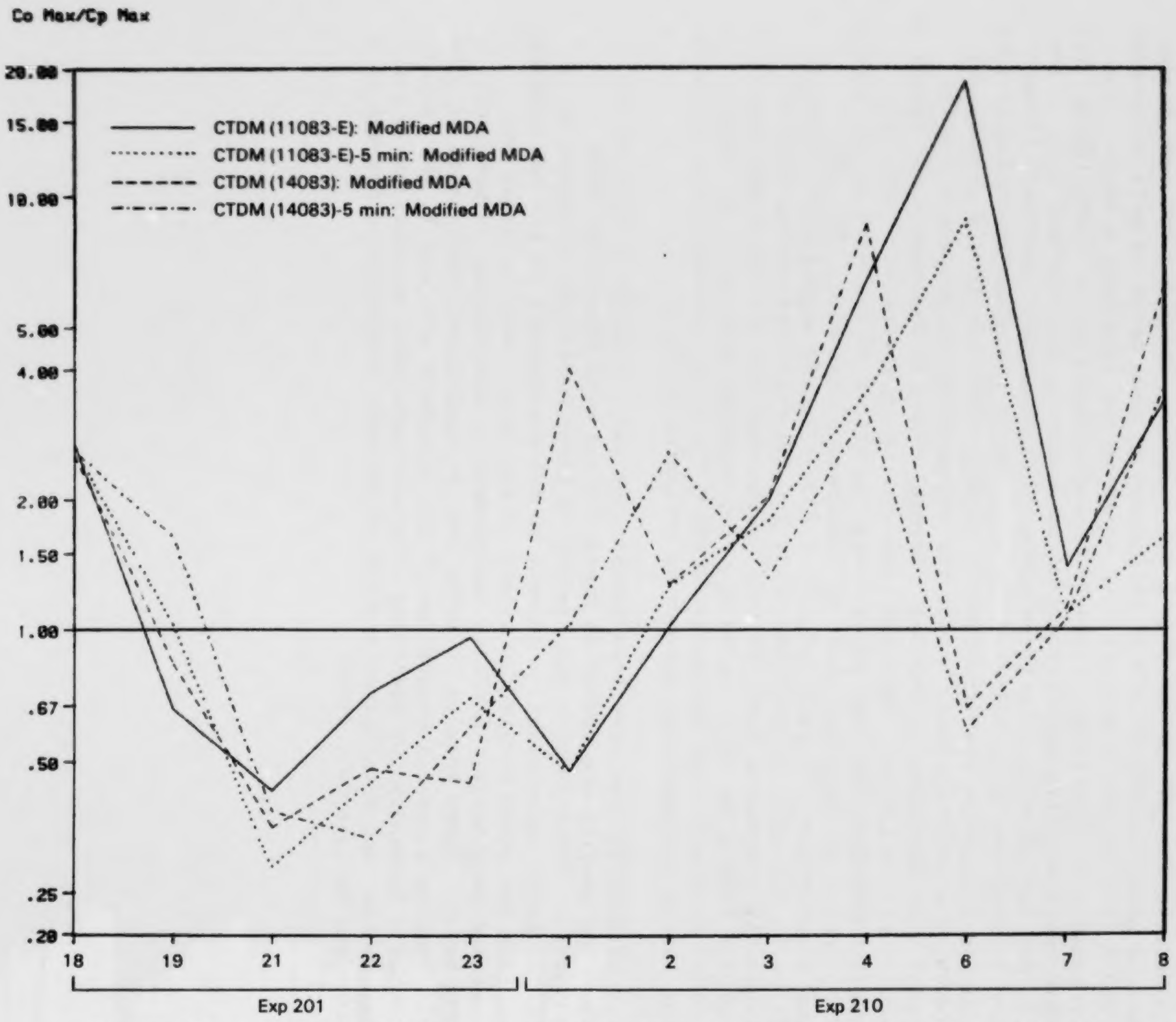

Figure 38. CTDM (11083-E) and CTDM (14083) C_o (peak)/C_p (peak) residuals for Experiments 201 and 210 with the modified MDA.

TABLE 4. COMPARISON OF MODEL PERFORMANCE STATISTICS
FOR CTDM (14083) AND CTDM (11083-E) USING THE
SHIS #1 MDA

	Peak Concentrations (Unpaired in Space)						All Concentrations		
	$\underline{m}_a$	$\underline{s}_a$	$\underline{r}_a$	$\underline{m}_g$	$\underline{s}_g$	$\underline{r}_g$	$\underline{m}_a$	$\underline{s}_a$	$\underline{r}_a$
CTDM (14083)	0.7	30.9	0.87	1.32 (1.23)	3.35 (3.3)	0.89	-0.94	14.8	1.03
CTDM (11083-E)	3.3	27.4	0.90	1.37 (1.23)	3.2 (3.3)	0.99	0.50	12.7	1.13

Note: ( ) m_g and s_g values are computed with "$C_p = 0$" entries removed.

SECTION 4

THE HOGBACK RIDGE EXPERIMENT

4.1 Geographic and Meteorological Setting

The Hogback Ridge (HBR) was selected as the site for the second Small Hill Impaction Study (SHIS #2). HBR is located in the northwestern corner of New Mexico, about 15 miles west of Farmington. It lies on the semiarid Colorado Plateau near the western slopes of the San Juan Mountains (Figure 39). Three rivers--La Plata, Animas, and Chaco--drain into the San Juan River near Farmington. The terrain features of the area include occasional isolated ridges (e.g., HBR), isolated promontories (e.g., Shiprock), and low mesas and plateaus. The area is characterized by a sparse vegetative cover of desert shrubs and grasses.

SHIS #2 was conducted in the environs of an approximately 1.5-km long section of the ridge north of the San Juan River (Figure 40). Here, the Hogback is oriented NNE-SSW and rises about 85 m above its base elevation. HBR extends from just north of the SHIS #2 experimental area to about 8 miles south of the San Juan River. The ridge splits where the San Juan and Chaco Rivers flow westward and forms separate "hogbacks." The two southern sections, separated by the Chaco River, are shown in Figure 41 as viewed with a telephoto lens from the SHIS #2 site; the plume from the Four Corners plant is passing over the ridge. Waughan Arroyo is located just east (upwind) of the experimental section. Farther east a series of irregular mesas, arroyos, and surface coal mines extend all the way to Farmington. Figure 42 presents a view of the experimental section of HBR from the east, and Figure 43 shows the area east of the section, as viewed from the top of HBR.

Because of substantial reserves of coal and the adequate water supply from the San Juan River, two major electric generating facilities operate in the region. The San Juan Power Plant is located just east of the experimental area, and the Four Corners Power Plant is located south of the San Juan River. Public Service Company of New Mexico (PNM) and Arizona Public Service Company (APS), the respective operators of the two generating stations, have sponsored several meteorological and air quality measurement programs. The National Weather Service operates a weather station at the Farmington (FMN) Airport. Consequently, there was a wealth of meteorological data available during the site selection and experimental design phases.

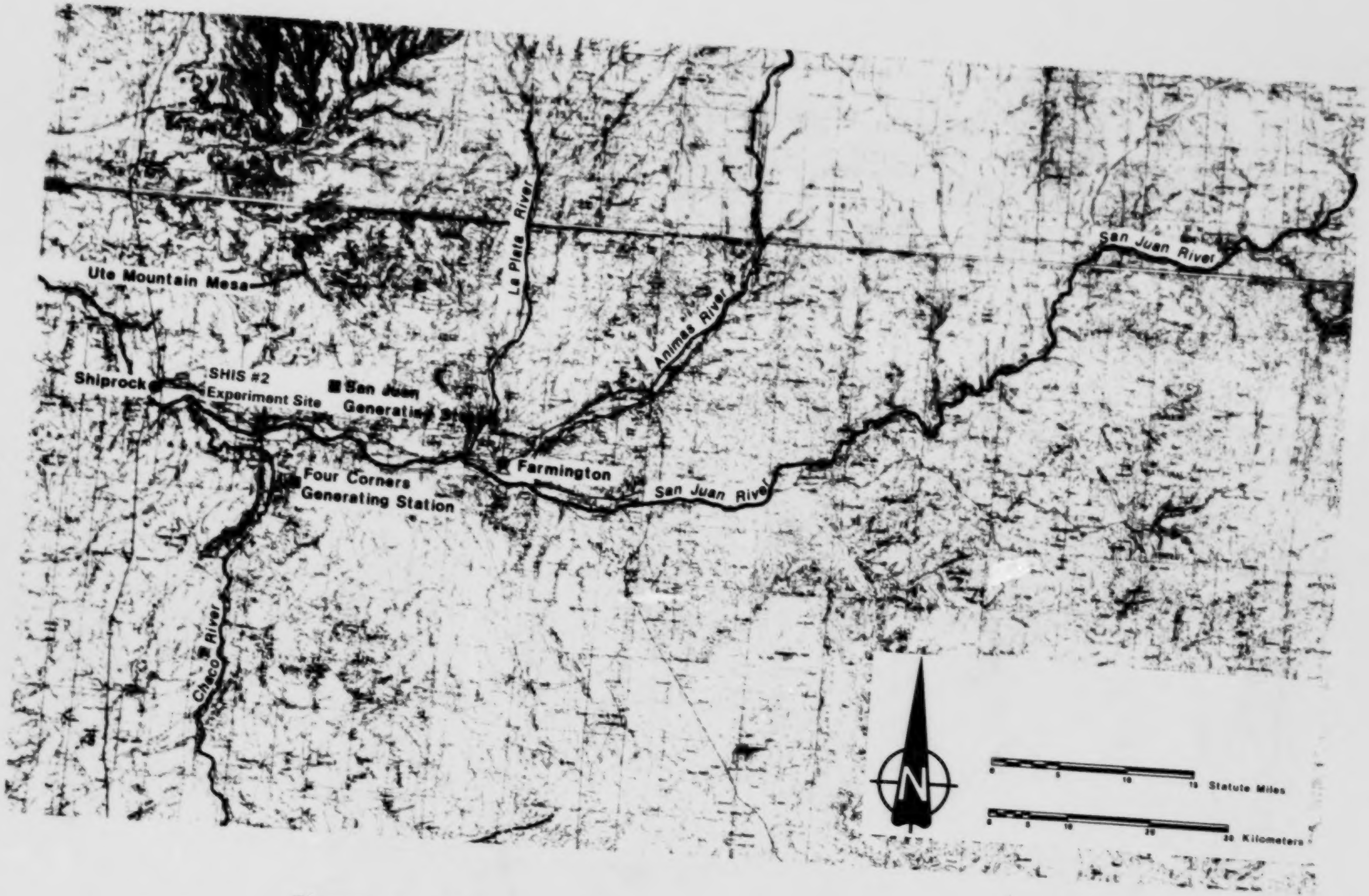
Ute Mountain Mesa
La Plata River
Animas River
San Juan River
Shiprock
SHIS #2
Experiment Site
San Juan
Generating Station
Farmington
Four Corners
Generating Station
San Juan River
Chaco River
N
0
5
10
15
Statute Miles
0
5
10
20
30
Kilometers

Figure 39. Region around the SHIS #2 at the Hogback Ridge.

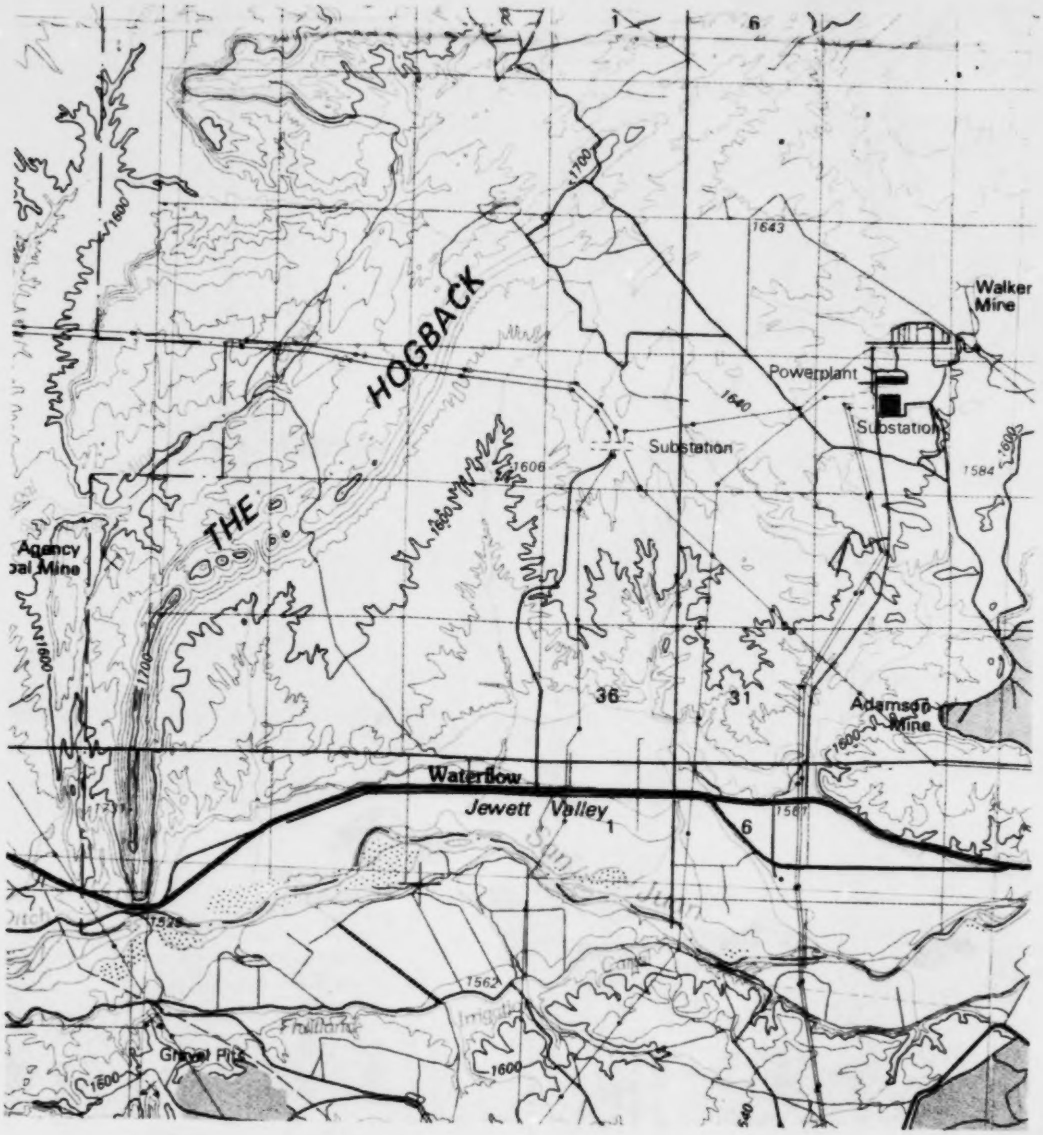
THE HOGBACK
Walker Mine
Powerplant
Substation
Substation
Agency Coal Mine
Adamson Mine
Waterflow
Jewett Valley
36
31
6
1
1643
1640
1606
1600
1700
1584
1567
1562
1528
Gravel Pits
Fruitland
Irrigation
San Juan

Figure 40. The SHIS #2 site. Contour interval 20 m.

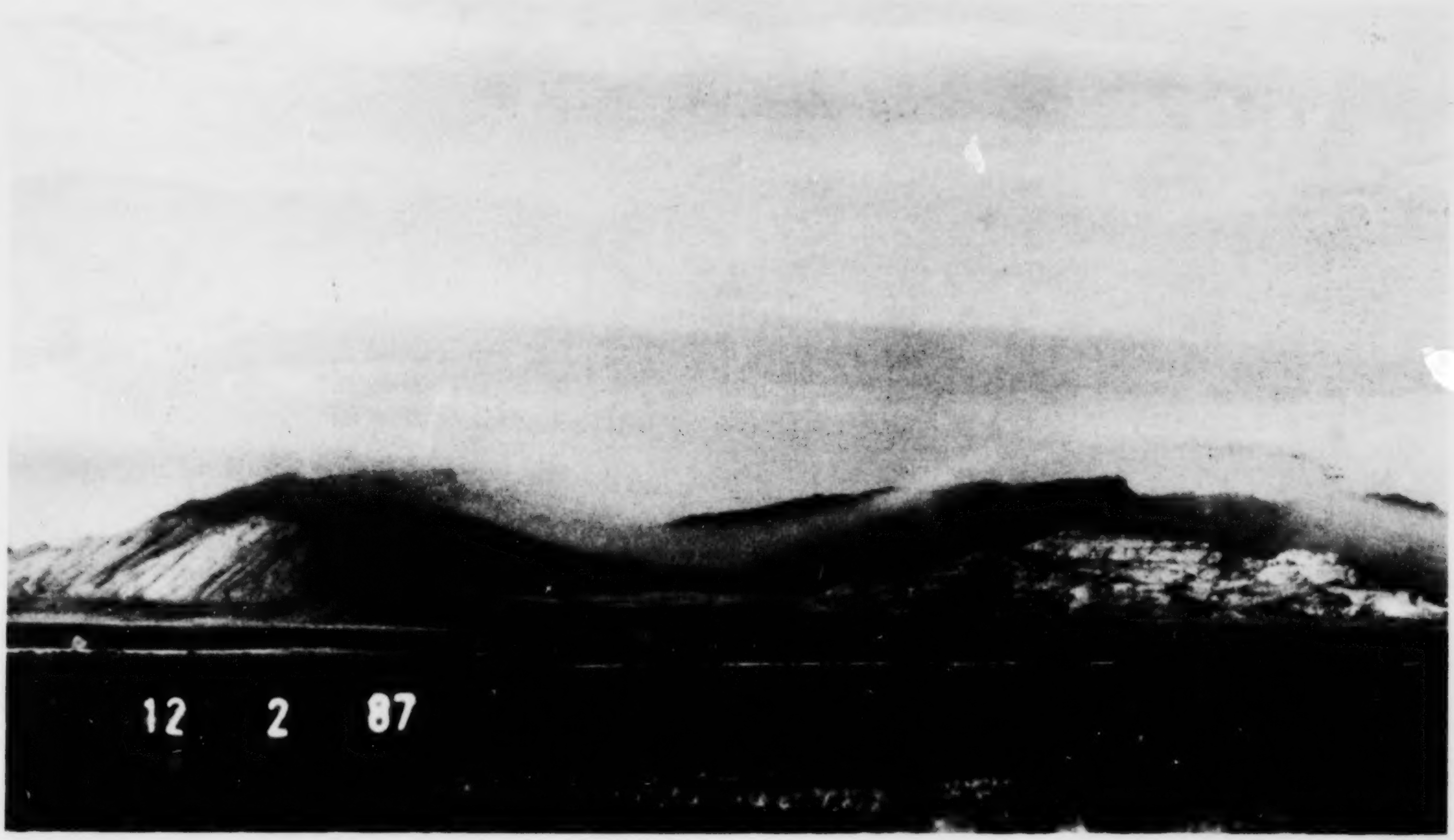

Figure 41. View of Hogback south of the San Juan River.

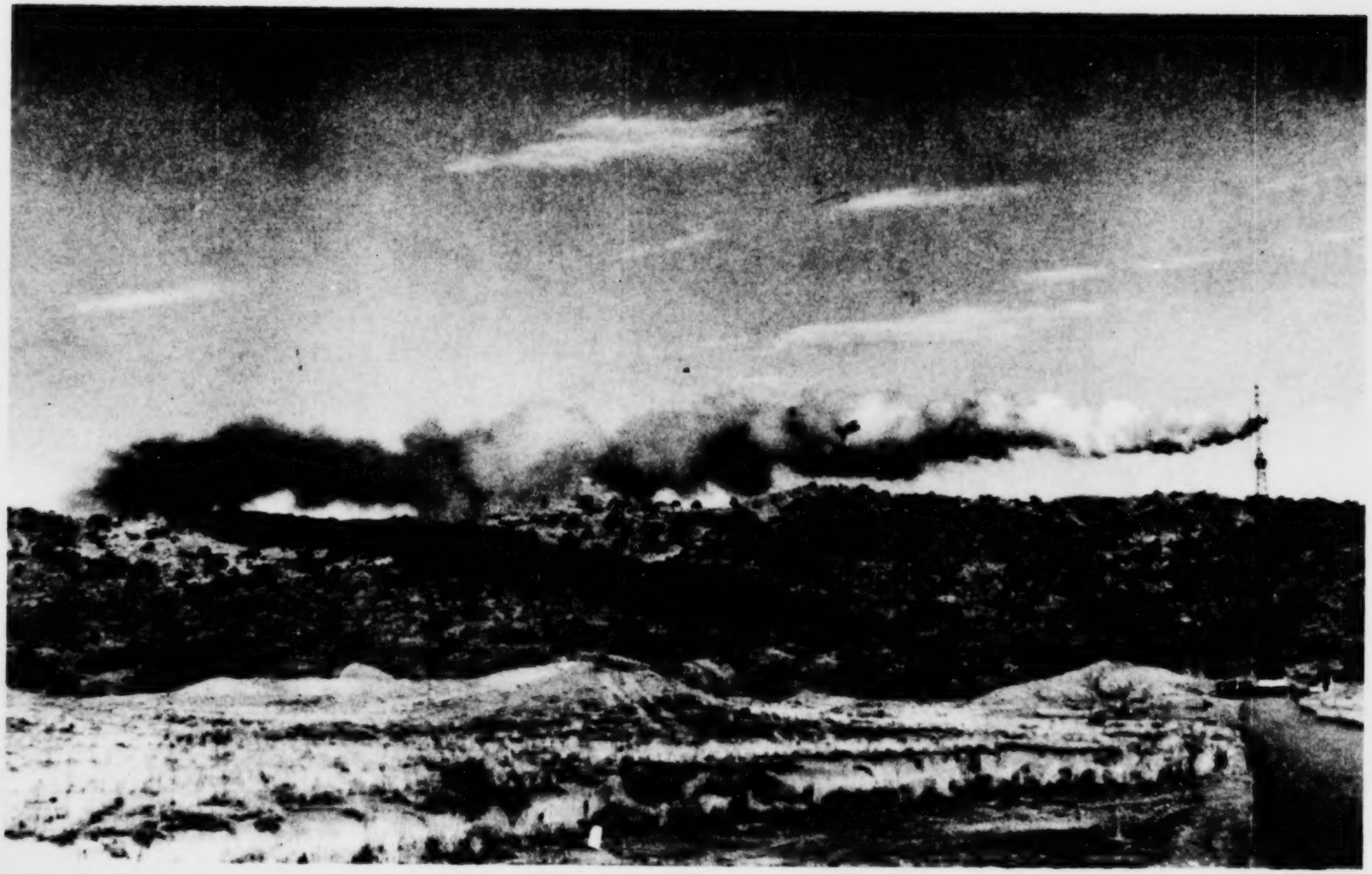

Figure 42. View of the Hogback experiment site from the east.

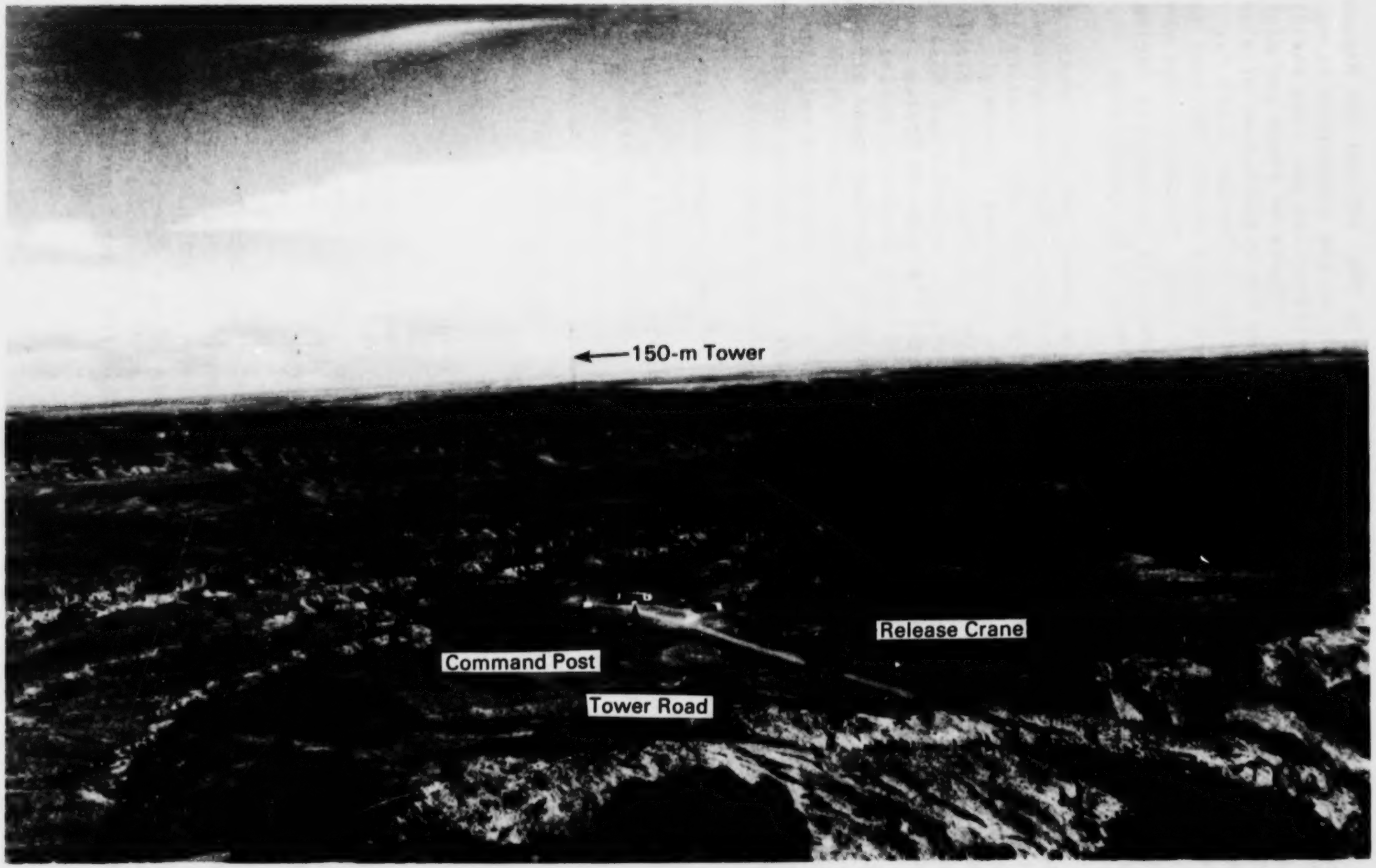
150-m Tower
Release Crane
Command Post
Tower Road

Figure 43. View toward the south-east from the Hogback.

The meteorological measurements taken by PNM, APS and the National Weather Service provide detailed information on the dispersion climatology of the HBR region. Most of the available information has been analyzed and summarized recently by Moore et al. (1981). Figure 44 shows two wind roses derived from FMN data. The first rose shows the distribution of winds during 1976; the second shows the distribution of Oct-Dec winds for stability "E" conditions. Figure 45 shows October hourly FMN wind roses for four nighttime hours--2200, 0000, 0200, and 0400. Evidently, the wind typically "turns around" (Crow 1975) from westerly to easterly during the night as the drainage from the San Juan Mountains is established.

Drainage periods occur often during the summer and fall months and produce stable easterly flows toward HBR at night. The drainage and turnaround days are characterized by light winds all day. Cooling in the evening and night results in strong surface inversions. Dense air flows from the mountains down the river valleys and the Chaco wash. Stable air flows toward HBR along the San Juan River valley, around Pinon Mesa from the northeast and occasionally from the southeast. Figure 46 (taken from Moore et al. 1981) illustrates a typical summer morning downslope drainage flow situation. Figure 47 shows representative early morning upper air soundings during easterly drainage situations. The deep stable layer, which is uncoupled from the synoptic westerly winds aloft, continues well into the morning until convective turbulence destroys the inversion, and the flow near the ground is again coupled with the synoptic winds aloft.

In summary, the available meteorological data suggested that frequent stable easterly winds occur at night during the fall months. This was the principal reason for selecting HBR as the site for SHIS #2. Other reasons included: (1) HBR is the dominant terrain feature in the area of interest; (2) the area is easily accessible and has electric power available; (3) PNM provided records of meteorological data taken on and near HBR and was willing to provide the data in real-time during the experiment; and (4) the Bureau of Land Management, which manages the HBR and the area to its east, granted permission to use the ridge.

4.2 Preliminary Flow Visualization Experiment

A preliminary flow visualization study was conducted at a section of HBR just south of the power transmission lines (see Figure 40) during the period June 6 - June 11, 1982. Scientists from ERT, EPA/Terrain Effects Branch (TEB), EPA/Fluid Modeling Facility (FMF), NOAA/Wave Propagation Lab (WPL) and the Los Alamos Scientific Lab (LASL) participated.

Meteorological data were obtained using two tethersondes, pibals and fixed meteorological sensors on three towers (two 10-m towers on the Hogback and a 200-ft tower east of the arroyo) operated by PNM. Smoke was released using smoke candles and canisters suspended from a 600-ft^3 blimp at a location approximately 150 m east-southeast of the road along the base of ridge and 300 m south of the major transmission lines crossing the ridge.

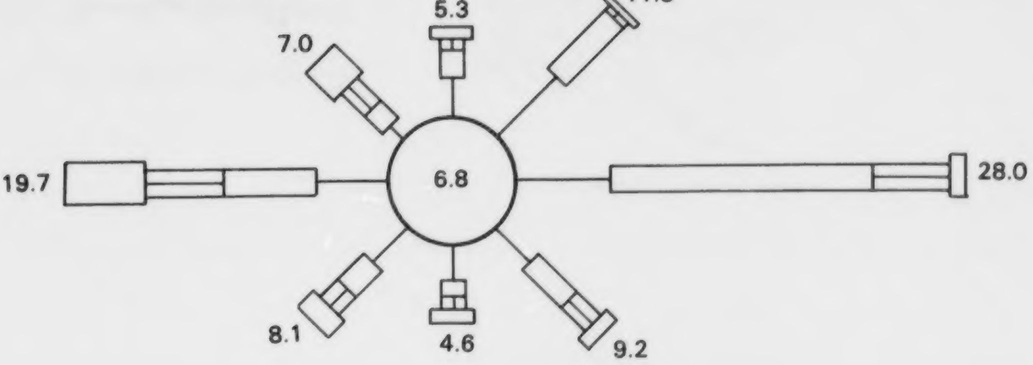

Figure 44(a). Climatological annual wind rose for Farmington, N.M. (2927 valid data points, 3-hour NWS data for 1976).

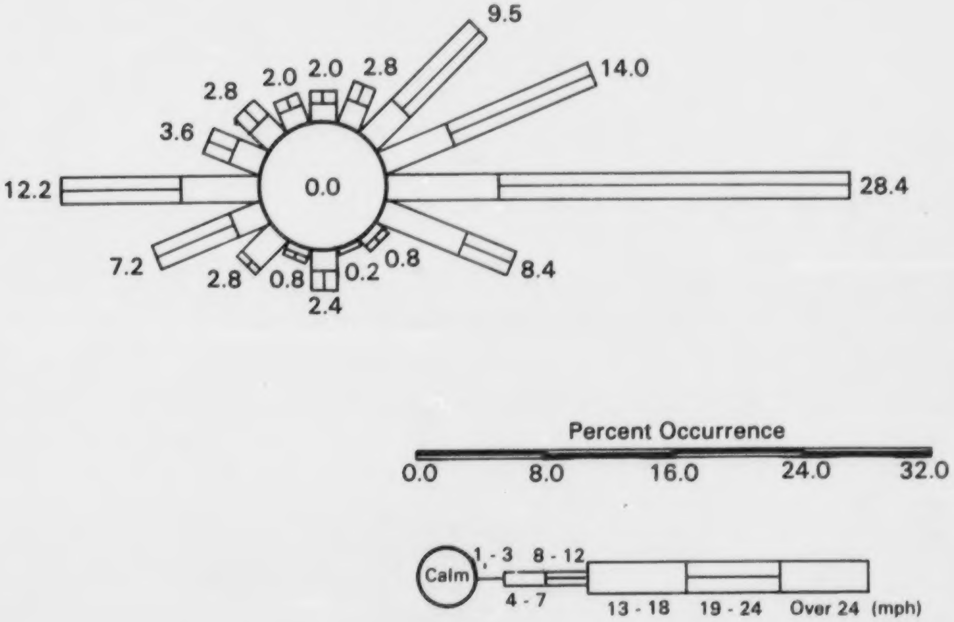

Figure 44(b). October-December stability E Farmington wind rose.

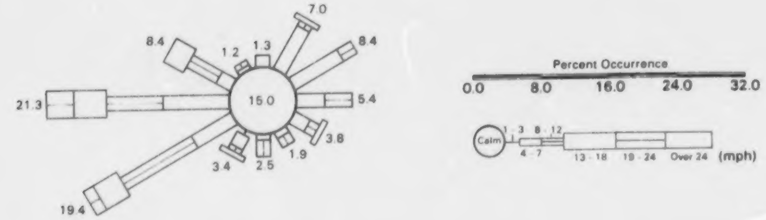

Farmington, New Mexico — Airport (FAA) October (1977-1981) Hourly Rose - Hour (LST) = 22

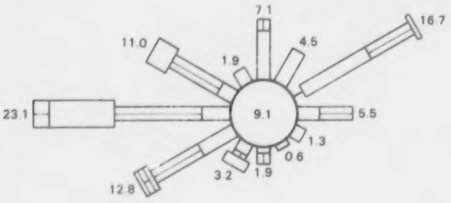

Farmington, New Mexico — Airport (FAA) October (1977-1981) Hourly Rose - Hour (LST) = 24

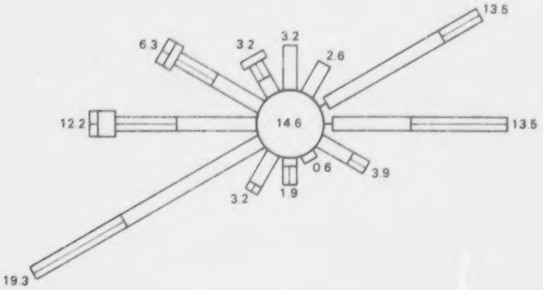

Farmington, New Mexico — Airport (FAA) October (1977-1981) Hourly Rose Hour (LST) = 02

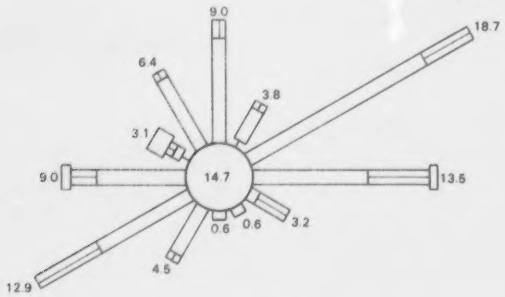

Farmington, New Mexico — Airport (FAA) October (1977-1981) Hourly Rose - Hour (LST) = 04

Figure 45. October hourly wind roses for four nighttime hours: 2200, 0000, 0200, and 0400 MST.

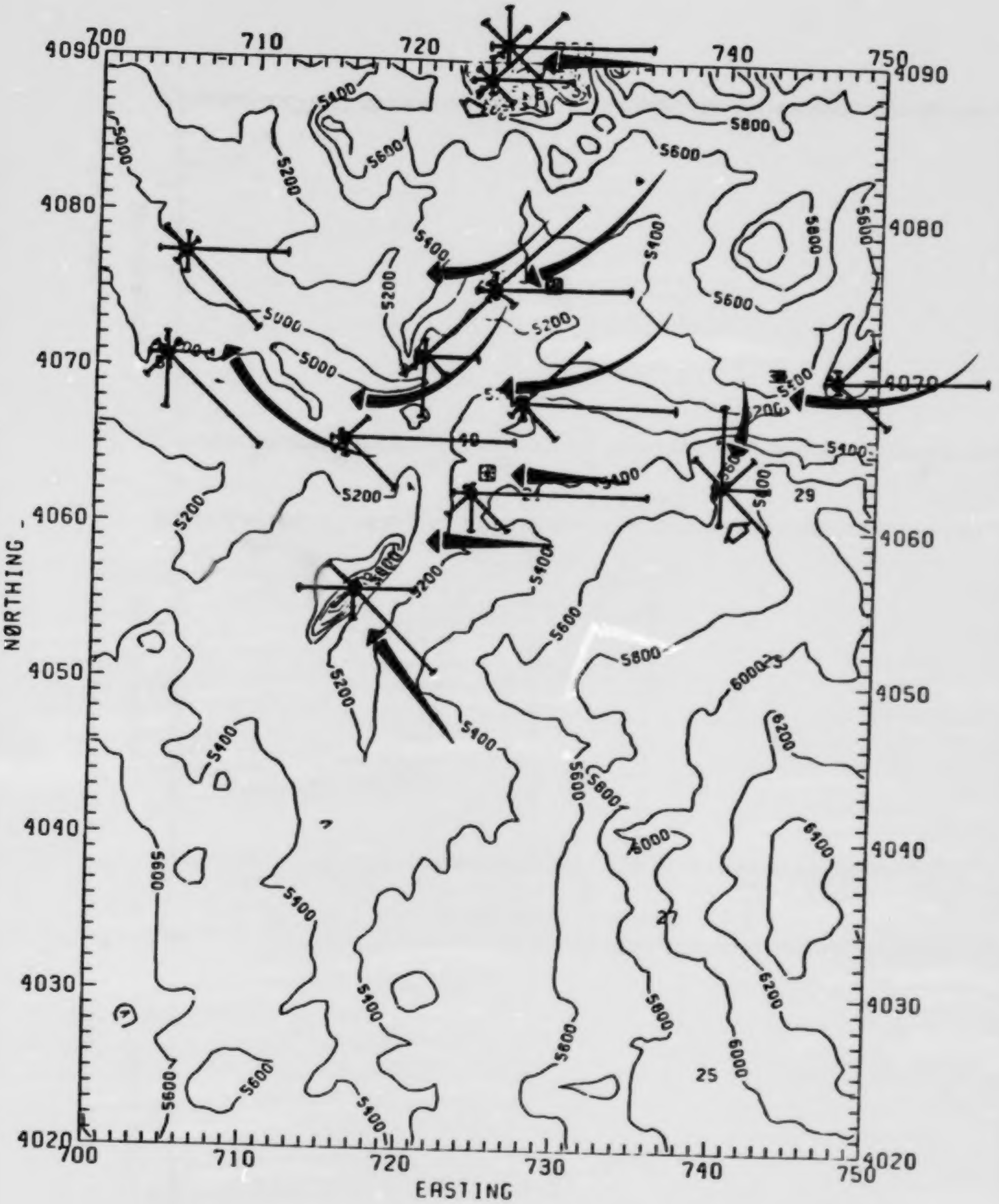
700
710
720
740
750
4090
4080
4070
4060
4050
4040
4030
4020
730
NØRTHING
EASTING
5000
5200
5400
5600
5800
6000
6200
6400
29
27
25

Figure 46. Summer morning downslope drainage flow. (Taken from Moore et al. 1981.) The squares (⊞) indicate the San Juan and Four Corners power plants. The SHIS #2 site is just west of San Juan at UTM coordinates 722 E, 4074 N.

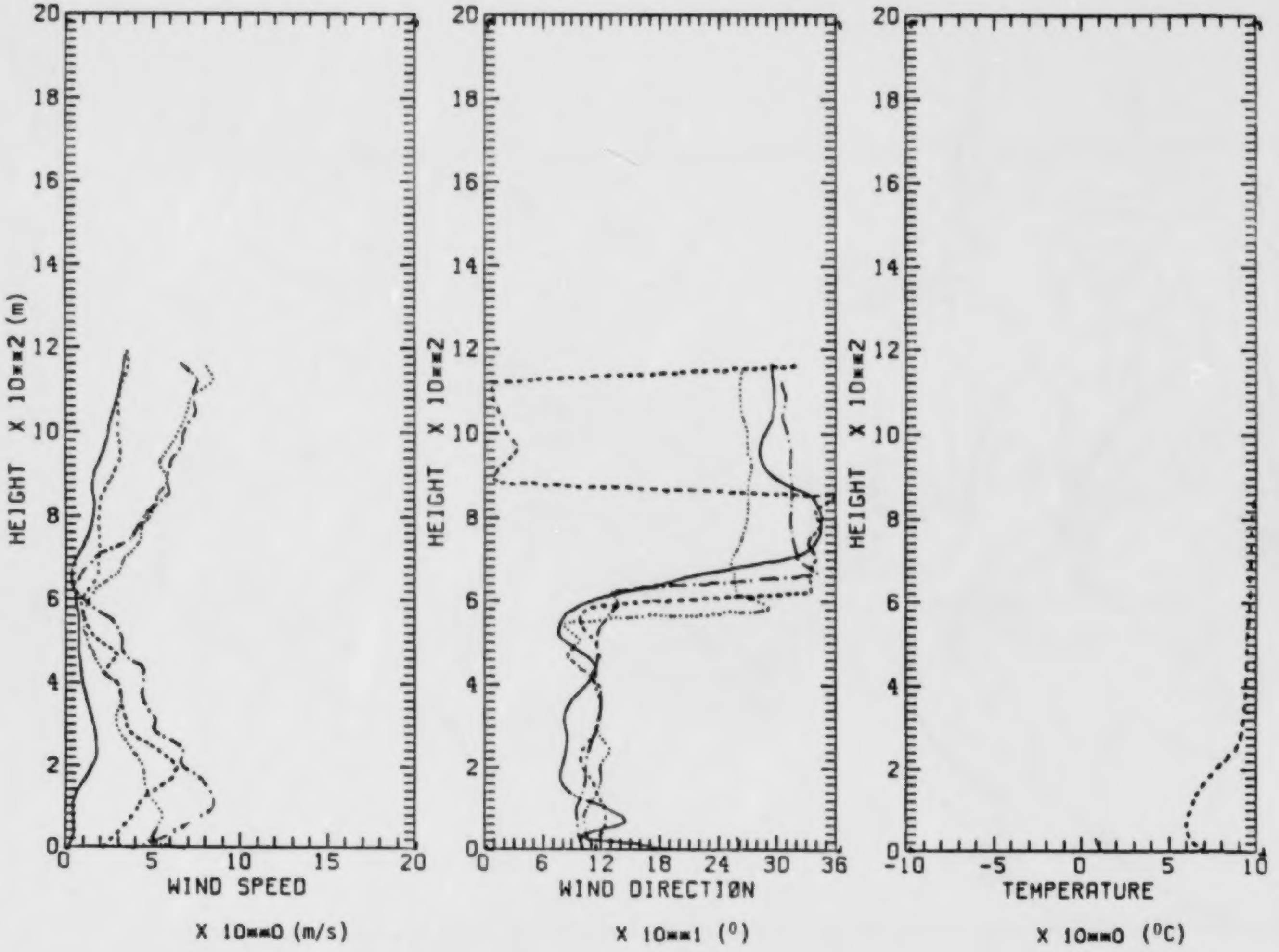

Figure 47. Upper air soundings at Four Corners Power Plant during turnaround meteorological conditions. (Taken from Moore et al. 1981.)

WPL operated a tethersonde near the blimp to document meteorological conditions near the source. LASL operated a tethersonde east of Waughan Arroyo to document conditions upwind of the source. In addition, EPA released pibals and neutrally buoyant ballons.

The flow visualization experiments were documented with 35 mm cameras and 8 mm movie cameras. The meteorological data and the photographs were analyzed to aid in the SHIS #2 experimental design. Specifically, the flow visualization experiment helped in the following areas:

- selection of the section of HBR for SHIS #2,
- location of the roads for the release crane,
- location of the tracer gas sampler locations,
- location of the meteorological towers and other meteorological sensing devices, and
- location of the lidar.

In addition, photographs and tethersonde data were analyzed to test the critical dividing-streamline height (H_c) concept for the Hogback. Table 5 summarizes three experiments during which plumes released above H_c went up and over the ridge, and plumes below the H_c stagnated and tended to remain horizontal. The release height is denoted by z_r.

4.3 Fluid Modeling in Support of the SHIS #2 Experimental Design

During September 1982, a series of wind tunnel and towing tank flow visualization experiments were conducted at the EPA FMF to provide input to the SHIS #2 experimental design. The studies were designed to investigate:

- plume height above the surface over the hill crest and at the upwind edge of the hill,
- apparent size of any plume deformation upwind of the hill,
- lee wave importance and structure, and
- sensitivity of the plume trajectory to "wind angle."

This information was then used to (1) guide the design of the smoke and tracer gas release protocols at HBR, and (2) help select sampler and camera locations.

Two models of the Hogback were used--one for the tow-tank and a second for the wind tunnel. Each has a scaled radius equivalent to 800 m, and the northernmost point is the prominent peak just north of the high tension power lines near PNM station 105. The ends of the models were extended to the walls of the test chambers. Peak elevations above the base plate did not exceed 14 cm (84 m, scaled). Each model was covered with approximately 3 mm size gravel.

Two tests were made in the wind tunnel. One test was done with the ridge perpendicular to the flow, the other with the ridge rotated by 30°. Because the flow was very turbulent (boundary layer about 1-m thick) with the trip fence in place, the fence was removed to gain a better measure of plume centerline height.

TABLE 5. PRELIMINARY VISUALIZATION EXPERIMENT EXAMPLES OF H_c ANALYSES

1. 11 June 1982

z_r = 40 and 60 m at 0539MDT
H_c = 37 m at 0456 (WPL #21 ascent)
10 m at 0528 (WPL #21 descent)
6 m at 0503 (LASL #35 ascent)

Observer comment: Smoke largely made it over from both release heights.

Photos: Narrow plumes definitely above H_c.

2. 11 June 1982

z_r = 60 m at 0620
H_c = 8 m at 0557 (WPL #22 ascent)
39 m at 0626 (WPL #22 descent)
1 m at 0603 (LASL #36 descent)

Photos: Narrow plume above H_c

3. 10 June 1982

z_r = 15 and 35 m at 0650
H_c = 30 m at 0635 (WPL #17 ascent)
19 m at 0650 (WPL #17 descent)

Observer comment: The 15-m level is very diffuse and the 35-m level maintains some integrity and it has some definite direction to it. The 15-m level release is going right down to the ground within a few tens of meters from the source. Smoke from the 35-m release seems to be approaching the hill slope but getting up and over. The 15-m smoke release is involved in all the hillocks at the bottom of the Hogback but seems to be getting up and over the ridge. It does not appear to be blocked.

Photos: H_c is between 15 and 35 m.

In the first test, smoke was released 10 cm above the floor of the tunnel. The centerline appeared to be about 9-11 cm above the surface of the model near the base of the hill, and about 6 cm above the surface at the crest (1 cm = 6 m). Therefore, the plume maintained its initial height upwind of the hill and approached the crest surface at nearly half its initial height. This is approximately consistent with what would be expected in potential flow. The plume was forced to speed up over the crest of the ridge, but no region of deformation could be seen upwind of the hill.

In the second test, the flow angle produced little additional effect on streamline height but did produce a small plume path deflection. Although the deflection was difficult to quantify, it was estimated to be about 8 cm (about 1/2 the visible plume width). Because the smoke was released about 800 m from the crest (scaled), this deflection ($\sim$50 m, scaled) was less than 4°.

Eight individual tests (Table 6) were run in the tow-tank. The first three were run with Froude numbers of 0.8, 1.0, and 2.0 and with a wind direction of 118° (wind flow perpendicular to the ridge). In the cases of $Fr_H = 0.8$ and 1.0, tow speeds were set to produce H_c values of 0.2 H and 0.0 H. Consequently, bulk Froude numbers were probably less than 1.0 in both tows, due to the mixed layer near the surface of the model.

Dye streaks were released at heights of 2, 6, 10, 14, 18, 22, 25, 30, 35, 40, and 45 cm at the upstream edge of the baseplate. These heights are referenced to the water surface. The dye streamer released at 2 cm was mixed in a stagnation region upstream of the ridge during the first tow.

Tows 4 and 5 had $Fr_H = 1.0$ and 2.0, respectively, based on the linear density profile above the surface mixed layer (no mixed layer was present during the first tow at $Fr_H = 1.0$). Dye release heights were switched to 2, 10, 18, 25, 35, and 45 cm. Dye released at 10 cm ($\sim$60 m, scaled) rose to 15 cm above the surface at the upstream edge of the Hogback face in both tows and dropped back to 9 cm and 10 cm (Fr = 1.0, 2.0) at the crest except near the end of the fourth tow (Figure 48) when the dye passed over the crest at an elevation of about 3 cm. Table 7 summarizes the measured heights of the 10-cm streamer for five experiments.

In experiments 6 and 7 the model was rotated 10° and retowed at $Fr_H = 1.0$, and 2.0. Streamline deflections at 2 cm were small in both tows. A rough estimate puts it at 2-3°. A final experiment 8 was done with $Fr_H = \infty$ (neutral conditions).

The FMF flow visualization experiments suggested that during unstratified conditions the streamline patterns are similar to those expected from potential flow theory. The plume should approach HBR at its initial elevation upwind of the ridge, and flow over the crest at nearly half its height. During the weakly stratified simulated conditions, the tow-tank experiments suggested a rise in streamlines near the upwind base of the hill and a fall over the crest to near or slightly lower than its

TABLE 6. FMF TOW-TANK EXPERIMENTS

Tow No.	Direction	Fr_H	Remarks
HOG 1	118°	0.8	Slight shifting at lower levels toward south, but all streamers over ridge top. Strong contraction of streamers observed on lee side. Slow motion below hill top.
HOG 2	118°	1.0	More pronounced shift of lower level streamers to south, but for shorter time period. Wider spreading on lee side. Rotor observed at 4-5 hill heights on lee side. Lower streamers upwind.
HOG 3	118°	2.0	Straight narrow plumes. Less contraction in lee.
HOG 4	118°	1.0	Dye released at 2, 10, 18, 25, 35, 45 cm. Stack visibility good. Fairly wide diffusion in lower levels. Blockage noted upstream.
HOG 5	118°	2.0	Plumes somewhat wider. Distance from crest to 1st max. in lee wave ∿ 4.9 m.
HOG 6	108°	1.0	Lower plumes twist or deviate to south upstream consistently, straighten out downstream.
HOG 7	108°	2.0	Slight S-shape in trajectory.
HOG 8	108°	∞	More plume meandering. Wider dispersion.

TABLE 7. MEASURED HEIGHTS OF THE 10-cm HIGH STREAMER AT THE UPWIND BASE AND CREST OF THE HBR MODEL

	Height (cm) at Upstream Base	Height (cm) at Crest
HOG 4 $Fr_H = 1.0$		
	14	8.5
	15	9
	15	9
	15	8
	15	7
	14	5
	12	3
HOG 5 $Fr_H = 2.0$		
	15	9.5
	15	10
	15	11
	15	10
	15	9.5
HOG 6 $Fr_H = 1.0$		
	12	8.5
	14	9
	14	9
	14	8
	15	8
HOG 8 $Fr_H = \infty$		
	13	9
Wind Tunnel $Fr_H = \infty$		
	10	6

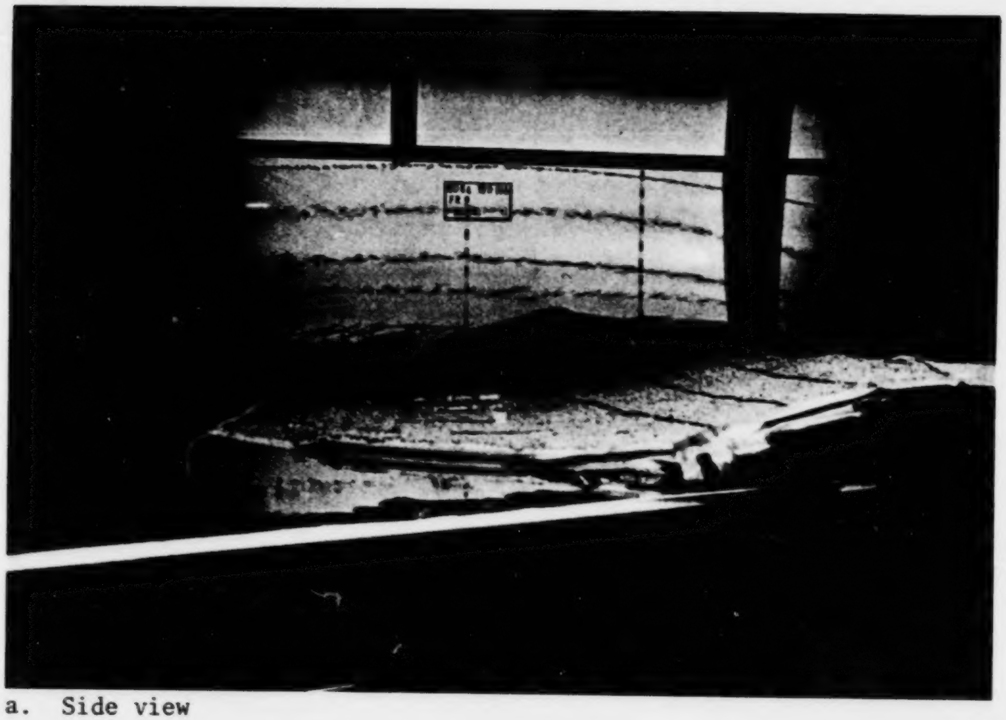

a. Side view

b. Top view

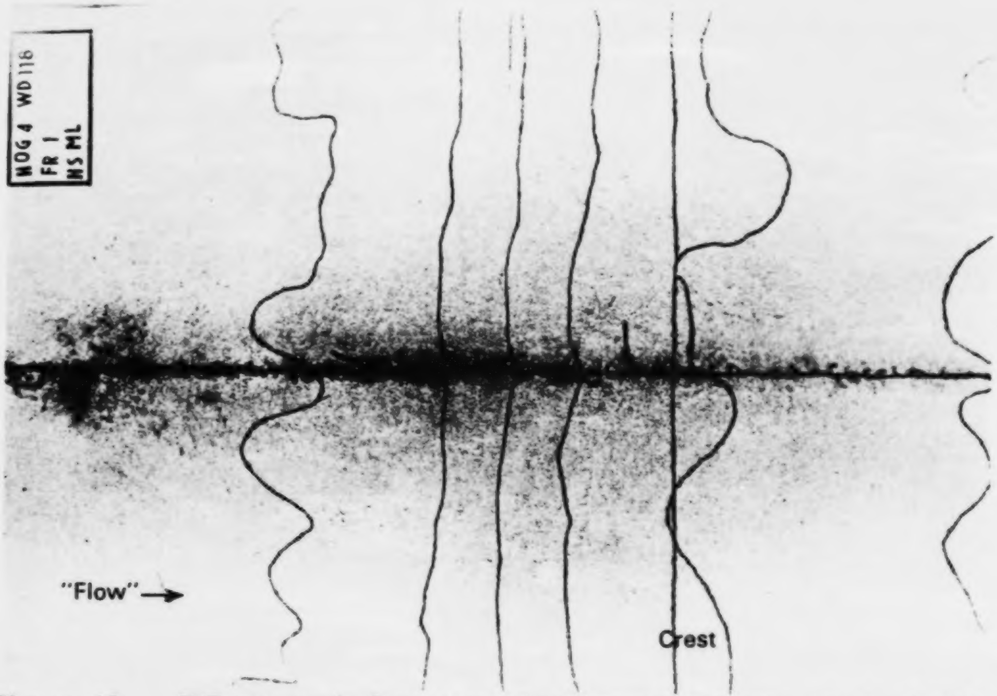
HOG 4 WD118
FR 1
NS ML
"Flow"→
Crest

Figure 48. FMF tow tank flow visualization experiment - Hogback Ridge (wind direction = 118°, Fr = 1.0).

initial height.* Low-level releases near or below H_c are expected to experience considerable mixing. Wind direction variability will not be significantly amplified.

4.4 Experimental Design

The SHIS #2 at the Hogback was designed to obtain meteorological, flow visualization, and tracer gas emission and concentration data in the vicinity of a nearly two-dimensional ridge in order to enlarge the modeling data base and to provide a good basis for testing, evaluating, and refining the modeling concepts developed from the CCB data base and the various FMF experiments. The experimental methods of the SHIS #2 were similar to those used and tested at CCB. The experiment was conducted at the Hogback from October 5 - October 29, 1982 and included:

- Releases of two tracer gases (SF_6 and Freon 13B1 (CF_3Br)) and oil-fog, using a mobile 150-ft crane and a tower as source platforms;
- Fixed meteorological measurements:
    - a 150-m tower instrumented at ten levels,
    - a 30-m tower instrumented at five levels,
    - a 10-m tower instrumented at three levels,
    - a 60-m tower instrumented at two levels,**
    - two monostatic acoustic sounders,
    - a doppler acoustic sounder, and
    - three optical crosswind anemometers;
- Two tethersondes:
    - one operated at source elevation to document meteorological conditions representative of the source, and
    - one operated to measure vertical profiles of meteorological parameters upwind of the ridge;
- Ground-level tracer gas concentrations;
- Lidar measurements; and
- Photographs and videotapes.

---

*The initial rise (e.g., from 10 cm to 15 cm) near the base of the HBR model was not expected. Initial analyses of the SHIS #2 photographs suggest the occurrence of this phenomenon in the field, although the results are currently obfuscated by the thermal plume rise of the oil-fog plume.

**Tower P was operated by PNM. PNM maintained temperature and temperature difference sensors on the tower. ERT installed two cup-and-vane sensors for SHIS #2. In addition, PNM operated a network of instruments in the area, including two 10-m towers on the Hogback. The PNM data were displayed in real-time at the ERT command post.

After three smoke visualization experiments, 11 combined tracer and flow visualization experiments were performed. The three initial experiments were conducted to (1) understand the autumn weather conditions at HBR (the preliminary experiment was conducted in June), (2) gain experience working at the HBR site, and (3) finalize the release and sampling protocols. During the 11 tracer and simultaneous flow visualization experiments, SF_6 and CF_3Br were released, sampled and analyzed for concentrations on the ridge. The meteorological data were archived and displayed in real-time by a system of onsite minicomputers. The real-time information on ambient meteorological conditions and the flexibility of releasing oil-fog and tracer gases at a wide variety of heights and locations allowed the field managers real-time control of the experiment in the selection of source positions to obtain useful information for model development purposes. The real-time meteorological feed-back was supplemented by near real-time lidar observations and an approximately 48-hour turnaround time on the photographs. Figure 49 illustrates the layout of the SHIS #2.

The SHIS #2 participants and their principal responsibilities were*:

- ERT
  - overall CTMD project management
  - field management and control (selection of experiment times, release locations, heights, etc.)
  - the 150-m and 60-m meteorological towers
  - site logistics (power, roads, security, weather forecasts, etc.)
  - quality assurance
- NOAA ARLFRO
  - tracer gas releases, sampling and analysis
  - oil-fog generator
  - the 10-m and 30-m towers
  - telemetry and meteorological data archive and display system
- NOAA WPL
  - lidar
  - two sonic anemometers and data acquisition system at the 150-m tower
  - two monostatic acoustic sounders
  - one doppler acoustic sounder
  - three optical anemometers
  - one tethersonde
- Morrison-Knudsen Company (under subcontract to ARLFRO)
  - oil-fog plume photographs (five positions)
  - video tapes of the plume

---

*The details of the SHIS #2 are presented in the "Work Plan for the Small Hill Impaction Study No. 2," ERT Document P-B348-620, September 1982.

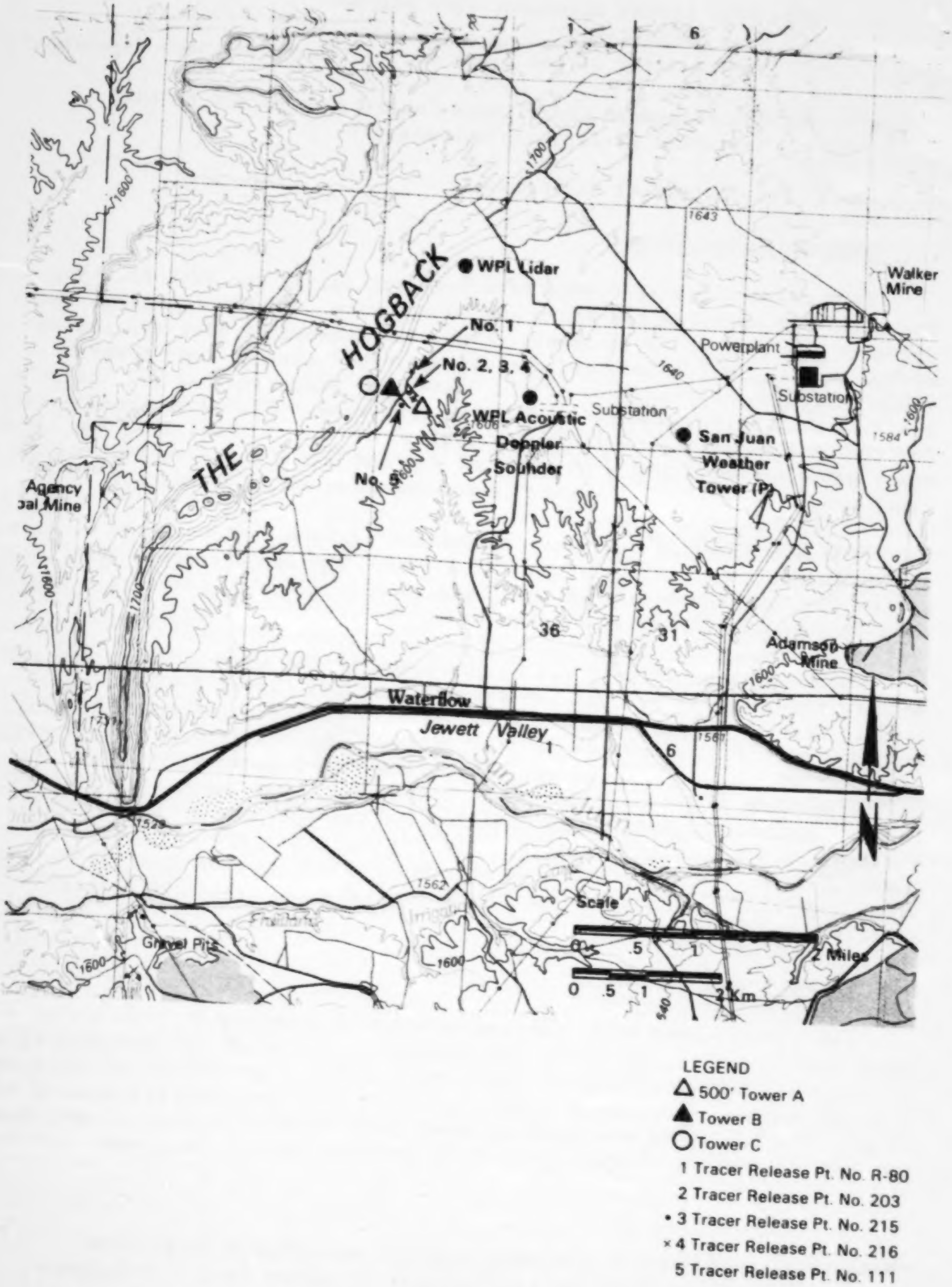
THE HOGBACK
WPL Lidar
No. 1
No. 2, 3, 4
No. 5
WPL Acoustic Doppler Sounder
Substation
San Juan Weather Tower (P)
Walker Mine
Powerplant
Substation
Agency
oal Mine
Adamson Mine
Waterflow
Jewett Valley
Gravel Pit
36
31
6
1
1643
1640
1584
1600
1700
1567
1562
1525
Scale
0 .5 1 2 Miles
0 .5 1 2 Km
N
LEGEND
△ 500' Tower A
▲ Tower B
○ Tower C
1 Tracer Release Pt. No. R-80
2 Tracer Release Pt. No. 203
• 3 Tracer Release Pt. No. 215
× 4 Tracer Release Pt. No. 216
5 Tracer Release Pt. No. 111

Figure 49. SHIS #2 field experiment layout.

- NOAA ATDL (under agreement with ARLFRO)
    - one tethersonde
    - video tapes of the plume during the first three experiments

- TRC Environmental Consultants (under subcontract to ERT)
    - external quality assurance audit

4.4.1 Meteorological Measurements

Meteorological Towers

Four meteorological towers were operated during the SHIS #2. ERT installed and operated the 150-m and 60-m towers. ARLFRO installed and operated the 10-m and 30-m towers. Tables 8A through D list the instruments, heights, and direct and derived measures* for the four towers. Table 9 provides definitions of the measures. Approximately 242 5-minute and 71 1-hour measures were archived in real-time. ARLFRO was responsible for the data collection and display system (see Section 4.4.2). The 150-m tower was also outfitted with a tracer gas and smoke release platform and winch assembly to allow releases to an elevation of approximately 75 m.

NOAA WPL provided two sonic anemometer systems that measured u, v, w, and temperature at a high frequency (20 Hz). The sonic systems were located at the 40-m and 5-m levels of the 150-m tower. WPL also provided a separate data logging system to archive the sonic data.

The purpose of Tower A was to characterize the approach flow and the meteorological conditions at the release heights. Tower B (30 m) was located west of the main road toward the base of the Hogback to document changes in flows and turbulence intensities in this region of highly distorted flow. Tower C (10 m) was located at the windward side of the top of the Hogback to document the wind, temperature, and turbulence field below 10 m over the hill crest. The 60-m Tower P was operated by PNM. ERT installed two wind sensors on it to help document the approach flow well upwind of HBR. PNM also operated other meteorological instruments in the area (Figure 50), data from which were available in real-time during SHIS #2 as half-hour averages.

Tethersondes

Two tethersondes were operated to measure temperature, horizontal wind speed and direction, pressure, and humidity. One sonde was operated by ATDL to characterize meteorological conditions within a few meters of the source. A second sonde was operated by WPL to obtain vertical profiles east of the ridge. The WPL sonde was operated near Tower B until October 15 and near the doppler sounder through the end of the experiment. Data were recorded

---

*Measure is used here to indicate a direct measurement (e.g., the u-component of the wind) or a calculated parameter (e.g., turbulence intensity).

TABLE 8A. 150-M TOWER A INSTRUMENTS
(Tower base @ 1604m MSL)

							Elevator			
Height (m)	2	5	10	20	30	40	60	80	100	150
Props (10)	x	x	x	x	x	x	x	x	x	x
Cups (3)				x		x	x			
T (1)	x									
ΔT (9)		x	x	x	x	x	x	x	x	x
TF (2)		x				x				
Measures										
U, V, W	x	x	x	x	x	x	x	x	x	x
UX, VX				x		x	x			
S, D	x	x	x	x	x	x	x	x	x	x
SX, DX				x		x	x			
TF		x				x				
T	x									
DT, TC		x	x	x	x	x	x	x	x	x
SU, SV, SW	x	x	x	x	x	x	x	x	x	x
SD	x	x	x	x	x	x	x	x	x	x
SDX				x		x	x			
UW	x	x	x	x	x	x	x	x	x	x
WT		x				x				
ST		x				x				

TABLE 8B. 30-M TOWER B INSTRUMENTS
(Tower base @ 1619m MSL)

Height (m)	1	5	10	20	30
Props (3)		x		x	x
Cups (3)	x		x		x
T (1)	x				
ΔT (4)		x	x	x	x
Measures					
U, V, W		x		x	x
UX, VX	x		x		x
S, D		x		x	x
SX, DX	x		x		x
T	x				
DT, TC		x	x	x	x
SU, SV, SW		x		x	x
SD		x		x	x
SDX	x		x		x
UW		x		x	x

TABLE 8C. 10-M TOWER C INSTRUMENTS
(Tower base @ 1687m MSL)

Height (m)	2	5	10
Props (3)	x	x	x
T(1)	x		
ΔT (2)		x	x
Measures			
U, V, W	x	x	x
S, D	x	x	x
T	x		
DT, TC		x	x
SU, SV, SW	x	x	x
SD	x	x	x
UW	x	x	x

TABLE 8D. 60-M TOWER P INSTRUMENTS
(Tower base @ 1620m MSL)

Height (m)	9.1	18.3	59.7	61.0
Props (0)				
Cups (2)		x		x
T (1)	*			
Δ T (1)			*	
Measures				
UX, VX		x		x
SX, DX		x		x
SDX		x		x
T	x			
DT, TC			x	

*PNM Instruments

TABLE 9. DEFINITIONS OF THE MEASURES

U, V, W	Vector averaged wind components - props	m/s
UX, VX	Vector averaged wind components - cups	m/s
S, D	Scalar mean wind speed and direction - props	m/s, degree
SX, DX	Scalar mean wind speed and direction - cups	m/s, degree
TF	Fast Thermistor Temperature	°C
T	Slow RTD Temperature	°C
DT, TC	Slow RTD ΔT, and calculated T (T(2m)* + DT)	°C
SU, SV, SW	Turbulence Scales - sigma-u, sigma-v, sigma-w	m/s
SD, SDX	Sigma-theta (props), sigma-theta (cups)	degree
UW, WT	$\overline{U'W'}$, $\overline{W'T'}$	$(m/s)^2$, m/s °C
ST	Standard Deviation of TF	°C

---

* Or 1 m for the 30-m tower and 9.1 m for the 60-m tower.

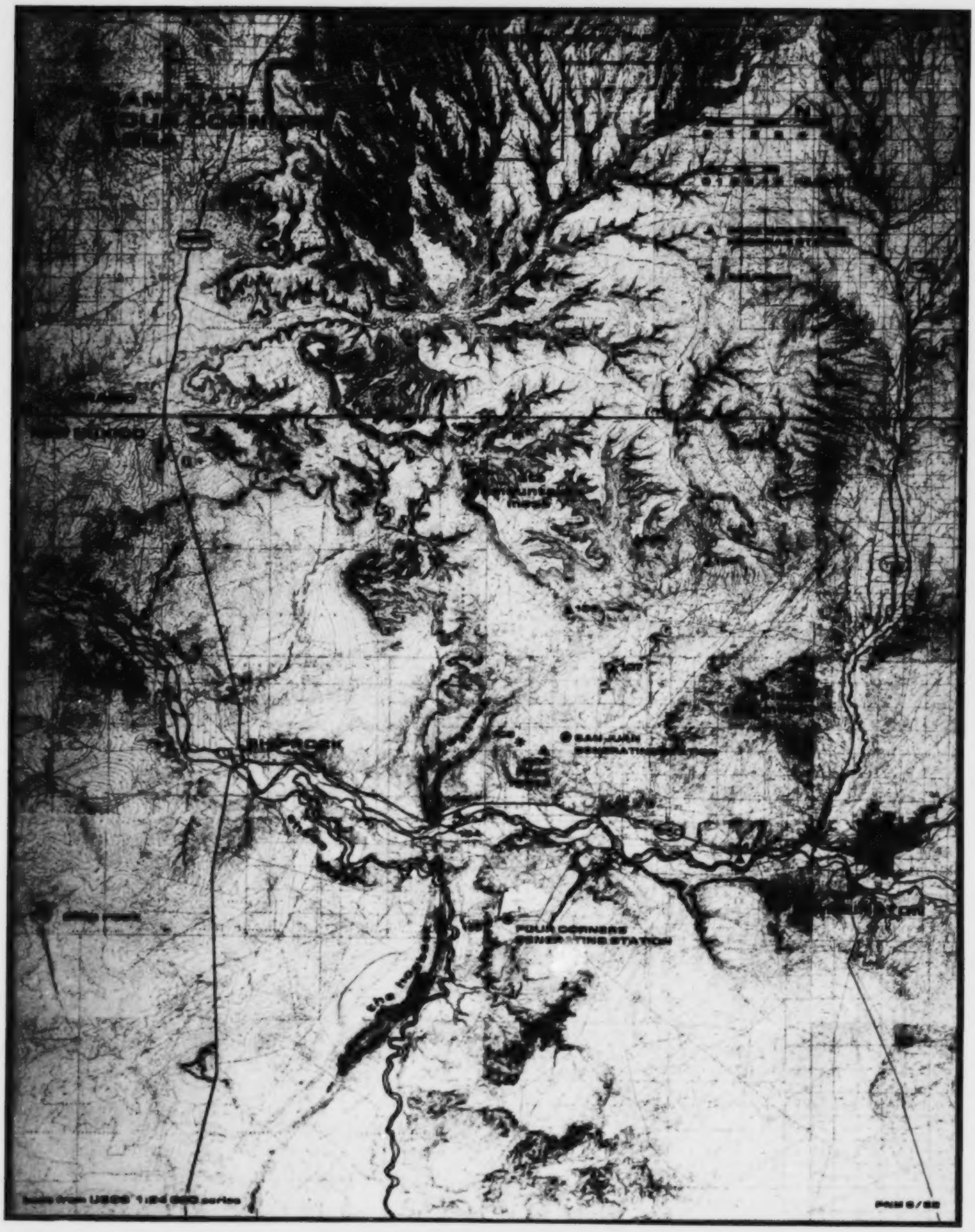
SHIPROCK
SAN JUAN GENERATING STATION
FOUR CORNERS GENERATING STATION

Figure 50. PNM air quality and meteorological monitoring sites.

on digital cassette tape for processing. Real-time paper copies were available to help guide the experiment.

Monostatic Acoustic Sounders

Two monostatic acoustic sounders provided data from which the vertical profile of turbulence and stability of the planetary boundary layer above the sounder were inferred. The two sounders were operated around the clock and the data were recorded on facsimile charts. This information was useful for experimental guidance by showing the development in time of the vertical structure of the lower atmosphere, particularly the arrival of air masses with different characteristics of temperature profile, shear, and turbulence.

One monostatic sounder was operated near Tower B upwind of the Hogback. A second sounder was operated in the vicinity of the 150-m tower, about 800 m east of the ridge.

Doppler Acoustic Sounder

The doppler acoustic sounder measured the vertical profile of the horizontal wind velocity in the planetary boundary layer above the sounder. Vertical resolution was 15 m with adequate signals to a height of typically 1 km. The doppler acoustic sounder was installed about 2 km east of the targeted segment of the ridge in the vicinity of the Shiprock Substation (Figure 49).

Optical Crosswind Anemometers

An optical crosswind anemometer measures the path-averaged wind across the line-of-sight path between a transmitter and receiver. Three were used in the SHIS #2 (Figure 52).

4.4.2 Meteorological Data System (MDS)

NOAA ARLFRO provided a real-time Meteorological Data System (MDS) to acquire, process, display, and store data. Figure 51 depicts the component structure of the system. Operating continuously during each experiment, the MDS sampled the 86 meteorological sensor inputs, calculated the derived measures, and displayed selected parameters and profiles. Data from the 10-m, 30-m and 60-m towers were transmitted by ARLFRO radio links. The 150-m tower data were transmitted by shielded signal cable.

Additional meteorological data were available from the PNM stations in the area. The stations of particular relevance are located on top of the Hogback; station 103 is about 5 km SW of the experiment area, and station 105 is just to the north of the experiment area. The PNM data were available as half-hour averages, which were intercepted from the PNM RF communications links at the 60-m tower and telemetered by ARLFRO's radio link to the command post near the 150-m tower, where they were displayed on a line printer at each half-hour scan.

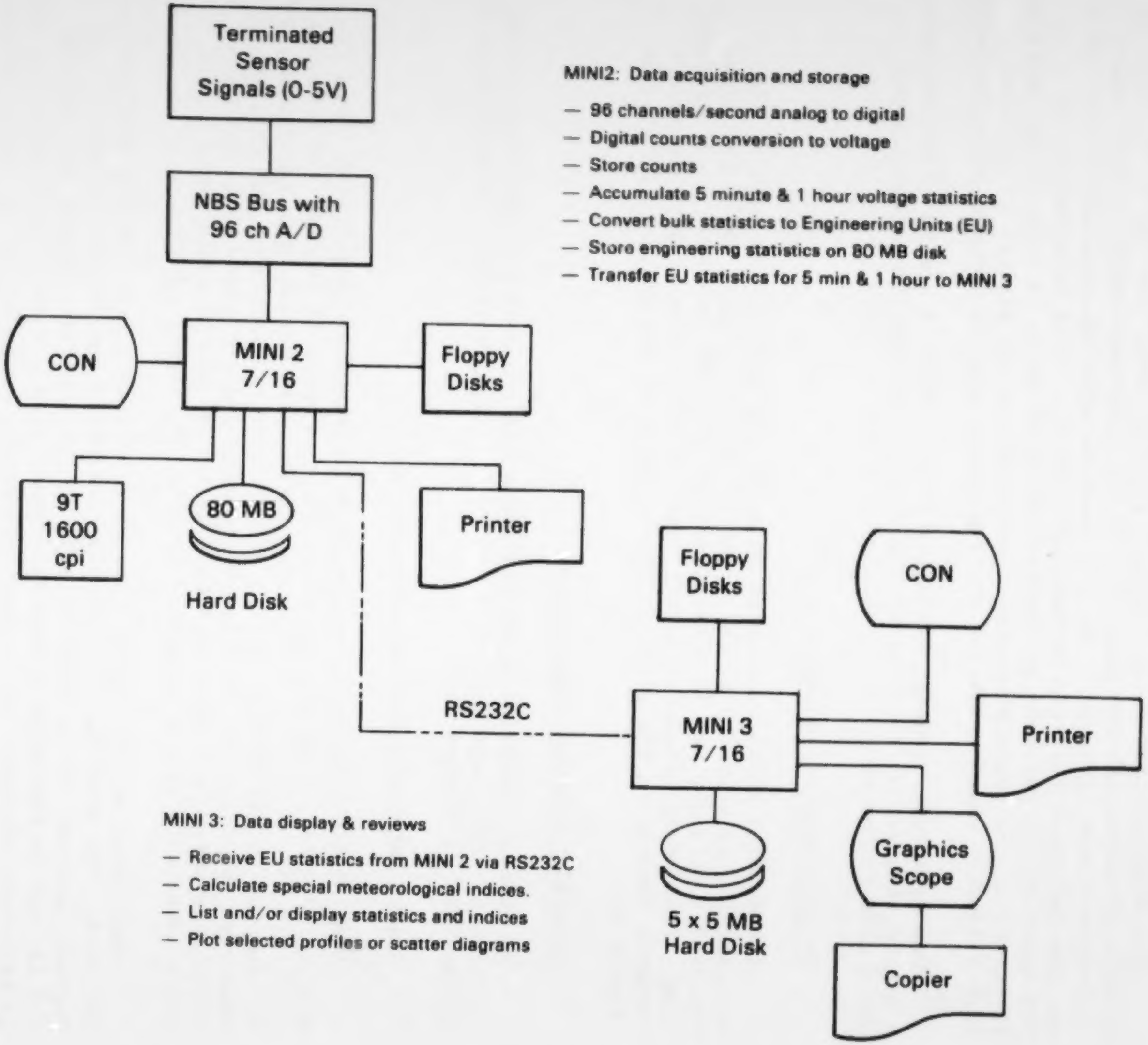
Terminated Sensor Signals (0-5V)
NBS Bus with 96 ch A/D
CON
MINI 2 7/16
Floppy Disks
9T 1600 cpi
80 MB
Hard Disk
Printer
MINI2: Data acquisition and storage
— 96 channels/second analog to digital
— Digital counts conversion to voltage
— Store counts
— Accumulate 5 minute & 1 hour voltage statistics
— Convert bulk statistics to Engineering Units (EU)
— Store engineering statistics on 80 MB disk
— Transfer EU statistics for 5 min & 1 hour to MINI 3
RS232C
Floppy Disks
CON
MINI 3 7/16
Printer
5 x 5 MB Hard Disk
Graphics Scope
Copier
MINI 3: Data display & reviews
— Receive EU statistics from MINI 2 via RS232C
— Calculate special meteorological indices.
— List and/or display statistics and indices
— Plot selected profiles or scatter diagrams

Figure 51. Meteorological data aquisition system.

4.4.3 Tracer Gas Release, Sampling and Analysis

Tracer Release System

Tracer releases were made from the 150-m tower and from locations on the three roads east of HBR. The roads were culverted, graded and graveled to support the 150-ft crane that lifted the oil-fog generator and the tracer gas tubes. Two tracer gases, SF_6 and CF_3Br, were released at different heights from the tower or the boom of the mobile crane. The SF_6 release was co-located with the oil-fog release and dispersed from a common nozzle. Occasionally, the SF_6 and oil-fog were released from the tower while the CF_3Br was released from the crane at a different location.

The SF_6 and CF_3Br tracer gases were stored in individual compressed gas cylinders at ground level. Piping carried each gas through a linear mass flow meter (LFM) system to the point of discharge into the atmosphere. A time history of each tracer release was used to describe the rate and quantity of release of tracer. The LFM measured and displayed the rate of gaseous tracer discharge via real-time digital display, the total amount of gas discharged via a digital counter, and the analog output voltage directly proportional to the flow rate. The voltage was logged and monitored on a strip chart recorder. Pre- and post-test release weights of gas tracer cylinders were measured by certified scales. Beginning and ending times of tracer release and the time and character of any deviations from the design rate-of-release were logged.

Tracer Sampling

Tracer samples were collected in 2-liter Tedlar bags at about 110 locations on the ridge. ARLFRO operated 125 samplers during each approximately 8-hour experiment. Twenty samplers were used to get 10-minute averages at five locations (4 samplers x 12 bags = 48 10-minute samples for each of the five locations). The remaining 105 were used to get 1-hour samples. Two of the 1-hour samplers were operated on the 30-m tower and one on the 10-m tower.

The bag samples were collected by means of modified EMI AQSIII or similar type of air sampler. Each sampler used 12 separate pumps, bags, and external tubes to draw in ambient air to fill the individual 2-liter Tedlar bags. The system was battery powered and electronically programmed in function and timing. Time was set and maintained by a crystal-controlled digital clock accurate to within 1 minute per month. Beginning and ending sampling times for the individual (sequential) whole-air samples were controlled by this clock. The actual local time (MDT) for beginning of the sampling sequence (in each unit) was preprogrammed during servicing by sampling team technicians within about 20 hours prior to the start of each experiment.

The sampler locations (Figure 52) were selected by ERT scientists on the basis of the June preliminary flow visualization experiments, the FMF wind tunnel and tow-tank simulations, and the meteorological data collected by PNM. Tables 10 and 11 summarize the characteristics of the sampling grid. The sampler locations were selected to provide the widest horizontal

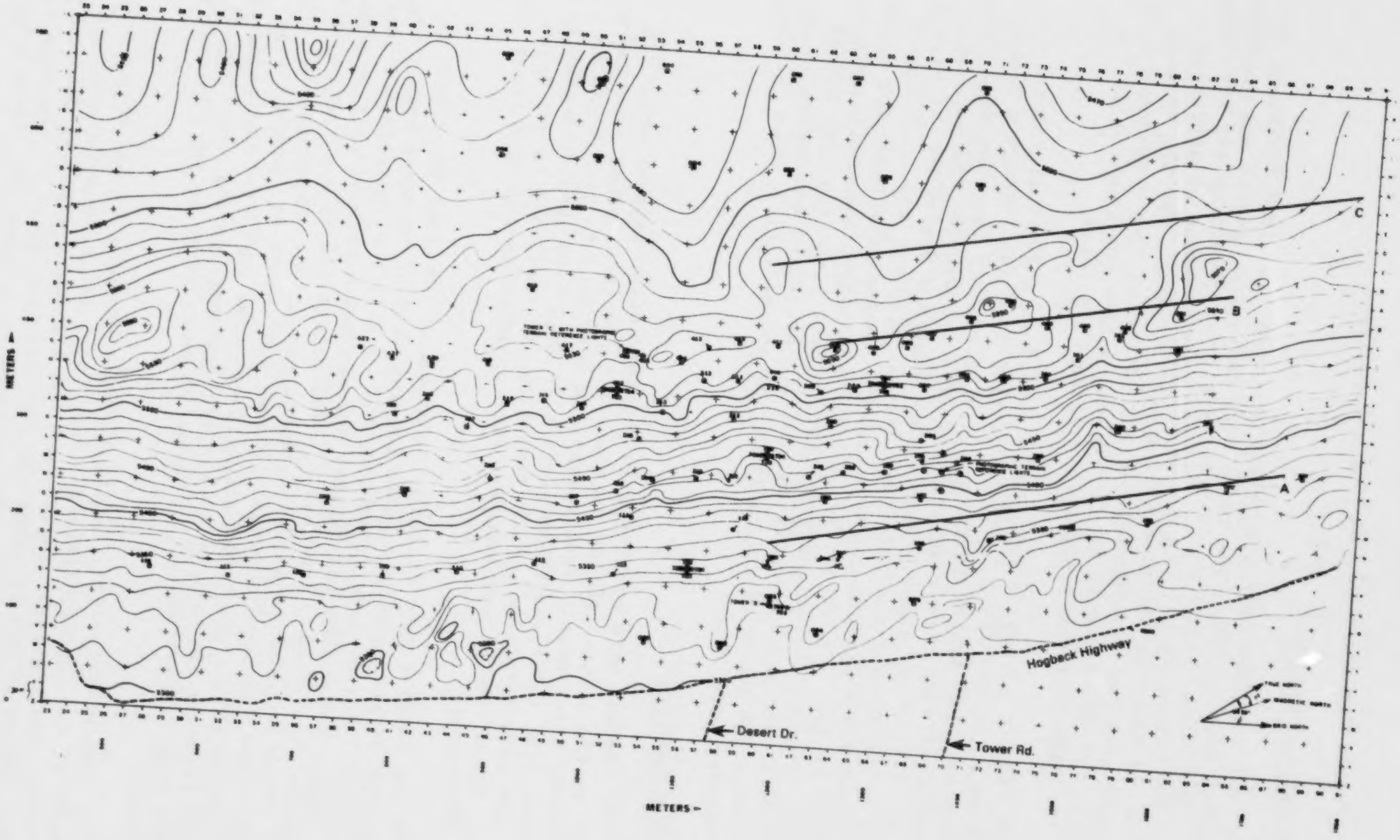
C
B
A
Hogback Highway
Desert Dr.
Tower Rd.
METERS
METERS

Figure 52. SHIS #2 tracer sampler locations and optical anemometer paths A, B, and C (approximate).

TABLE 10. PRIMARY SAMPLER LOCATIONS

A. Four Primary Sampler Rows on Windward Face of HBR

- #1 is ~10 m above the base of Tower B
  - 16 locations centered (approx) on Tower B (60-series stakes)
  - 80-m horizontal spacing covering 1200 m
- #2 is ~25 m above #1
  - 17 locations centered (approx) on Tower B (60-series stakes)
  - 40-m horizontal spacing out to 200 m, ~80-m spacing to approx 460 m from center; total range is 920 m.
- #3 is ~25 m above #2
  - 21 locations centered (approx) on Tower B (60-series stakes)
  - 40-m horizontal spacing covering 800 m
- #4 follows "crest"; mean height is ~10 m above #3
  - 22 locations centered (approx) on Tower B (60-series stakes)
  - nominal 40-m spacing covers 860 m

B. Three Secondary Rows on "Windward" Face of HBR

- #1 lies among hillocks at base of HBR
  - 5 samplers centered on Tower B
  - middle is at Tower B; adjacent 2 are atop hillocks near the road; 2 "ends" are in low areas adjacent to these.
  - row covers 280 m
- #2 lies between primary rows #1 and #2 (~13 m above #1)
  - 4 samplers centered (approx) on Tower B
  - 100-m spacing covers 300 m
- #3 lies between primary rows #2 and #3 (~13 m above #2)
  - 4 samplers centered (approx) on Tower B
  - 100-m spacing covers 300 m

C. Two Lee-Side Rows

- 6 samplers in each row
- centered near Tower B (60-series stakes)
- 100-m spacing along and between rows
- covers 500 m along each row
- covers out to 280 m beyond crest

TABLE 11. ADDITIONAL SAMPLERS

A. Co-located Samplers: two locations along center of grid: one on primary row #1, and one on primary row #3 (10 m and 60 m above the base of Tower B, respectively).

B. 10-minute Samplers: five locations: one at grid center along primary row #2; two along primary row #1, 80 m to either side of center; two along primary row #3, 280 m apart, centered 20 m south of grid center.

C. Background Samplers: one on the east side of Waughan Arroyo; one near the doppler acoustic radar near the substation on the high ground east of the east arroyo.

D. "Edge" Samplers: one to the north of the grid on the road up to the top of HBR beyond the lidar; one to the south where the San Juan River flows through a gap in the ridge.

E. Elevated Samplers: one on Tower C at ∿ 8 m; two on Tower B at ∿ 14 and 28 m.

coverage near the base of HBR and the highest resolution between half way up the ridge and the top. Three primary rows followed the height contours, and the fourth row defined its crest. Samplers were deployed less densely in the lee of the crest.

Tracer Analysis System

The Tedlar bag samples were analyzed for SF_6 and CF_3Br by electron-capture gas chromatography. Eight automated adaptations of 1972 Lovelock prototype gas chromatographs were used to set up a gas lab (Figure 53) in Farmington. The functional steps of the analysis are shown in Figure 54. The laboratory analysis process had a sample bag check-in, an assignment to a particular GC and subsequent analysis, and the output of an area proportional to gas tracer concentration. These areas, along with measurements of pressure, temperature, and physical constants, permitted calculations of tracer concentrations. The calibrated response of individual GCs was checked by injections and analyses of "known standard" reference mixtures of the tracer gases instead of the unknown sample bag mixtures.

4.4.4 Flow Visualization

Oil-Fog Releases

The generation and release of oil-fog for lidar, visual, and photographic observations were accomplished by the injection of corvus oil into the exhaust of a small turbine engine. The rate of oil injection, and the ensuing fog density, were coordinated by the field operations director. Fifty-five gallon oil drums and pumps provided oil to the generator. The rate of pumping was monitored by a liquid rate-of-flow meter and was adjusted by means of a valve. The operator recorded the start and end times, the indicated oil flow rates, and any alterations.

Lidar Sampling

The plume-mapping lidar (or laser radar) scanned vertically through the plume at several distances downwind from the source to produce three-dimensional data on the fraction of light backscattered to the lidar by particles within the plume. Plume position, dispersion, shape, and proximity to terrain will be calculated as a function of time from processed data. The lidar transmitter is a frequency-doubled Nd:YAG* laser emitting pulses in the green portion of the spectrum at rates up to 10 Hz. Vertical scans through the plume can be completed at a typical rate of two per minute. The slower ruby laser used at SHIS #1 was installed as a back-up in case of unanticipated failure of the Nd:YAG laser.

---

*Nd:YAG denotes a laser using an Yttrium-Aluminum-Garnet crystal doped with Neodimium.

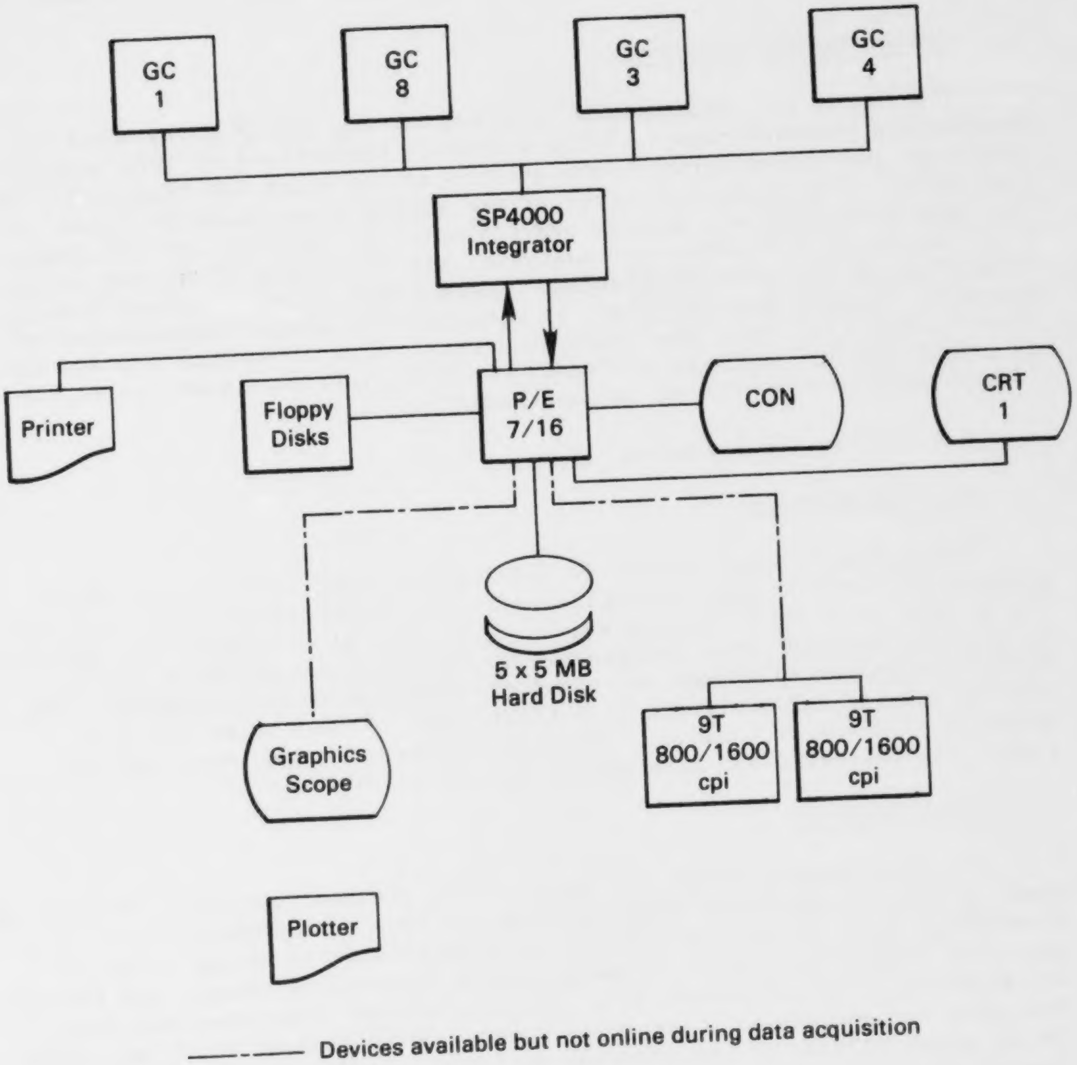
GC 1
GC 8
GC 3
GC 4
SP4000 Integrator
Printer
Floppy Disks
P/E 7/16
CON
CRT 1
5 x 5 MB Hard Disk
Graphics Scope
9T 800/1600 cpi
9T 800/1600 cpi
Plotter
Devices available but not online during data acquisition

Figure 53. Gas chromatography data acquisition system.

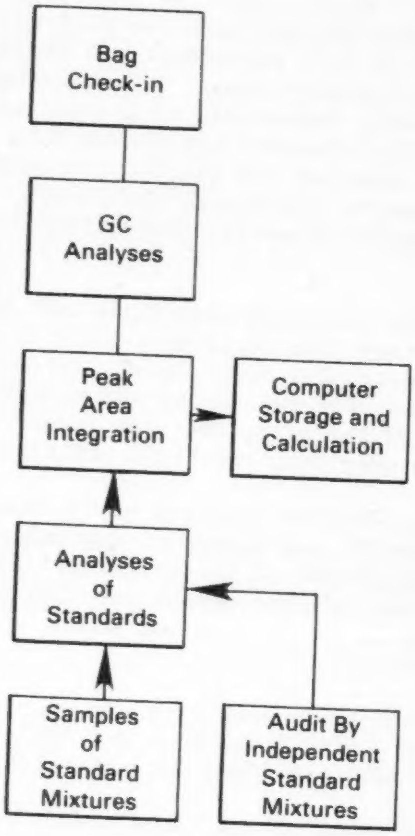
Bag
Check-in
GC
Analyses
Peak
Area
Integration
Computer
Storage and
Calculation
Analyses
of
Standards
Samples
of
Standard
Mixtures
Audit By
Independent
Standard
Mixtures

Figure 54. Tracer gas analysis system.

The lidar recorded data on 9-track digital magnetic tape for later processing. Some real-time information was available on plume behavior for experimental guidance. The lidar was located about 2 km NNE of the tracer release area (Figure 49).

Photography Program

Morrison-Knudsen Company, Inc., as subcontractor to NOAA ARLFRO, was responsible for all photographic work for SHIS #2. The work consisted of continuous video tape of each experiment and photographs taken every five minutes from each of five positions. The photographs were taken during all periods of smoke release, regardless of tracer release or other project considerations. Morrison-Knudsen was responsible only for photography and video taping; ARLFRO operated the oil-fog generator, and ERT provided a 60-inch carbon arc lamp to illuminate the plume. The arc lamp was located just north of the doppler acoustic sounder (Figure 49), east of the main arroyo.

Three photography positions were fixed and two were roving. One of the fixed positions was the 120-m level of the 150-m tower. The other two fixed photographers were positioned to the north and south of the release east of the base of the ridge. The two roving photographers chose positions that allowed photography of the plume near the ridge top or of other meteorological phenomena not in view from the fixed positions.

The photographic archive consists of 11 binders of color slides covering experiments 1 through 15, one binder of supplemental slides, and 24 two-hour video tapes. During periods of smoke release, and in the absence of other technical difficulties, 60 photographs were taken each hour (five photographers each taking 12 photographs per hour). The photography program is summarized as follows:

- five 35-mm cameras with data backs to document time of photo, etc.
- color film (Kodak Ektachrome ASA 200)
- one videocamera equipped with Starlight-scope
- locations:
    - 120-m level of the 150-m tower
    - north of the release area east of the ridge base
    - south of the release area east of the ridge base
    - two roving photographers to get best pictures of plume dynamics
- five-minute exposure (12 photos/hour/camera) at night; shorter exposures in sunlight but same frequency
- turnaround - slides within 48 hours
- lighting - carbon arc lamp revolving once every 30 seconds.

4.5 Preliminary Field Study Results

4.5.1 Summary of HBR Data Base

The three flow visualization and 11 combined flow visualization and tracer experiments at HBR have produced an extensive data base that covers a wide variety of dispersion conditions and concentration patterns for modeling purposes. SF_6 was released (Table 12) during 91 experimental hours and CF_3Br during 88 hours. The tracers and oil-fog were released at seven different locations during the course of SHIS #2 at elevations ranging from 5 m to 75 m. The release locations (Figure 49) varied from 333 m (R-80) to 800 m (Tower A) from the crest of the ridge.

Table 13 summarizes the number of hours with tracer releases and tracer sampling for each SHIS #2 day. The experiments typically started around midnight and lasted until after dawn. Approximately 80 1-hour average SF_6 and CF_3Br concentrations were produced every hour (Table 13). More than 7500 1-hour average surface-level concentrations of SF_6 and of CF_3Br were sampled and analyzed during SHIS #2.

Three samplers were suspended above the ground from the shorter meteorological towers; two hung at approximately 14 and 29 m on the 30-m tower at the base of the ridge, and one at about 7.5 m on the 10-m tower on the crest. These samplers yielded more than 230 additional 1-hour concentrations of either tracer gas. At each of five surface sampling sites, four sampler boxes were set out to gather 10-min samples on which to base assessment of concentration variability during periods less than 1-hour long. Approximately 1600 10-min samples of each tracer gas were analyzed.

ARLFRO has prepared the SHIS #2 tracer gas data base. A tape of concentration data and isopleth maps (hard copies and slides) have been given to the EPA Project Officer. After he witheld a randomly selected subset of the data base for independent model testing (see Section 5.1), a tape and the maps of the remaining tracer data were given to ERT. This "learning" tracer gas data base has been used for the analyses presented in the remainder of this report.

As discussed in Section 4.4, the tower meteorological data were archived in real-time via the MDS. During the first few experiments of SHIS #2, it became apparent that the meteorological data contained "noise." Subsequent investigations during and after the experiment have suggested four types of noises: (1) large "hits" or "spikes" which produced apparent full-scale voltages from the instruments, (2) "cross-talk" or "skips" between MDS channels such that signals from one channel were picked up by another channel, (3) a high frequency, apparently random low-voltage oscillation that was attributed to 60-cycle AC, and (4) an apparent 2- to 4-sec noise.

Figure 55 shows a plot of raw, unedited, 1-sec Tower A ΔT data (in counts) taken between 2200 and 2300 on October 22, 1982. The excursions to 0 and 4095 are evident. It is also evident that signals from one channel are being picked up by another channel. This channel-skipping appears as vertical lines within the band of traces on the plot, the lines being composed in this case of skips from channels 72 to 73, 73 to 74, etc. in general, although some scans, like those near minute 31, involve only channels 77 through 79 or some other subset of channels. Skipping is particularly frequent in minutes 53 to 55 of this hour.

TABLE 12. NUMBER OF SHIS #2 EXPERIMENTAL HOURS WITH TRACER GAS RELEASES AND CONCENTRATIONS

			Tracer Releases		Tracer Concentrations	
Experiment	Date	Oil-Fog	SF_6	CF_3Br	SF_6	CF_3Br
1	5	4	-	-	-	-
2	6	5	-	-	-	-
3	7	6	-	-	-	-
4	11	9	7	6	7	6
5	12	7	7	7	7	7
6	12-13	8	8	8	9	9
7	14	7	7	7	7	7
8	14-15	9	9	9	9	9
9	20	5	5	5	5	5
10	22	10	10	10	11	11
11	22-23	9	9	9	10	10
12	24	9	9	9	10	10
13	25	1*	-	-	-	-
14	25-26	10	9	8	12	12
15	28-29	11	11	10	12	12
TOTAL**		110	91	88	99	98

---

*Experiment 13 was terminated due to unfavorable weather.

**There are more hours of concentration data than there are of tracer release because samples obtained after the tracer releases were terminated were analyzed.

TABLE 13. SUMMARY OF TRACER CONCENTRATION DATA

		SF_6			CF_3Br		
Experiment	Date	One-Hour	One-Hour Tower	10-min	One-Hour	One-Hour Tower	10-min
4	11	523	13	108	487	13	101
5	12	497	21	103	496	21	103
6	12-13	695	18	120	696	18	119
7	14	527	18	95	526	20	82
8	14-15	659	23	189	666	23	186
9	20	393	10	62	396	10	62
10	22	842	23	165	839	23	168
11	22-23	798	28	215	795	28	211
12	24	765	23	134	764	23	135
14	25-26	936	26	214	919	26	214
15	28-29	930	28	209	918	28	209
Subtotals		7565	231	1614	7502	233	1590

Total SF_6 9410 Total CF_3Br 9325

GRAND TOTAL 18,735

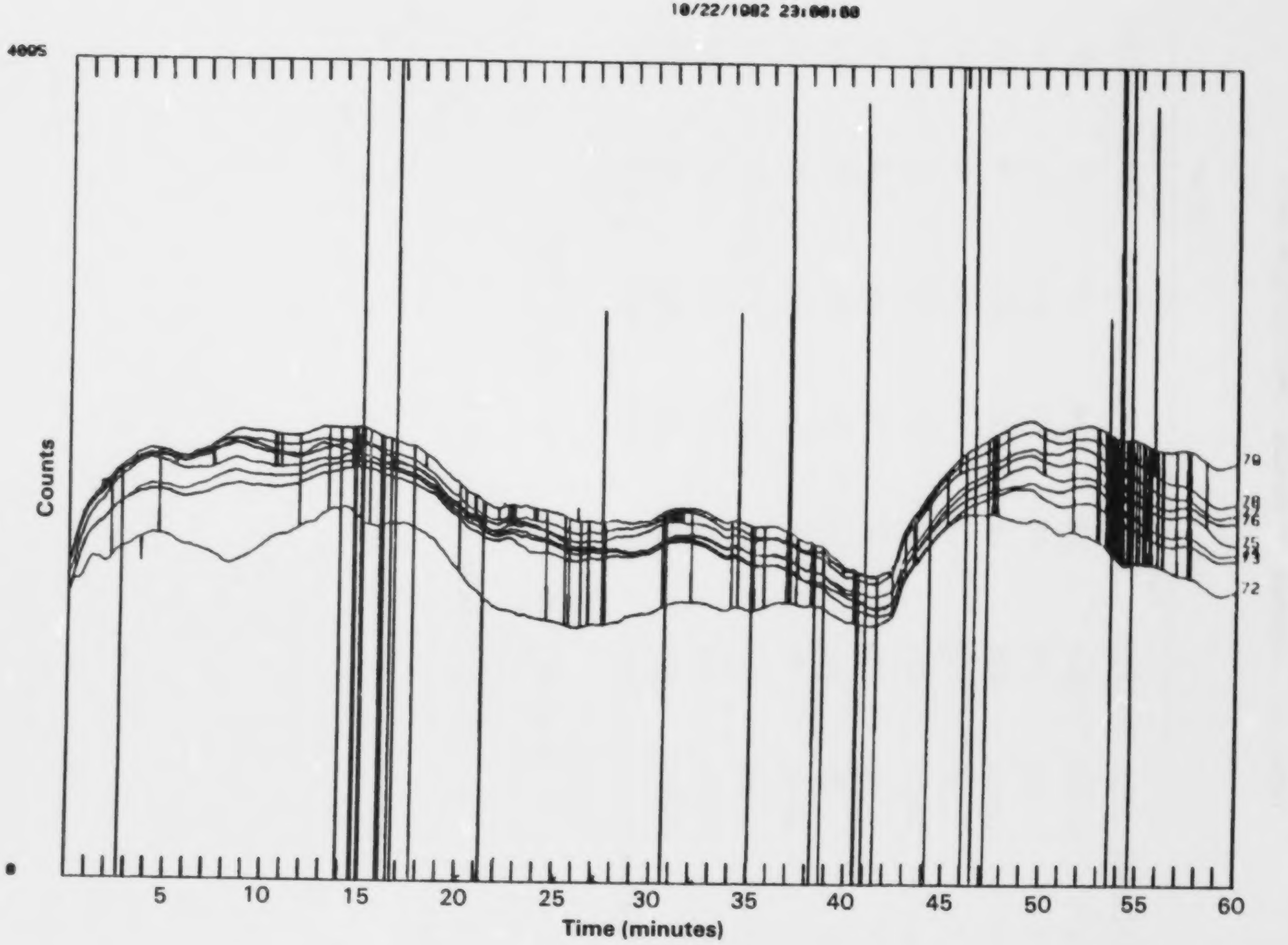

Figure 55. Raw Tower ΔT (counts) from 10 m to 150 m.

The "hits" and "skips" can be characterized as follows:

- When a hit strikes a channel (between 1 and 16) on a multiplexer/A-D board, it usually drives the counts to 0 (0.000 Vdc) or 4095 (5.120 Vdc). This hit will then appear on all subsequent channels (up to and including channel 16) on that board for that scan, although sometimes a hit that first appears as a 0 will be a 4095 in subsequent channels.

- There are two subclasses of hits, whose characteristics are sufficiently different that they may be manifestations of different phenomena.
  - The hit may not drive the counts to either limit but to some number like 19 or 23, which recurs in subsequent channels and may happen more than once in a few minutes. This sort of hit might result from dropped bits in the A-D conversion.
  - The hit may show a gradual change from a "good" value on one channel to bad values on subsequent channels, finally settling on a limit value (0 or 4095) after a few channels in the scan.

- A skip seems to put the datum from channel n + 1 (occasionally n + 2) into channel n. Once a channel skip occurs, all subsequent channels also skip to the next channel on that board. Channel 16 appears not to skip to channel 1 but to give correct values.

Due to these patterns of hits and skips, channel 1 yields the "cleanest" data on each board; channel 16 has the most hits, and channel 15 the most skips. As much as 30% of the data on channel 15 may be affected by these errors for some periods.

Both ARLFRO and ERT staff tried to alleviate the noise problems during non-experiment hours at the Hogback. Between experiments 8 and 9, the six 16-channel multiplexer boards were reconfigured so that none served instrument outputs from more than one tower, and additional grounding of the components of the control data collection system was done. These changes seemed to remove most of the problem with the 60-H_z noise and the 2- to 4-sec noise, which may in fact have been different ways of looking at the same phenomenon, but did not eliminate the big spikes and channel cross-talk or skipping.

ARLFRO and ERT scientists continue working on the hit and channel-skipping phenomena. Preliminary methods have been developed and implemented to filter the hits and skips. The effects of the 60-H_z noise are impossible to remove from the data. A procedure for isolating the 2- to 4-sec noise has been developed and tried on several periods of data, but no method has been developed for removing this noise from the data. The latter two types of noise have little effect on the average meteorological data but may degrade the turbulence statistics and covariances.

A first attempt to remove the hits and skips has been made by ARLFRO staff using data collected during the 17 hours selected for initial modeling and analysis (see Section 5.1). ARLFRO filtered the hits and skips, applied non-cosine response correction factors developed in 1978 by Dr. John F. Clarke* to the prop data, and converted the counts to engineering units. They have not yet investigated the 60-H_z and 2 to 4-sec noises, nor have they "recovered" any of the cross-channel data. Substantial work remains to refine and complete the tower meteorological data base.

Of the remaining SHIS #2 measurements, the WPL and ATDL tethersonde data have been processed and delivered. The WPL data include tables and plots of profiles of pressure, relative humidity, mixing ratio, wind speed, wind direction and potential temperature up to altitudes of about 375 m. The ATDL data include tabulations and plots of 15-minute averages and standard deviations of wind speed, wind direction, and the vector wind components, u and v, from the tethersonde flown near the smoke source. The WPL monostatic acoustic sounder data have also been delivered as photographs of the facsimile output from the sounder located near Tower A. The wind speed data from the three optical anemometers have been received from WPL as 10-min averages displayed in both graphical and tabular forms. The archive of photographs is also complete. No doppler acoustic sounder nor lidar data are yet available. Preliminary 20-minute average sonic anemometer data, excepting heat and momentum fluxes, are available from the real-time output for the 17 hours selected for preliminary analysis (see Section 5). WPL is currently reducing the sonic data.

In summary, the following data are currently (i.e., as of 31 May 83) available from the HBR experiment:

- SF_6 and CF_3Br concentrations and hourly average emissions data;
- Preliminary, edited tower meteorological data for the 17 hours;
- Unedited tower meteorological data;
- Tethersonde data;
- Monostatic acoustic sounder records;
- Optical anemometer data;
- Preliminary sonic anemometer data (taken from the real-time output in the field); and
- Complete photographic archive.

---

*These corrections were developed from wind tunnel experiments with modified R.M. Young wind component transmitters rather than with the Climatronics instruments used at CCB and HBR. The Young instruments have a vertical offset of several inches between the U and V arms, which reduces the interference of one with the other, whereas the Climatronics systems do not. Furthermore, the Young instruments were modified by a plumb-bob leveling device that altered the flow uniquely. Non-cosine corrections were developed for the Climatronics instruments by ERT for application to the CCB data-base (Greene and Heisler 1982) but were based on less extensive experimentation than Clarke's.

4.5.2 Overview of SHIS #2 Results

The flow visualization and tracer experiments at the Hogback have produced an extensive (still evolving) data base. The real-time experimental selection of release locations and heights based on the MDS output produced concentration patterns for a wide variety of dispersion conditions. These data will be used to evaluate and refine the modeling approaches developed with the CCB data base. Initial analysis of the 17-hour data base suggests that the concept of a critical dividing-streamline height is appropriate for stable flows toward HBR. Releases below H_c dispersed in the "blocked" flow and produced peak ground-level concentrations (GLC) on the windward face of the ridge. Releases above H_c dispersed in a flow that went over the ridge and produced peak GLC's near the ridge crest and on its lee side.

Figure 56 shows isopleths of hourly CF_3Br concentrations (χ/Q) measured during experiment 5 (October 12, 1982) between 0500-0600. A band of concentrations above 50 $\mu sec/m^3$ was observed from the ridge base to near its crest. The highest χ/Q of 387 $\mu sec/m^3$ was measured about 15 m uphill (sampler 105, see Figure 52) from the intersection of Hogback Highway and Tower Road. The tracer gas was released at location 203 at a height of 15 m. The calculated H_c was 47.9 m. Note that the CF_3Br dispersed up and over HBR while producing the maximum GLC at a ridge elevation roughly equal to the release height. This seems to be different from the CCB results, which show that releases below H_c tend to disperse along the sides of the hill rather than up and over. An initial analysis of the HBR data suggests that tracer gases released below H_c are often eventually transported up and over.

Figure 57 shows CF_3Br concentration (χ/Q) measured during experiment 15 (October 29, 1982) between 0200 and 0300. The tracer gas was released from the 40-m level of Tower A, above the calculated H_c of 24.4 m. Only a few non-zero GLC's were measured, and these occurred on the lee side of the ridge.

Roughly eight concentration patterns were observed during SHIS #2:

1. Tracer gas distributed front and back of HBR
2. Primarily front side
3. Primarily lee side
4. Along upwind base
5. Near top
6. Near top and on lee
7. Spots
8. Nothing

Figure 56 exemplifies pattern 2 and Figure 57 exemplifies pattern 3 (or 7). Other examples are given in subsection 4.5.4.

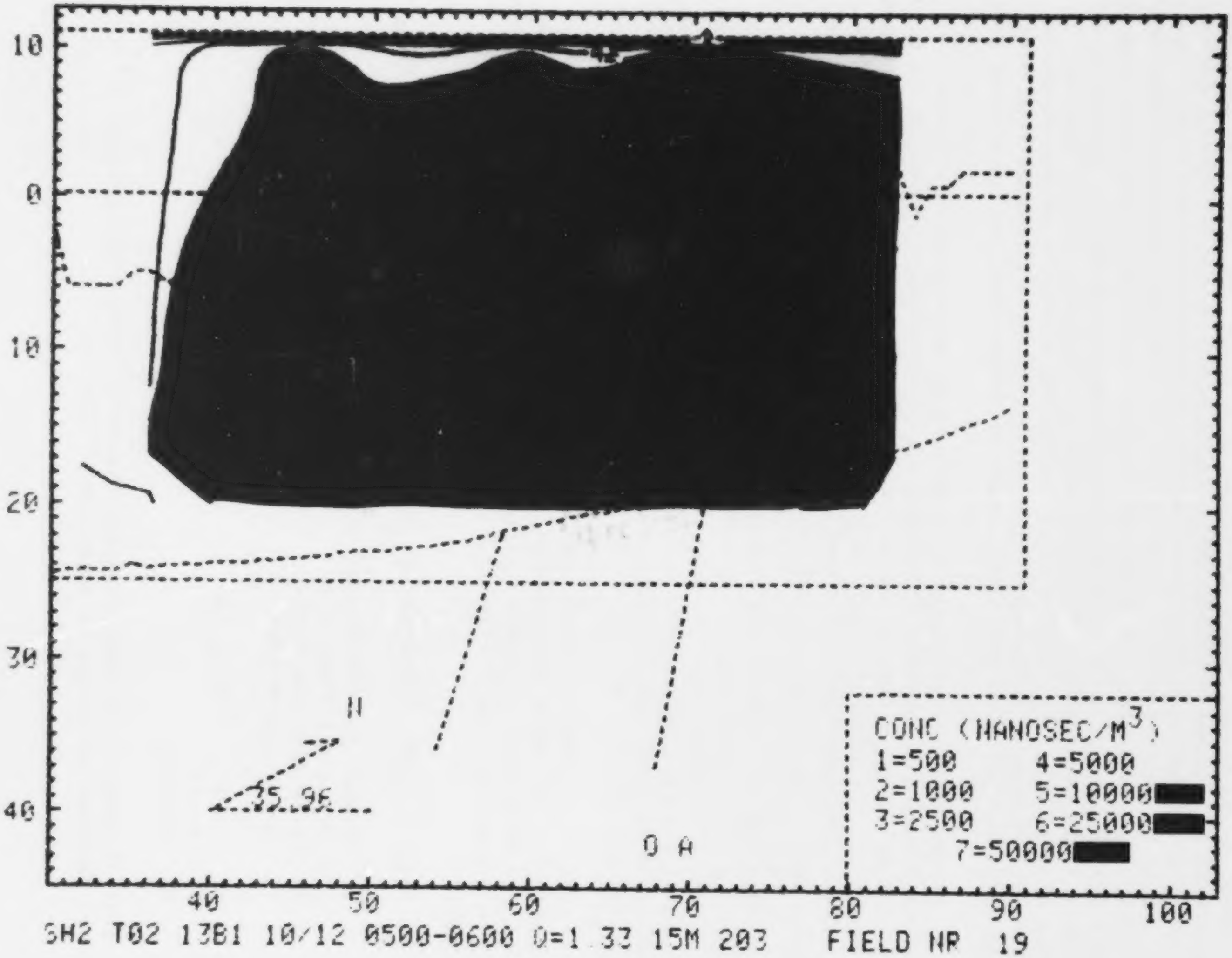

Figure 56. Hourly CF_3Br concentrations (10/12/82, 0500-0600 MDT).

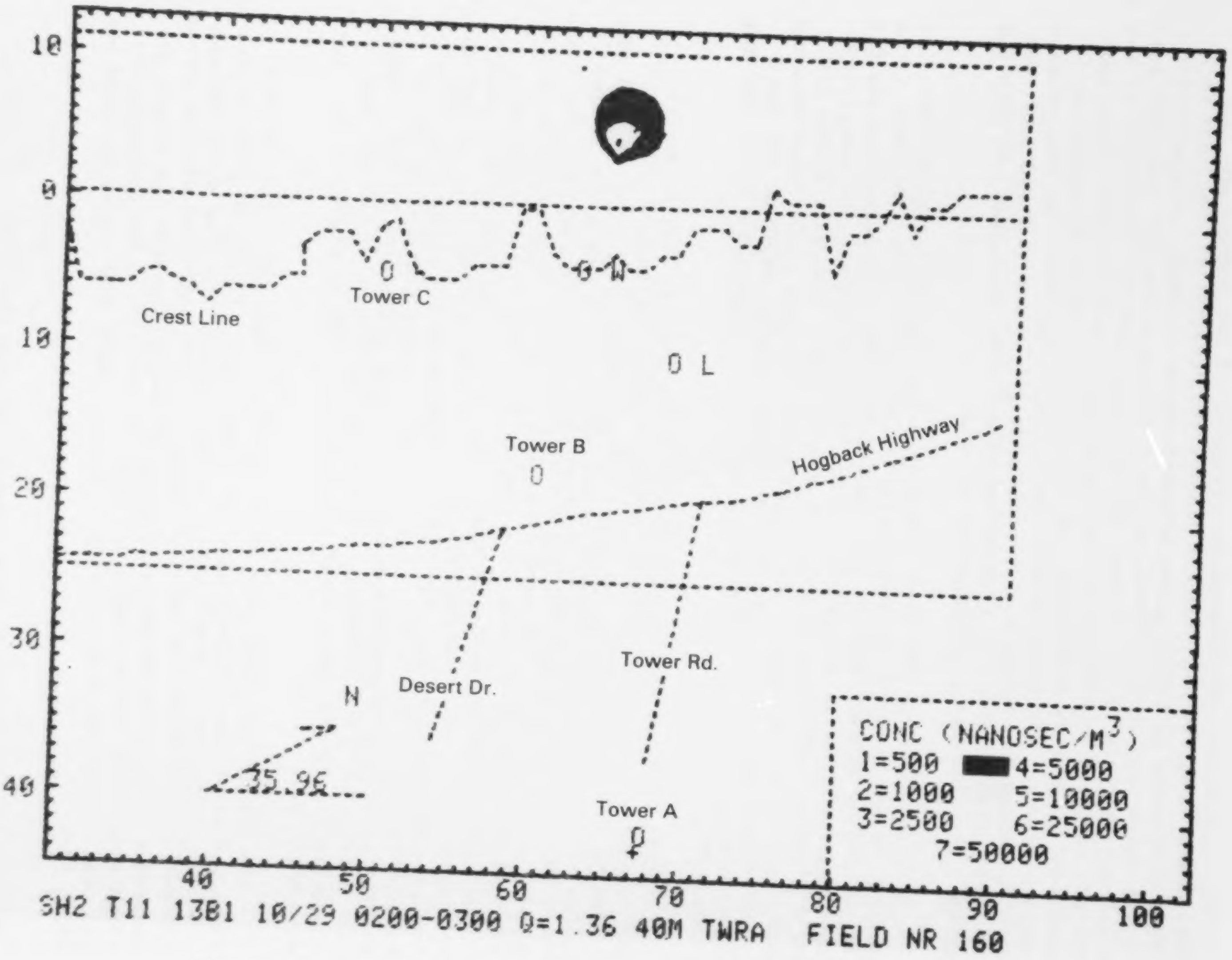

Figure 57. Hourly CF_3Br concentrations (10/29/82, 0200-0300 MDT).

4.5.3 Comparison with SHIS #1 Results

The essentially two-dimensional character of the Hogback and the three-dimensional character of CCB dictate the behavior of the flows that affect dispersion of tracer gases released upwind of these terrain features. Despite these very basic differences, an analysis of the CCB data base and an initial analysis of the 17-hour HBR data base show the importance of the critical dividing streamline in discriminating between types of flows and subsequent dispersion conditions. At CCB, releases below H_c tended to remain horizontal and travel around the sides of the hill. At HBR, releases below H_c tended to stagnate, producing high GLC on the windward side, but then were often* eventually transported up and over the ridge. At both CCB and HBR, releases above H_c flowed up and over.

At this time only the 17-hour HBR data base has been analyzed and modeled, so any results are preliminary and not conclusive. However, it is interesting to compare some of the results from HBR with those from the CCB experiments. Table 14 summarizes the five highest χ/Q and the associated meteorological conditions observed at HBR and CCB. Generally higher χ/Q were measured at the ridge. The higher concentrations at HBR were measured at elevations at least as high as the release height, while at CCB the higher concentrations were frequently measured at elevations lower than the release height.

Figure 58 shows a plot of maximum χ/Q vs. $1-H_c/z_r$ for the entire CCB data base and for the 17-hour HBR data base. The higher χ/Q at CCB tended to occur when $z_r \approx H_c$, while at HBR the higher χ/Q were measured when $z_r \lesssim H_c$. Since the ridge is basically two-dimensional, the higher values could be explained by the highly variable and generally stagnant flow below H_c and, if the average wind were directed toward the ridge, the tracer gas would be transported directly to a sampler near the release elevation. Flows below H_c at CCB tended to remain essentially horizontal with some uphill transport and generally preferred one side of the hill. Figure 59 shows a concentration (ppt) map for CCB experiment 206, hour 8 (the hour with the highest χ/Q of 164). The pattern of concentrations is fairly horizontal and is elongated northward along the north side of CCB. Compare this pattern with the patterns in Figure 56 and Figure 77 (in the next subsection). At HBR there seems to be eventual uphill transport for flows even below H_c.

The higher concentrations at CCB occurred when the transport wind direction was close to the stagnation streamline. Figure 60 shows a plot of the CCB χ/Q vs. $\Delta\theta/i_y$, where $\Delta\theta/i_y$ is the ratio of the wind angle between the actual wind direction and the stagnation wind direction divided by the crosswind turbulence intensity. A large value implies that the tracer gas plume would have little chance of "hitting" the hill. The data show that the peak GLC values occurred when $\Delta\theta/i_y \approx 1$. Small GLC values occurred when $\Delta\theta/i_y \geq 5.0$.

---

*Not all releases below H_c were transported over the ridge. If the winds near the release had a substantial component parallel to the ridge, then the tracer stayed below the crest.

TABLE 14. FIVE HIGHEST χ/Q OBSERVED AT HBR* and CCB

Experiment		Hour	χ/Q (μsec/m^3)	z_r(m)	$u(z_r)$(m/s)	H_c(m)	Sampler Elevation(m)
HBR	4	4	117	20	1.3	26	29
	5	2	83	15	1.3	32	23
	5	6	387	15	1.2	48	32
	11	3	167	20	1.1	54	53
	14	4	104	20	1.7	18	20
CCB	206	6	115	35	1.8	37	25
	206	8	164	35	1.8	37	25
	211	5	98	20	2.3	25	30
	214	3	103	24	1.6	43	0
	214	7	120	24	2.7	11	30

---

*Based on the 17-hour data base. The highest χ/Q observed at HBR was 549 μsec/m^3 during 0600-0700 on the 14th.

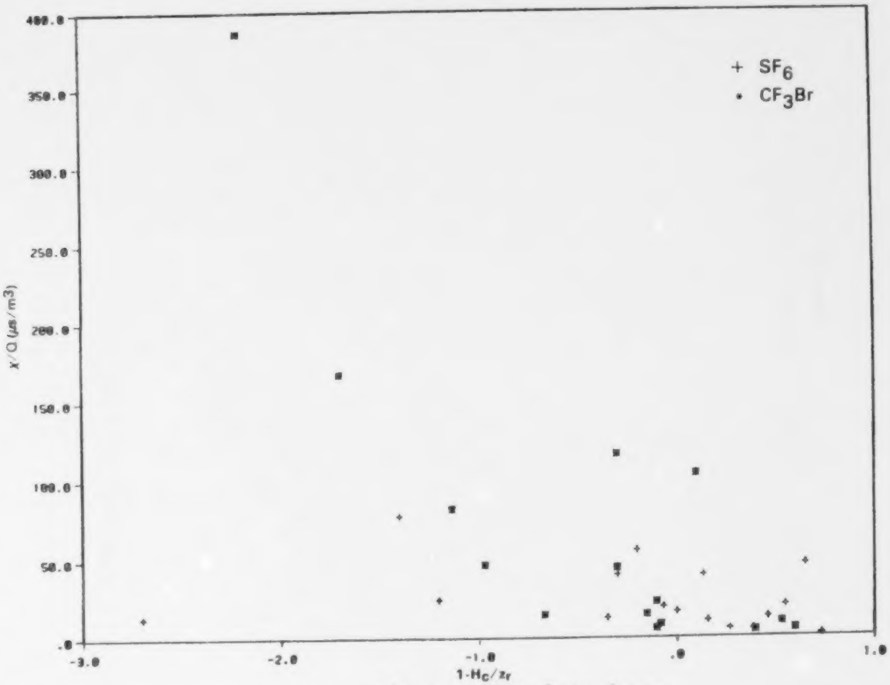

a. 17-hour HBR data base.

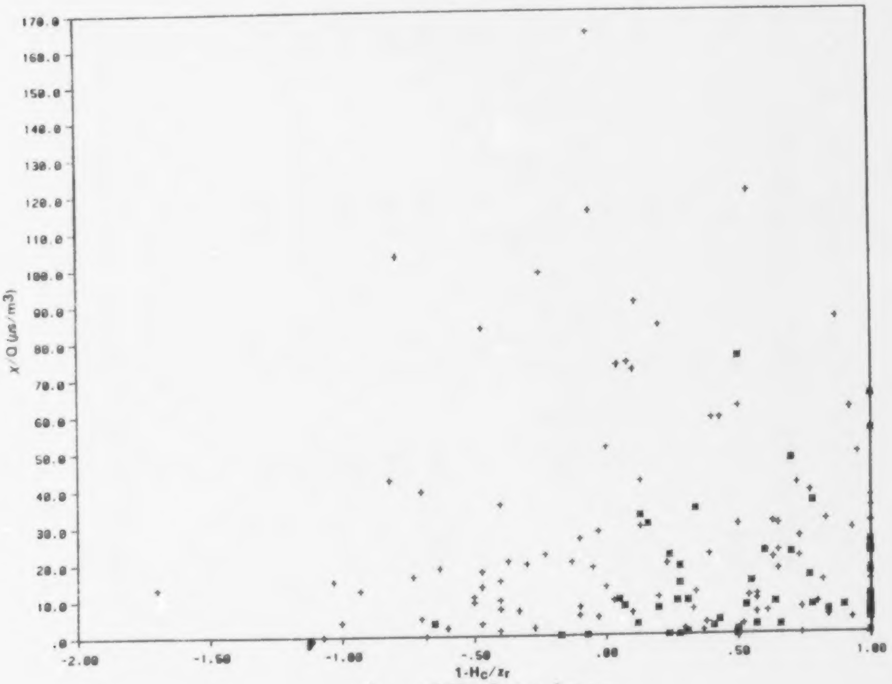

b. CCB data base.

Figure 58. Maximum hourly χ/Q ($\mu sec/m^3$) vs. $1-H_c/z_r$.

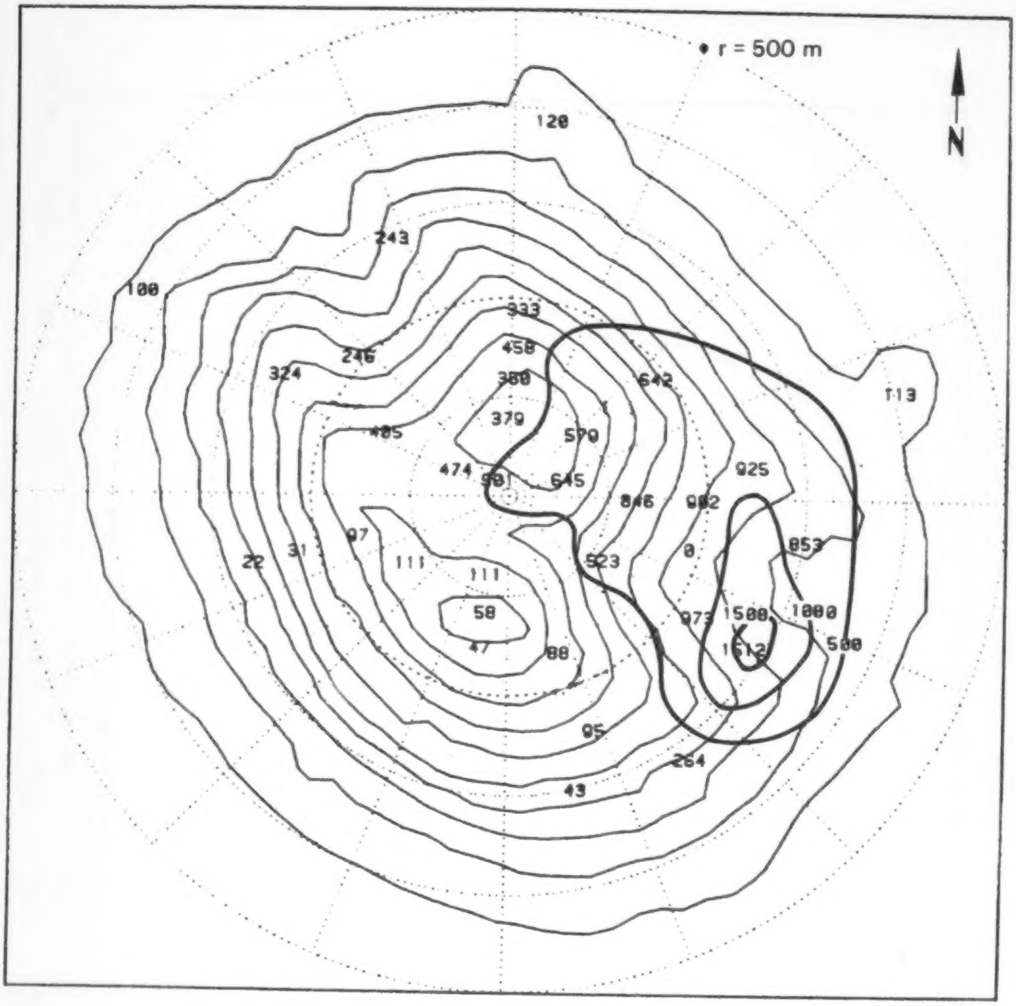

Figure 59. Observed SF_6 concentrations (ppt) for CCB Experiment 206, hour 8 (0700-0800 MST). Source: r = 595.9 m, $\theta = 123.6^\circ$, net height = 29.5 m, Q = .062 g/s.

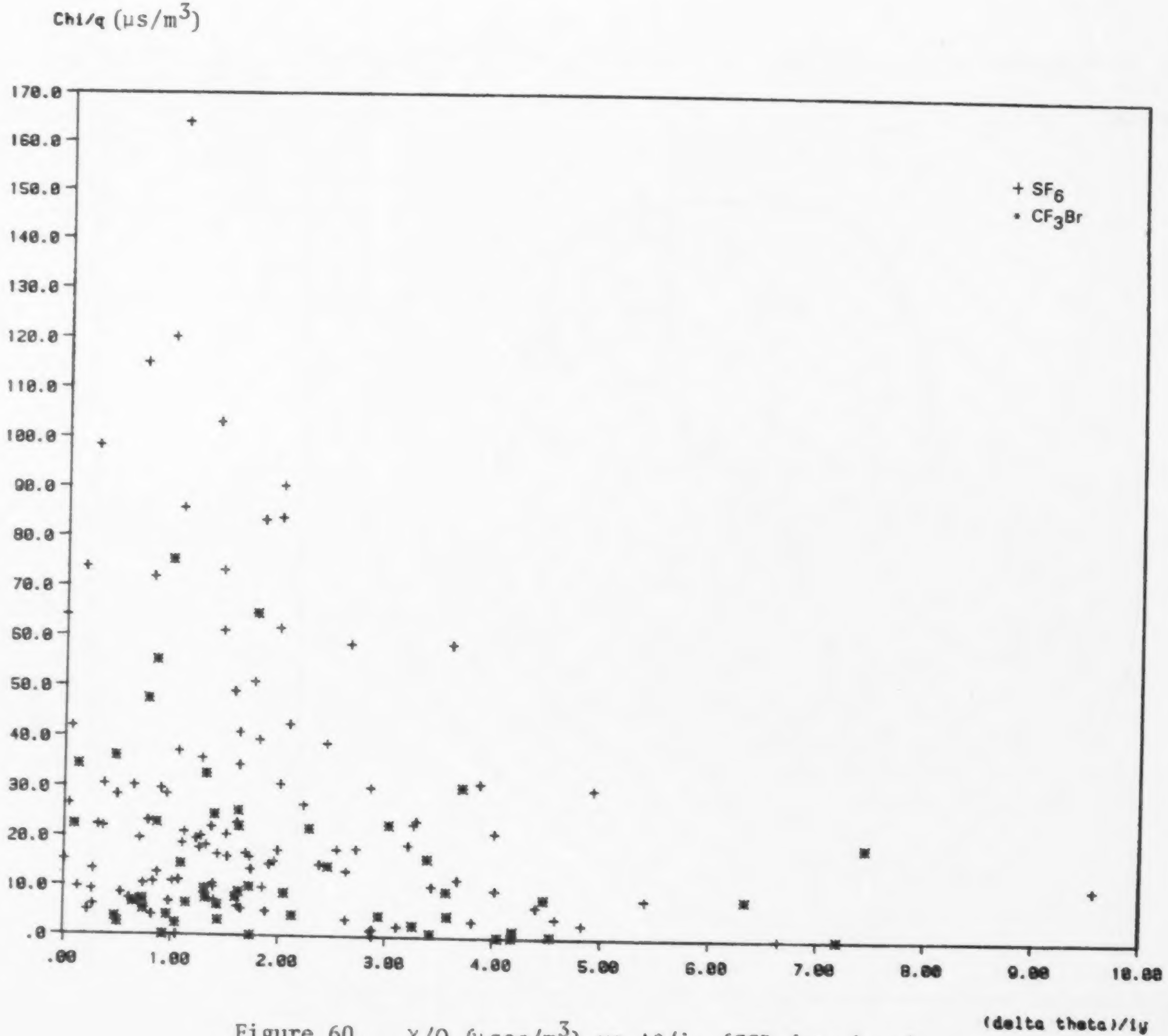

Figure 60. χ/Q (μsec/m^3) vs. $\Delta\theta/i_y$ (CCB data base).

Large concentrations were observed at HBR whenever the average wind direction approached the ridge, even for releases below H_c.

In summary, there are several similarities and differences among the results from the two experiments:

- Observed peak χ/Q values were greater at HBR than at CCB;
- H_c discriminates between the flow regimes;
- At CCB the peak GLC values occurred when $z_r \approx H_c$; at HBR the peak GLC values occurred when $z_r \leq H_c$;
- At CCB the peak GLC values frequently occurred at elevations less than the release height; and
- At HBR the peak GLC values frequently occurred at elevations near or above the release height but below H_c.

4.5.4 Example Results from Specific Experiments

To illustrate some of the experimental results, the remainder of this section will discuss three case study hours:

- Experiment 4 (October 11, 1982) - 0300 - 0400 MDT
- Experiment 10 (October 22, 1982) - 0300 - 0500 MDT.

Experiment 4, the first in which the tracer gases were released, represents a situation where the oil-fog and SF_6 plumes rose to an altitude of 60-80 m and were transported in an ESE wind toward the ridge. The wind direction variability and turbulence were sufficient to produce high SF_6 concentrations throughout nearly the entire sampler network, although the peak values were measured near the crest. The CF_3Br plume remained near the critical dividing-streamline height and produced peak concentrations on the windward side of HBR. Experiment 10 (0300-0500) illustrates a case in which relatively steady oil-fog and SF_6 plumes were transported up and over HBR and produced the peak GLC on the lee side. The CF_3Br was released below H_c and produced a wide pattern of GLC on the windward side of the ridge.

Experiment 4 (0300-0400)

The easterly drainage was established between 0100 and 0200 on October 11. By 0300 ESE winds were blowing towards the Hogback. The oil-fog and SF_6 were released from location 216 (see Figure 49) at a height of 30 m. The CF_3Br was released from 216 at a height of 20 m. Figure 61 is a photograph (five-minute exposure), taken from the 120-m level of Tower A at 0315 MDT, of the oil-fog plume going over the Hogback at the north end of the sampling network. Figure 62 is a side view of the plume at the same time; it shows sufficient vertical turbulence to produce SF_6 concentrations on the windward face of the ridge. By 0340 the oil-fog plume had moved south of the light cross (Figure 63). In short, the photographs show that the oil-fog and co-located SF_6 plumes were initially located near the north end of the sampler grid and then moved to the center of the grid with enough turbulence to produce GLC everywhere on the ridge.

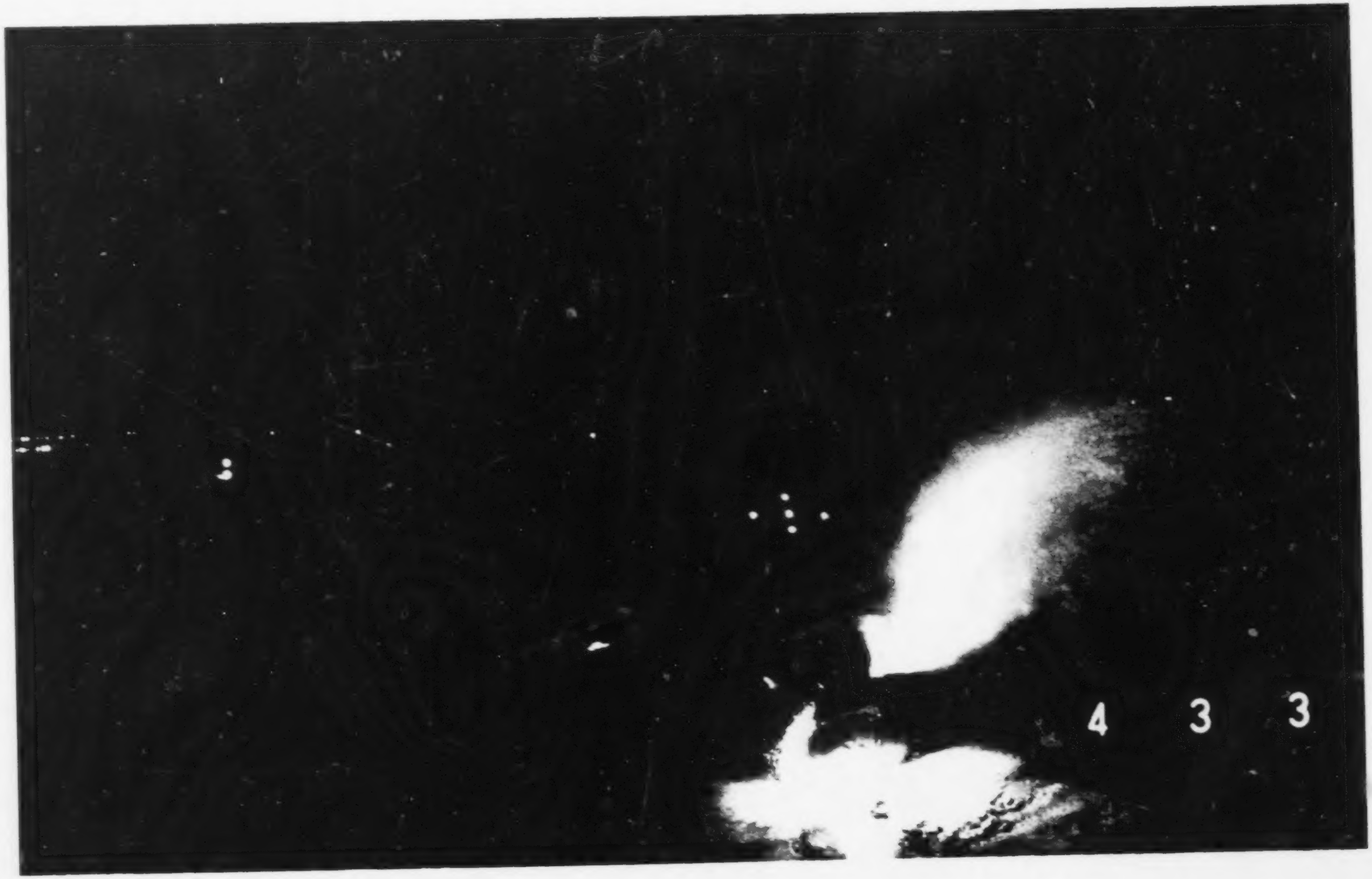

Figure 61. Five-minute exposure from Tower A (Experiment 4, 10/11/82, 0315 MDT).

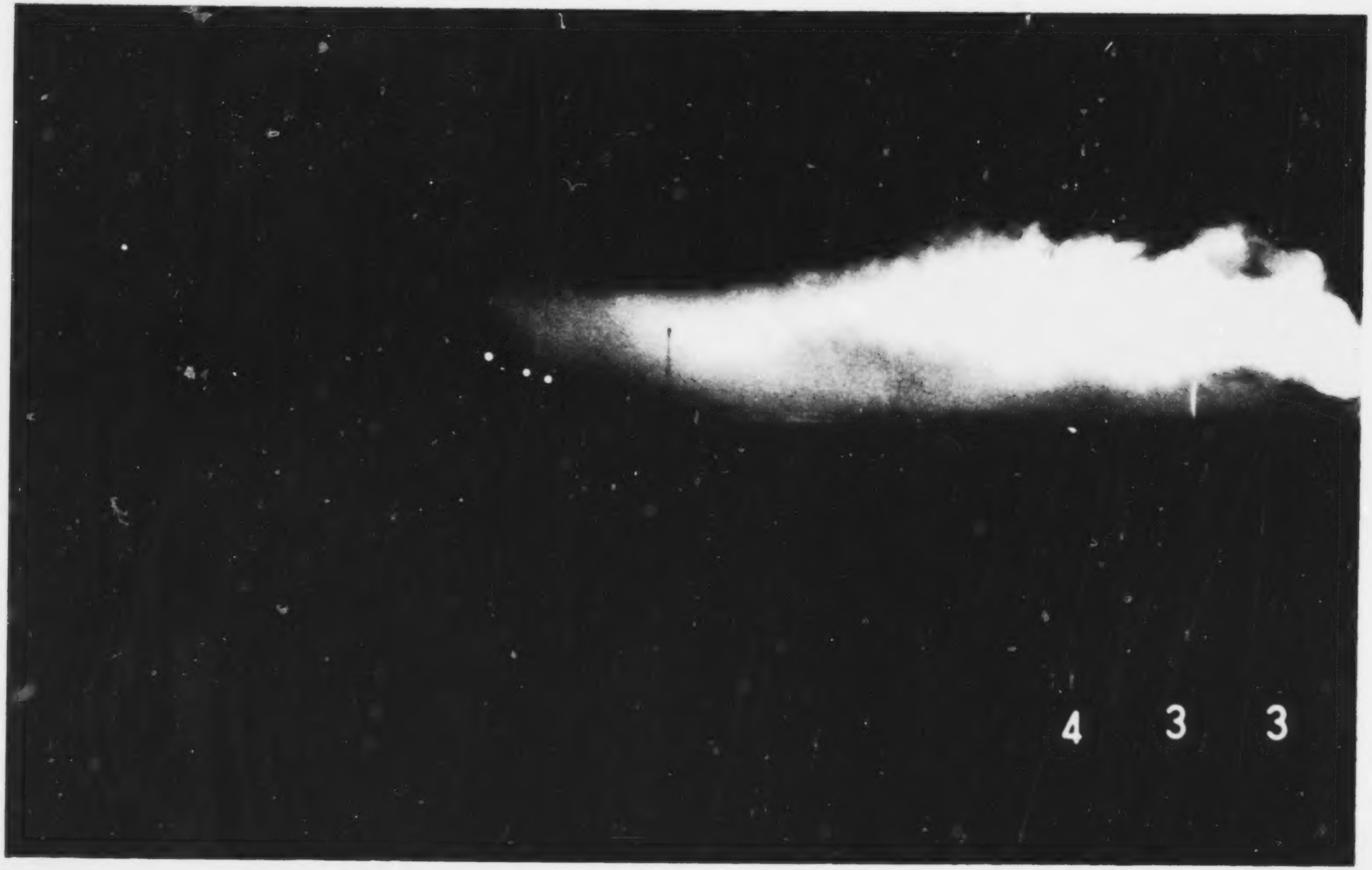

Figure 62. Five-minute exposure from HBR south of target area (Experiment 4, 10/11/82, 0315 MDT).

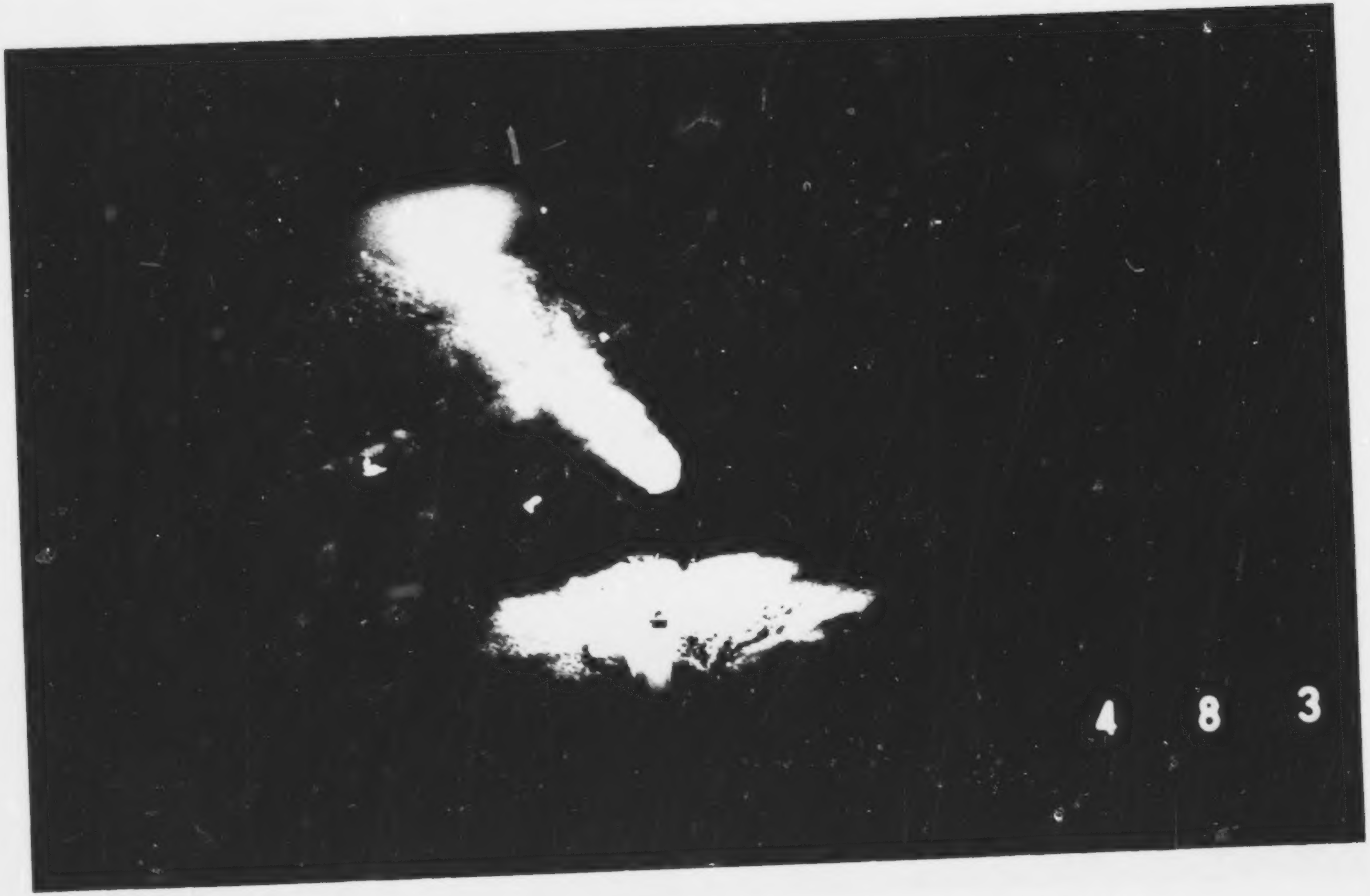

Figure 63. Five-minute exposure from Tower A (Experiment 4, 10/11/82, 0340 MDT).

Figure 64 shows vertical profiles of hourly average wind direction*, wind speed, and temperature derived from the Tower A measurements. On the basis of this information and measurement from the photographs, the oil-fog plume rose to about 60-80 m and was transported toward HBR in the ESE winds. Time-series of 5-minute average winds measured on Towers A, B, and C, and 5-minute winds estimated from the photographs are plotted in Figures 65 and 66.

A map of one-hour SF_6 concentrations is given in Figure 67. Figure 68 gives the along-hill (approximately crosswind) distribution of hourly SF_6 concentrations for nine sampling "rows." Figure 69 identifies the row plotted by each symbol in Figure 68 and Table 15 defines the rows by their sampler numbers. There is a wide area of relatively high (greater than 5.0 $\mu sec/m^3$) concentrations over most of the ridge. The peak values were measured near the ridge crest and on its lee side.

Figure 70 gives a map of hourly CF_3Br concentrations, and Figure 71 shows the along-hill distribution. The peak values occurred south of Desert Drive at an elevation of 5470 ft (row 4), an altitude about 10 m higher than the release elevation. Note that the wind direction at 40 m in Figure 64 is consistent with the observed concentration pattern.

Experiment 10 (0300-0500)

The morning of October 22, 1982 also experienced an easterly drainage wind. The drainage became well established just after midnight, and by 0300 ESE winds were directed toward HBR at about 2 m/sec. The oil-fog, SF_6, and CF_3Br were released from Tower A--the oil-fog and SF_6 at 50 m, the CF_3Br at 30 m.

Figures 72 and 73, photographs taken from Tower A and from the ridge crest south of the target area, show a coherent plume going up and over HBR at 0330 MDT. The second 5-minute exposure (Figure 73) shows some plume material diffusing to ground-level near the ridge crest. The profiles of hourly meteorological variables are given in Figure 74. Time-series of 5-minute wind directions are given in Figures 75 and 76.

According to the photographs and the measured wind directions, the oil-fog (and SF_6) plume dispersed steadily up and over HBR south of the light cross. The plume rose to an altitude above H_c (50.1 m) as it was

---

*The profile plots of wind direction, wind speed, and temperatures were produced in the following manner. The 5-minute temperatures and the prop wind speeds and directions were used to compute 1-hour mean temperatures, scalar wind speeds, and unit vector u [sin WD] and unit vector v [cos WD] wind direction components. This was done for each instrument level of Tower A [2,5,10,20,30,40,60,80,100,150 m]. A "spline under tension" method was used to interpolate the meteorological variables for every 5 m between instrument levels on Tower A. The splined u and v unit vector components were used to derive the unit vector wind direction.

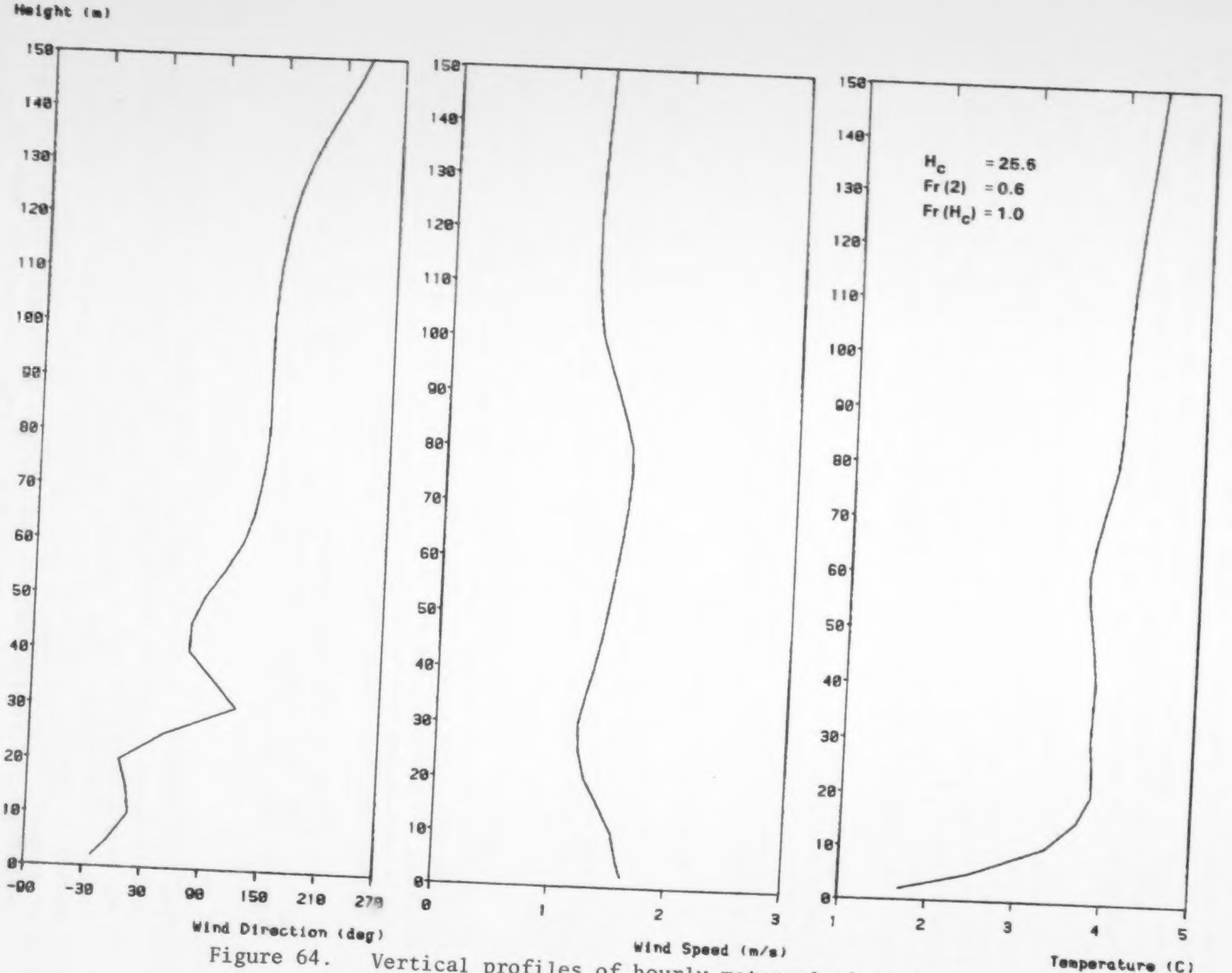

Figure 64. Vertical profiles of hourly meteorological data (Tower A, Experiment 4, 10/11/82, 0300-0400 MDT).

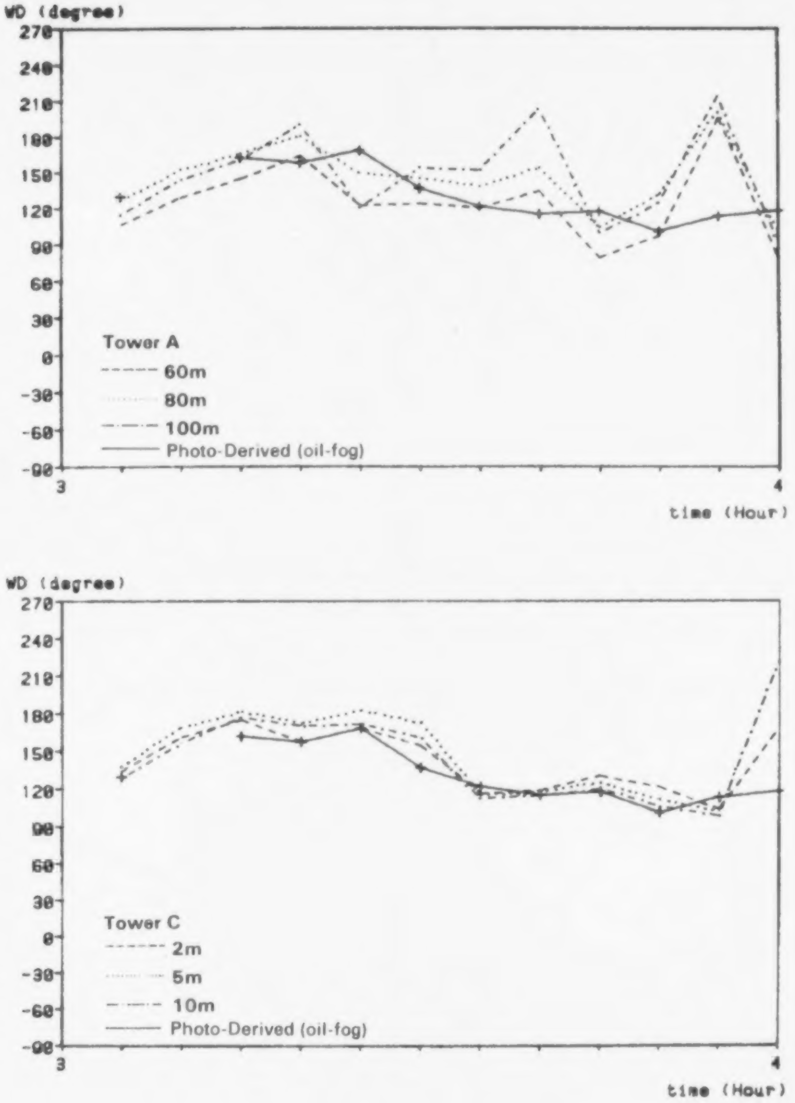

Figure 65. Time-series of 5-minute wind directions from Tower A and Tower C (Experiment 4, 10/11/82, 0300-0400 MDT).

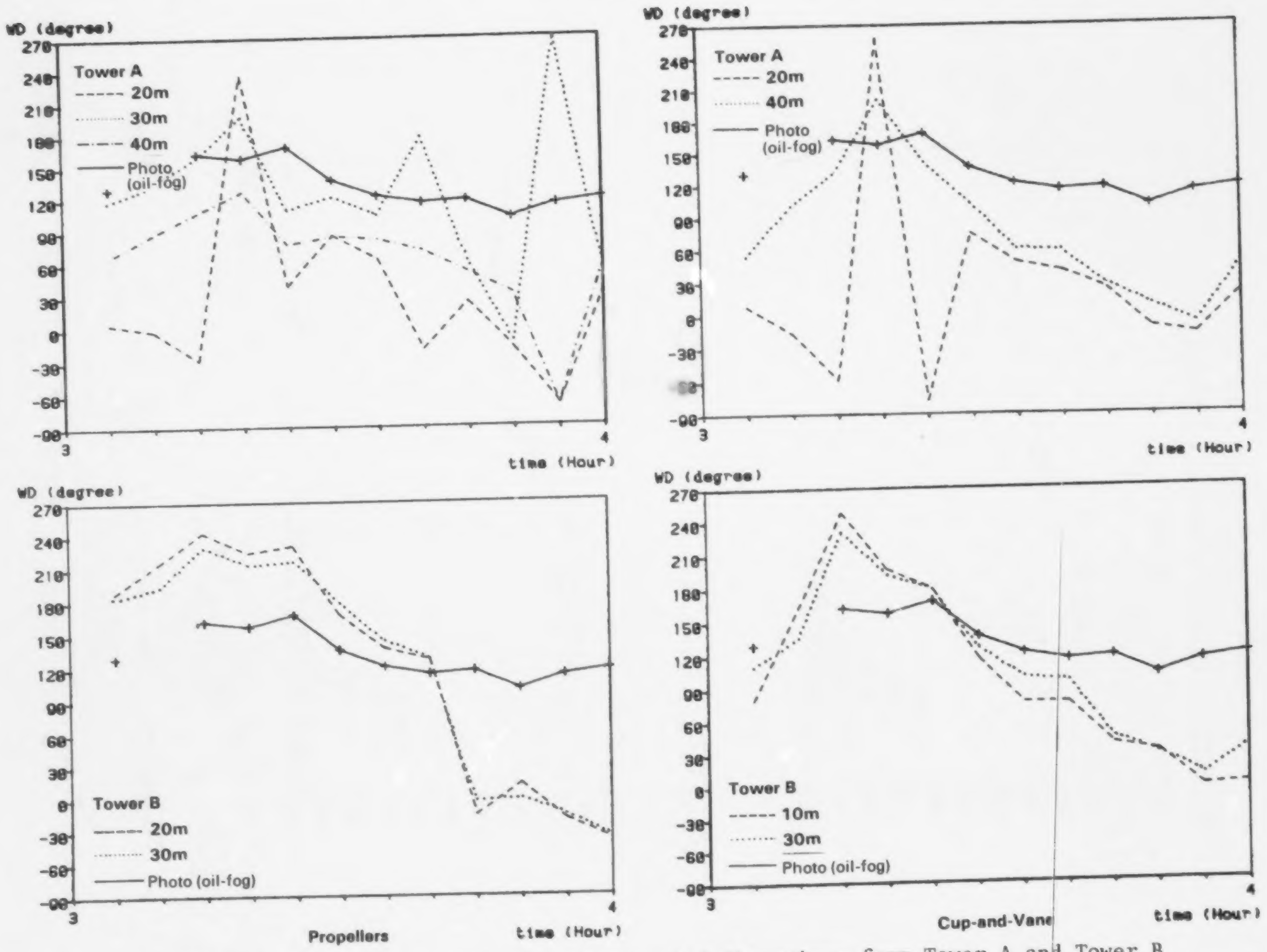

Figure 66. Time-series of 5-minute wind directions from Tower A and Tower B (Experiment 4, 10/11/82, 0300-0400 MDT).

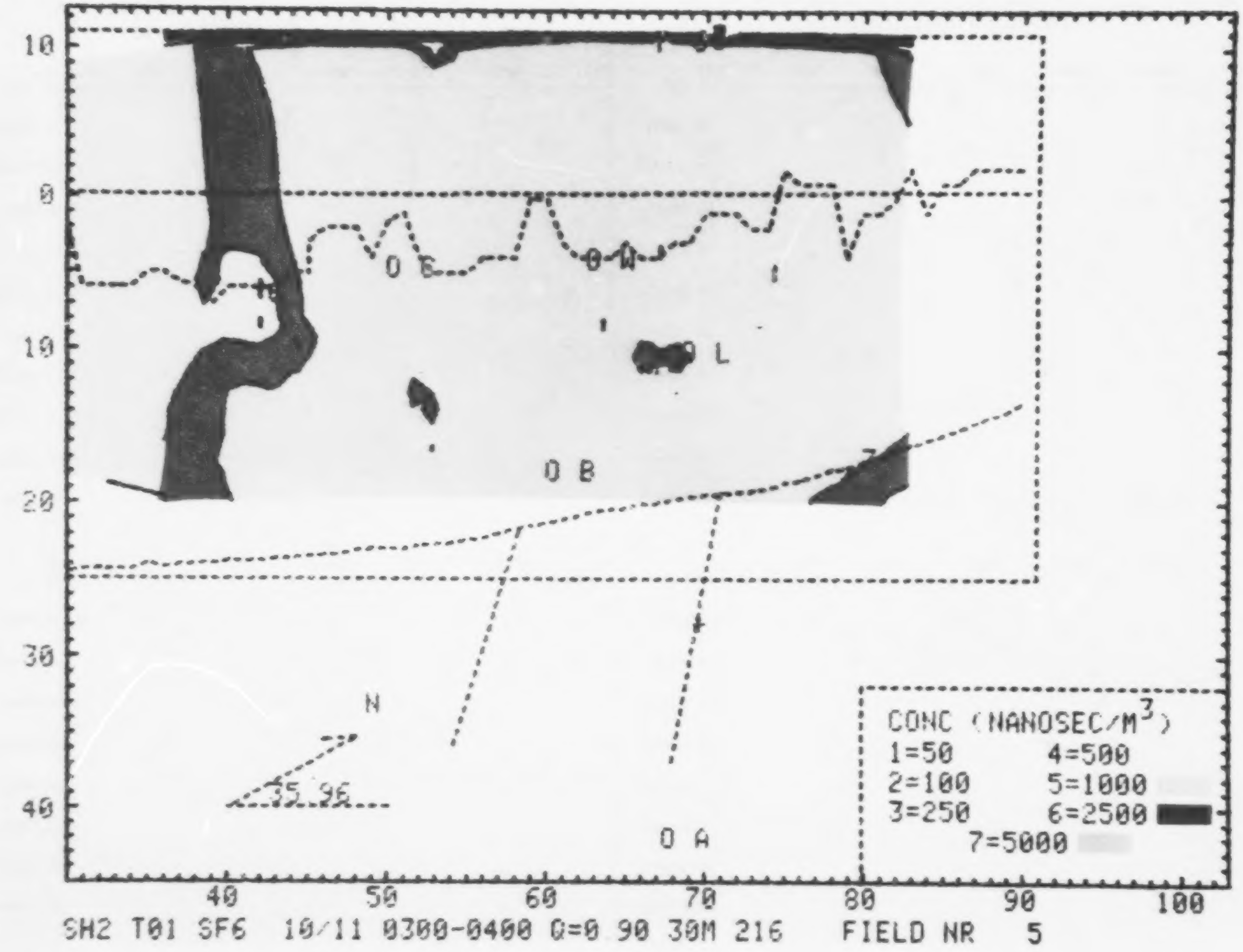

Figure 67. Hourly SF_6 concentrations (Experiment 4, 10/11/82, 0300-0400 MDT).

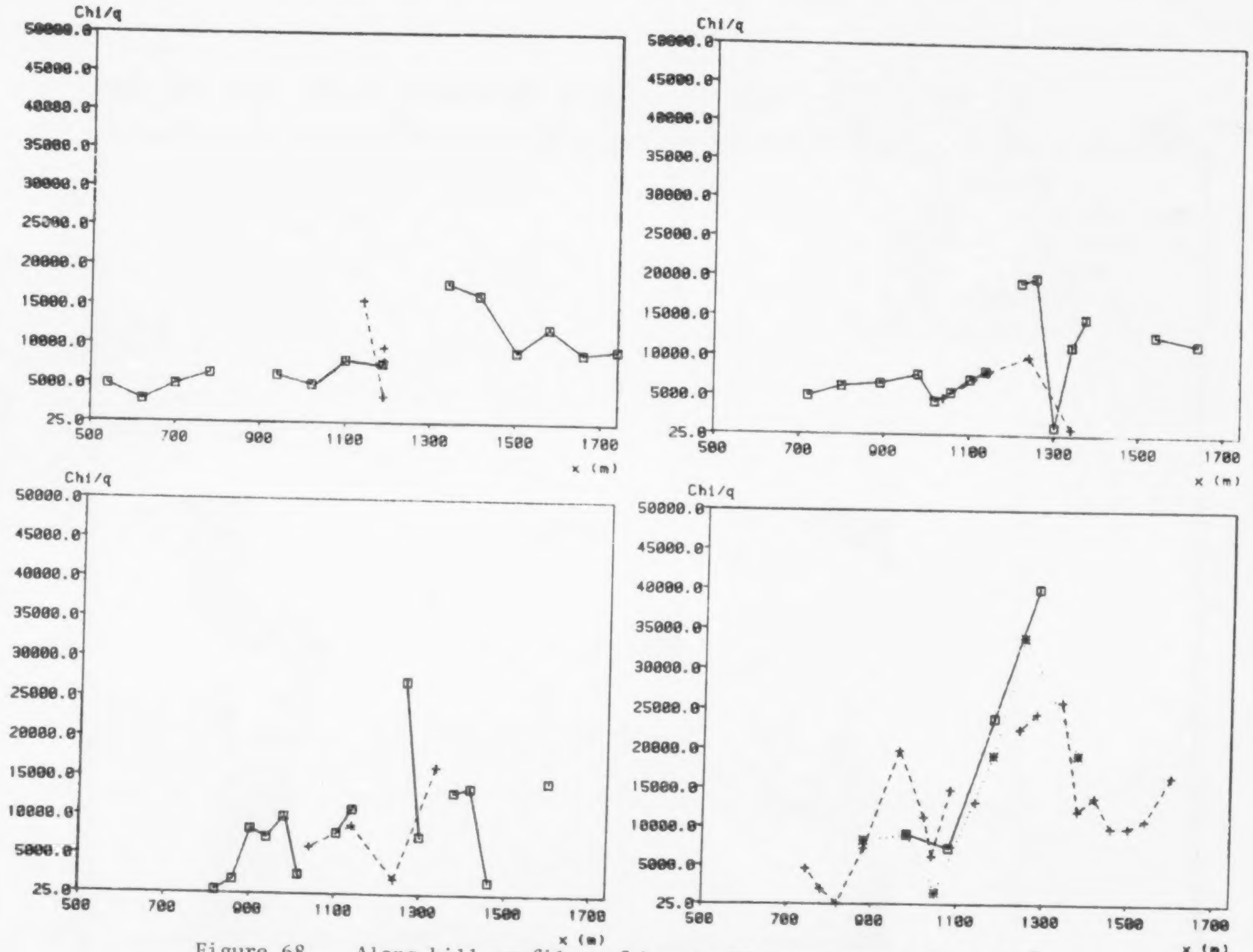

Figure 68. Along-hill profiles of hourly SF_6 concentrations (ns/m^3) (Experiment 4, 10/11/82, 0300-0400 MDT).

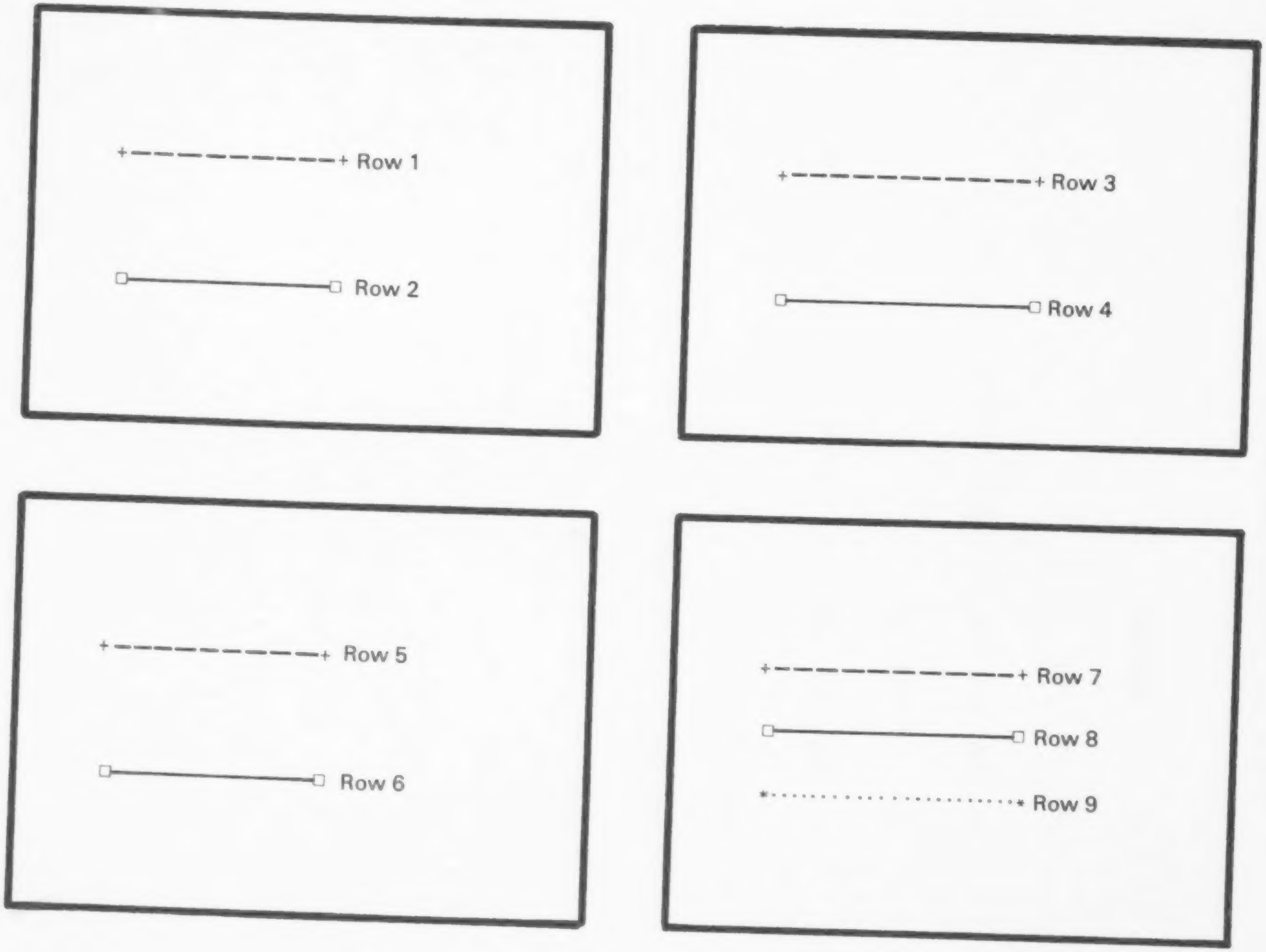
Row 1
Row 2
Row 3
Row 4
Row 5
Row 6
Row 7
Row 8
Row 9

Figure 69. Hogback samplers by rows

TABLE 15. HOGBACK SAMPLERS BY ROW

Row	Samplers
1	1-5, 702, 703
2	101-106, 711-714, 109, 809, 721-724, 112-118
3	107, 108, 110, 111
4	201-205, 207, 208, 210, 731-734, 211, 213, 214, 216-220
5	206, 209, 212, 215
6	301-307, 741-744, 308-313, 751-754, 314-319, 810
7	401-417, 419-422, 701
8	501-506
9	601-606

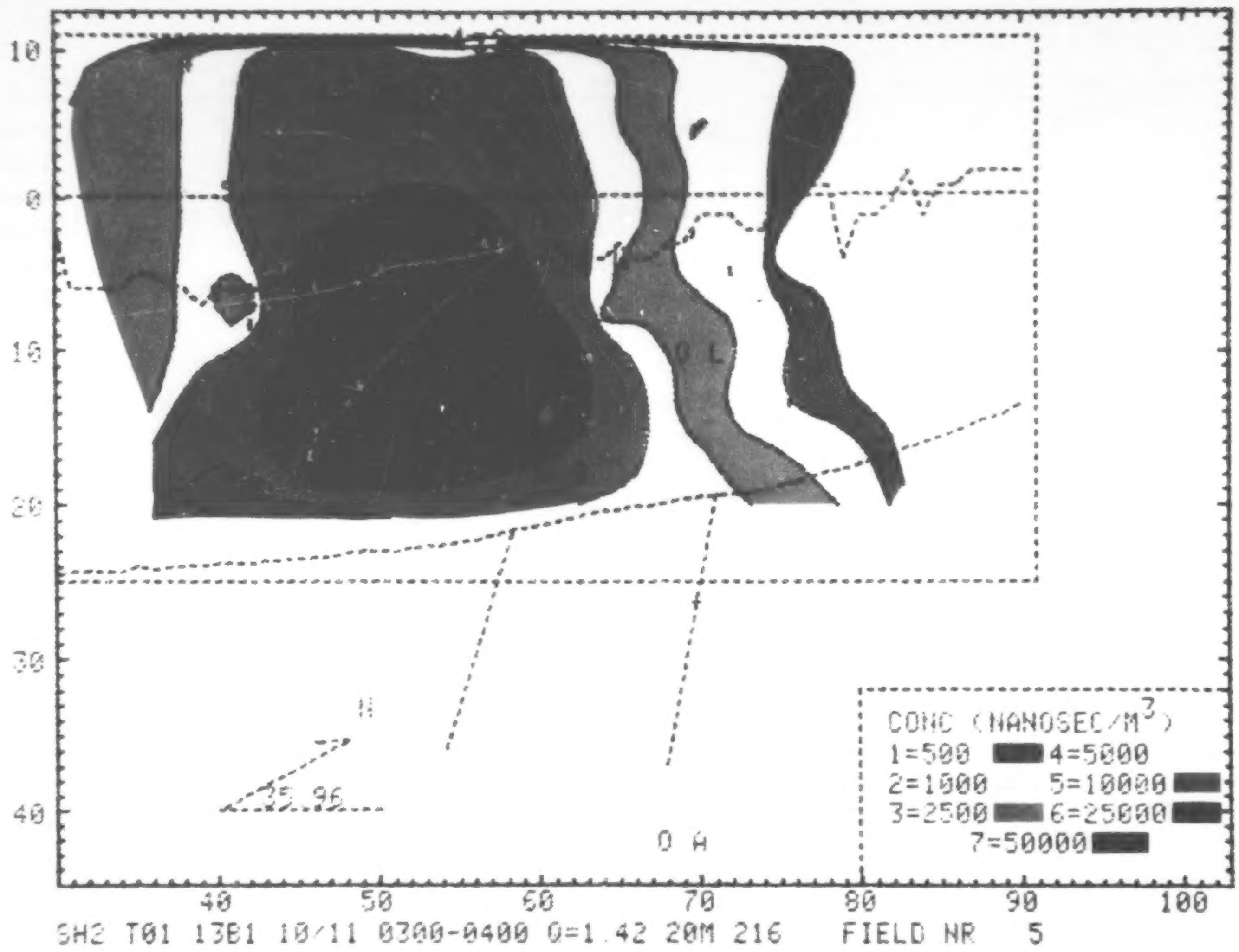

Figure 70. Hourly CF_3Br concentrations (Experiment 4, 10/11/82, 0300-0400 MDT).

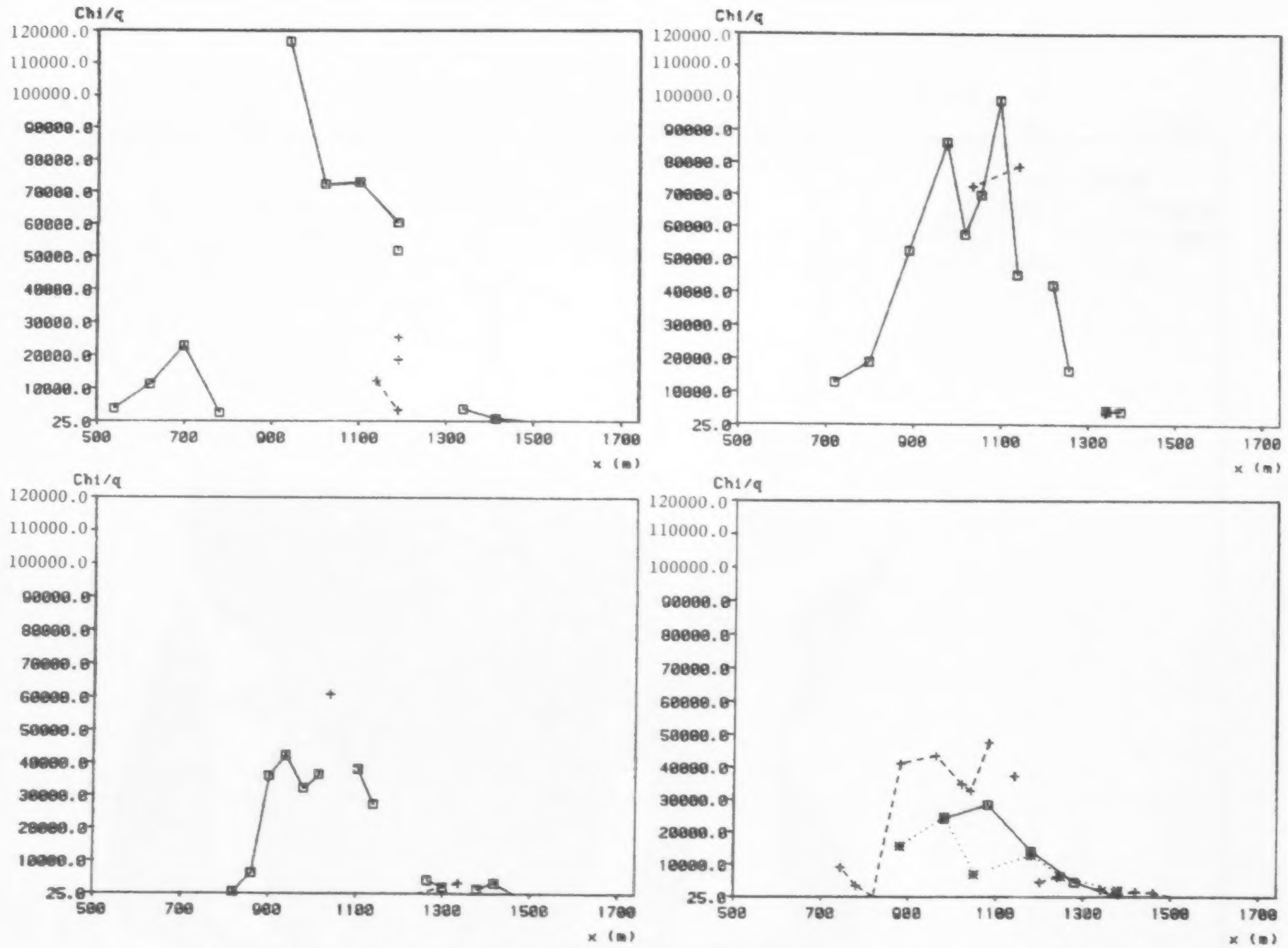

Figure 71. Along-hill profiles of hourly CF_3Br concentrations (ns/m^3) (Experiment 4, 10/11/82, 0300-0400 MDT).

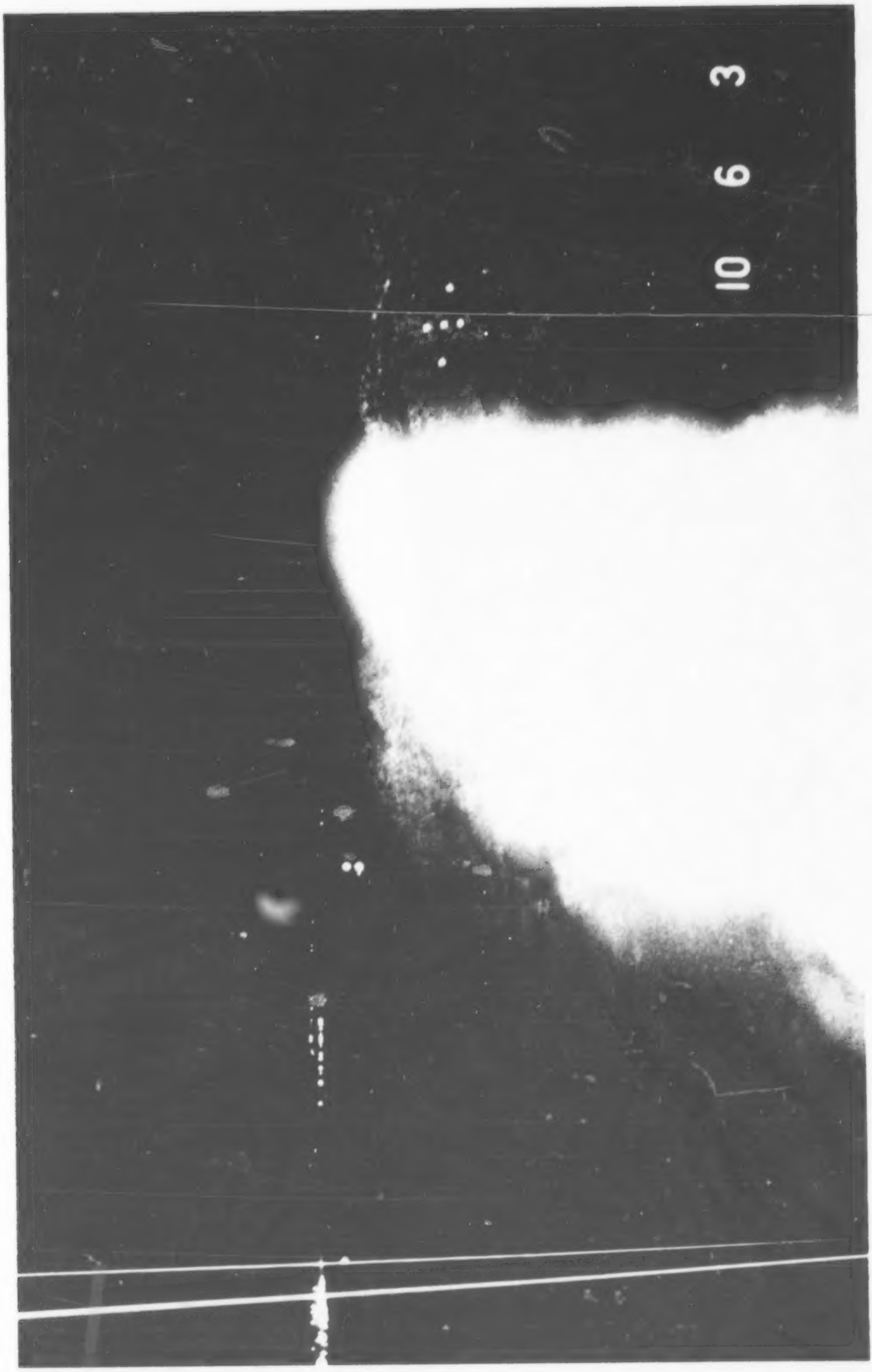

Figure 72. Five-minute exposure from Tower A (Experiment 10, 10/22/82, 0330 MDT).

Figure 73. Five-minute exposure from HBR south of target area, (Experiment 10, 10/22/82, 0330 MDT).

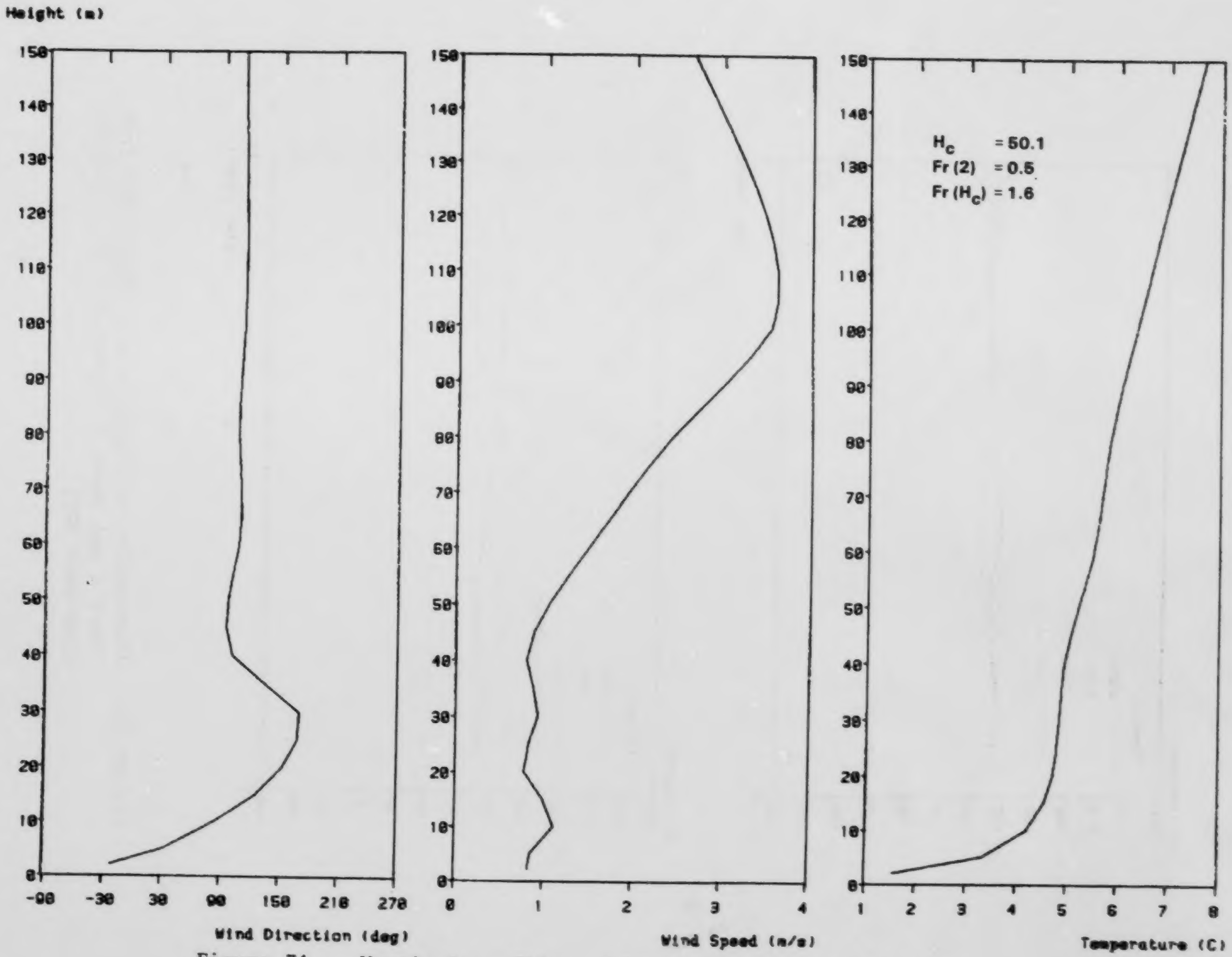

Figure 74. Vertical profiles of hourly meteorological data (Tower A, Experiment 10, 10/22/82, 0300-0400 MDT).

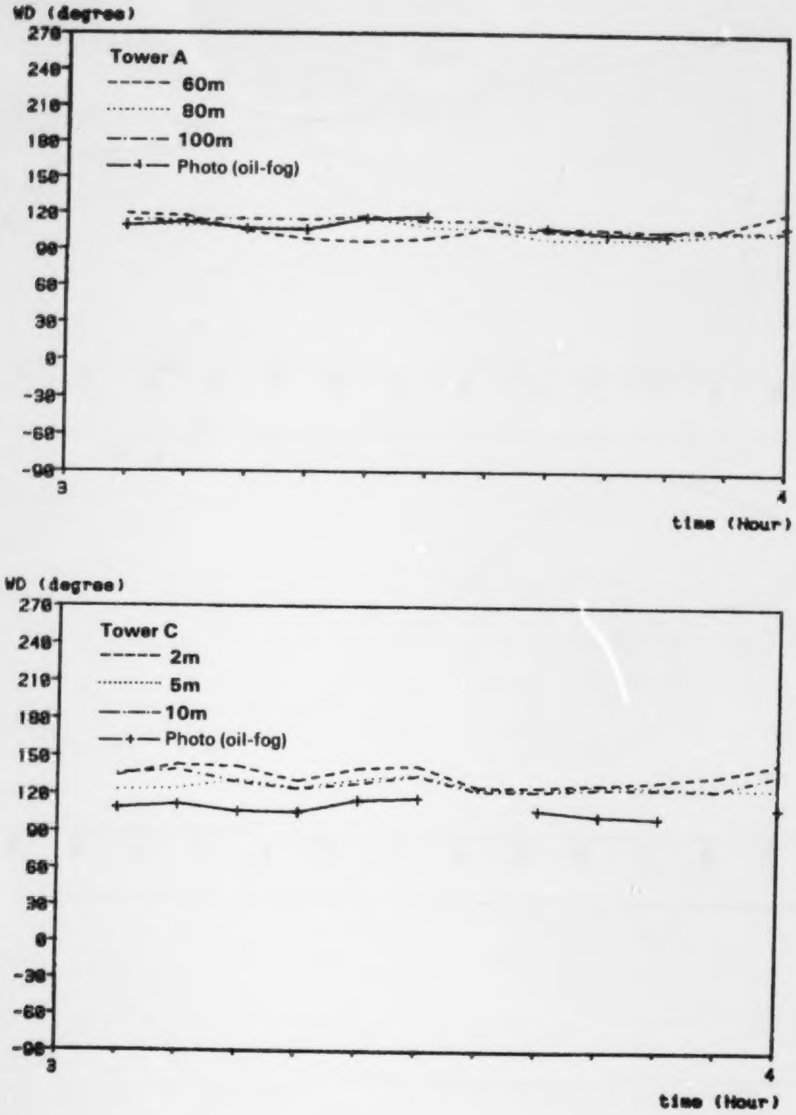

Figure 75. Time-series of 5-minute wind directions from Tower A and Tower C (Experiment 10, 10/22/82, 0300-0400 MDT).

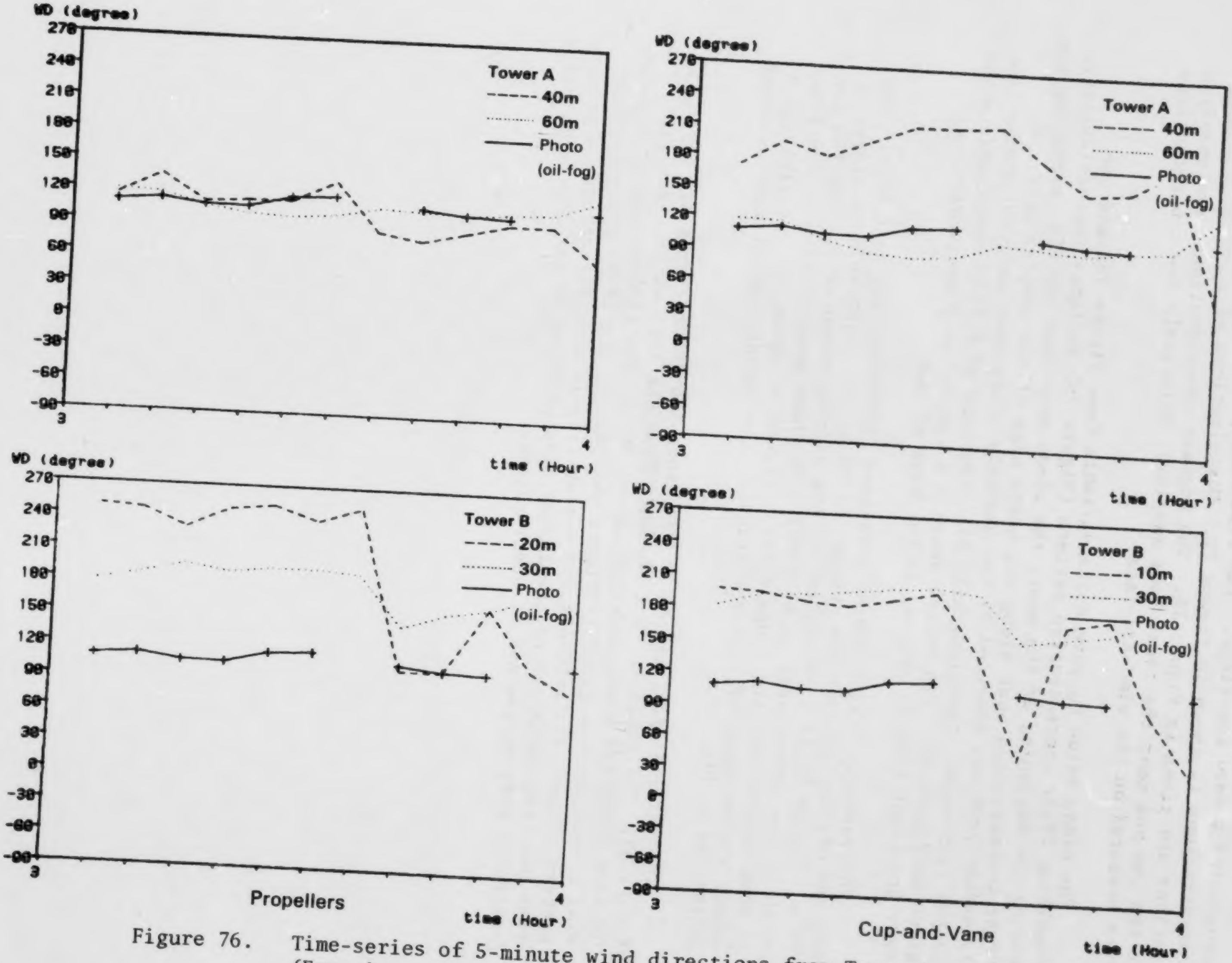

Propellers

Cup-and-Vane

Figure 76. Time-series of 5-minute wind directions from Tower A and Tower B (Experiment 10, 10/22/82, 0300-0400 MDT).

transported toward the ridge. The resulting pattern of hourly average SF_6 concentrations is shown in Figure 77. Distributions of along-hill concentrations are given in Figure 78. The highest concentrations were measured in the lee and near the crest (one sampler). Relatively low concentrations were measured on the windward face.

The winds below H_c were quite variable (see Figure 76) and the resulting CF_3Br concentration pattern (Figure 79) reflects the variability. During the beginning of the hour, the winds were from the SSE, producing the CF_3Br concentration peak along the north edge of the sampler grid. A secondary peak was produced by the easterly winds that occurred during the second half-hour. The along-hill distributions of Freon concentrations are given in Figure 80. Two values above 5.0 $\mu sec/m^3$ were measured--one near the crest (row 7) and one at the base of HBR.

The easterly drainage wind persisted throughout the next hour. The SF_6 and oil-fog release was changed to 70 m; the CF_3Br release stayed at 30 m. Figure 81 is a photograph of the oil-fog plume taken from the crest south of the target area at 0425 MDT. It shows more lifting of the plume as it goes up and over the ridge crest. Figure 82 shows the distribution of hourly ground-level SF_6 concentrations. The highest values were measured on the lee of HBR.

The vertical profiles of hourly winds and temperatures are given in Figure 83. The winds at 70 m remained from the ESE, while there was a layer of more southerly winds centered around 30 m. The time-series of 5-minute wind directions are given in Figure 84. Again, the CF_3Br concentration pattern (Figure 85) reflects the variability in wind directions--a primary peak near the north end of the target area produced by the SSE winds and a secondary peak at the end of Desert Drive.

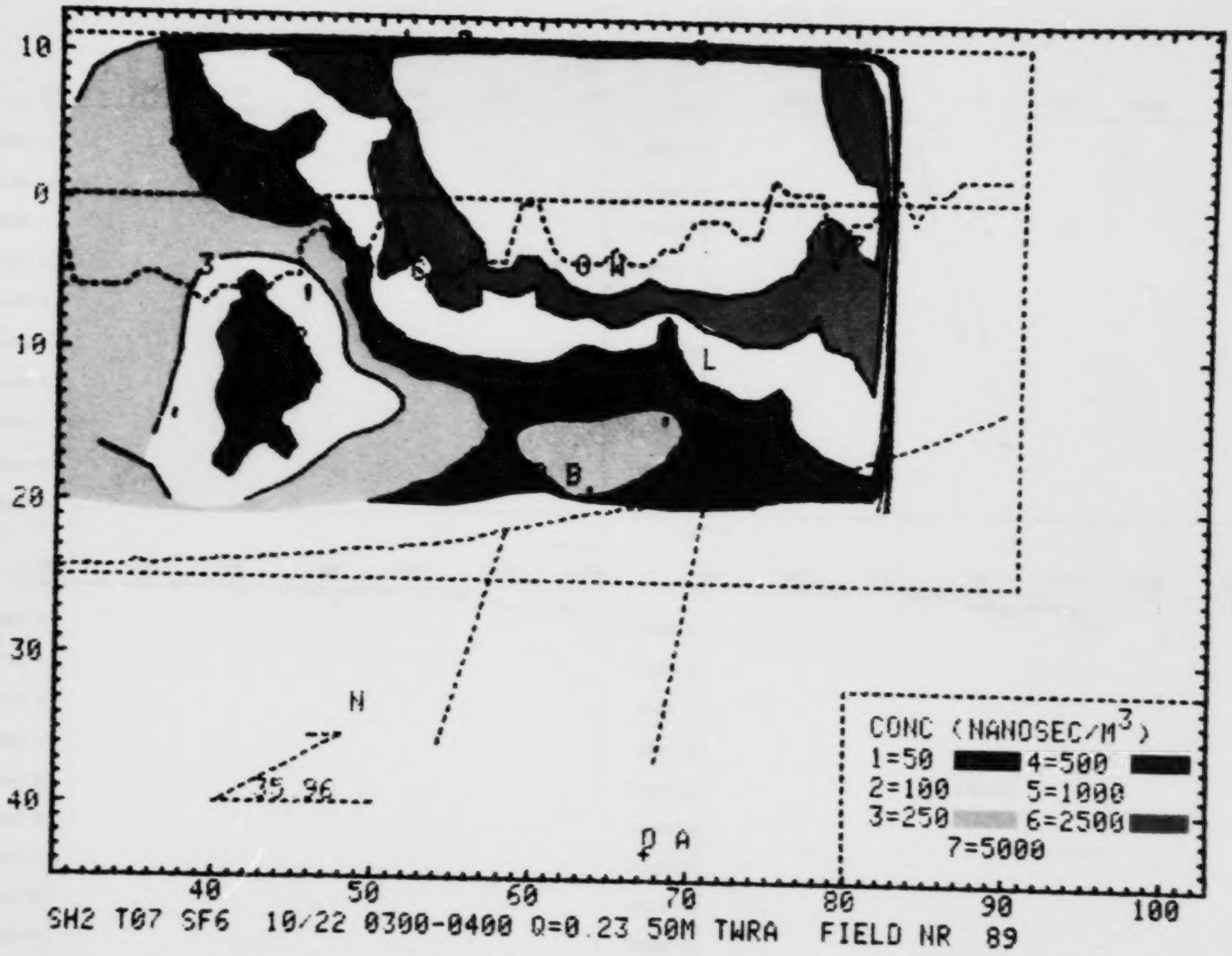

Figure 77. Hourly SF_6 concentrations (Experiment 10, 10/22/82, 0300-0400 MDT).

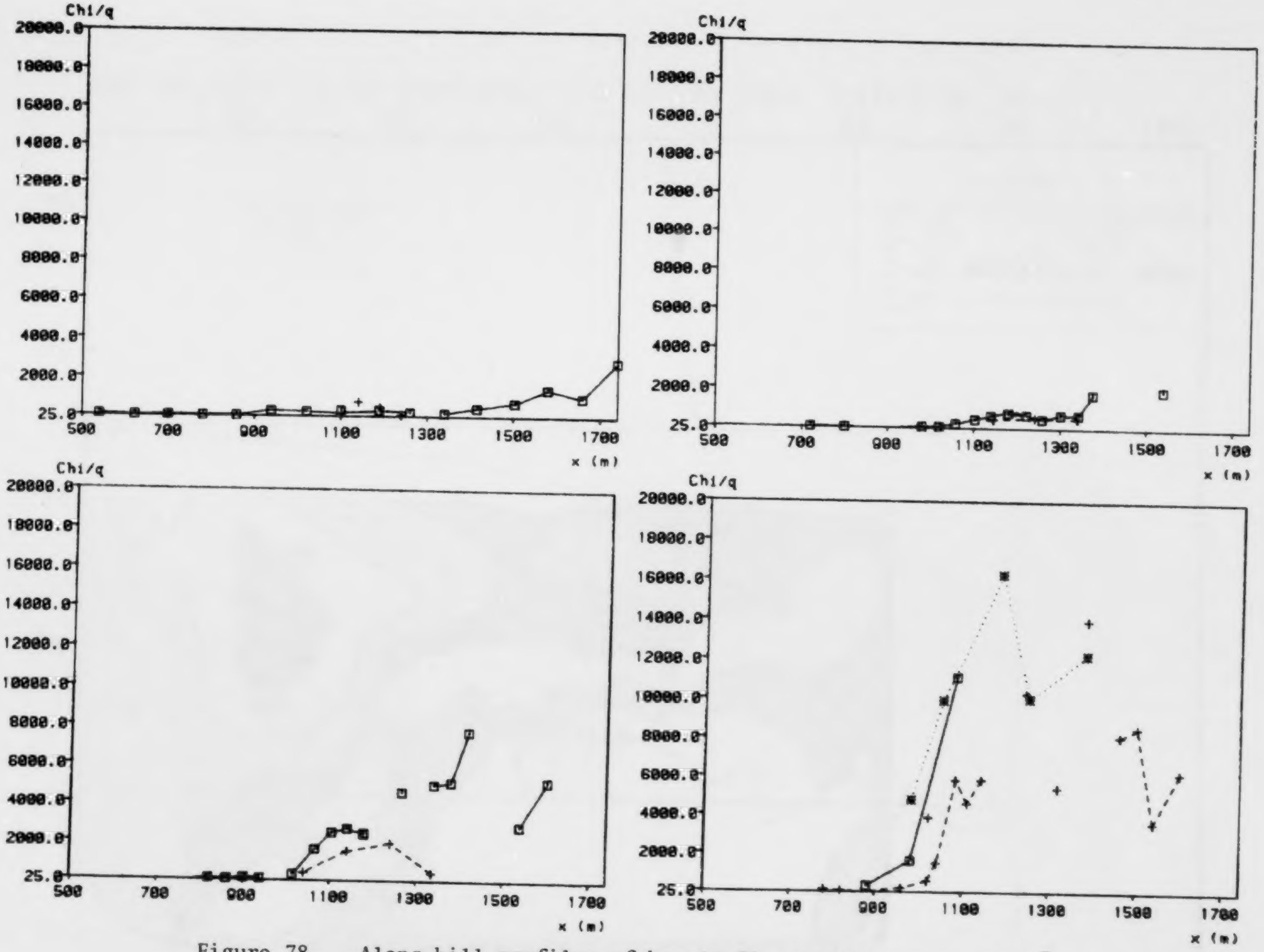

Figure 78. Along-hill profiles of hourly SF_6 concentrations (ns/m^3) (Experiment 10, 10/22/82, 0300-0400 MDT).

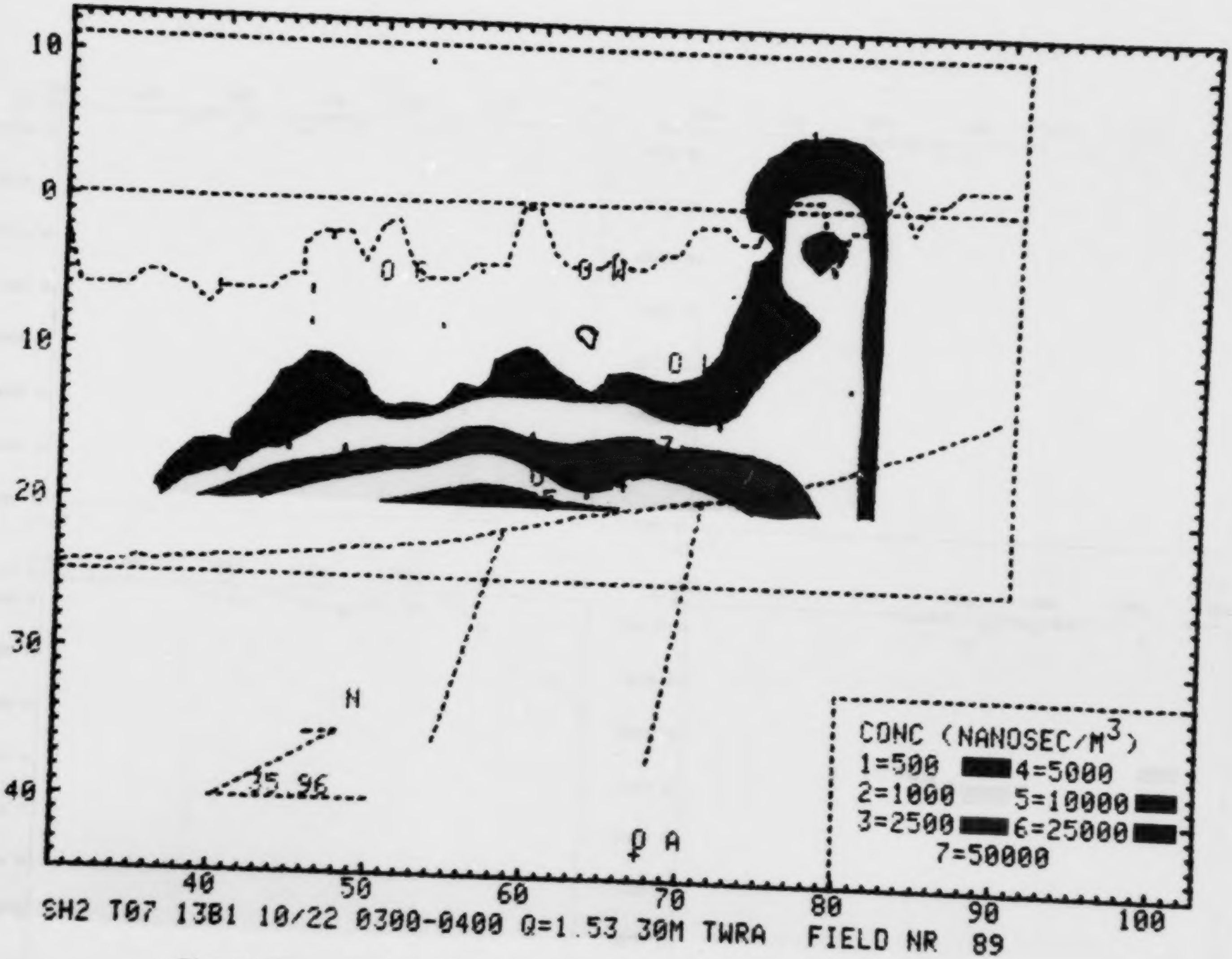

Figure 79. Hourly CF_3Br concentrations (Experiment 10, 10/22/82, 0300-0400 MDT).

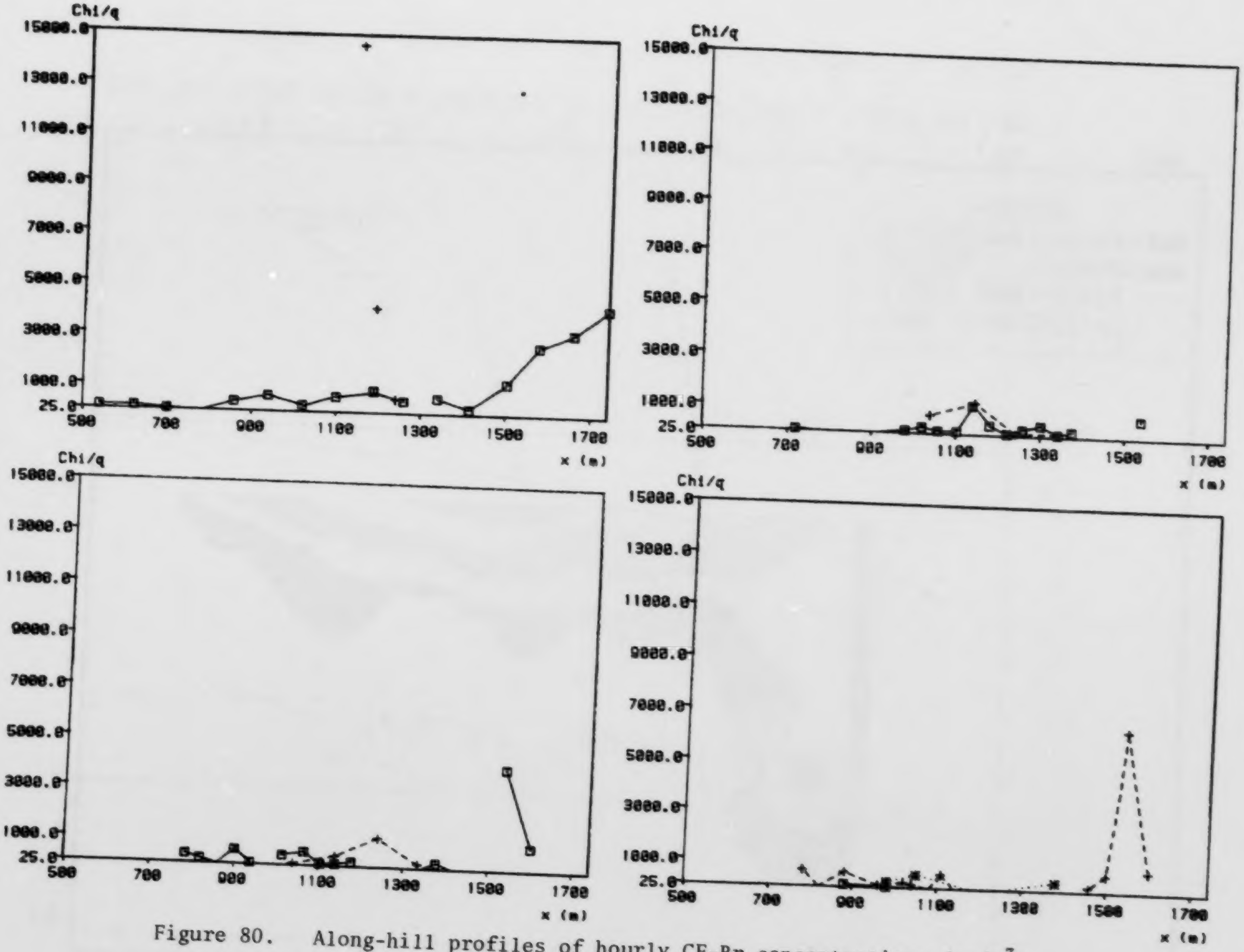

Figure 80. Along-hill profiles of hourly CF_3Br concentrations (ns/m^3) (Experiment 10, 10/22/82, 0300-0400 MDT).

Figure 81. Five-minute exposure from HBR south of target area, (Experiment 10, 10/22/82, 0425 MDT).

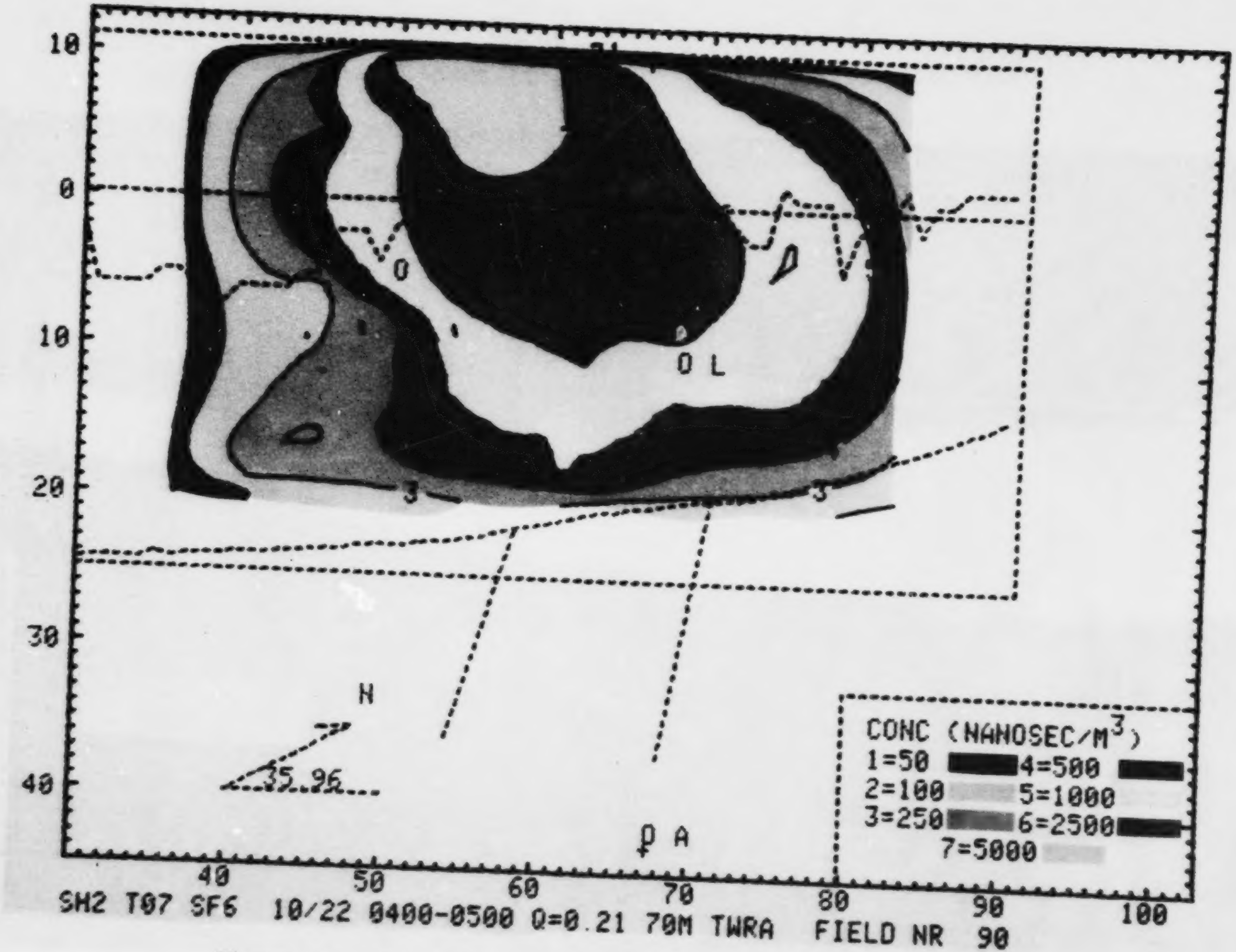
10
0
10
20
30
40
0
0 L
3
3
N
35.96
A
CONC (NANOSEC/M^3)
1=50
2=100
3=250
4=500
5=1000
6=2500
7=5000
40
50
60
70
80
90
100
SH2 T07 SF6 10/22 0400-0500 Q=0.21 70M TWRA FIELD NR 90

Figure 82. Hourly SF_6 concentrations (Experiment 10, 10/22/82, 0400-0500 MDT).

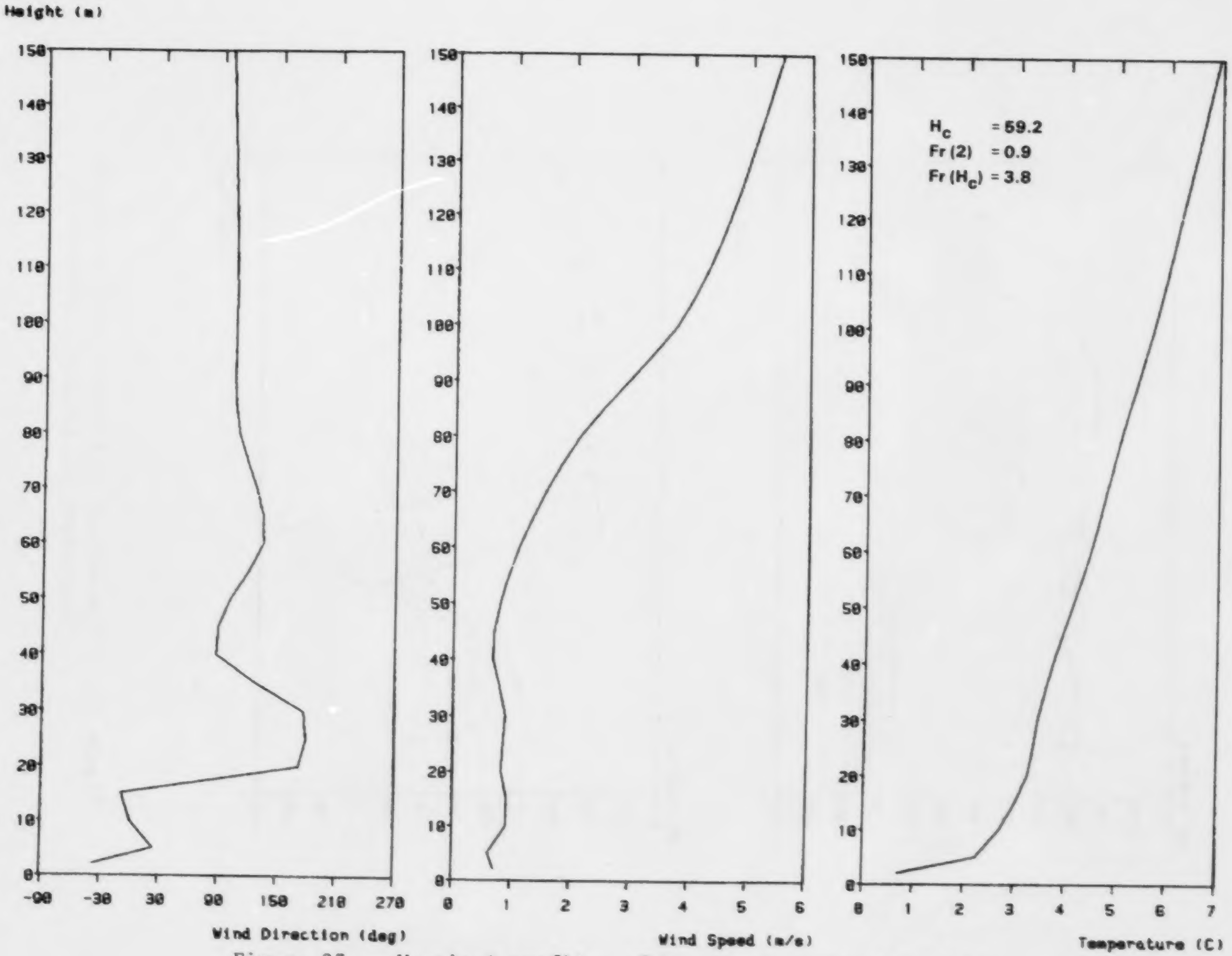

Figure 83. Vertical profiles of hourly meteorological data (Tower A, Experiment 10, 10/22/82, 0400-0500 MDT).

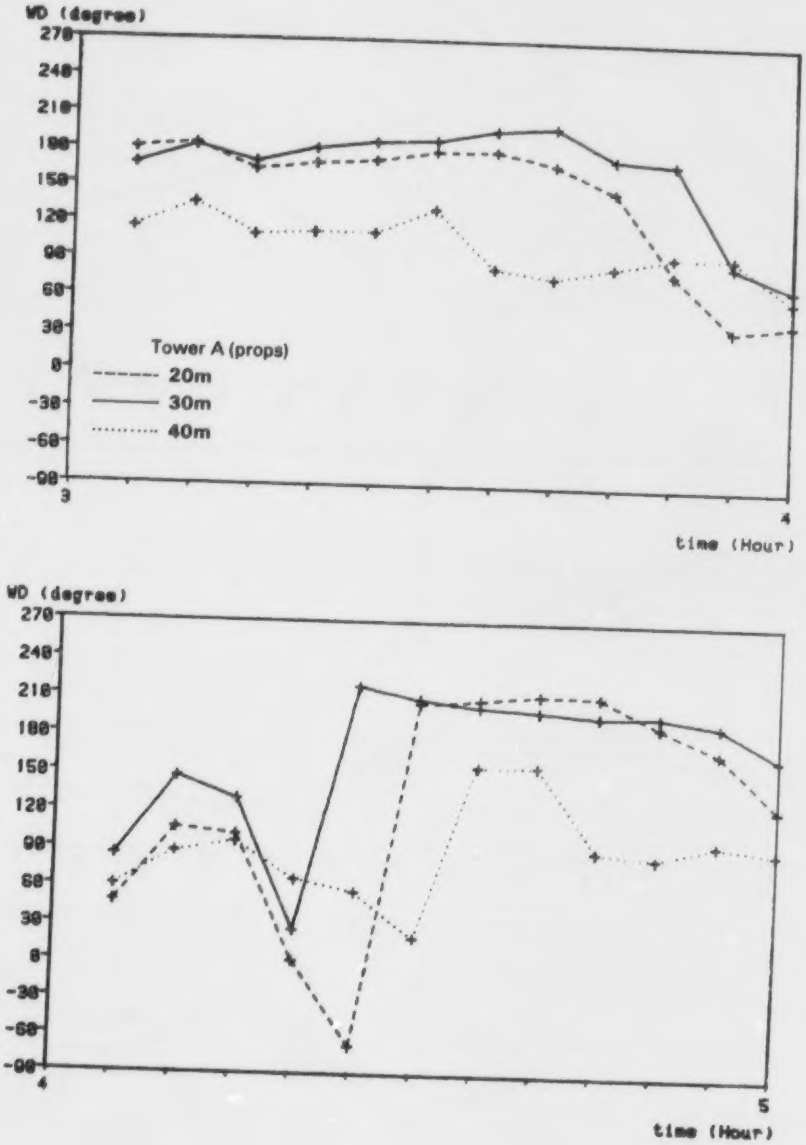

Figure 84. Time-series of 5-minute wind directions (Experiment 10, 10/22/82, 0400-0500).

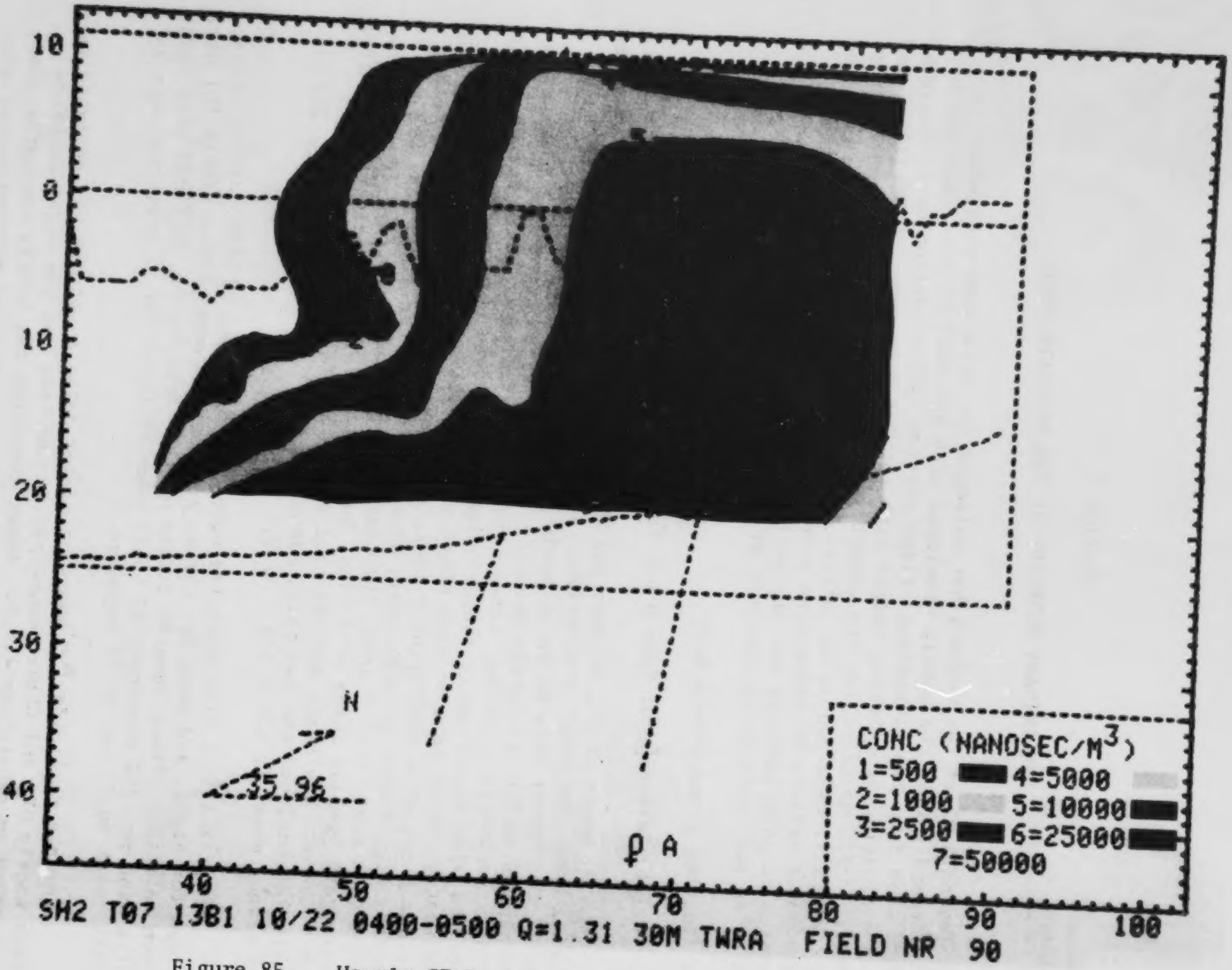

Figure 85. Hourly CF_3Br concentrations (Experiment 10, 10/22/82, 0400-0500 MDT).

SECTION 5

PRELIMINARY MODELING OF THE HBR DATA BASE

The SHIS #2 at the Hogback has enlarged the data base with which to evaluate and refine the models developed with the SHIS #1 data base and to extend them to a two-dimensional ridge setting. This section describes the first evaluation of existing models with the HBR data base. CTDM(11083) and CTDM(11083-E), modified for the geometry and topography of HBR, and COMPLEX I and COMPLEX II were run on an initial 17-hour data base that was selected to represent a variety of dispersion conditions. Model calculations were compared to observations, and the performance of the three models was evaluated and compared to the SHIS #1 results.

5.1 Initial 17-Hour Data Base

5.1.1 Selection of Case Hours for Model Evaluations

The 91 hours of SF_6 release and 88 hours of CF_3Br release were examined to pick hours for model evaluation. The first step was the selection of a set of the tracer data to be withheld by the EPA Project Officer for independent model validation purposes. The selection procedure involved tossing (actually spinning) three coins. All experiment hours for which the unedited wind direction at source height was between 60° and 170° were candidates; there were 66 such hours. If the first coin toss for each hour yielded three of a kind (prob = 1/4), a second toss was made to determine whether SF_6, Freon, or both would be withheld. If the first toss was not three of a kind (prob = 3/4), the next hour was investigated. If the second toss again yielded three of a kind, both tracers were withheld (prob = 1/4 x 1/4 = 1/16). Two heads and one tail on the second toss meant SF_6 was withheld; one head and two tails meant Freon was withheld. The probability of either event is 1/4 x 3/8 = 3/32.

The results of this exercise were that SF_6 was withheld for six hours, Freon for eight, and both for three, so that 20 tracer hours (Table 16) have been selected. There were 86 tosses of the three coins; 20 (23%) were three of a kind vs. 25% expected; 27 (31%) were 2H,1T vs. 37.5% expected; and 39 (45%) were 1H,2T vs. 37.5% expected.

For the remaining 159 hours of tracer data, a pattern was assigned to each hourly SF_6 and CF_3Br concentration map based on the eight patterns discussed in subsection 4.5.2. After examining the hourly concentration patterns, photographs, log book comments, and unedited meteorological data for each experiment hour, a set of 42 hours was selected. A priority was then assigned to each of the 42 hours (6-GOOD, 21-MEDIUM, 15-LOW) by

TABLE 16. SHIS #2 TRACER DATA WITHHELD FOR MODEL VALIDATION PURPOSES

Exp. No.	Hour MDT	WD* and WS** at SF_6 Release Ht.		Release Ht. SF_6	Freon	H_c***	Location	$Fr(H_c)$	Fr(2m)
SF_6 to be Withheld									
4	06-07	112	0.7	30	20	60	216	2.25	0.54
5	00-01	67	3.9	40	25	26	203	1.83	0.70
9	06-07	62	4.6	40	20	31	203	1.90	0.46
10	00-01	Var	0.6	30	20	62	203	Not yet available	
12	05-06	101	3.0	75	50	40	A	2.68	0.89
15	08-09	102	1.8	50	40	-	A	-	-
Freon to be Withheld									
5	06-07	168	1.4	30	25	76	203	0.40	0.26
10	01-02	87	1.0	30	20	36	203	0.86	0.06
10	09-10	116	1.9	70	30	11	A	1.70	1.77
11	00-01	106	0.6	40	20	50	203	2.23	0.52
11	04-05	100	2.3	50	25	36	A	2.01	0.78
12	08-09	111	3.0	50	40	16	A	1.51	2.29
15	05-06	80	1.1	50	40	-	A	-	-
15	09-10	125	1.4	50	40	-	A	-	-
Both to be Withheld									
6	00-01	114	2.2	40	30	22	111	0.95	0.32
6	05-06	88	2.0	35	25	35	203	2.32	1.07
9	08-09	112	2.5	40	20	19	203	1.90	1.05

---

*Unedited wind direction estimated for SF_6 release height.

**Unedited wind speed (m/s).

***Calculated from the unedited meteorological data.

analyzing concentration patterns and other information to select a variety of situations. The final selection of 17 hours, presented in Table 17, was based on obtaining a good distribution of concentration patterns, meteorological situations, release locations, and release heights for the modeling. Table 18 summarizes various statistics based on the preliminary meteorological data for the 17 hours.

5.1.2 Construction of Model Inputs

Tracer Data

The release crane position, the time and duration of tracer releases, the emission rates of each gas, and the height of the tracer release above the local surface were recorded in release logs maintained by ARLFRO during the experiment at HBR. The survey data were used to determine the locations of the release point, which were expressed in the hill coordinate system, a polar grid (r,θ,z) centered at Tower A. The base elevation used in this system is 1600 m.

Plume Rise

The oil-fog generator produced enough heat flux to cause a thermally-induced rise in the oil-fog and co-located SF_6 plumes. A first attempt was made to calculate the effective release height of the SF_6 plume for model input by using a method devised by Halitsky (1961) for single-camera measurements of smoke plumes.

Analyses of the wind direction time series and wind speed and temperature profiles were also used to guide the estimate of the plume rise.

Wind Data

A "spline under tension" method, as discussed in Section 2.1, was used to interpolate wind speeds and directions between instrument levels on Tower A. The 5-minute prop wind speeds and directions from Tower A were first broken into wind components, and the components were interpolated to obtain the horizontal wind speed and direction at plume height for each 5-minute period.

For those 5-minute periods in which photographs taken from the 150-m tower were available, wind directions estimated from the photo images were substituted for the splined wind direction data. These photo-derived wind directions could only be estimated for the SF_6 release because only the SF_6 was emitted with the oil-fog.

A scalar average of the 5-minute interpolated wind speeds was used to form the 1-hour mean wind speed. A 1-hour vector average of unit vectors along each 5-minute wind direction was used to form the 1-hour mean wind direction.

TABLE 17. SHIS #2 HOURS SELECTED FOR INITIAL MODELING

Exp.	Date/Time	Release Location	$z_r(SF_6)$	Pattern	$z_r(CF_3Br)$	Pattern
4	11/0300-0400	216	30	1E	20	2S
4	11/0400-0500	216	40	1S	30	2S
5	12/0100-0200	203	30	6C	15	2C
5	12/0500-0600	203	20	1E	15	2C
6	13/0100-0200	111	30	6S	20	1C/N
8	15/0100-0200	215	10	1C	5	2E
8	15/0200-0300	215	10	5C	5	4C/S
8	15/0600-0700	215	30	1N	30	1N
10	22/0300-0400	A	50	6N	30	4C
10	22/0400-0500	A	70	3C	30	2N
11	23/0200-0300	203	40	5/4C	20	1E/S
11	23/0500-0600	A	50	6S	25	1S
12	24/0200-0300	A	75	7	40	1N
12	24/0600-0700	A	75	7	25	8
14	26/0300-0400	203	40	1S	20	2E
15	29/0100-0200	R80/A	20	1E	40	4C/7
15	29/0200-0300	R80/A	20	1S	40	3/7

TABLE 18. 17-HOUR DATA BASE SUMMARY STATISTICS

1. Number by release location

216/215	203	111	A	R80
10	8	2	12	2

2. Number by local release height

≤ 10m	11-20	21-30	31-40	41-50	> 50
4	9	8	7	3	3

3. Number by height of source above the ground

≤ 20m	21-30	31-40	41-50	51-60	> 61
2	2	8	6	2	14

4. Number by wind direction

S (>120°)	E (120-45)	N (<45)
9	19	6

5. Number by concentration pattern

	1	2	3	4	5	6	7	8
17 Hours								
#	13	7	2	3	2	4	2	1
%	38	21	6	9	6	12	6	3
Entire Data Set								
#	67	52	3	11	4	16	7	4
%	41	32	2	7	2	10	4	2

Critical Dividing-Streamline Height (H_c)

The prop wind speed and temperature profiles from Tower A were used to compute the 5-minute values of H_c by means of the integral formula presented in the CTMD First Milestone Report, and first suggested by Sheppard (1956). These 5-minute values were then averaged to 1-hour values. The effective height of HBR was taken to be 85 m.

Brunt-Vaisala Frequency (N)

For each 5-minute period, the Brunt-Vaisala frequency (N) was estimated at plume height by evaluating the temperature change along the splined temperature profile in the immediate vicinity ($z_r \pm 0.1$ m) of the plume height to obtain the local temperature gradient. These 5-minute values were then averaged to 1-hour values.

Stability Class

The Turner dispersion stability class was calculated from cloud cover and wind speed data. The cloud cover was estimated from photographs and the wind speed was a 1-hour scalar average measured by the props at the 10-m level on Tower A.

Turbulence Parameters

A comparison between the 5-m and 40-m turbulence data from the sonic and the prop systems (Table 19) at the same elevation proved that the two systems were inconsistent. Due to uncertainties with proper prop response corrections, the sonic data were used to calculate the turbulence parameters.

One-hour values of u, v and σ_w obtained from the NOAA/WPL sonic anemometers on Tower A at 5 m and 40 m were used to derive the vertical intensity of turbulence (i_z) at plume height. The sonic data were linearly interpolated to the plume height if this height was less than 40 m; otherwise the 40-m i_z was used. Sigma-w (σ_w) at plume height was calculated by multiplying the interpolated sonic i_z data with the Tower A propeller wind speed interpolated at plume height by means of the "spline under tension" algorithm used in the MDA (see Section 2). This methodology preserves the sonic i_z data within the model. Five-minute average sigma-v data were set equal to the 1-hour sigma-w data for input to the PDF form of CTDM(11083 and 11083-E).

5.1.3 Summary of Model Input Data

Table 20 lists for each tracer gas all of the inputs to the models evaluated with SHIS #2 data in this report. The time and date for each of the 17 experiment-hours is followed by the release location (r,θ), the emission rate (Q), the release height above the local ground elevation, the estimated plume rise, the effective plume elevation above the zero contour (1600 m MSL), the critical dividing-streamline height (H_c), the hourly average wind speed and direction, the Brunt-Vaisala frequency (N), the Turner Stability Class, and sigma-w (σ_w).

TABLE 19. COMPARISON OF WIND MEASUREMENTS AT 40 M FOR 17 HOGBACK STUDY HOURS

			1-Hour Vector Resultant							
			Speed (m/s)			Direction (degrees)			1-Hr σ_w (m/s)	
Experiment	Date '82	Hr (MDT)	Cup & Vane	Props	Sonic	Cup & Vane	Props	Sonic	Props	Sonic
4	10/11	03-04	0.51	0.87	0.36	63	69	78	.34	.18
		04-05	1.17	1.62	0.92	45	49	42	.35	.15
5	10/12	01-02	1.45	2.52	1.81	94	55	102	.36	.25
		05-06	1.62	0.37	0.84	220	175	210	.34	.12
6	10/13	01-02	2.47	2.97	1.20	66	67	106	.45	.19
8	10/15	01-02	0.19	0.77	0.27	192	74	283	.16	.09
		02-03	1.30	2.04	1.12	71	69	60	.16	.11
		06-07	1.17	1.46	1.35	153	113	150	.22	.23
10	10/22	03-04	0.57	0.72	0.75	189	99	176	.11	.13
		04-05	0.47	0.57	0.41	212	87	202	.13	.15
11	10/23	02-03	0.72	0.62	0.36	204	116	206	.09	.10
		05-06	1.76	2.58	1.78	86	81	80	.23	.35
12	10/24	02-03	1.37	1.39	1.38	166	130	138	.08	.10
		06-07	3.43	4.66	3.36	81	82	82	.22	.34
14	10/26	03-04	1.88	2.80	1.87	76	74	79	.22	.32
15	10/29	01-02	1.05	1.68	0.48	44	49	112	.14	.14
		02-03	2.09	2.97	1.94	62	97	74	.12	(.15)*

---

*2 periods (40 min) only.

These data are from preliminary versions of the measurements as reduced by NOAA/WPL amd NOAA/ARLFRO; sonic data to within ± 25% est.

TABLE 20. SUMMARY OF MODEL INPUT DATA FOR SF_6 AND CF_3Br RELEASES

	Experiment No. (Date)	End Time	Source Location r(m)	Source Location θ(°)	Emission (g/sec)	Release Height (m AGL)	Plume Rise (m)	Effective Source Elevation*(m)	H_c (m)	Average Wind Speed (ms^{-1})	Average Wind Direction (°)	N (s^{-1})	σ_w (ms^{-1})	Stability Class
SF_6														
	4 (10/11)	400	324.9	312.1	0.90	30	40	82.4	26	1.6	131.7	.0302	.787	F
	4	500	324.9	312.1	0.76	40	41	93.4	14	1.9	104.5	.0295	.304	E
	5 (10/12)	200	454.8	313.0	0.54	30	15	62.4	32	2.5	86.0	.0311	.350	F
	5	600	454.8	313.0	0.60	20	50	87.4	48	1.3	109.5	.0289	.178	F
	6 (10/13)	200	391.7	271.7	0.32	30	15	57.5	22	3.1	74.5	.0347	.484	F
	8 (10/15)	200	334.9	312.2	0.24	10	68	90.9	48	1.6	114.8	.0396	.515	F
	8	300	334.9	312.2	0.24	10	47	69.9	37	2.5	63.8	.0350	.250	F
	8	700	334.9	312.2	0.23	30	30	72.9	39	2.6	132.3	.0342	.445	F
	10 (10/22)	400	0.0	0.0	0.23	50	10	63.4	50	1.5	108.7	.0324	.267	F
	10	500	0.0	0.0	0.21	70	10	83.4	59	2.1	107.6	.0366	.771	F
	11 (10/23)	300	454.8	313.0	0.27	40	15	72.4	54	1.2	142.0	.0276	.343	F
	11	600	0.0	0.0	0.29	50	5	58.4	27	3.6	98.3	.0318	.713	F
	12 (10/24)	300	0.0	0.0	0.31	75	0	78.4	46	3.2	121.9	.0392	.221	F
	12	700	0.0	0.0	0.31	75	5	83.4	20	5.5	98.8	.0278	.556	F
	14 (10/26)	400	454.8	313.0	0.30	40	10	67.4	18	3.4	97.7	.0297	.585	D
	15 (10/29)	200	574.9	330.1	0.30	20	45	86.7	44	1.0	110.7	.0188	.279	F
	15	300	574.9	330.1	0.30	20	0	41.7	24	2.8	31.2	.0533	.222	E
CF_3Br														
	4 (10/11)	400	324.9	312.1	1.42	20	0	32.4	26	1.3	3.9	.0173	.391	F
	4	500	324.9	312.1	1.23	30	0	42.4	14	1.4	54.4	.0225	.206	E
	5 (10/12)	200	454.8	313.0	1.31	15	0	32.4	32	1.3	39.9	.0240	.148	F
	5	600	454.8	313.0	1.33	15	0	32.4	48	1.2	164.0	.0415	.220	F
	6 (10/13)	200	391.7	271.7	1.35	20	0	32.5	22	2.7	35.9	.0424	.390	F
	8 (10/15)	200	334.9	312.2	1.00	5	0	17.9	48	1.9	15.7	.1038	.165	F
	8	300	334.9	312.2	1.00	5	0	17.9	37	1.9	19.0	.0658	.160	F

---

*Plume elevation (after plume rise) above 1600 m MSL.

TABLE 20. SUMMARY OF MODEL INPUT DATA FOR SF_6 AND CF_3Br RELEASES (Continued)

Experiment No. (Date)	End Time	Source Location r(m)	Source Location θ(°)	Emission (g/sec)	Release Height (m AGL)	Plume Rise (m)	Effective Source Elevation*(m)	H_c (m)	Average Wind Speed (ms^{-1})	Average Wind Direction (°)	N (s^{-1})	σ_w (ms^{-1})	Stability Class
CF_3Br (Cont.)													
8	700	334.9	312.2	0.96	30	0	42.9	39	1.4	149.9	.0280	.297	F
10 (10/22)	400	0.0	0.0	1.53	30	0	33.4	50	0.9	170.1	.0188	.228	F
10	500	0.0	0.0	1.31	30	0	33.4	59	0.9	177.0	.0301	.291	F
11 (10/23)	300	454.8	313.0	0.94	20	0	37.4	54	1.1	79.1	.0432	.190	F
11	600	0.0	0.0	1.31	25	0	28.4	27	1.3	77.8	.0257	.236	F
12 (10/24)	300	0.0	0.0	1.35	40	0	43.4	46	1.6	132.6	.0437	.110	F
12	700	0.0	0.0	1.32	25	0	28.4	20	4.9	90.0	.0399	.573	F
14 (10/26)	400	454.8	313.0	0.93	20	0	37.4	18	1.7	59.2	.0198	.342	D
15 (10/29)	200	0.0	0.0	1.36	40	0	43.4	44	1.8	63.1	.0275	.502	F
15	300	0.0	0.0	1.36	40	0	43.4	24	3.0	76.2	.0442	.228	E

---

*Plume elevation (after plume rise) above 1600 m MSL.

5.2 Complex Terrain Models Evaluated

Valley, COMPLEX I, COMPLEX II, CTDM(11083), and CTDM(11083-E) have been run on the preliminary 17-hour data base for SHIS #2 at HBR. Valley, COMPLEX I, and COMPLEX II required no modifications for application to HBR, aside from a change in the sampler grid data. CTDM, however, required several changes.

CTDM needs terrain data to select stagnation streamlines, impingement points, and to identify which receptors are subject to Wrap-type calculations. For CCB, the polar coordinate system is fixed at the center of the hill, and a general terrain profile is specifed by

$$a(h) = 970\ h^{-0.38} \tag{59}$$

where h is measured in meters from the 944.9 m MSL height contour. For HBR, the polar coordinate system is centered at Tower A, and the hill profile perpendicular to the ridge from Tower A is assumed to extend to infinity along the local tangent to the ridge. The hill profile is fit by the equation

$$h = -.42\ (807-r)\ (1-\exp(-253/(807-r))) + 91 \tag{60}$$

where r is measured from Tower A along the perpendicular to the ridge, and h is the terrain height above 1600 m MSL. Note that Tower A lies 807 m from the ridge top, at an elevation of 1603.6 m ASL.

Figure 86 summarizes the HBR geometry contained in CTDM. The height contours across the sampler grid on the eastward face of HBR define a tangent plane oriented approximately 27° from true north. The ridge is considered to be two-dimensional. For Lift computations, the local radius of curvature is set to infinity, and no streamline deflection is allowed in the horizontal. For Wrap computations, the stagnation streamline is defined to follow a 117° wind, and the distance to a receptor is the sum of the distance to the receptor-height contour along 117°, and the distance measured along the ridge from this point of intersection to the receptor. If a receptor lies on the lee side of HBR, then no Wrap computations are made because the layer below H_c is assumed to remain on the windward side of the ridge. Receptor heights are adjusted to equal the dividing-streamline height for performing a Lift computation at lee-side receptors below H_c.

5.3 Overall Performance Statistics

The data listed in Table 21 were used to run CTDM(11083), CTDM(11083-E), Valley, COMPLEX I and COMPLEX II. The model calculations were compared to 1-hour average SF_6 and CF_3Br concentrations taken from the 17-hour HBR data base. Table 21 summarizes the residual statistics. The results are based on both tracer gases (17 hours each). Columns labeled "Peak Concentrations" refer to the highest C_o/Q and C_p/Q values unpaired in space, but paired in time, and the columns labeled "All Concentrations" refer to values paired in space and time. Tables 22 through 25 give the

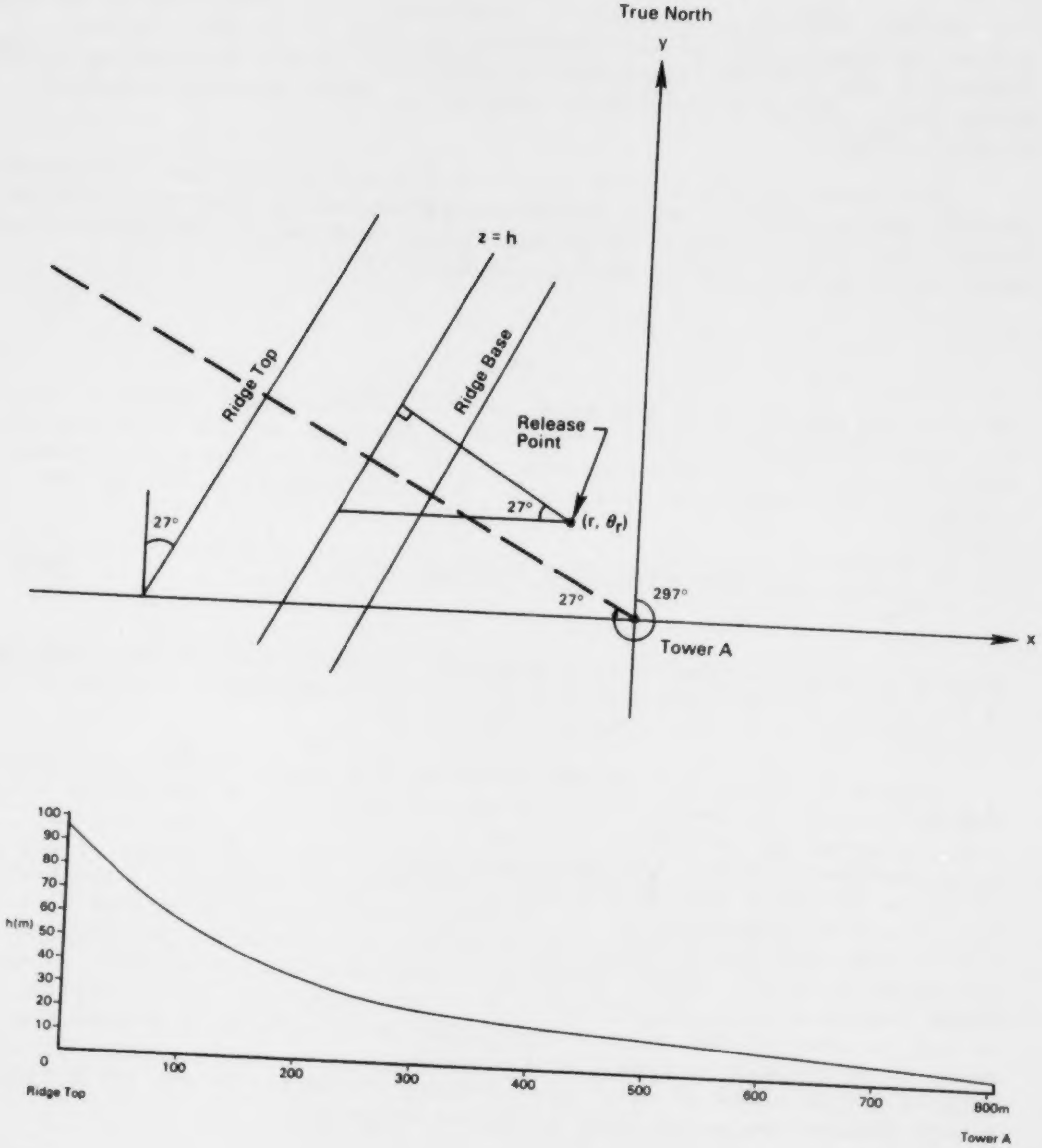
True North
y
z = h
Ridge Top
Ridge Base
Release Point
27°
27°
(r, θ_r)
27°
297°
Tower A
x
100
90
80
70
60
h(m)
50
40
30
20
10
0
Ridge Top
100
200
300
400
500
600
700
800m
Tower A

Figure 86. Height section and orientation of idealized HBR relative to Tower A, as represented in CTDM.

TABLE 21. MODEL PERFORMANCE STATISTICS, 17-HOUR HBR DATA BASE

	Peak Concentrations						All Concentrations		
	m_a	s_a	r_a	m_g	s_g	r_g	m_a	s_a	r_a
CTDM(11083-E)	27.5	71.1	4.6	2.00 (2.35)	5.7 (5.9)	1.91	7.6	25.3	4.65
CTDM(11083)	28.4	70.6	4.6	2.05 (2.5)	4.3 (5.11)	1.24	7.0	25.4	3.96
Valley	-34.3	87.1	3.3	0.24	3.7	2.49*	-	-	-
COMPLEX I	-61.0	81.9	1.03	0.26 (0.19)	4.1 (2.5)	1.45	-1.6	41.0	1.09
COMPLEX II	-266.0	275.2	0.94	0.11 (0.09)	12.4 (4.4)	2.45	-2.1	72.2	1.03

Notes: 1. M_a s_a, r_a have units of μs/m^3
2. ( ) denotes m_g and s_g values s_g calculated with C_p = 0 values removed.

* Valley does better at HBR on the r_a measure because the low releases ran into the hill at short range; therefore, 10/ $\sigma_z(x)$ was large at times. This actually gave Valley a larger $\sigma(C_p)$ than CTDM!

results of the 34 individual hourly simulations for all the models except Valley. It should be emphasized that these results are very preliminary because the meteorological measurements used to derive the model input need further editing and refinement.

The residual statistics show that CTDM(11083) and CTDM(11083-E) underestimate peak C_o/Q values by roughly a factor of 2.0. On the other hand, Valley and the COMPLEX models overestimate the peak observed values by roughly a factor of 4.0 or more. m_a for the space/time-paired concentrations is lowest for the two COMPLEX models. The noise and resolution statistics are large for all the model calculations.

The tables of the results for each hour show that the overall performance statistics are generally dominated by extreme values. For example, Table 23 shows that for seven of the 34 tracer-hours the ratio of the peak C_o to the peak C_p is greater than 9.0. The input wind directions and modeled concentrations for these hours suggest that CTDM (11083-E) largely missed the hill. Similarly, Table 25 shows that COMPLEX I completely missed the hill for six of the hours.

Several of the problem simulations occurred for wind directions nearly parallel to HBR and for releases below the calculated H_c. Further analysis of the variability of the 5-minute average wind directions for a few hours suggests that CTDM should be reformulated for releases below H_c at HBR. For example:

- Is the concept of a single stagnation streamline wind direction of 117° relevant for these highly variable flows?
- Should the PDF form or Gaussian form of CTDM be applied?
- How should the recirculation of pollutant material from the south (or north) of the sample grid be handled by the model?
- In addition to the data refinement issue, are the Tower A data representative of the plume dispersion conditions, given the highly variable nature of the flow below H_c?

Experiment 11 (0200-0300) exemplifies some of these concerns. Estimates of 5-minute winds for the release height and from the 5-m, 10-m and 30-m levels of Tower B are listed in Table 26. The wind data estimated for the release height indicate that the CF_3Br plume should have impacted on HBR for only about a 10-15 minute period during the middle of the hour. The Tower B 10-m data suggest a more prolonged impact, from about 0215 through 0245 (see Figure 56). In any event, the CF_3Br plume was probably swept from the south side of HBR to north of the sampler grid during the course of the hour, so that the samplers were influenced by plume material for a considerable part of the hour.

The PDF reflects the wide range (18.2 - 225.0°) of wind directions measured on Tower A; hence, CTDM(11083) and CTDM(11083-E) produced very low concentrations ($\overline{C}_p$ = 0.6 and 0.2, respectively). The COMPLEX I and COMPLEX II models produced relatively high concentrations ($\overline{C}_p$ = 50.3 and

TABLE 22. RESULTS OF HOURLY CTDM(11083-E) SIMULATIONS

(17-HOUR HBR DATA BASE)

Exp	Hr	#	$\overline{Co}$	σ(Co)	CoMax	$\overline{Cp}$	σ(Cp)	CpMax	CoMax/ CpMax	$\overline{Co-Cp}$	σ(Co-Cp)
SF_6											
4	4	81	10.6	7.5	40.1	3.0	2.4	9.2	4.38	7.5	7.2
4	5	77	12.5	11.9	46.7	1.1	1.1	4.8	9.74	11.5	11.9
5	2	69	3.6	4.4	19.6	8.2	10.0	38.0	.51	-4.5	8.9
5	6	73	22.6	15.6	78.3	2.8	2.9	10.6	7.38	19.8	14.6
6	2	75	.7	1.0	5.1	2.1	2.9	11.7	.43	-1.3	3.0
8	2	65	6.1	3.7	20.9	3.5	2.7	8.1	2.57	2.7	3.9
8	3	77	2.6	2.4	13.1	2.1	2.1	6.1	2.15	.4	2.9
8	7	85	4.2	7.7	40.5	3.5	6.1	22.4	1.81	.7	5.3
10	4	82	2.6	3.6	16.3	7.1	7.7	28.5	.57	-4.5	8.5
10	5	75	1.9	2.0	10.5	1.1	1.2	3.7	2.81	.7	1.8
11	3	89	2.8	1.9	12.6	4.8	8.9	36.4	.35	-1.9	9.0
11	6	88	2.7	2.9	12.5	1.6	1.6	6.3	1.97	1.2	2.7
12	3	80	.1	.6	4.8	3.4	3.4	10.3	.46	-3.4	3.5
12	7	86	.0	.1	1.1	1.2	1.7	4.9	.23	-1.2	1.7
14	4	79	7.1	4.9	20.0	3.1	3.3	13.4	1.49	4.0	5.3
15	2	74	11.5	5.5	24.5	6.2	11.2	44.1	.56	5.3	12.1
15	3	86	17.2	18.8	55.9	3.7	6.0	26.2	2.13	13.5	16.7
CF_3Br											
4	4	78	22.4	27.2	116.7	3.9	2.7	16.2	7.18	18.4	27.3
4	5	67	.5	1.6	9.1	5.8	10.0	35.4	.26	-5.3	9.7
5	2	69	21.9	22.4	82.9	4.8	8.0	62.9	1.32	17.0	23.2
5	6	74	86.8	77.5	386.6	1.2	1.7	11.9	32.53	85.6	76.4
6	2	75	8.5	6.2	22.8	2.7	2.8	17.5	1.30	5.8	6.0
8	2	65	1.1	.7	5.3	.0	.0	.0	9999.99	1.1	.7
8	3	78	1.4	3.4	16.1	.0	.0	.1	286.28	1.4	3.4
8	7	84	7.1	11.2	45.1	3.3	5.0	20.0	2.26	3.8	8.5
10	4	83	.7	1.8	14.6	.3	.3	1.0	14.83	.4	1.9
10	5	76	10.9	11.2	47.0	.3	.3	.9	49.73	10.5	11.2
11	3	88	60.8	43.9	167.2	.2	.2	.8	216.75	60.6	44.0
11	6	89	2.3	1.5	8.3	2.1	1.4	4.9	1.70	.2	1.9
12	3	84	4.0	4.9	14.8	4.4	3.5	13.5	1.10	-.4	5.3
12	7	84	.2	.8	5.0	1.5	2.5	8.6	.58	-1.3	2.7
14	4	79	20.1	22.8	115.6	9.2	9.8	51.3	2.25	10.9	20.3
15	2	73	.3	.8	5.6	.3	.5	2.2	2.59	.0	1.0
15	3	83	.1	.4	4.0	1.7	4.3	23.4	.17	-1.6	4.3

TABLE 23. RESULTS OF HOURLY CTDM(11083) SIMULATIONS

(17-HOUR HBR DATA BASE)

Exp	Hr	#	$\overline{Co}$	σ(Co)	CoMax	$\overline{Cp}$	σ(Cp)	CpMax	CoMax/ CpMax	$\overline{Co-Cp}$	σ(Co-Cp)
SF_6											
4	4	81	10.6	7.5	40.1	3.4	2.3	8.7	4.61	7.2	7.0
4	5	77	12.5	11.9	46.7	.1	.1	.4	128.93	12.5	11.9
5	2	69	3.6	4.4	19.6	5.6	6.3	18.4	1.07	-2.0	5.4
5	6	73	22.6	15.6	78.3	.9	1.0	3.2	24.77	21.7	15.2
6	2	75	.7	1.0	5.1	1.5	2.2	8.9	.58	-.8	2.2
8	2	65	6.1	3.7	20.9	3.0	2.3	6.7	3.14	3.1	3.7
8	3	77	2.6	2.4	13.1	.8	.9	3.0	4.40	1.7	2.3
8	7	85	4.2	7.7	40.5	2.9	4.8	14.4	2.82	1.3	4.8
10	4	82	2.6	3.6	16.3	10.1	10.0	28.3	.58	-7.5	10.3
10	5	75	1.9	2.0	10.5	1.6	1.6	3.9	2.68	.3	2.0
11	3	89	2.8	1.9	12.6	6.7	12.0	37.8	.33	-3.8	12.0
11	6	88	2.7	2.9	12.5	2.1	2.1	6.2	2.00	.6	2.5
12	3	80	.1	.6	4.8	1.0	.9	3.4	1.43	-.9	1.1
12	7	86	.0	.1	1.1	.4	.6	2.0	.56	-.4	.6
14	4	79	7.1	4.9	20.0	1.6	1.4	5.0	3.97	5.6	4.7
15	2	74	11.5	5.5	24.5	4.6	7.6	26.3	.93	6.9	9.2
15	3	86	17.2	18.8	55.9	3.0	5.1	21.9	2.55	14.2	16.6
CF_3Br											
4	4	78	22.4	27.2	116.7	6.3	3.5	19.6	5.96	16.0	27.5
4	5	67	.5	1.6	9.1	5.2	8.7	24.9	.37	-4.7	8.5
5	2	69	21.9	22.4	82.9	8.2	10.1	62.9	1.32	13.6	25.7
5	6	74	86.8	77.5	386.6	2.5	3.1	12.3	31.55	84.3	76.5
6	2	75	8.5	6.2	22.8	4.1	3.5	17.5	1.30	4.4	6.1
8	2	65	1.1	.7	5.3	.0	.0	.0	9999.99	1.1	.7
8	3	78	1.4	3.4	16.1	.0	.0	.2	65.35	1.4	3.4
8	7	84	7.1	11.2	45.1	6.5	10.1	39.8	1.13	.6	8.5
10	4	83	.7	1.8	14.6	.9	.8	2.6	5.56	-.2	2.2
10	5	76	10.9	11.2	47.0	.9	.9	3.0	15.42	10.0	11.2
11	3	88	60.8	43.9	167.2	.6	.6	2.6	65.38	60.2	44.1
11	6	89	2.3	1.5	8.3	4.5	2.9	10.4	.80	-2.2	3.1
12	3	84	4.0	4.9	14.8	11.7	9.7	37.8	.39	-7.7	9.8
12	7	84	.2	.8	5.0	2.9	4.8	14.8	.34	-2.7	4.9
14	4	79	20.1	22.8	115.6	13.2	11.3	51.0	2.27	6.9	21.5
15	2	73	.3	.6	5.6	.7	1.2	4.8	1.17	-.4	1.4
15	3	83	.1	.4	4.0	1.4	3.7	19.6	.20	-1.4	3.7

TABLE 24. RESULTS OF HOURLY COMPLEX I SIMULATIONS

(17-HOUR HBR DATA BASE)

Exp	Hr	#	$\overline{Co}$	σ(Co)	CoMax	$\overline{Cp}$	σ(Cp)	CpMax	CoMax/ CpMax	$\overline{Co-Cp}$	σ(Co-Cp)
SF_6											
4	4	81	10.6	7.5	40.1	16.3	46.6	162.4	.25	-5.8	46.3
4	5	77	12.5	11.9	46.7	18.0	58.5	133.7	.35	-5.5	39.0
5	2	69	3.6	4.4	19.6	20.0	38.6	108.6	.16	-16.4	37.5
5	6	73	22.6	15.6	78.3	16.5	51.0	210.9	.37	6.1	44.0
6	2	75	.7	1.0	5.1	1.9	11.3	74.3	.07	-1.2	10.9
8	2	65	6.1	3.7	20.9	11.8	35.9	158.3	.13	-5.7	33.8
8	3	77	2.6	2.4	13.1	7.9	20.3	80.1	.16	-5.3	19.7
8	7	85	4.2	7.7	40.5	9.5	27.6	99.8	.41	-5.3	22.4
10	4	82	2.6	3.6	16.3	37.1	47.9	125.4	.13	-34.6	47.8
10	5	75	1.9	2.0	10.5	14.3	25.6	77.8	.14	-12.4	24.8
11	3	89	2.8	1.9	12.6	17.4	59.3	225.5	.06	-14.5	59.5
11	6	88	2.7	2.9	12.5	9.5	16.4	51.3	.24	-6.8	15.4
12	3	80	.1	.6	4.8	11.0	18.8	51.1	.09	-10.9	18.8
12	7	86	.0	.1	1.1	5.2	9.8	28.3	.04	-5.2	9.9
14	4	79	7.1	4.9	20.0	2.9	7.7	26.1	.77	4.2	7.3
15	2	74	11.5	5.5	24.5	17.5	65.1	272.3	.09	-6.0	65.0
15	3	86	17.2	18.8	55.9	7.7	21.1	98.6	.57	9.5	25.0
CF_3Br											
4	4	78	22.4	27.2	116.7	.0	.0	.0	9999.99	22.4	27.2
4	5	67	.5	1.6	9.1	10.5	33.5	136.6	.07	-10.0	33.3
5	2	69	21.9	22.4	82.9	14.8	43.2	190.9	.43	7.1	47.3
5	6	74	86.8	77.5	386.6	9.4	40.6	210.2	1.84	77.5	83.9
6	2	75	8.5	6.2	22.8	.0	.0	.0	9999.99	8.5	6.2
8	2	65	1.1	.7	5.3	.0	.0	.0	9999.99	1.1	.7
8	3	78	1.4	3.4	16.1	.0	.0	.0	9999.99	1.4	3.4
8	7	84	7.1	11.2	45.1	16.8	47.6	181.3	.25	-9.8	45.4
10	4	83	.7	1.8	14.6	.0	.0	.0	9999.99	.7	1.8
10	5	76	10.9	11.2	47.0	.0	.0	.0	9999.99	10.9	11.2
11	3	88	60.8	43.9	167.2	50.3	84.2	223.9	.75	10.5	79.9
11	6	89	2.3	1.5	8.3	14.1	36.4	142.4	.06	-11.9	36.3
12	3	84	4.0	4.9	14.8	23.4	39.9	114.3	.13	-19.4	36.8
12	7	84	.2	.8	5.0	7.0	12.9	40.9	.12	-6.8	13.0
14	4	79	20.1	22.8	115.6	29.2	57.1	234.5	.49	-9.1	57.0
15	2	73	.3	.8	5.6	2.2	10.7	60.8	.09	-1.9	10.6
15	3	83	.1	.4	4.0	2.4	8.7	42.5	.09	-2.4	8.8

TABLE 25. RESULTS OF HOURLY COMPLEX II SIMULATIONS

(17-HOUR HBR DATA BASE)

Exp	Hr	#	$\overline{Co}$	σ(Co)	CoMax	$\overline{Cp}$	σ(Cp)	CpMax	CoMax/ CpMax	$\overline{Co-Cp}$	σ(Co-Cp)
SF_6											
4	4	81	10.6	7.5	40.1	16.6	84.0	597.5	.07	-6.0	83.9
4	5	77	12.5	11.9	46.7	14.8	49.1	296.9	.16	-2.3	49.9
5	2	69	3.6	4.4	19.6	20.4	68.0	394.0	.05	-16.8	67.0
5	6	73	22.6	15.6	78.3	9.5	44.4	310.9	.25	13.1	46.2
6	2	75	.7	1.0	5.1	.0	.1	.7	7.60	.7	1.0
8	2	65	6.1	3.7	20.9	6.7	49.9	405.5	.05	-.6	49.4
8	3	77	2.6	2.4	13.1	5.3	27.1	198.6	.07	-2.7	27.0
8	7	85	4.2	7.7	40.5	6.9	39.1	286.5	.14	-2.7	36.4
10	4	82	2.6	3.6	16.3	44.9	112.4	500.3	.03	-42.3	112.0
10	5	75	1.9	2.0	10.5	19.5	62.6	335.7	.03	-17.6	61.7
11	3	89	2.8	1.9	12.6	20.2	116.7	875.6	.01	-17.4	116.8
11	6	88	2.7	2.9	12.5	8.9	29.9	160.4	.06	-6.2	29.8
12	3	80	.1	.6	4.8	11.8	36.6	187.0	.03	-11.7	36.6
12	7	86	.0	.1	1.1	6.0	21.8	117.0	.01	-6.0	21.8
14	4	79	7.1	4.9	20.0	2.2	7.3	39.0	.51	4.9	7.4
15	2	74	11.5	5.5	24.5	20.2	131.4	1076.7	.02	-8.7	131.4
15	3	86	17.2	18.8	55.9	4.8	14.7	64.9	.86	12.5	19.7
CF_3Br											
4	4	78	22.4	27.2	116.7	.0	.0	.0	9999.99	22.4	27.2
4	5	67	.5	1.6	9.1	12.8	56.2	334.0	.03	-12.3	56.1
5	2	69	21.9	22.4	82.9	22.0	89.6	478.5	.17	-.2	92.5
5	6	74	86.8	77.5	386.6	9.3	78.2	677.6	.57	77.5	111.9
6	2	75	8.5	6.2	22.8	.0	.0	.0	9999.99	8.5	6.2
8	2	65	1.1	.7	5.3	.0	.0	.0	9999.99	1.1	.7
8	3	78	1.4	3.4	16.1	.0	.0	.0	9999.99	1.4	3.4
8	7	84	7.1	11.2	45.1	21.9	103.0	628.5	.07	-14.9	102.3
10	4	83	.7	1.8	14.6	.0	.0	.0	9999.99	.7	1.8
10	5	76	10.9	11.2	47.0	.0	.0	.0	9999.99	10.9	11.2
11	3	88	60.8	43.9	167.2	62.4	202.1	945.8	.18	-1.6	197.1
11	6	89	2.3	1.5	8.3	12.1	72.8	553.6	.01	-9.9	72.7
12	3	84	4.0	4.9	14.8	17.9	70.7	479.1	.03	-13.9	69.2
12	7	84	.2	.8	5.0	6.0	21.0	122.8	.04	-5.8	21.1
14	4	79	20.1	22.8	115.6	31.7	74.6	376.8	.31	-11.6	75.9
15	2	73	.3	.8	5.6	.2	1.9	16.0	.35	.1	1.9
15	3	83	.1	.4	4.0	2.1	11.6	76.2	.05	-2.1	11.6

TABLE 26. EXPERIMENT 11 (0200-0300) FIVE-MINUTE AVERAGE WINDS*

Time	CF_3Br Release Height (20 m)	Tower B Props		
		5 m	10 m	30 m
0205	19.7/0.8	341.6/0.1	270.9/0.2	170.6/0.5
0210	18.2/1.0	82.2/0.1	270.4/0.2	187.4/0.7
0215	21.4/1.3	35.4/0.3	79.9/0.4	170.5/0.4
0220	22.3/1.6	15.7/1.1	46.4/0.7	69.8/0.3
0225	36.8/2.0	23.5/0.9	50.4/0.9	56.9/0.7
0230	53.6/1.5	36.9/0.4	64.5/0.9	70.6/0.7
0235	95.1/0.8	173.1/0.3	86.2/0.5	94.9/0.7
0240	157.5/0.7	151.0/0.3	63.6/0.6	93.6/0.6
0245	184.5/1.0	150.4/0.3	11.8/0.2	168.8/0.5
0250	200.0/0.8	175.8/0.6	237.2/0.3	187.2/1.2
0255	225.0/0.9	170.6/0.6	241.2/0.5	189.5/1.8
0300	197.0/1.2	197.3/0.6	236.9/0.5	181.8/1.5

---

*Degrees/m sec^{-1}

62.4, respectively) because of the narrower simulated crosswind distribution of the CF_3Br about the mean direction.

It is obvious that the CTDM(11083-E) calculations would have better simulated the observations if the Tower B 10-m winds had been used. Photographs and visual observations of the oil-fog plume during other experiments suggest that during highly variable wind situations aged plume material is often transported from the south (or the north) over the sampling array. This is probably what is happening during experiment 11 (0200-0300). This type of "sloshing" phenomenon is not handled by the current models and should be considered during subsequent model development efforts.

Because of the uncertainty in modeling the CF_3Br data with the wind directions based on Tower A data interpolated to release height, a second series of model runs was made with the bi-variate Gaussian form of CTDM(11083-E), assuming that the mean wind was directed from the source to the area of greatest observed concentrations on the ridge. These changes tend to place the peak of the horizontal distribution closer to the stagnation wind direction assumed in the model for material below H_c, and they place the peak of the distribution for material above H_c at those receptors with the greater observed concentrations.

As expected, these changes cause peak modeled concentrations to increase considerably in many cases. The net effect can be seen in the overall performance statistics. When the results of modeling the CF_3Br data with the bi-variate Gaussian form of CTDM(11083-E) and the modified mean wind directions are combined with the previous model results for SF_6, the mean bias (mg) of the residuals of peak concentrations is nearly 1.0, although the noise remains large ($s_g = 4.3$, $s_a = 75.6$). The resolution improves considerably: r_a (peaks) drops from 4.6 to 1.5; r_a (all concentrations) drops from 4.7 to 2.2; and r_g (peaks) drops from 1.6 to 1.2. This exercise serves to demonstrate that there is plenty of latitude for improving the performance of CTDM at HBR.

In summary, the results of the initial HBR modeling are tentative. None of the models reproduce the observations very well and no model is better than any other. Several new issues must be considered in simulating dispersion below H_c at the Hogback.

SECTION 6

SUMMARY, CONCLUSIONS, AND RECOMMENDATIONS FOR FURTHER STUDY

This Third Milestone Report has documented the evaluation of several complex terrain models using the complete SHIS #1 MDA. The model performance measures suggest that CTDM(11083-E) is significantly better than the other models. The report also describes in detail the further progress made to date in analyzing the SHIS #1 experiment-hours and in improving CTDM. It provides an overview of the SHIS #2 at the Hogback and describes the preliminary results from this field experiment as well as the modeling of a 17-hour subset of the HBR data base.

6.1 Principal Accomplishments and Conclusions

The Small Hill Impaction Study #2

The Hogback Ridge field study has achieved its objective of extending the modeling data base to include a detailed set of meteorological data, tracer concentrations, lidar data and photographic data from a two-dimensional ridge site. The field program has produced a set of about 179 tracer-hours for model testing, evaluation and refinement.

An initial analysis of the SHIS #2 data base suggests that the concept of a critical dividing-streamline height is appropriate for stable flows toward HBR. Tracer gas released below H_c disperses in a highly variable, "blocked" flow and produces relatively large ground-level concentrations on the windward face of the ridge. Tracer gas emitted above H_c disperses in a flow that travels over the ridge and produces peak ground-level concentrations near the ridge crest and on its lee side.

Like SHIS #1, SHIS #2 has verified the basic concepts of the experimental design. The release of gaseous and visible tracers from a mobile crane or fixed tower, using real-time meteorological data to guide the selection of release locations and heights, has resulted in a data base that covers a wide variety of dispersion conditions and concentration patterns.

The meteorological data from four towers were archived in real-time via an onsite system of minicomputers. During the first few experiments, it became apparent that the archived data contained noise. Several subsequent modifications to the data system were successful in reducing this noise. ARLFRO and ERT scientists are currently working on eliminating the noise from all of the archived data. Initial editing suggests that most of the noise can be removed although there are subtle high frequency effects that need further investigation. The latter effects will have no influence on the mean meteorological data but may degrade the turbulence statistics and covariances.

The SHIS #1 Modelers' Data Archive (MDA)

A Modelers' Data Archive (MDA) has been prepared and submitted to the EPA Project Officer. It is intended to be used by modelers in simulating concentrations at Cinder Cone Butte and is available from the Project Officer. The MDA consists of meteorological data that were objectively interpolated from the Tower A measurements specifically for the heights of release of the SF_6 and CF_3Br tracer gases. It also includes hourly emission rates and ground-level tracer gas concentrations. The MDA is continually evolving to include the meteorological data that are found to be most representative of dispersion conditions at plume height. As plume photographs, lidar data, and meteorological data are analyzed further, the MDA will be supplemented and changes will be submitted to the Project Officer.

The Complex Terrain Dispersion Model (CTDM)

The Lift and Wrap models reported in the Second Milestone Report have been combined into one model, the Complex Terrain Dispersion Model. CTDM represents the first step in developing a practical regulatory model. It was designed to combine both "Wrap" and "Lift" flow and dispersion assumptions so that a plume near H_c would exhibit characteristics consistent with both, and it was designed to provide a better method for treating surface reflection of plume material in complex terrain. Two versions of CTDM were prepared for testing: CTDM (11083) and CTDM (11083-E). 'E' denotes an enhancement to the effective size of σ_z over the terrain. This enhancement is similar in some respects to the "terrain factor" used in other models such as COMPLEX I and COMPLEX II.

Comparative Model Performance Evaluations

CTDM(11083-E), CTDM(11083), Valley, COMPLEX I and COMPLEX II computations of 1-hour average SF_6 and CF_3Br concentrations were compared with measured values from 153 SHIS #1 tracer hours. The model performance measures indicate that CTDM(11083-E) performs significantly better than the other models. However, both CTDM(11083-E) and CTDM(11083) tend to underestimate the peak observed concentrations on average. Yet the bias of the residuals based on predicted and observed concentrations paired in space and time is lowest for CTDM(11083-E).

Valley and the two COMPLEX models tend to overestimate the peak observed concentrations on average, and have higher biases than the two CTDM models. The noise and resolution statistics for all the models are large and, in short, there is still substantial room for model improvement.

Twelve hours from Experiments 201 and 210 were used to test certain MDA modifications suggested by detailed case-studies, and also to gauge the importance of simulating the 5-minute sequence of meteorology in obtaining 1-hour average concentration estimates with CTDM(11083-E). The results indicate that the MDA modifications could significantly improve overall model performance, but that simulating each 5-minute period of an hour does not consistently improve the hourly concentration estimates.

Investigations of Plume Growth

Detailed analyses of the Tower A turbulence intensity data, lidar data, and photographic data collected during CCB Experiments 201 and 210, as well as comparisons of i_z data with lidar measurements from the other experiments, have shown that the following expression for σ_z adequately simulates plume growth upwind of CCB to distances of about 1 km:

$$\sigma_z = \frac{\sigma_w t}{(1 + t/2T_L)^{0.5}}$$

where $T_L = \gamma^2/N$.

The data suggest that $\gamma \sim 0.5$, which is consistent with the Pearson et al. (1981) estimate that γ, a molecular exchange coefficient, could range from 0.1 to 0.8.

CTDM Modifications and Testing

The case-study analyses of SHIS #1 Experiments 201 and 210 have suggested three principal areas for modifying CTDM(11083):

- An enhancement in the size of the effective σ_z over the hill is required for the part of the plume that diffuses or is released above H_c.
- The form of this enhancement must recognize the relative importance of increased plume dilution and decreased streamline heights above the surface, and it must include the effects of lee waves.
- A more nearly continuous transition between Wrap and Lift computations is needed near H_c.

These model modifications were formulated and implemented to create CTDM(14083). Because a portion of the formulation was designed on the basis of the results of case-study analyses of Experiments 201 and 210, CTDM(14083) was tested on the complete 153-hour MDA as well as on the twelve hours from Experiments 201 and 210 so that an overall comparison of model performance with CTDM(11083-E) could be made. The resulting measures of model performance (m_a, s_a, r_a, m_g, s_g, r_g) were nearly the same for CTDM(11083-E) and CTDM(14083) so that CTDM(14083), when using the initial MDA, is not a significant improvement over CTDM(11083-E). However, the comparison using the twelve case-study hours indicated that the placement of peak concentrations is improved significantly, even though there appears to be a need to include some degree of plume dilution upwind of the hill in both the Lift and Wrap modules.

Preliminary Modeling of the SHIS #2 Data Base

CTDM(11083), CTDM(11083-E), Valley, COMPLEX I, and COMPLEX II calculations of 1-hour average SF_6 and CF_3Br concentrations were compared with concentrations obtained for 17 SHIS #2 hours (34 tracer-hours). The performance evaluations show that none of the models simulates the observations very well. CTDM(11083) and CTDM(11083-E) underestimate the peak observations by roughly a factor of 2.0; the other models overestimate the concentrations by about a factor of 4.0. The performance statistics for all models show a great deal of noise.

Several questions arise from an analysis of the model simulations:

- How relevant is the concept of a single stagnation streamline (as in Wrap)?
- Does the recirculation of tracer material from the south (or north) of the HBR target area affect measured concentrations? If so, how can this phenomenon be modeled?
- How can meteorological data be selected to represent the highly variable flow below H_c?

These questions must be addressed in the subsequent model development efforts. It also should be emphasized that the modeling results are preliminary because of the problems with the tower meteorological data.

6.2 Recommendations for Further Study

Further analysis of the SHIS #1 and SHIS #2 data bases are required to improve and test CTDM and to extend it to ridge and other terrain settings. These analyses must be supplemented by new fluid modeling investigations.

6.2.1 The SHIS #1 Data Base

The case-study approach to analyzing the CCB data should continue. Experiments 201 and 210 have provided insight on refining the Lift modeling approach. Because the higher χ/Q values measured at CCB occurred on the windward face, renewed emphasis should be given to analyzing the Wrap modeling approach with data from experiments like 206 (see CTDM Second Milestone Report). The case-study approach will also help update the entire MDA by investigating photo- and lidar-derived wind directions and turbulence intensity data.

More theoretical work and data analysis are needed to refine the modeling of dispersion close to and above H_c. Numerical potential flow modeling and physical modeling will help in formulating streamline distortion effects. The case-studies will help modify and evaluate the resultant formulation for α and T in the Lift module, and also the resultant changes to the simulation of streamline distortion and plume dilution in the Wrap module.

CTDM must also be modified with a view towards simulating flow and dispersion around terrain features more complicated than CCB. We have seen that successful modeling of the SHIS #2 data will require some additional reformulation of such basic components of CTDM as the stagnation streamline. What terrain height should be used in calculating H_c for less ideal terrain shapes? How does the "H_c surface" vary over rolling terrain between the meteorological measurement site and the major terrain feature being modeled? Similar questions must be posed and answered within a larger framework for CTDM so that the refined modeling concepts contained in it can be transferred to other terrain geometries.

Closely allied to these modifications of CTDM are considerations of how CTDM, as developed for SHIS #1 and #2, will be applied to the upcoming full-scale study. Certain components of CTDM will be considered more important on this scale than others. For example, with the relatively slow growth of σ_z for elevated plumes in stably stratified atmospheres, σ_z may be wholly determined by the initial buoyancy-dominated growth near the source so that the proper specification of nonbuoyant plume growth over distances of 1 to 2 km, which is so important in understanding the SHIS #1 data, may have little relevance. Similarly, certain aspects of the formulation of Lift designed to simulate concentrations over the crest and in the lee of major terrain features may assume considerably greater importance than the Wrap formulations if the plume is expected to be near or above terrain height much of the time. The characteristics of new versions of CTDM should be explored via sensitivity studies to understand how the model will perform on larger scales.

The question of model sensitivity to the detail of the available input data must also be addressed. The SHIS #1 and #2 data have underscored the need for exceptional resolution in the meteorological data in order to understand and model the observed concentrations. As CTDM becomes more refined, it will necessarily become more dependent on the availability of detailed input data. For practical regulatory application, parameterized "cousins" of CTDM must be developed to retain the more important features of CTDM while reducing the input data requirements. This process will not only yield a version of CTDM capable of producing "screening calculations"; it will also help define the absolute minimum information needed for "refined" modeling within the current regulatory permitting framework.

6.2.2 The SHIS #2 Data Base

Before significant progress can be made in modeling HBR, segments of the SHIS #2 data base must be studied and intercompared. The work falls into two principal categories: refining the measured data and assessing the representativeness of that data for modeling the tracer gas plumes.

Four types of noises have been identified in the tower meteorological measurements taken at the Hogback. Considerable additional work will be required to filter these noises from the data and to refine the meteorological data base. The so-called 60-H_z and 2-to-4-sec noises have yet to be characterized and no methods have been developed to eliminate them from the data.

A necessary initial step in the data refinement process is to obtain more propeller response and F460 cup-and-vane response characteristics from wind tunnel tests, especially at low-wind speeds. We recommend using the EPA FMF wind tunnel to perform these tests. Another necessary step is to compare the sonic, propeller and cup-and-vane anemometer data. A careful evaluation of the turbulence statistics from the sonic vs. propeller anemometers is especially important for modeling. Once the instrument response characteristics are better understood, the data can be adjusted to the extent possible, and the overall accuracy of the various measurements can be assessed.

The issue of data respresentativeness must be addressed if we are to construct a reasonable MDA for SHIS #2. Many pieces of data are available to help us construct a detailed spatial and temporal picture of the variability in the flow.

Temperature data from the three main towers and the tethersondes must be integrated to create a cross section of the vertical structure of the flow upwind and over HBR, and this structure must be compared with the acoustic sounder records. This structure will also be particularly useful in modeling the plume rise of the jet-fogger plume containing the SF_6 tracer gas.

Wind data from the doppler sounder well upwind of HBR should be studied to characterize the large-scale incident flow, and the wind data from all of the towers, the tethersondes, and the wind directions obtained from images of the smoke plume will be needed to understand the relationship among the vertical temperature structure, the incident flow stucture, and the wind variability measured just upwind of and over HBR. It is the flow and turbulence in this zone that determined the concentration patterns measured at HBR.

With a refined data base, and a rudimentary understanding of the forces affecting transport and diffusion of plume material upwind of HBR, the case-study integration of SHIS #2 data can proceed. Key elements in successfully modeling the observed tracer gas concentrations include:

- extending the latest version of CTDM(14083) to HBR,
- verifying plume rise and σ_z development algorithms with plume photography and lidar data,
- creating the HBR MDA, and
- summarizing spatial and temporal patterns in measured concentrations, with special emphasis on the 10-minute data and the concentrations measured on Towers B and C.

REFERENCES

Burt, E.W. 1977. Valley Model User's Guide. EPA-450/2-77-018. U.S. Environmental Protection Agency, Research Triangle Park, NC.

Cline, A.K. 1974. NCAR, Comm. ACM 17, 4, p221.

Crow, L.W. 1975. "Meteorological Data Analysis Based on Monitoring Stations and Meteorological Data, January - December 1974. Joint Environmental Program," No. 153, Loren W. Crow Associates, Denver, Colorado.

Environmental Protection Agency 1981. "Regional Workshop on Air Quality Modeling: A Summary Report," Source Receptor Analysis Branch, OAQPS, Research Triangle Park, NC.

Fox, D.G. 1981. Judging Air Quality Model Performance: A Summary of the AMS Workshop on Dispersion Model Performance. Bull Am. Meteorol. Soc., 62: 599-609.

Gifford, F.A. 1980. Smoke as a Quantitative Atmospheric Diffusion Tracer, Atm. Env., 14: 1119-1121.

Greene, B.R., and S. Heisler 1982. EPA CTMD Quality Assurance Project Report for SHIS #1. ERT #P-B348-350.

Halitsky, J. 1961. Single Camera Measurement of Smoke Plumes. Int. J. Air & Water Poll., 4: Nos. 3/4, 185-198.

Holzworth, G.C. 1980. The EPA Program for Dispersion Model Development for Sources in Complex Terrain. Second Joint AMS-APCA Conference on Applications of Air Pollution Meteorology, New Orleans, LA.

Horst, T.W. 1973. Corrections for Response Errors in a Three-Component Propeller Anemometer. JAM, 12: 716-725.

Hovind, E.L., M.W. Edelstein, and V.C. Sutherland 1979. Workshop on Atmospheric Dispersion Models in Complex Terrain. EPA-600/9-79-041. U.S. EPA, Research Triangle Park, NC.

REFERENCES (Continued)

Hunt, J.C.R. and R.J. Mulhearn 1973. Turbulence Dispersion from Sources Near Two-Dimensional Obstacles. *Journal of Fluid Mechanics 61*: 245-274.

Hunt, J.C.R. and K.J. Richards 1982. Stratified Shear Flow over Low Hills. To be published.

Lavery, T.F., A. Bass, D.G. Strimaitis, A. Venkatram, B.R. Greene, P.J. Drivas, and B. Egan 1982. *EPA Complex Terrain Model Development Program: First Milestone Report - 1981*. EPA-600/3-82-036, U.S. EPA, Research Triangle Park, NC, 304p.

Londergan, R.J. 1980. *Validation of Plume Models: Statistical Methods and Criteria*. EA-1673-54. Electric Power Research Institute, Palo Alto, CA.

Moore, G.E., R.G. Ireson, C.S. Liu, R.E. Morris, A.B. Hudischewskyj, and T.W. Tesche 1981. *Air Quality and Meteorology of Northwestern New Mexico*, Draft Final Report No. 81203. Arizona Public Service.

Pearson, H.J., J.S. Puttock and J.C.R. Hunt 1981. A Statistical Model of Fluid Element Motions and Vertical Diffusion in a Homogeneous Stratified Turbulent Flow. *J. Fluid Mech. 129*: 219-249.

Rhoads, R.G. 1982. "Addendum to Workshop Summary Report," OAQPS, U.S. EPA, Research Triangle Park, NC.

Sheppard, P.A., 1956. Airflow over Mountains, *Quart. J. Roy. Meteor. Soc.*, *82*: 528-9.

Smith, R.B. 1980. Linear Theory of Stratified Hydrostatic Flow Past an Isolated Mountain. *Tellus*, *32*: 348-364.

Snyder, W.H. and J.C.R. Hunt 1983. Turbulent Diffusion From A Point Source in Stratified and Neutral Flows Around A Three-Dimensional Hill; Part II, Laboratory Measurements of Surface Concentrations. (Submitted to *Atmospheric Environment*).

Strimaitis, D.G., A. Venkatram, B.R. Greene, S.R. Hanna, S. Heisler, T.F. Lavery, A. Bass and B.A. Egan 1983. *EPA Complex Terrain Model Development Program: Second Milestone Report - 1982*. EPA-600/3-83-015. U.S. EPA, Research Triangle Park, NC, 375p.

Venkatram, A. 1982. A Framework for Evaluating Air Quality Models. *Boundary-Layer Meteor.*, *24*: 371-385.

REFERENCES (Continued)

Williamson, H.J. and R.R. Krenmayer 1980. Analysis of the Relationship Between Turner's Stability Classifications and Wind Speed and Direct Measurements of Net Radiation. Second Joint Conference on Applications of Air Pollution Meteorology, March 24-27, AMS, Boston.

APPENDIX A

LABORATORY SIMULATION OF NEUTRAL PLUME DISPERSION OVER CINDER CONE BUTTE

LABORATORY SIMULATION OF NEUTRAL PLUME DISPERSION OVER CINDER CONE BUTTE

Comparison with Field Data

by

Roger S. Thompson,
William H. Snyder*
and Robert E. Lawson, Jr.*

Meteorology and Assessment Division
Environmental Sciences Research Laboratory
Environmental Protection Agency
Research Triangle Park, NC 27711

April 1983

*On assignment from the National Oceanic and Atmospheric Administration, U.S. Department of Commerce.

INTRODUCTION

The purpose of this series of experiments was to duplicate, in the laboratory, the field experiments performed by Environmental Research & Technology, Inc. (ERT) at Cinder Cone Butte, Idaho. In this particular study, a one-hour period (1700-1800 MST) of Case 202 was modeled. Meteorological measurements during this period indicated that atmospheric conditions were neutral. The laboratory study was performed in the Meteorological Wind Tunnel, a facility well-suited for modeling neutral atmospheric flow. Measurements of vertical profiles of wind speed, ground-level concentrations, and vertical and lateral profiles of concentration were made during the wind tunnel experiments. This report describes the conduct of the study, makes comparisons of field and laboratory measurements, and discusses some additional observations of the laboratory study.

SUMMARY OF FIELD OBSERVATIONS

The experimental data collection network used in the field has been described by Lavery, et al. 1982. For the one-hour period considered here (Case 202, October 17, 1980, 1700-1800 MST), the meteorological data were fairly complete. The concentration data contained only nine, non-zero, one-hour average concentrations; however, an additional 14 non-zero, one-hour values were computed from ten-minute concentration data. There were five reported zero one-hour concentrations and an additional ten zero values computed from the ten-minute data.

Meteorological Data

Examination of the NOAA Daily Weather Map series for October 17 and 18 showed synoptic conditions at Cinder Cone Butte (CCB) during Case 202 to be dominated by a weak high pressure system centered over southern Washington. Skies were clear with surface winds light and variable during the morning. Surface temperatures ranged from a low of about 1°C to an afternoon high of about 12°C. Upper level winds (500 mb) were from the north at 10-12 m/s.

Under these synoptic conditions, atmospheric stability is dominated by surface heating and cooling. Stable conditions prevail during the early morning hours due to formation of a radiation inversion and, as surface heating increases during the day, there is a transition to near-neutral and finally neutral or slightly unstable conditions. During the late afternoon and evening, the reverse process takes place as insolation decreases and surface radiation begins to dominate. The hour examined in this case study (1700-1800 MST) falls just prior to sunset (1800 MST) and, on the basis of these synoptic conditions, would be in a transition from near-neutral conditions to stable conditions. Examination of the detailed meteorological data from CCB shows that this trend is, in fact, taking place as the stability is initially neutral (D stability) and becoming more stable (E stability) toward the end of the hour.

Wind speed and wind direction were measured and recorded at five levels (2, 10, 40, 80 and 150 m) and temperature at eight levels (2, 10, 20, 40, 60, 80, 100, and 150 m) on the tower (Tower A) located 2 km north of CCB. These data are summarized in Table A-1. Five-minute averages were recorded at the time corresponding to the end of the period. The table contains the u (westerly), v (southerly), and w (upward) components of the wind as determined from the u,v,w anemometers in m/s. Computed from these are the five-minute averages of wind speed (WS), wind direction (WD), along-wind turbulence intensity (IX), cross-wind turbulence

TABLE A-1. METEOROLOGICAL DATA FROM TOWER A. CASE 202, OCTOBER 17, 1980; 1700-1800 MST.

a) z = 2 m

TIME	U	V	W	WS	WD	IX	IY	IZ
17.083	2.859	-3.299	0.127	4.366	319.08	19.257	14.076	3.910
17.166	3.641	-2.566	0.127	4.455	305.17	17.889	13.001	3.675
17.250	3.641	-2.908	0.127	4.660	308.61	15.152	13.685	3.167
17.333	3.495	-2.859	0.127	4.515	309.28	15.054	12.317	3.480
17.416	3.104	-2.859	0.127	4.220	312.65	17.107	16.325	3.832
17.500	3,055	-3.152	0.108	4.390	315.90	15.543	11.339	3.871
17.583	3.152	-2.859	0.166	4.256	312.20	17.693	14.565	4.340
17.666	3.446	-3.495	0.147	4.908	315.40	15.054	10.948	3.050
17.750	3.544	-3.348	0.147	4.875	313.37	17.498	10.264	3.988
17.833	3.201	-3.152	0.147	4.493	314.55	14.174	10.459	3.245
17.916	2.859	-2.713	0.127	3.941	313.49	13.685	11.828	3.832
18.000	2.761	-2.468	0.127	3.704	311.79	16.813	11.241	4.106

b) z = 10 m

TIME	U	V	W	WS	WD	IX	IY	IZ
17.083	3.788	-4.374	0.459	5.786	319.10	14.467	13.685	4.340
17.166	4.961	-3.495	0.479	6.068	305.16	14.076	11.535	3.597
17.250	4.619	-3.935	0.440	6.067	310.42	9.091	10.753	4.027
17.333	4.423	-3.983	0.381	5.953	312.00	17.302	9.873	2.972
17.416	3.788	-3.983	0.440	5.497	316.44	11.535	11.046	2.933
17.500	3.886	-4.374	0.440	5.851	318.38	10.068	7.918	4.066
17.583	4.423	-3.983	0.420	5.953	312.00	12.023	9.971	4.262
17.666	4.619	-4.570	0.479	6.497	314.69	10.362	7.820	3.910
17.750	4.472	-4.472	0.459	6.325	315.00	11.828	8.895	3.480
17.833	4.472	-4.326	0.440	6.222	314.04	10.459	7.527	3.089
17.916	3.837	-3.690	0.381	5.323	313.88	9.189	8.113	1.402
18.000	3.788	-3.544	0.362	5.187	313.09	10.068	8.798	

c) z = 40 m

TIME	U	V	W	WS	WD	IX	IY	IZ
17.083								
17.166	6.183	-5.303	0.205	8.145	310.62	8.309	9.384	3.050
17.250	5.645	-5.743	0.225	8.053	315.49	6.061	6.940	3.050
17.333	5.352	-5.694	0.166	7.814	316.77	5.767	6.256	2.620
17.416	4.717	-5.743	0.205	7.431	320.60	6.647	8.211	4.027
17.500	4.863	-5.987	0.186	7.713	320.91	6.843	5.474	2.698
17.583	5.352	-5.645	0.166	7.779	316.52	9.091	7.331	3.284
17.666	5.792	-5.938	0.225	8.295	315.71	6.354	5.670	3.206
17.750	5.743	-6.183	0.205	8.438	317.11	7.625	5.572	2.620
17.833	5.792	-5.938	0.186	8.295	315.71	4.399	4.399	2.385
17.916	5.156	-5.205	0.186	7.327	315.26	5.474	5.670	2.933
18.000	5.156	-5.499	0.166	7.538	316.83	5.670	5.279	2.268

TABLE A-1. METEOROLOGICAL DATA FROM TOWER A. CASE 202, OCTOBER 17, 1980; 1700-1800 MST (Continued)

d) z = 80 m

TIME	U	V	W	WS	WD	IX	IY	IZ
17.083	6.476	-5.645	0.342	8.591	311.07	4.594	7.722	3.480
17.166	7.600	-4.961	0.205	9.076	303.13	5.083	4.985	3.089
17.250	6.916	-5.547	0.166	8.866	308.73	3.519	3.812	3.050
17.333	6.134	-5.254	0.303	8.077	310.58	5.767	5.181	3.441
17.416	5.987	-5.205	0.362	7.934	311.00	4.692	6.256	4.027
17.500	6.281	-5.596	0.362	8.412	311.70	6.061	6.452	3.402
17.583	7.160	-5.352	0.303	8.939	306.77	5.083	4.399	3.206
17.666	7.454	-5.694	0.283	9.380	307.37	3.324	4.008	3.519
17.750	7.502	-5.841	0.283	9.508	307.90	3.519	3.715	2.776
17.833	7.502	-5.450	0.127	9.273	305.99	4.692	3.226	3.011
17.916	6.965	-5.205	0.264	8.695	306.77	4.497	4.594	3.011
18.000	6.965	-5.499	0.303	8.874	308.29	3.715	2.835	2.854

e) z = 150 m

TIME	U	V	W	WS	WD	IX	IY	IZ
17.083	6.329	-5.499	0.244	8.384	310.98	6.452	7.918	4.223
17.166	7.405	-5.303	0.205	9.108	305.60	3.324	4.399	3.324
17.250	6.769	-5.596	0.088	8.783	309.58	2.737	3.812	3.011
17.333	5.743	-5.645	0.342	8.053	314.50	6.647	6.256	4.731
17.416	6.183	-5.547	0.205	8.307	311.89	3.910	5.376	3.793
17.500	6.574	-5.743	0.225	8.729	311.14	3.812	6.354	3.910
17.583	7.258	-5.841	0.225	9.316	308.82	2.151	2.542	3.245
17.666	7.356	-6.036	0.088	9.515	309.37	2.151	2.444	2.972
17.750	7.893	-6.232	0.010	10.057	308.29	2.151	2.346	1.251
17.833	8.138	-5.743	0.049	9.960	305.21	2.151	1.760	1.877
17.916	7.551	-5.938	0.342	9.607	308.18	3.128	4.399	2.776
18.000	7.111	-6.134	0.068	9.391	310.77	1.075	1.271	2.190

f) Temperature

TIME	z = 2 m	z = 10 m	z = 20 m	z = 40 m	z = 60 m	z = 80 m	z = 100 m	z = 150 m
17.083	11.760		11.681	11.549	11.369	11.197	10.899	10.435
17.166	11.525	11.628	11.603	11.432	11.290	11.080	10.899	10.376
17.250	11.369	11.510	11.525	11.373	11.290	11.041	10.899	
17.333	11.369		11.525		11.369	11.119	10.899	10.435
17.416	11.447	11.608	11.603	11.413	11.290	11.061	10.899	10.376
17.500	11.447		11.525	11.334	11.212		10.899	
17.583	11.290	11.432	11.447	11.276	11.212		10.821	10.357
17.666	11.290	11.471	11.447	11.354	11.212		10.899	10.415
17.750	11.134	11.354	11.369	11.295	11.212	11.002	10.821	10.415
17.833	10.899		10.978	11.158	11.134		10.821	10.435
17.916	10.665				10.978		10.743	
18.000	10.352	10.728	10.821	10.865	10.899		10.743	10.337

intensity (IY), and vertical turbulence intensity (IZ) in percent. Table A-1f contains the five-minute average temperatures (°C) recorded for all eight levels.

One-hour average values of the meteorological parameters were computed from the available five-minute averages. A one-hour average wind vector was computed at each of the five levels of the tower as follows:

$$\overline{U} = \left[\left(\frac{1}{N}\sum_{i=1}^{N} u_i\right)^2 + \left(\frac{1}{N}\sum_{i=1}^{N} v_i\right)^2 \right]^{1/2}$$

$$\overline{\theta} = \arctan \left[\sum_{i=1}^{N} v_i \Big/ \sum_{i=1}^{N} u_i \right]$$

where u_i, v_i are the values of the westerly and southerly wind components for the i^{th} five-minute period and there are N periods containing valid data for the hour. The hour-average values of turbulence intensity were calculated in the direction of the hourly-mean wind, in the direction horizontally perpendicular to the mean wind direction, and in the vertical direction. The five-minute average turbulence intensities were projected onto these directions and the variance of the five-minute mean wind data was added in computing the hourly turbulence intensities.

$$I_1 = \left[\frac{\frac{1}{N}\sum_{i=1}^{N} \left[\left(\frac{IX_i WS_i \cos\Delta\theta_i}{100}\right)^2 + \left(\frac{IY_i WS_i \sin\Delta\theta_i}{100}\right)^2 + (WS_i \cos\Delta\theta_i)^2 \right] - \overline{U}^2}{\overline{U}^2} \right]^{\frac{1}{2}} \times 100\%$$

$$I_2 = \left[\frac{\frac{1}{N}\sum_{i=1}^{N} \left[\left(\frac{IX_i WS_i \sin\Delta\theta_i}{100}\right)^2 + \left(\frac{IY_i WS_i \cos\Delta\theta_i}{100}\right) + (WS_i \sin\Delta\theta_i)^2 \right]}{\overline{U}^2} \right]^{\frac{1}{2}} \times 100\%$$

$$I^3 = \left[\frac{\frac{1}{N}\sum_{i=1}^{N} \left(\frac{IZ_i WS_i}{100}\right)^2}{\overline{U}^2} \right]^{\frac{1}{2}} \times 100\%$$

where the subscript i again refers to the i^{th} five-minute period of the hour and $\Delta\theta_i = \theta_i - \theta$.

The one-hourly average values for each level of Tower A are contained in Table A-2. Vertical profiles of the five-minute average wind speeds are presented in Figure A-1. The one-hour average wind speed values are also indicated in Figure A-1 and on a log-linear scale in Figure A-2. From Figure A-2, z_o was found to be on the order of 5 to 8 cm. The boundary-layer thickness appears to be greater than 150 m. Vertical profiles of the five-minute and one-hour average temperature data are presented in Figure A-3. A line with the slope of the adiabatic lapse rate (Γ_d) is included in the figure. The environmental lapse rate closely follows the adiabatic lapse rate above about 10 m from the surface. This, together with the previously discussed wind data, indicates neutral stability for this period.

TABLE A-2. ONE-HOUR AVERAGE METEOROLOGICAL DATA FROM TOWER A

z (m)	$\bar{U}$ (m/s)	$\bar{\theta}$ (°)	I_1 (%)	I_2 (%)	I_3 (%)	$\bar{T}$ (°C)
2	4.39	312.6	18.1	14.1	3.7	11.21
10	5.88	313.7	13.6	11.7	3.7	11.53
20						11.41
40	7.89	316.5	8.1	8.0	3.0	11.31
60						11.21
80	8.79	308.2 (316.2)*	7.1	6.4	3.2	11.08
100						10.85
150	9.09	309.4 (316.4)*	7.7	6.1	3.1	10.40

*The anemometers at z = 80 and 150 m were oriented approximately 8° and 7° east of true north, respectively (Lavery, et al., 1982). The values in parentheses are corrected for this misalignment.

After the design and data collection of this wind tunnel experiment were completed, ERT prepared and released their First Milestone Report (Lavery, et al., 1982) on the field project. The quality assurance audit reported misalignment of the wind systems at the 80 m and 150 m heights on Tower A by 8° and 7° east of true north, respectively. Adjustments for these have been made in Table A-2, but not in Table A-1.

Concentration Data

The tracer experiment in the field was designed to examine ground-level concentrations from a point source upwind of an isolated hill. For Case 202, the source was located 1.0 km from the hill center at 319° from true north. Sulfur hexafluoride (SF_6) was released at a height of 50 m above the local ground surface. Examination of the topographical maps revealed that the local surface at this location was 8 m below the reference height selected as the base of the hill.

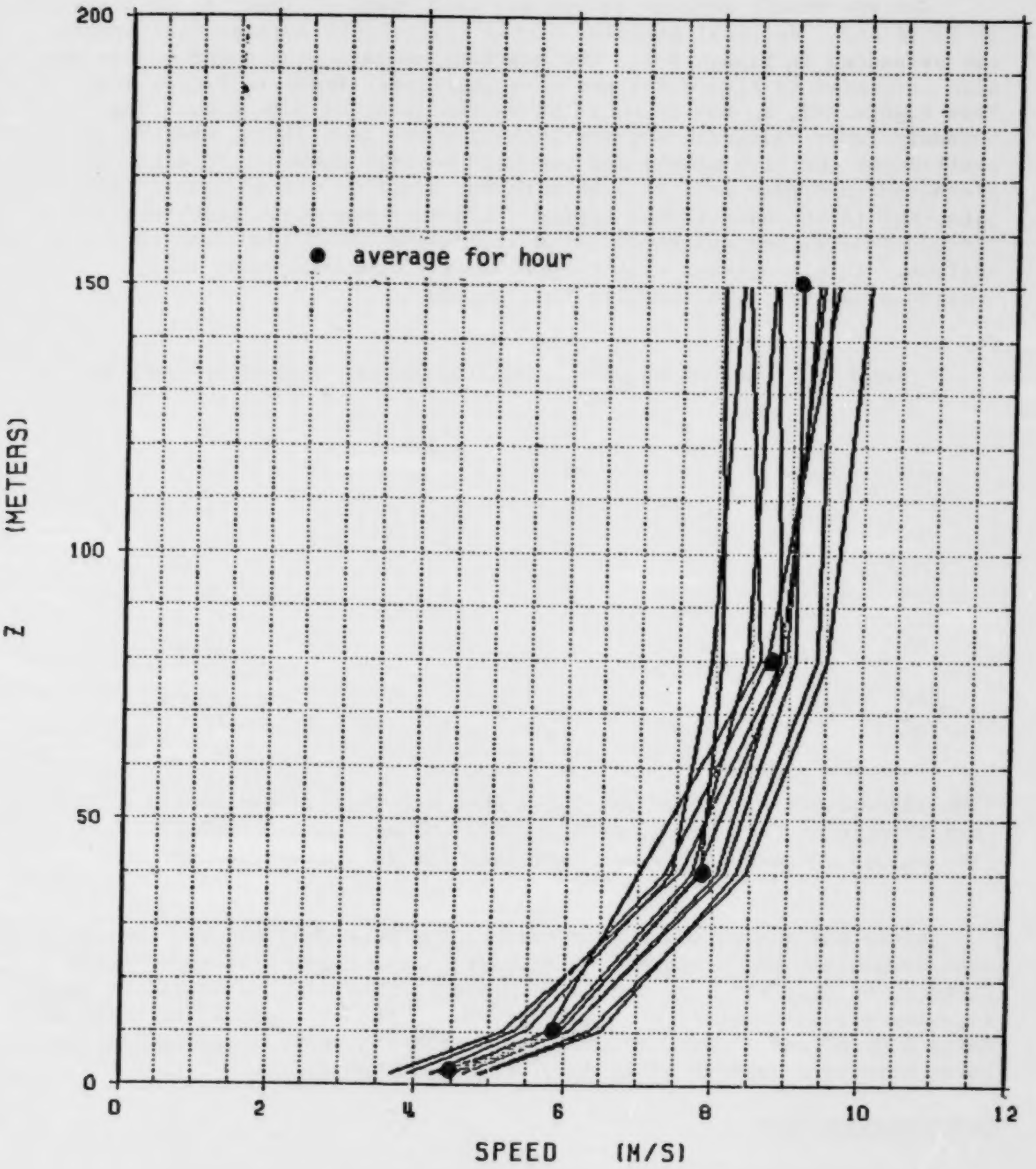

Figure A-1. Tower A, Case 202, 1700-1800, 5-minute wind speed values and hourly average wind speed as a function of height above ground.

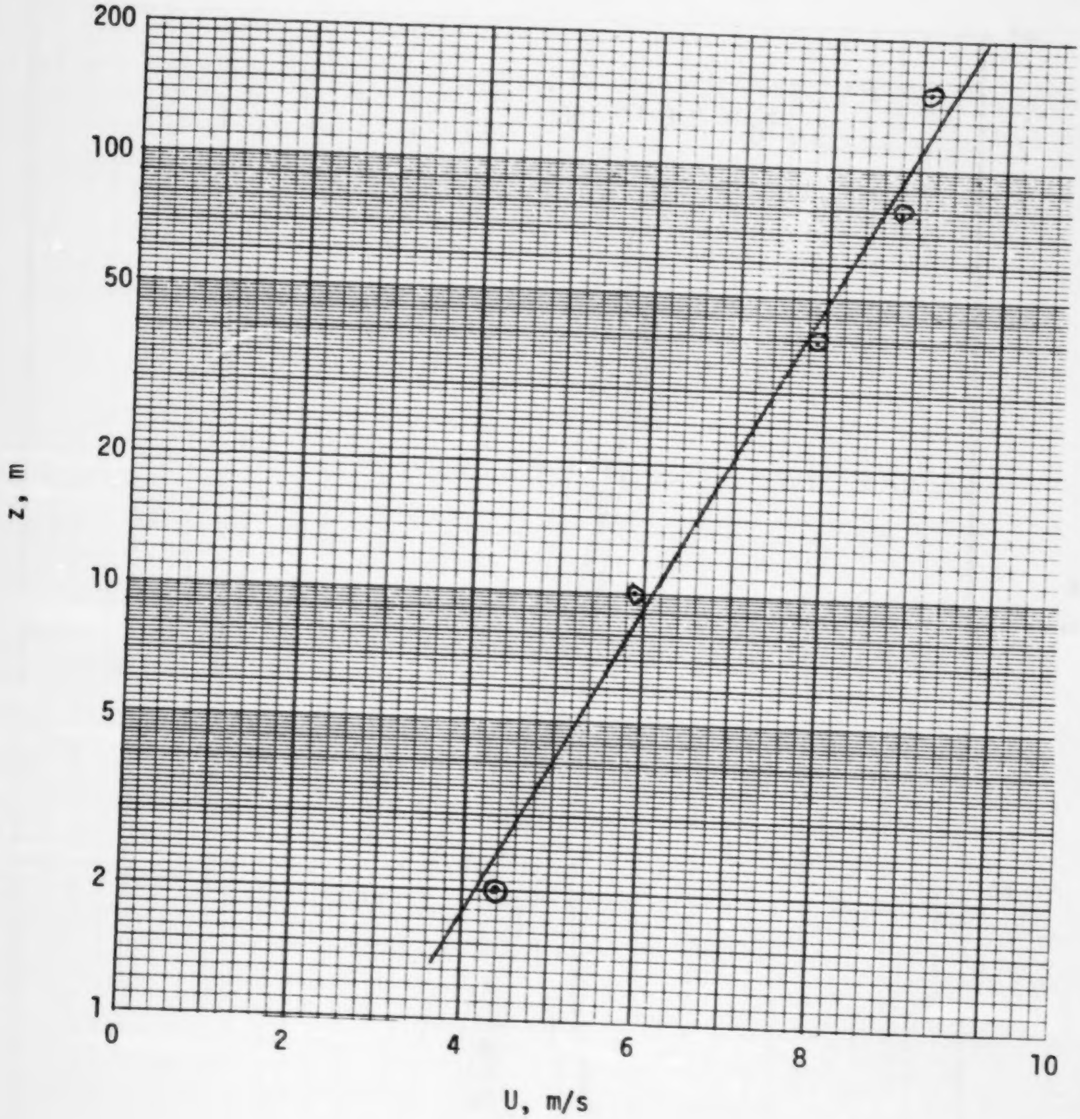

Figure A-2. Vertical profile of hourly average wind speed measured at Tower A, Case 202, 1700-1800.

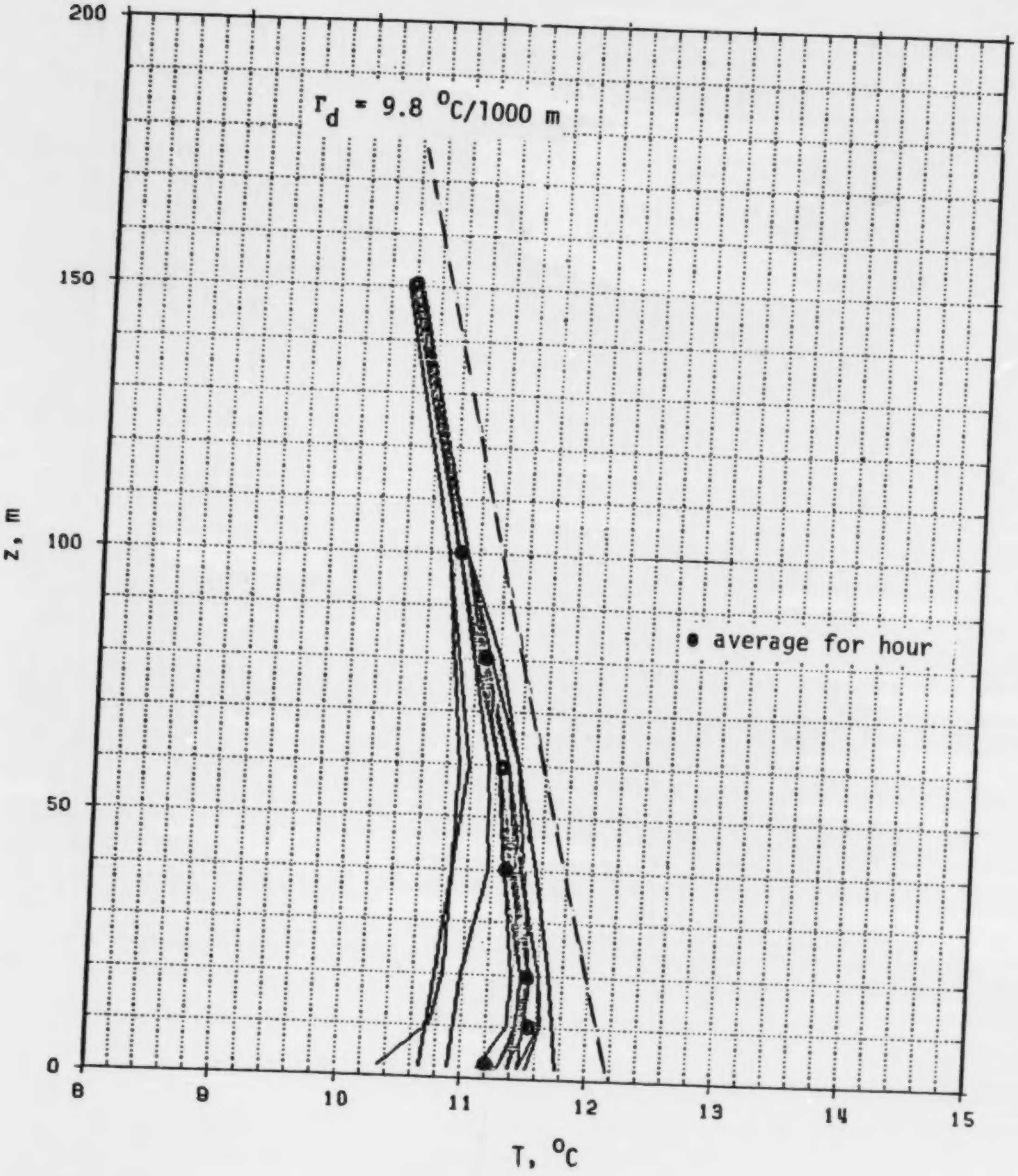

Figure A-3. Vertical profiles of five-minute averages of temperature at Tower A, Case 202, 1700-1800. The one-hour average values and a line with slope corresponding to the adiabatic lapse rate are also shown.

Time spent in moving the crane supporting the source into this position resulted in delay of the source beginning to emit until 1716, sixteen minutes into the hour of interest. For the remainder of the hour, the source emission rate was 0.080 (± 5.3%) g/s of SF_6.

Bag samples were collected at a network of 100 sampling stations on the hill surface. The locations of these stations are given in Table A-3 in both polar and rectangular coordinates as defined in Figure A-4. Sample ports were located on the model at corresponding positions and assigned identification numbers also listed in Table A-3.

A summary of the field concentration data is presented in Table A-4. The one-hour sample data required an adjustment to correct for the portion of the hour that the source was not operating and the sample pumps were. The ten-minute sample data indicate that the tracer was reaching the samplers near the beginning of the period 1720 to 1730 in that the concentrations measured during this period were roughly equal to those for the period 1730 to 1740. Therefore, the measured "one-hour concentrations" were multiplied by 1.5 (60 min/ 40 min) to correct for the sampling time. One-hour concentrations were computed from the ten-minute data by averaging the valid data for the four ten-minute periods at the end of the hour.

TABLE A-3. LOCATION OF SAMPLERS ON CINDER CONE BUTTE

FMF PORT	ERT PORT	ANGLE DEG.	R m	X m	Y m
1	37.01	8.0	510.0	70.98	505.04
2	37.02	8.0	449.0	62.49	444.63
3	37.03	8.0	391.0	54.42	387.19
4	37.04	8.0	308.0	42.87	305.00
5	37.05	8.0	275.0	30.27	272.32
6	37.06	8.0	250.0	34.79	247.57
7	37.07	8.0	277.0	31.59	224.79
8	37.09	8.0	177.0	24.63	175.28
9	37.10	8.0	154.0	21.43	152.50
10	37.11	8.0	122.0	16.98	120.81
11	37.12	8.0	81.0	11.27	80.21
12	37.20	8.0	193.0	26.86	191.12
13	37.26	8.0	19.0	2.64	18.82
14	34.10	30.0	146.0	73.00	126.44
15	31.90	52.0	146.0	115.05	89.89
16	31.96	53.0	154.0	122.99	92.68
17	31.07	53.0	200.0	159.73	120.36
18	31.09	53.0	154.0	122.99	92.68
19	31.26	53.0	107.0	85.45	64.39
20	31.05	53.0	246.0	196.46	148.05
21	29.04	68.0	187.0	173.38	70.05
22	28.26	71.0	420.0	397.12	136.74
23	28.11	75.0	75.0	72.44	19.41
24	27.03	83.0	260.0	258.06	31.69
25	26.03	90.0	360.0	360.00	0.00
26	26.05	90.0	208.0	208.00	0.00
27	26.06	90.0	142.0	142.00	0.00
28	63.03	98.0	315.0	311.93	-43.84
29	62.03	105.0	190.0	183.53	-49.18
30	60.03	120.0	362.0	313.50	-181.00
31	60.04	120.0	297.0	257.21	-148.50
32	60.22	120.0	235.0	203.52	-117.50
33	60.23	120.0	164.0	142.03	-82.00
34	60.24	120.0	124.0	107.39	-62.00
35	60.25	120.0	94.0	81.41	-47.00
36	60.26	120.0	43.0	37.24	-21.50
37	60.01	120.0	510.0	441.67	-255.00
38	60.02	120.0	410.0	355.07	-205.00
39	58.08	135.0	195.0	137.88	-137.89
40	58.07	137.0	240.0	163.68	-175.52
41	57.25	143.0	327.0	196.79	-261.16
42	57.26	143.0	140.0	84.25	-111.81
43	57.96	143.0	165.0	99.30	-131.78
44	57.13	143.0	165.0	99.30	-131.78
45	57.90	147.0	162.0	88.23	-135.87
46	56.03	150.0	255.0	127.50	-220.84
47	56.04	150.0	198.0	99.00	-171.47
48	56.05	150.0	86.0	43.00	-74.48
49	55.05	158.0	250.0	93.65	-231.80
50	55.13	158.0	204.0	76.42	-189.14

TABLE A-3. LOCATION OF SAMPLERS ON CINDER CONE BUTTE (Continued)

FMF PORT	ERT PORT	ANGLE DEG.	R m	X m	Y m
51	55.96	158.0	204.0	76.42	-189.15
52	55.26	159.0	165.0	59.13	-154.04
53	55.90	159.0	196.0	70.24	-182.98
54	54.04	165.0	301.0	77.90	-290.74
55	53.03	171.0	139.0	21.74	-137.29
56	53.04	173.0	260.0	31.68	-258.06
57	39.21	187.0	37.0	-4.51	-36.72
58	39.01	187.0	510.0	-62.16	-506.20
59	39.02	187.0	411.0	-50.09	-407.94
60	39.03	187.0	348.0	-42.41	-345.41
61	39.05	187.0	291.0	-35.47	-288.83
62	39.07	187.0	251.0	-30.59	-249.13
63	39.12	187.0	115.0	-14.02	-114.14
64	39.17	187.0	180.0	-21.94	-178.66
65	39.18	187.0	150.0	-18.28	-148.88
66	39.20	187.0	77.0	-9.38	-76.43
67	45.24	232.0	107.0	-84.32	-65.87
68	45.07	232.0	224.0	-176.52	-137.91
69	45.10	232.0	158.0	-124.51	-97.27
70	48.12	255.0	63.0	-60.85	-16.30
71	48.02	255.0	411.0	-397.00	-106.37
72	48.03	255.0	327.0	-315.86	-84.63
73	48.05	255.0	258.0	-249.21	-66.77
74	48.07	255.0	211.0	-203.81	-54.61
75	48.10	255.0	150.0	-144.89	-38.82
76	50.07	270.0	238.0	-238.00	0.00
77	64.05	277.0	282.0	-279.90	34.37
78	64.10	277.0	159.0	-157.81	19.37
79	65.03	285.0	252.0	-243.41	65.22
80	67.01	300.0	510.0	-441.67	255.01
81	67.02	300.0	416.0	-360.26	208.00
82	67.04	300.0	343.0	-297.04	171.50
83	67.05	300.0	311.0	-269.33	155.50
84	67.06	300.0	284.0	-245.95	142.00
85	67.13	300.0	230.0	-199.18	115.00
86	67.23	300.0	247.0	-213.91	123.50
87	67.24	300.0	178.0	-154.15	89.00
88	67.25	300.0	130.0	112.58	65.00
89	67.26	300.0	54.0	-46.77	27.00
90	69.07	315.0	200.0	-141.42	141.42
91	69.26	315.0	325.0	-229.81	229.81
92	70.08	322.0	151.0	-92.96	118.99
93	70.25	322.0	108.0	-66.49	85.11
94	70.25	333.0	275.0	-124.04	245.03
95	72.23	338.0	285.0	-106.76	264.25
96	72.24	338.0	211.0	-79.04	195.64
97	73.10	345.0	127.0	-32.87	122.67
98	73.11	345.0	105.0	-27.17	101.42
99	74.03	353.0	310.0	-37.78	307.69
100	74.04	353.0	197.0	-24.01	195.53

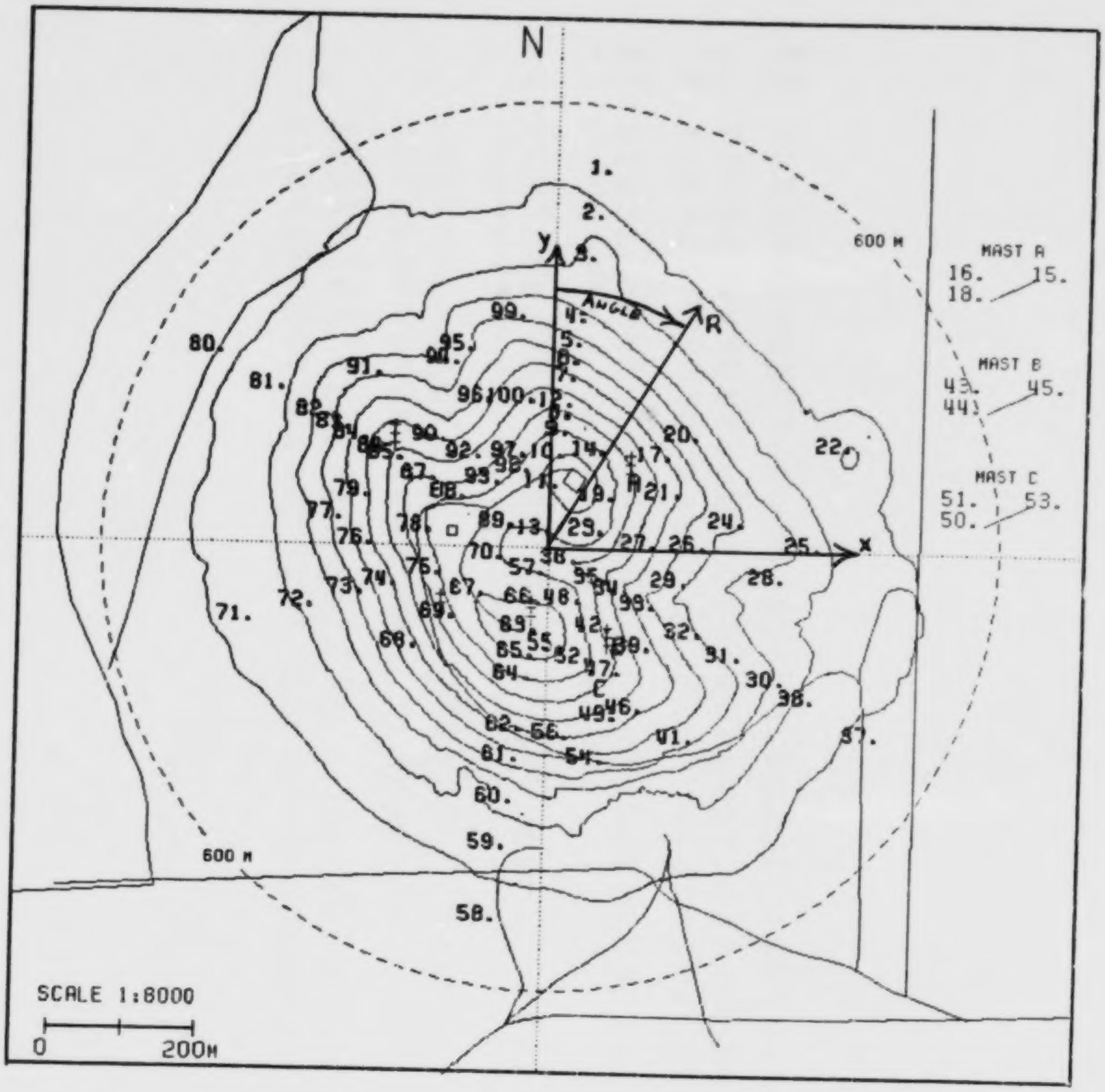
N
y
x
R
ANGLE
600 M
600 M
MAST A
16. 15.
18.
MAST B
43. 45.
44.
MAST C
51. 53.
50.
SCALE 1:8000
0
200M
1.
2.
3.
4.
5.
6.
7.
8.
9.
10
11.
12.
13.
14.
17.
19.
20.
21.
22.
23.
24.
25.
26.
27.
28.
29.
30.
31.
32.
33.
34.
35.
36.
37.
38.
39.
40.
41.
42.
46.
47.
48.
49.
52.
54.
55.
56.
57.
58.
59.
60.
61.
62.
63.
64.
65.
66.
67.
68.
69.
70.
71.
72.
73.
74.
75.
76.
77.
78.
79.
80.
81.
82.
83.
84.
85.
86.
87.
88.
89.
90.
91.
92.
93.
94.
95.
96.
97.
98.
99.
100.
A
B
C

Figure A-4. Map of Cinder Cone Butte showing coordinate systems and locations of the 100 ground-level samplers.

TABLE A-4. GROUND-LEVEL CONCENTRATIONS FROM FIELD EXPERIMENT

a) One-hour sample data

FMF Port Number	Measured Concentration (ppt SF_6)	Adjusted Concentration (ppt SF_6)
10	189.0	283.5
13	70.0	105.0
69	0.0	0.0
73	0.0	0.0
31	110.0	165.0
34	5.0	7.5
35	61.0	91.5
81	0.0	0.0
82	0.0	0.0
86	0.0	0.0
87	7.0	0.0
88	11.0	10.5
89	26.0	16.5
99	124.0	39.0
		186.0

b) Ten-minute sample data

FM Port Number	Measured Concentration in ppt of SF_6 for Ten-Minute Period Ending at						Average for 1720-1800
	1710	1720	1730	1740	1750	1800	
4	-	0	100	117	19	0	59
5	-	-	-	87	-	-	87
6	0	-	265	-	117	0	127
7	5	-	-	0	0	0	0
9	-	67	266	352	116	405	285
11	0	0	119	144	244	-	169
18	0	0	-	-	251	176	213
19	0	0	114	178	294	387	243
20	0	0	101	99	18	8	57
32	0	0	27	116	220	-	121
52	0	-	0	0	0	-	0
60	-	-	-	-	0	0	0
61	-	-	-	-	0	0	0
64	-	0	0	0	0	0	0
68	-	0	0	0	-	-	0
71	0	0	0	0	0	0	0
74	-	-	-	-	0	-	0
75	6	0	-	5	0	-	3
76	0	0	0	0	0	0	0
79	0	0	0	0	0	0	0
88	0	0	31	5	15	47	25
90	0	0	52	6	65	150	68
95	-	-	-	319	490	497	435
97	0	0	0	-	0	250	83
100	210	194	0	0	-	35	-*

---

*Data for port 100 were ignored because of high reported concentrations for 1700-1720 when source was not operating.

EXPERIMENTAL DETAILS

Model Specifications

The model was constructed of acrylic plastic by a vacuum-forming technique. The nominal scale was 1:640; after fabrication, the actual model scale was determined to be 1:647 in the horizontal and 1:694 in the vertical (model height = 14.4 cm). A survey of boundary-layer generation systems used in previous studies in the Meteorological Wind Tunnel revealed that a boundary layer produced, using 92 cm high vorticity generators, a 15 cm high fence, and a fine "Sanspray" TM surface would simulate the full-scale situation. The model was coated with gravel of the same size as that used in the Sanspray (average diameter on the order of 2 mm) and installed in the wind tunnel, along with the boundary-layer generation devices (see Figure A-5). The center of the hill was located 8.0 m downwind of the fence. The wind tunnel was operated at a freestream air speed of 4 m/s.

The source was constructed from a 0.32 cm O.D. brass tube that was bent over to emit the tracer in the direction of the wind and avoid any momentum plume rise. Ethylene (99.8% pure) was released at a rate of 50 cm^3/s, so that the effluent speed was approximately equal to the local mean air speed. Sampling ports were made using 0.24 cm O.D. brass tubing. The ports projected approximately 2 mm above the surface roughness, except for the mast mounted samplers, which were scaled in height in proportion to their field counterparts. The sample ports were connected to a scanning valve which allowed groups of 5 sampling ports to be connected to the laboratory's system of 5 flame ionization detectors (FID) for determination of tracer concentration. The FID's were calibrated before and checked after each experimental run of 100 samples. The background level of ethylene in the room was measured before and after each run and a linear interpolation algorithm was used to subtract the background from each sample. The analog output of the FID's was processed on the laboratory's minicomputer system using a digitizing rate of 1 Hz for 120 seconds, an adequate sampling time to obtain stable averages.

Conversion of Model Concentrations to Field Concentrations

To facilitate comparison of the field and laboratory data, the laboratory data were converted to equivalent full-scale values. Model concentration values were recorded in percent by volume of ethylene. The minicomputer program for collection and analysis of wind tunnel

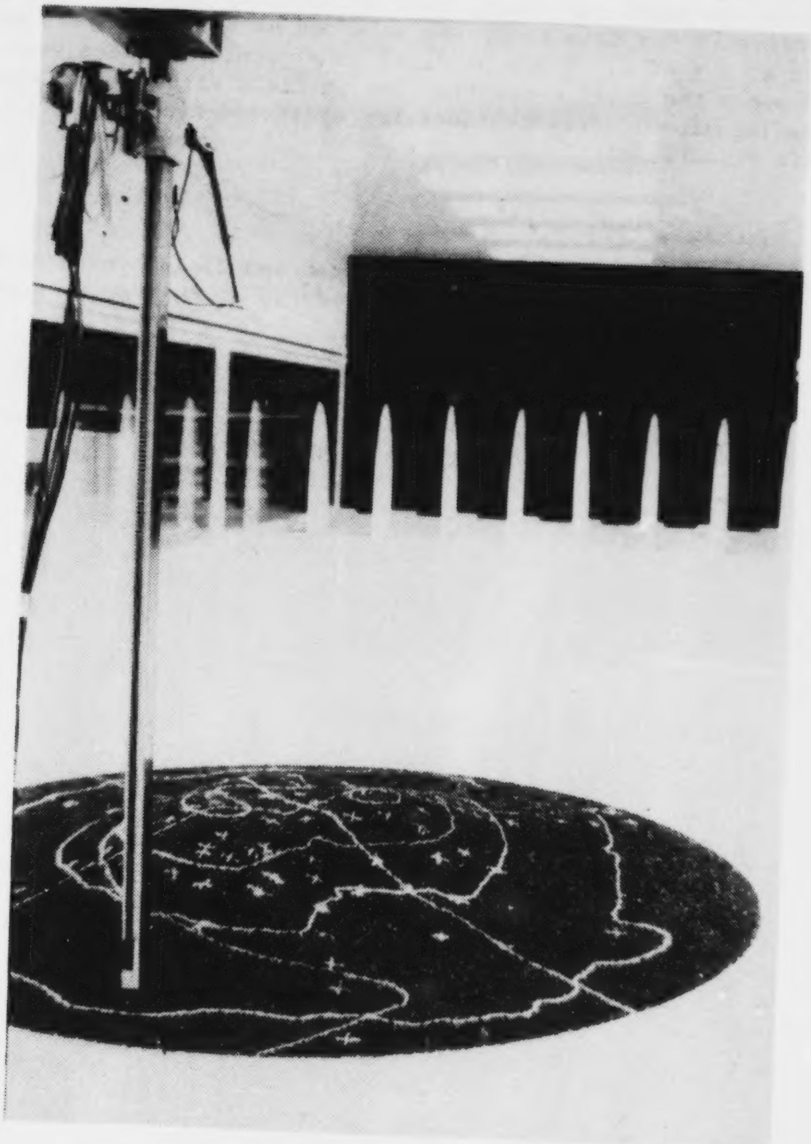

Figure A-5. Cinder Cone Butte model in the EPA Meteorological Wind Tunnel. Note vortex generators at test section entrance.

concentration data calculates a nondimensional concentration $\chi = CUH^2/Q$, where C is the measured concentration, U is the reference wind speed, H is the hill height, and Q is the tracer release rate. The absolute wind speed in the wind tunnel is arbitrary. However, to convert wind-tunnel tracer measurements to field values, a reference wind speed, at the same locations in the model and field, must be selected and used in computing χ. The reference for this study was selected as the wind speed measured on Tower A at z = 40 m. These nondimensional concentrations were then used to convert the model concentrations to field values using equivalence of the nondimensional concentrations for model and field ($\chi_m = \chi_f = \chi$). This results in:

$$C_f = \chi_m Q_f / U_f H_f^2 ,$$

where the subscripts m and f stand for model and field, respectively. Substituting in the field values for the period of this study gives

$$C(\text{ppt}) = \frac{\chi(0.080 \text{ gm SF}_6/\text{s})\ (10^{12} \text{ ppt})/(6.5\text{x}10^3 \text{ gm SF}_6/\text{m}^3)}{(7.89 \text{ m/s})\ (100 \text{ m})^2},$$

or $C(\text{ppt}) = 156\chi$.

PRESENTATION AND DISCUSSION OF RESULTS

For the sake of easy comparison, all wind-tunnel measurements have been converted to full-scale values according to the scaling concepts previously discussed.

Wind Field Measurements

Verification that the boundary layer developed in the wind tunnel was representative of that observed in the field was based on comparison of wind measurments at Tower A in the field with the vertical profile obtained in the wind tunnel upstream of the model. As mentioned above, the absolute wind speed in the wind tunnel is arbitrary. Adjustment of the wind-tunnel velocity profile to field values was based on matching the speeds for the model and field at the 40-m level on Tower A, the measurement nearest the height of the source. The mean wind speed comparison, shown in Figure A-6, is quite good with the exception of the measurement at $z = 80$ m on Tower A. Also presented in Figure A-6 are the data for the Tower B site located on top of the south peak of Cinder Cone Butte. The mean velocity measurements in the wind tunnel for this site are also in good agreement with the field data.

Vertical profiles of components of turbulence intensity were also computed from the wind tunnel data for the two locations discussed above. The longitudinal (direction of the mean wind) component and lateral (perpendicular to the mean wind) component of local turbulence intensity are shown in Figures A-7 and A-8, respectively. The vertical component was not measured in the wind tunnel. Overall, the turbulence levels in the wind tunnel are somewhat larger than the field values. The longitudinal values are about a factor of two greater and the lateral values are about one and a half times as large. Errors introduced by the excessive turbulence in the wind-tunnel flow can be estimated for flow over flat terrain. Pasquill (1962) has pointed out that for a given plume cross-section, the maximum ground-level concentration is determined by only the ratio of the vertical spread to the lateral spread of the plume. Thus, the magnitude of the maximum ground-level concentration should be correct. The change in the location of the maximum can be estimated by assuming plume spread to be proportional to turbulence intensity. For near-neutral conditions and a source height on the order of the height for this study, a 50% excess in turbulence intensity can be expected to result in the maximum ground-level concentration occurring 20% nearer to the source.

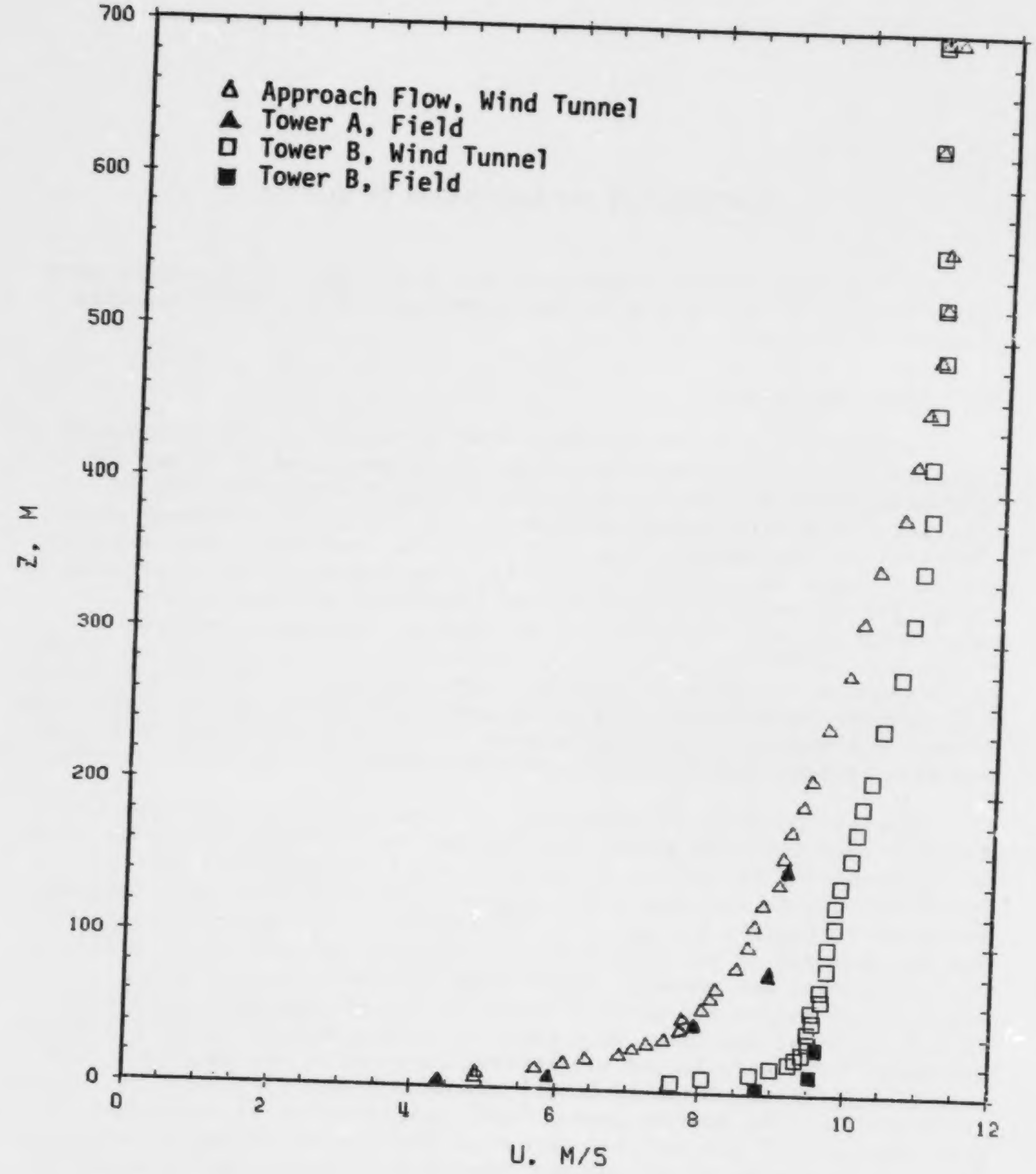

Figure A-6. Mean velocity measurements.

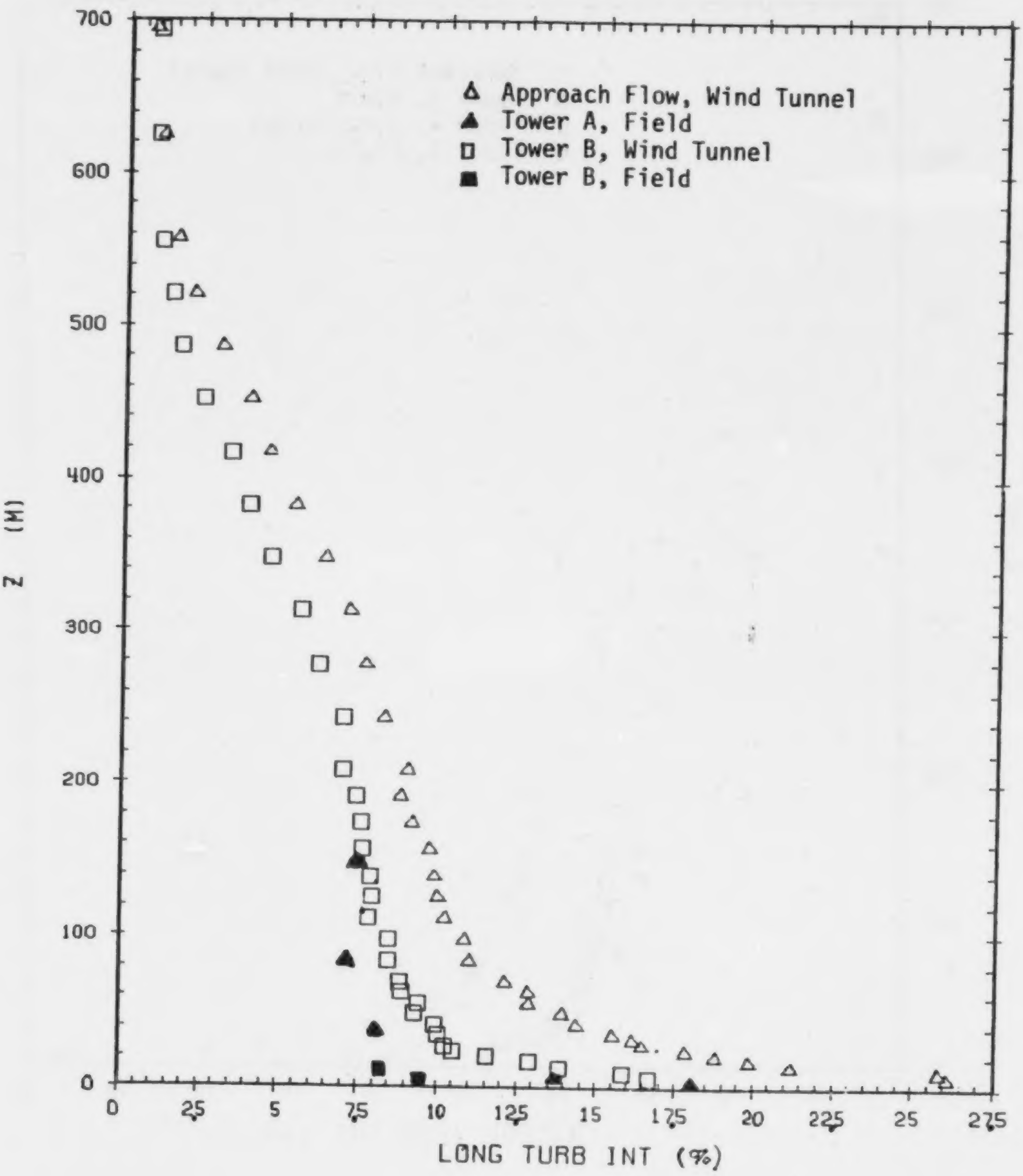

Figure A-7. Longitudinal turbulence intensity.

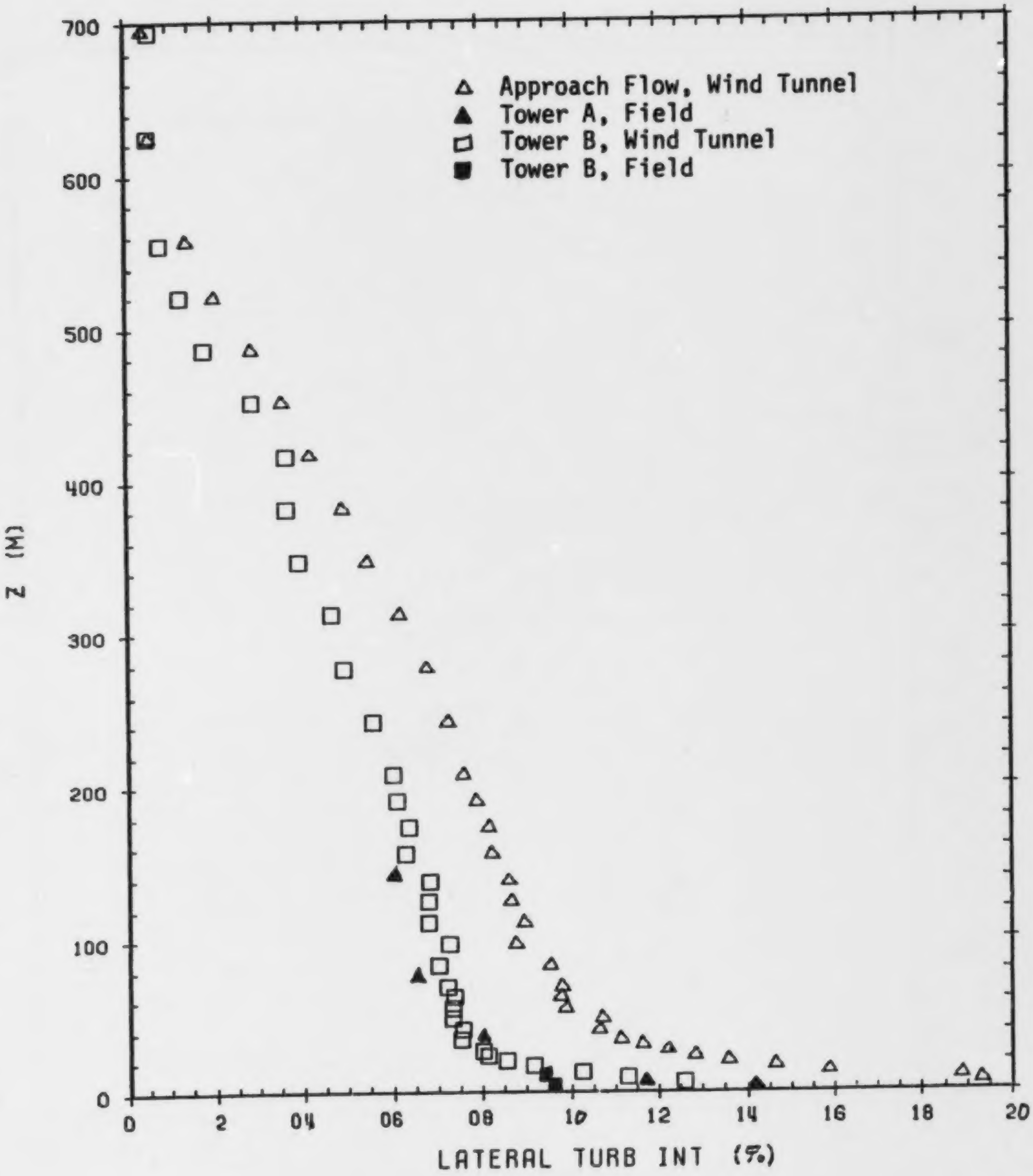

Figure A-8. Lateral turbulence intensity.

Ground-level Concentration Measurements

Data were collected in the wind tunnel for three different wind direction and stack height combinations. The first case was for an ambient wind direction of 312° and a stack height of 50 m (full-scale equivalent) above the wind-tunnel floor. This wind direction was selected as an average of the directions reported for Tower A before the corrections for alignment of the anemometers was later reported. The actual terrain near CCB has a gradual slope away from the butte and some undulations. For the second run, the wind direction was changed to 316° to correspond more nearly to the direction measured at the source height. Then, the difference in surface elevation at the source location and the field reference (8 m full scale) was accounted for by lowering the stack to match the height above the field reference. These situations, referred to as Runs 1 through 3, are summarized in Table A-5.

For each of the three runs, ground-level concentrations were measured at each of the 100 ports corresponding to field sampler locations. These data are presented as concentration maps in Figures A-9 through A-11. The available field data are shown for comparison in Figure A-12. Concentration isopleths were hand drawn on these maps to facilitate comparison. Results for each case can be compared with the field data to evaluate its success in reproducing the field results. In addition, the results from the laboratory runs can be compared with one another to determine the effects of changing wind direction and stack height.

TABLE A-5. WIND-TUNNEL EXPERIMENT SUMMARY

Case	Wind Direction	Stack Height: Above Wind-Tunnel Floor	Stack Height: Above Field Reference	Data Collected
1	312°	7.2 cm	50 m	100 surface port concentrations
2	316°	7.2 cm	50 m	100 surface port concentrations, 1 elevated lateral profile, and 1 elevated vertical profile
3	316°	6.05 cm	42 m	100 surface port concentrations

The concentrations for all three runs were, in general, a factor of two lower than the field values. Runs 1 and 2, with the higher source, exhibit bands of nearly uniform, maximum concentration that extend from a point on the upwind surface of the hill to the lee side of the hill. The wind direction for Run 1 differs from that of Run 2 by only 4°; however, the band of maximum concentration for Run 1 wraps around the side of the

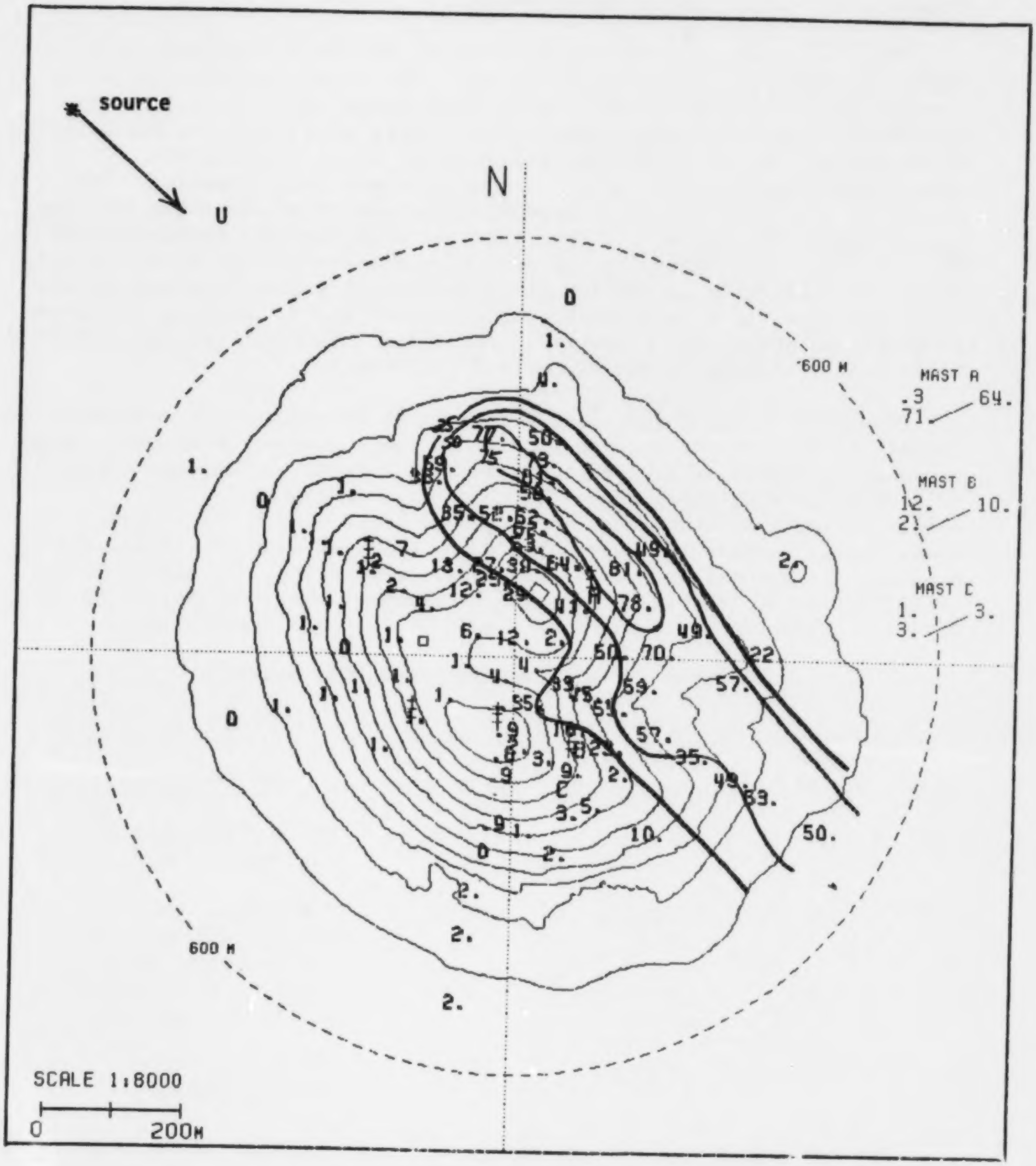
source
U
N
600 M
600 M
MAST A
.3
64.
71.
MAST B
12.
10.
21.
MAST C
1.
3.
3.
0
1.
1.
1.
0
0
2.
2.
2.
2.
50.
10.
53.
49.
35.
57.
22.
57.
49.
70.
78.
81.
64.
52.
50.
SCALE 1:8000
0
200M

Figure A-9. Concentration measurements for Run 1.

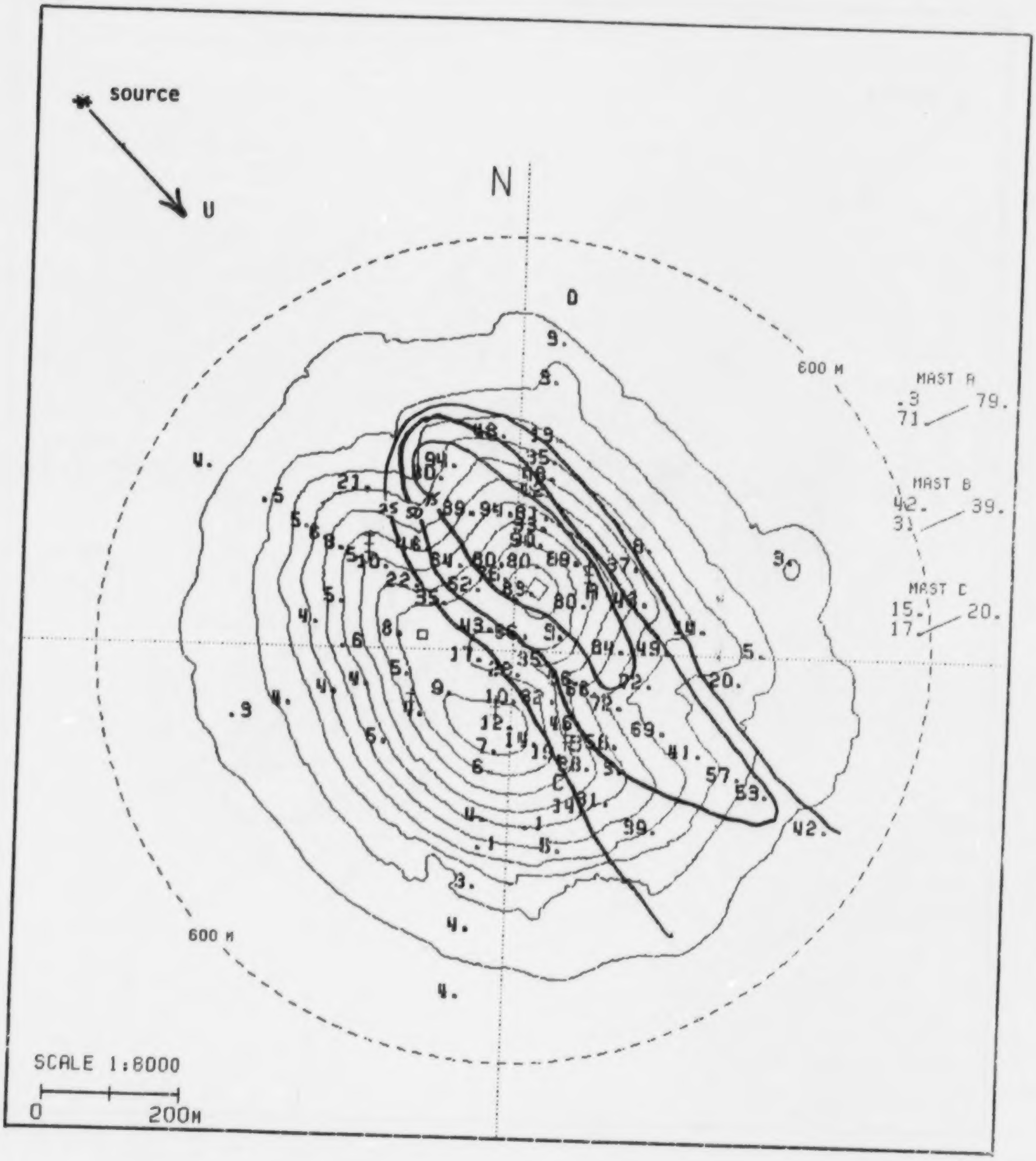
source
U
N
D
600 M
600 M
MAST A
.3
71
79.
MAST B
42.
31
39.
MAST C
15.
17
20.
SCALE 1:8000
0
200M

Figure A-10. Concentration measurements for Run 2.

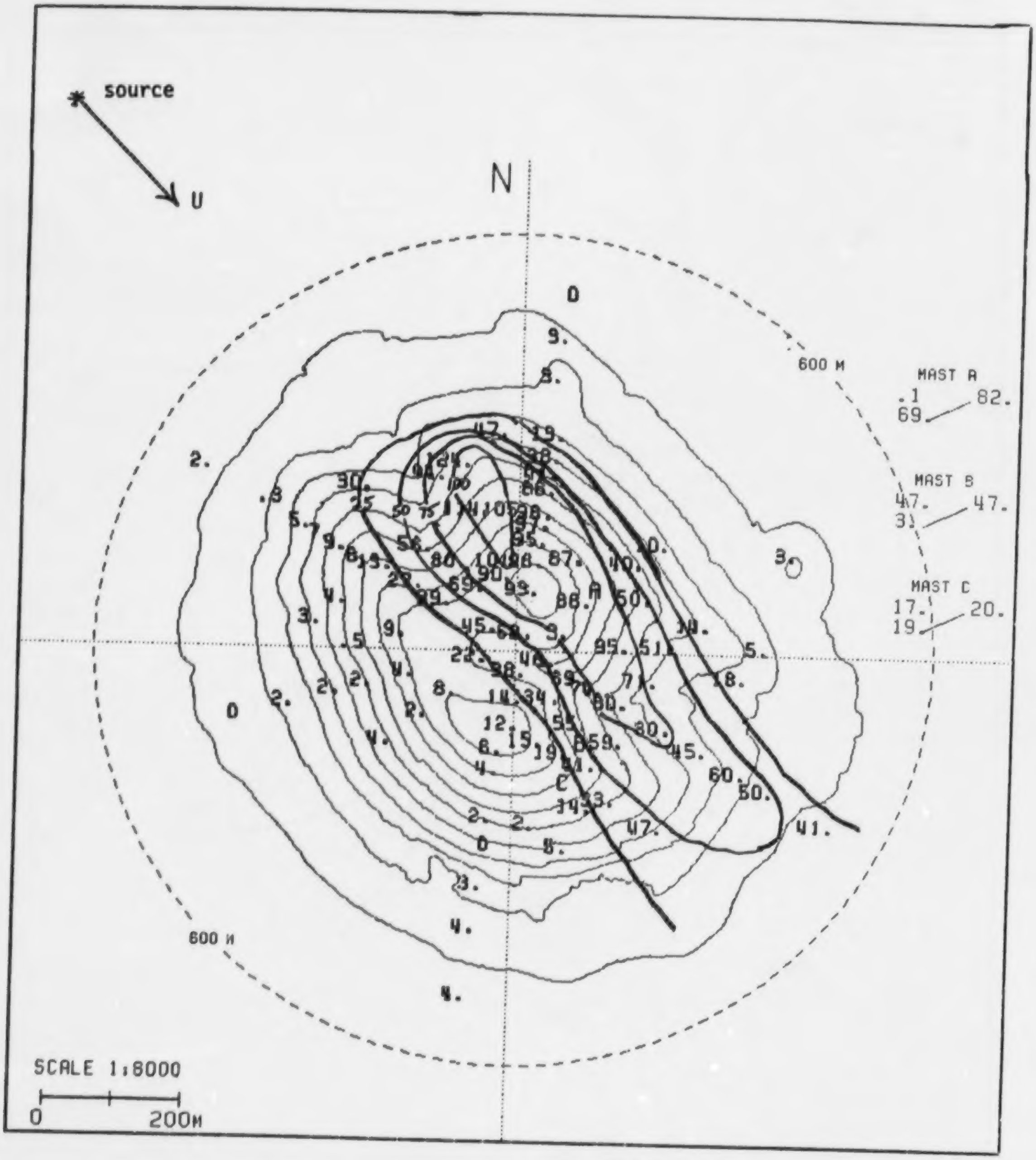
source
U
N
600 M
600 M
MAST A
.1
82.
69
MAST B
47.
47.
31
MAST C
17.
20.
19
SCALE 1:8000
0
200M

Figure A-11. Concentration measurements for Run 3.

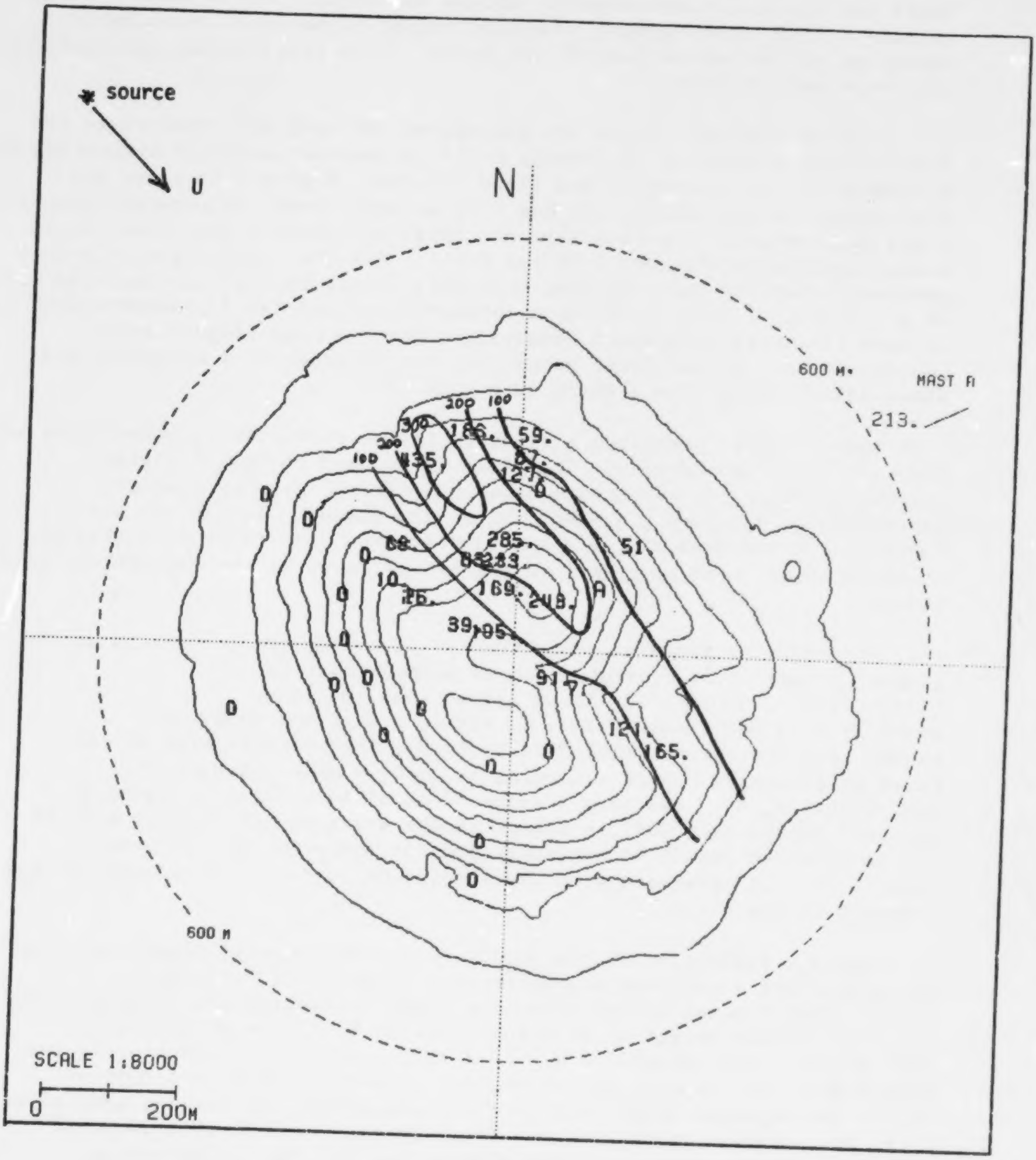
source
U
N
600 M
MAST A
213.
200
100
300
186.
59.
200
100
135.
87.
127.
285.
51.
68.
283.
10.
26.
169.
248.
A
39.
95.
91.
7.
121.
165.
0
600 M
SCALE 1:8000
0
200M

Figure A-12. Concentration measurements from field experiment.

butte and for Run 2 lays directly across the crest. Run 3, with a lower release height, shows a more localized region of maximum concentration occurring on the upwind face of the butte. This is in better agreement with the field data pattern.

Scatter diagrams of the concentrations for each run compared to the field values (Figures A-13 through A-15) are another means of evaluating the agreement of the laboratory and field results. Figure A-13 shows the wind-tunnel concentrations for Run 1 to be much lower, in general, than the field measurements. In this type of comparison, Runs 2 and 3 are nearly indistinguishable (Figures A-14 and A-15). However, there is much better agreement than for Run 1 in that most data points fall within an error band of a factor of 2. The difference between Run 2 and Run 3 concentrations can be seen in a scatter diagram comparing those two runs (Figure A-16). Concentrations, at the fixed receptors, from a stack 50 m in height are about 85% of those from a stack 42 m high.

Turner (1970) presented a solution to the diffusion equation known as the Gaussian plume formula. The plume is assumed to have Gaussian distributions in the vertical and lateral directions with standard deviations of σ_z and σ_y, respectively. The standard deviations are functions of downwind distance and are obtained, according to stability classification, from empirical relationships known as the Pasquill-Gifford curves.

According to Gaussian plume theory, with complete reflection at the ground, ground-level concentration is proportional to $(1/\sigma_z\sigma_y)\exp(-0.5(H/\sigma_z)^2)$. If we assume that the plume geometry does not change (i.e., σ_y and σ_z remain the same) and change only the stack height from H_1 to H_2, the concentration at the fixed point should change according to $C_2/C_1 = \exp(-0.5(H_2/\sigma_z)^2)/\exp(-0.5(H_1/\sigma_z)^2)$. Assuming a value of σ_z of 48 m (that measured in the wind tunnel over CCB), a change in the stack height from 42 m to 50 m can be shown to result in concentration decreases by 15%, in general. This is in good agreement with the comparison in Figure A-16, despite the presence of the hill.

Another evaluation of the applicability of Gaussian plume theory to the prediction of surface concentrations is shown in Figure A-17. Ground-level concentrations along the plume centerline are calculated for the field source height of 42 m for downwind distances of 200 to 2000 meters. Concentrations from CCB wind-tunnel Run 3 are plotted for comparison. The concentrations on the upwind hill face ($x < 1000$ m) follow the Gaussian plume pattern for D stability. On the lee side of the hill, the measured concentrations decrease more rapidly with downwind distance than the Gaussian plume predictions and the concentrations approach values predicted for C stability.

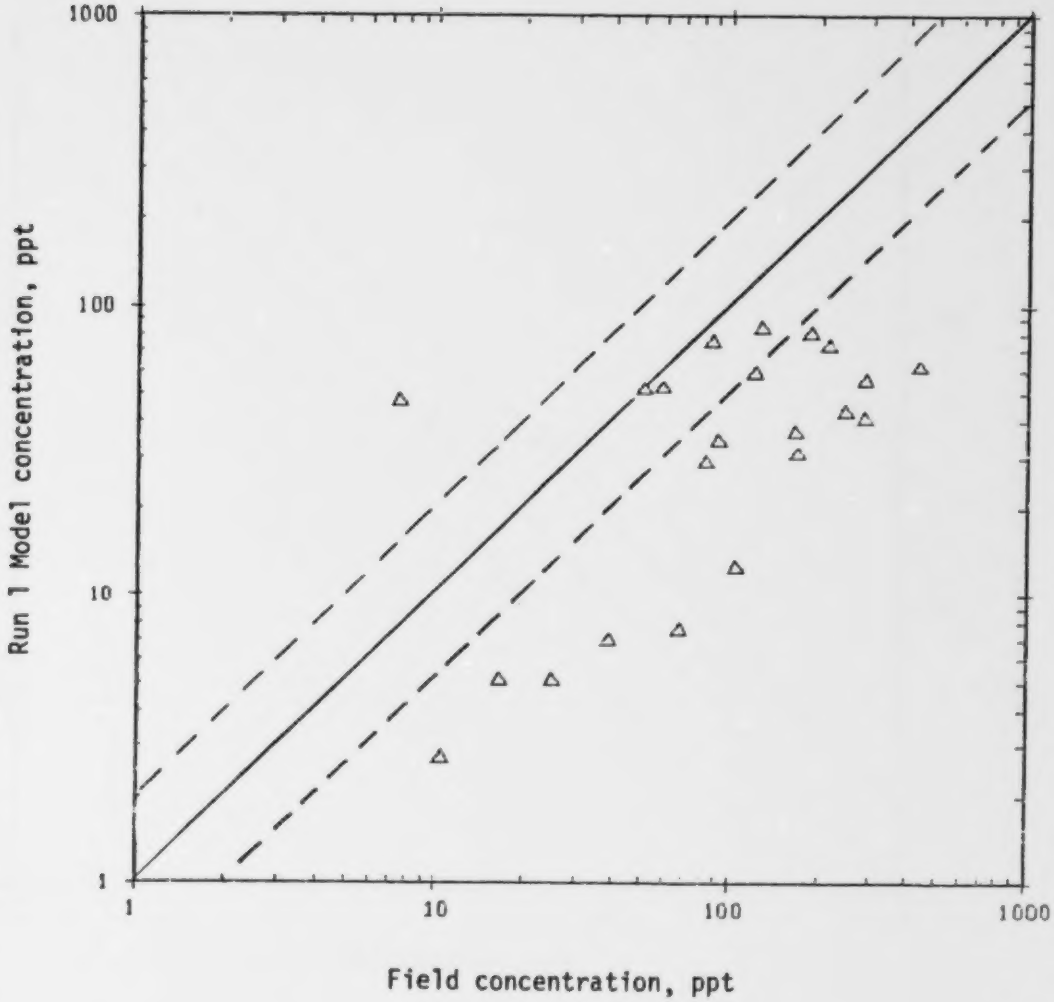

Figure A-13. Comparison of concentrations from Run 1 with field data. In addition, of the fifteen field sampler locations for which zero concentration was recorded, fourteen were below 4 ppt in the wind tunnel.

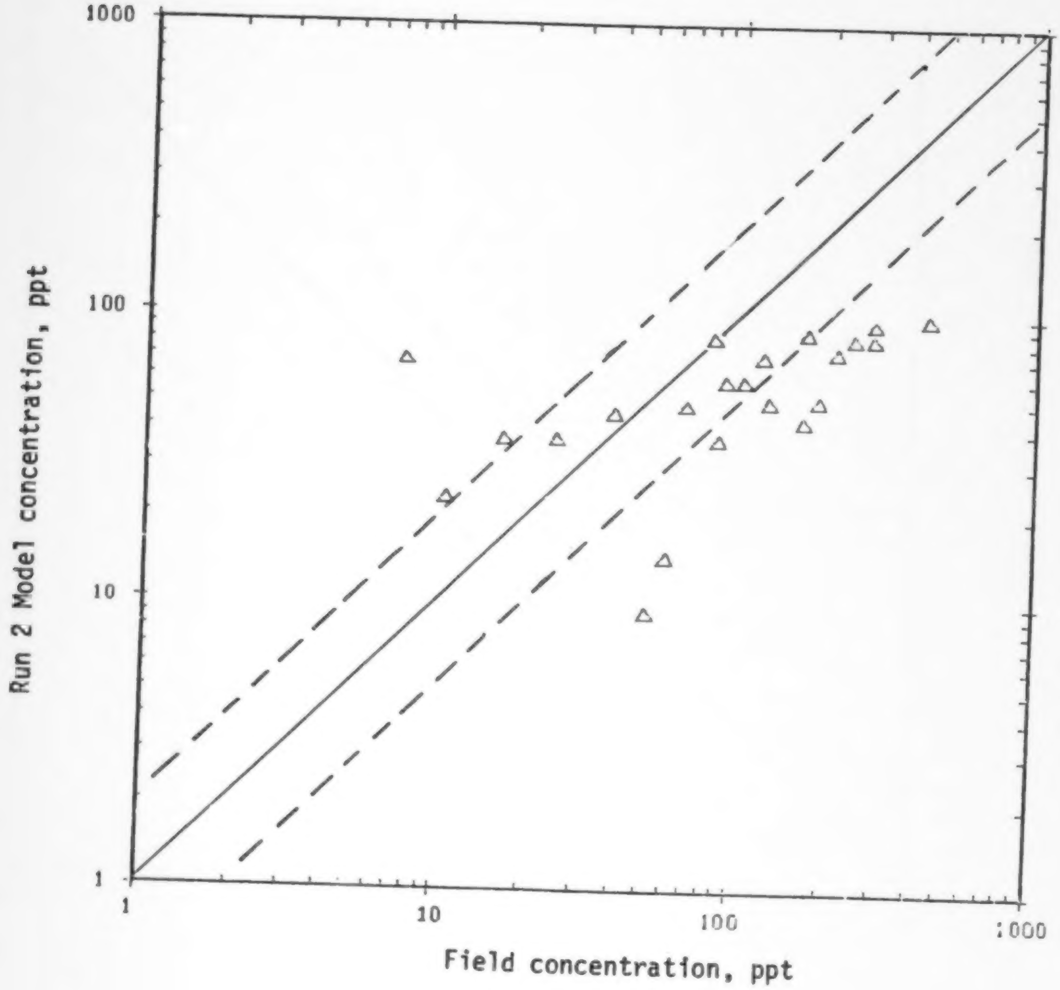

Figure A-14. Comparison of concentrations from Run 2 with field data. In addition, of the fifteen field sampler locations for which zero concentration was recorded, thirteen were below 7 ppt in the wind tunnel.

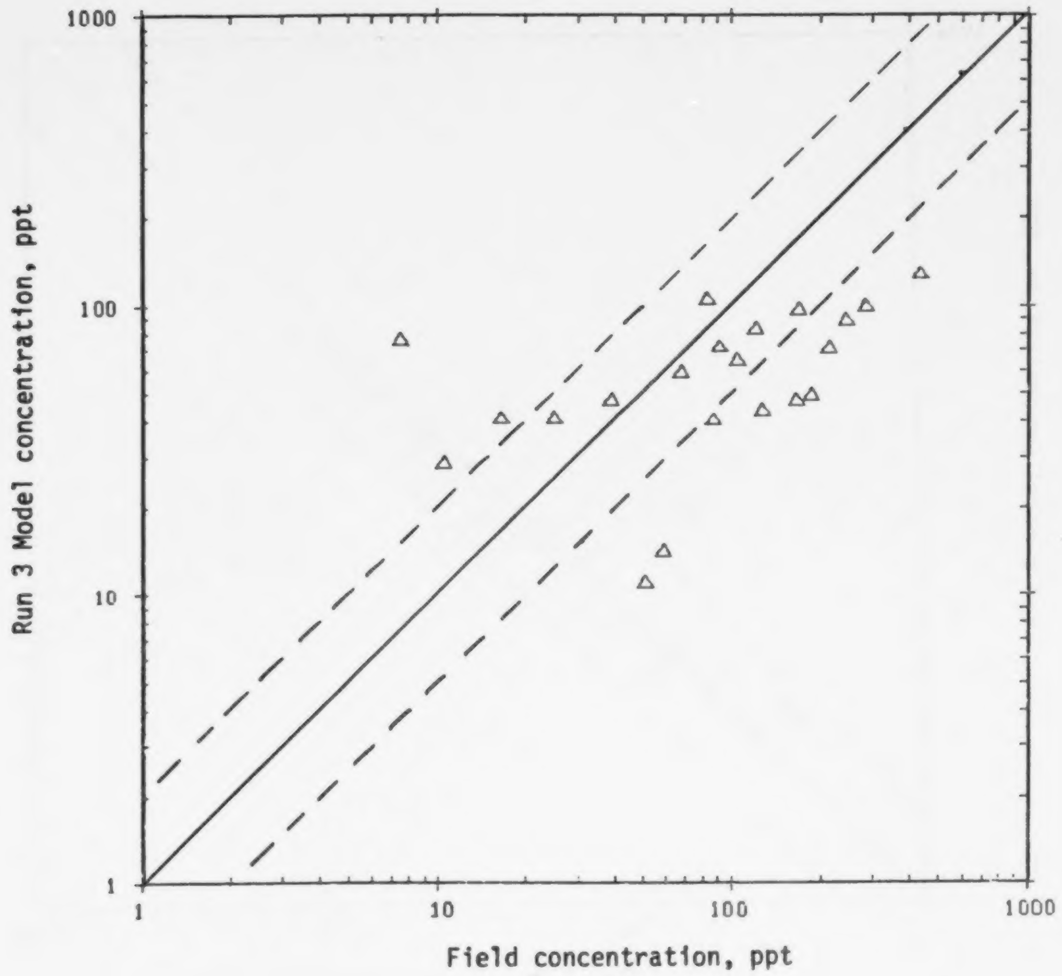

Figure A-15. Comparison of concentrations from Run 3 with field data. In addition, of the fifteen field sampler locations for which zero concentration was recorded, thirteen were below 9 ppt in the wind tunnel.

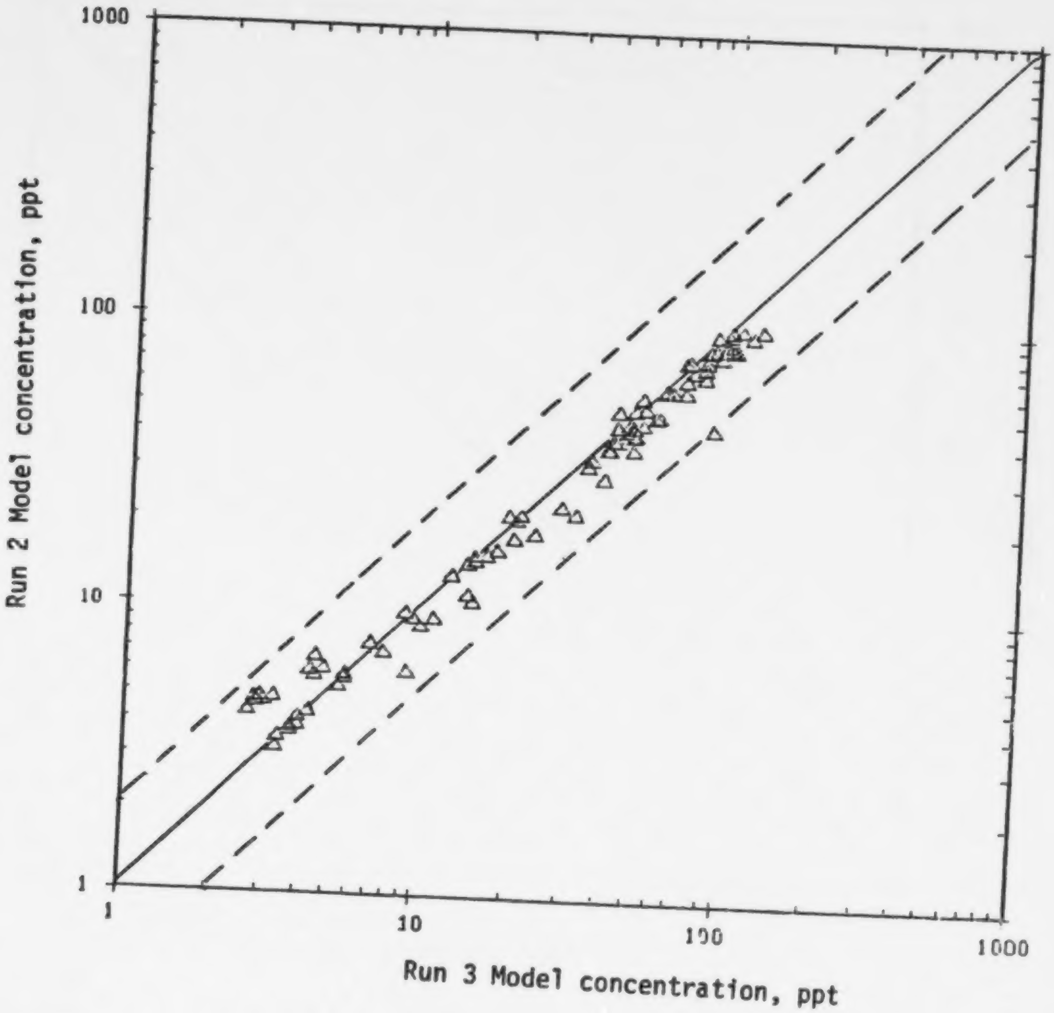

Figure A-16. Comparison of concentrations from Run 2 with concentrations from Run 3.

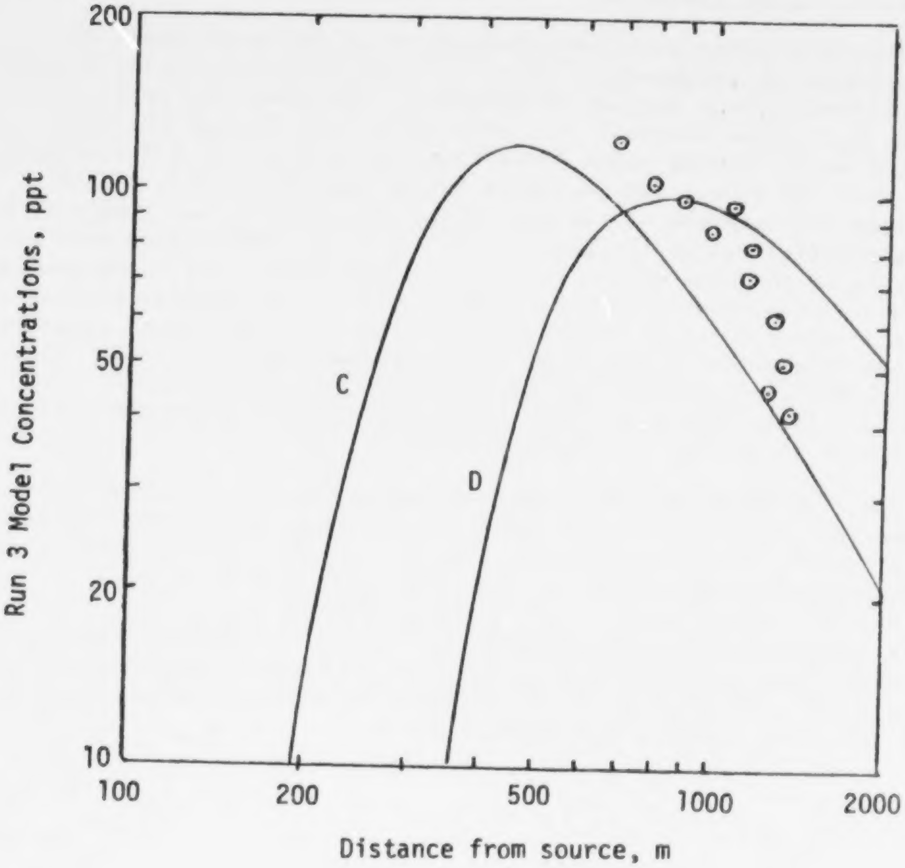

Figure A-17. Ground-level concentrations along plume centerline for Run 3 compared with Gaussian plume predictions for flat terrain. Source height is 42 m; curves are for stability categories C and D.

Elevated Plume Measurements

The field experiments were limited to direct measurement of concentration at ground-level only. A lidar system was used, however, to make oil-smoke plume density measurements from which the vertical plume spread, σ_z, can be derived. For this first hour of Case 202, σ_z, computed as an "hourly value," was found to be 8.2 m at a distance of 200 m from the source and 15.1 m at 520 m from the source. These positions are upstream of the hill where the plume is not likely to be strongly influenced by the presence of the hill. These data were not available at the time of the wind-tunnel experiments and corresponding laboratory measurements were not made. However, a vertical profile and elevated lateral profile of concentration in the wind-tunnel plume were obtained (Figures A-18 and A-19) above the butte during Run 2. The vertical profile was based at FMF port number 9 (see Table A-3 for location). The lateral profile was obtained at this downwind distance, at a height of 46 m above the local surface.

Best-fit Gaussian plume profiles were found for the wind-tunnel data and are shown in Figures A-18 and A-19. Complete reflection was assumed at the surface in calculating the best fit to the vertical profile data. The dispersion coefficients derived from these best-fits are $\sigma_y = 67.3$ m and $\sigma_z = 46.6$ m. This σ_y corresponds to a Pasquill-Gifford stability category D. The σ_z is shown with the available lidar measurements and compared with Pasquill-Gifford values in Figure A-20. The wind-tunnel value falls between Categories C and D, while the lidar values are between D and E.

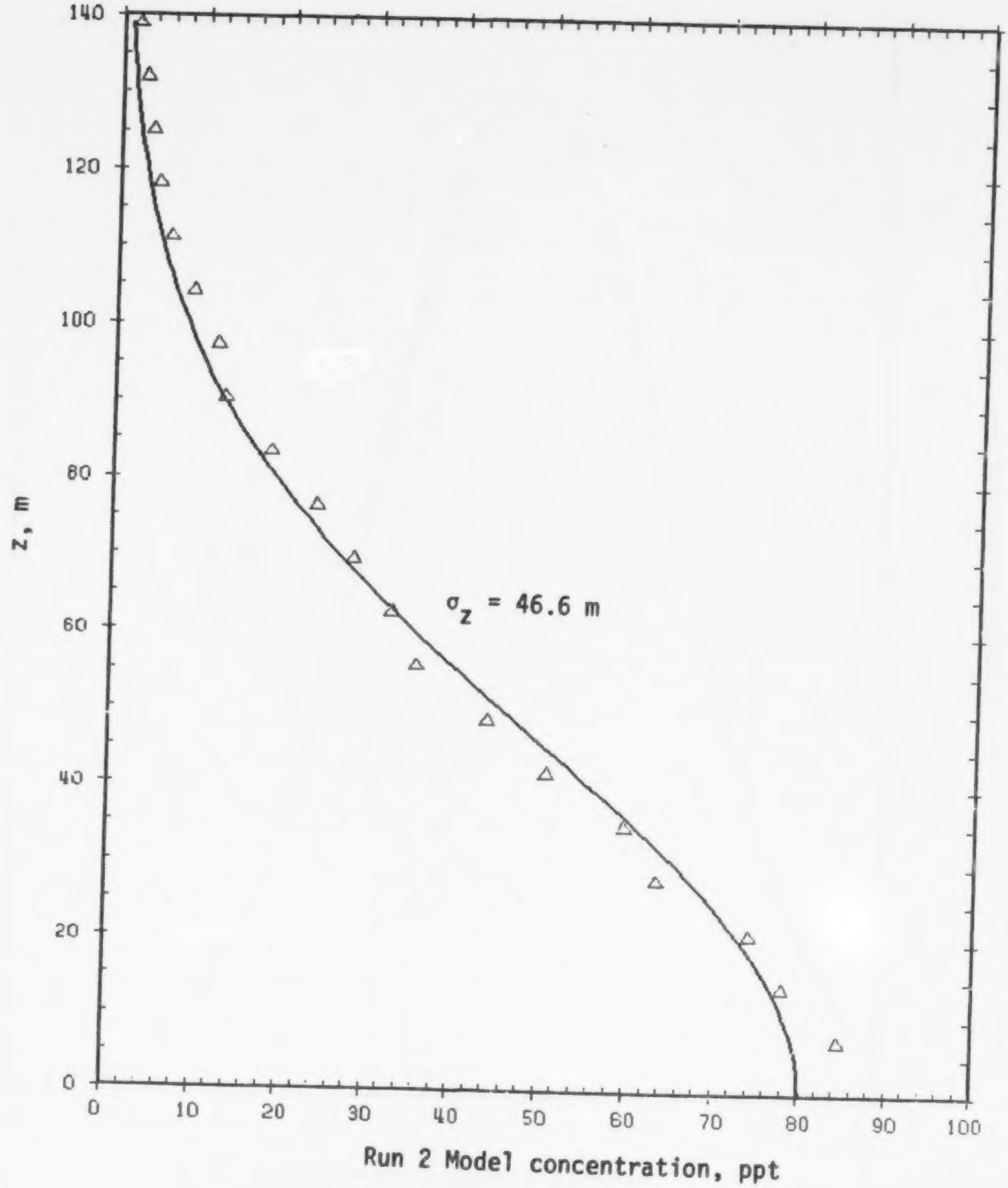

Figure A-18. Vertical profile of concentration above port number 9 of Cinder Cone Butte model in Meteorological Wind Tunnel.

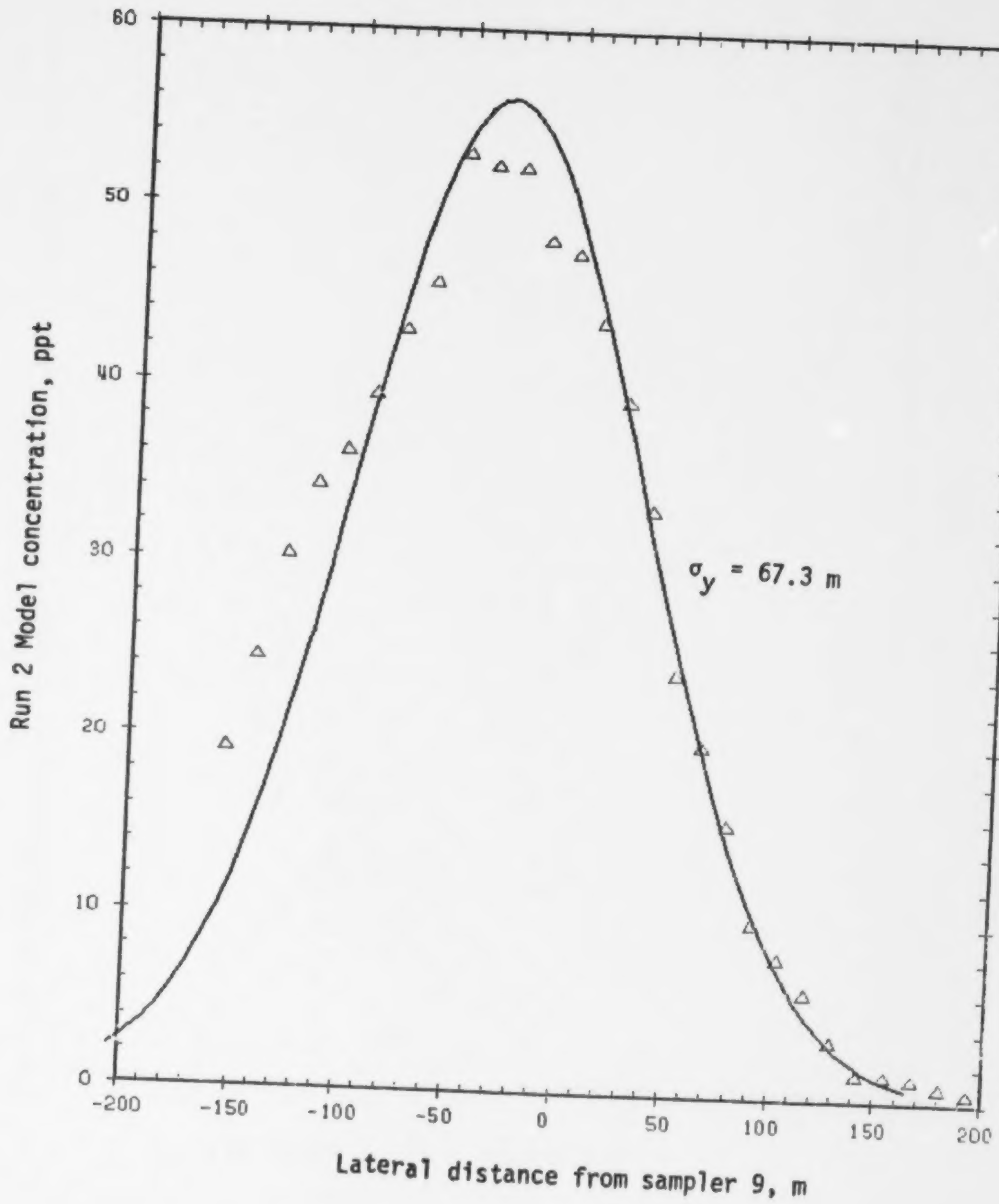

Figure A-19. Lateral profile of concentration above Cinder Cone Butte model in Meteorological Wind Tunnel at a height of 46 m above the local surface at port number 9.

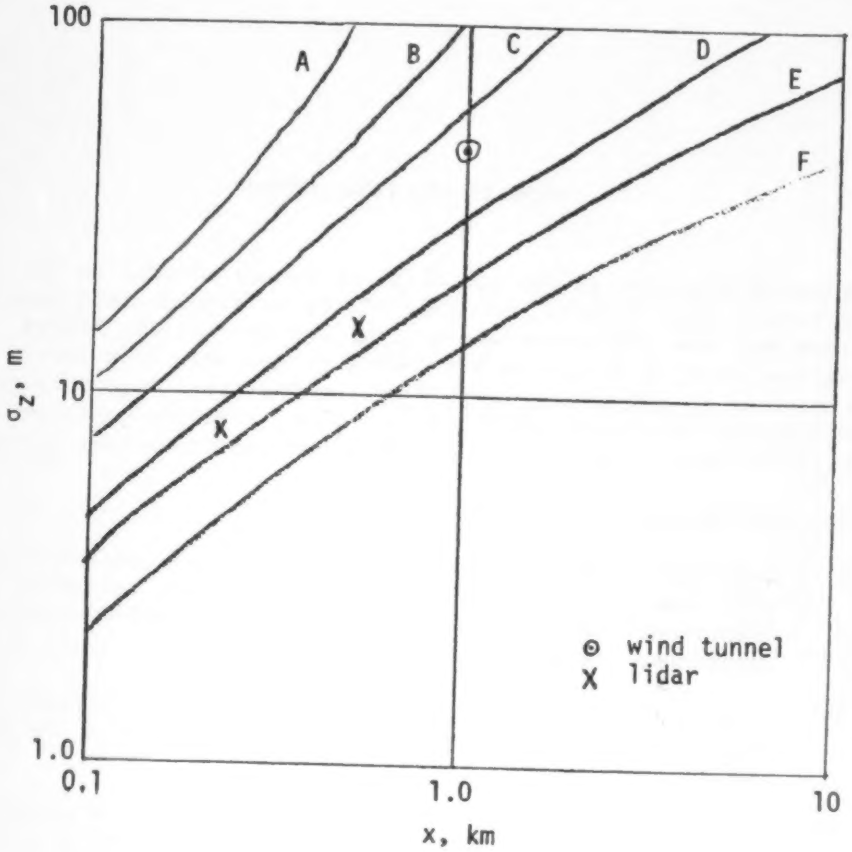

Figure A-20. Vertical plume spread coefficients determined from lidar measurements in the field and concentration profile in the wind tunnel compared with Pasquill-Gifford values.

SUMMARY AND CONCLUSIONS

A one-hour period of the CCB field study was modeled in the EPA Meteorological Wind Tunnel. Analysis of the available field data indicated that the atmosphere was neutral for the period. Three combinations of wind direction and source height were used in the study. Concentrations at 100 ground-level sampling positions were obtained for comparison with available field values. Also, elevated profiles of concentration were obtained through the plume over the crest of the hill.

The conclusions of this study are:

1) Modeling neutral flow over this three-dimensional hill in the wind tunnel, Run 3, reproduced the measured, non-zero, field concentrations to within a factor of 2 for 43% of the sample locations; 71% were within a factor of 3.

2) Changing the approach flow wind direction only 4° resulted in a significant shift in the concentration pattern on the hill surface.

3) Changing only the stack height from 42 m to 50 m resulted in a 15% reduction of ground-level concentrations, in general. This is in agreement with the Gaussian plume theory relationship for the dependence of ground-level concentrations on stack height.

4) Plume spread as determined by computing σ_y and σ_z from lateral and vertical tracer concentrations over the hill top compared well with Pasquill-Gifford values for flat terrain.

5) Concentrations measured on the upwind face of the hill compared closely with Gaussian plume theory predictions. However, concentrations measured on the lee surface of the hill decreased with distance at a faster rate than Gaussian plume theory predicts.

The absolute effects of the presence of the hill on the plume and ground-level concentrations cannot be resolved by this data base. Additional measurements with the hill and reference measurements in the absence of the hill must be made to evaluate the effects of the hill. The wind tunnel data presented here compares reasonably well with the field data and offers some additional ground-level concentration measurements as well as measurements within the elevated plume which can be used to extend the field study data base.

REFERENCES

Lavery, T.F., Bass, A, Strimaitis, D.G., Venkatram, A., Green, B.R., Drivas, P.J. and Egan, B.A., 1982: EPA Complex Terrain Model Development Program; First Milestone Report - 1981, EPA-600/3-82-036, U.S. EPA, Research Triangle Park, NC, 304p.

Pasquill, F., 1962: Atmospheric Diffusion, D. Van Nostrand Company Ltd., London, England, 297p.

Turner, D.B., 1970: Workbook of Atmospheric Dispersion Estimates, Office of Air Programs, Pub. No. AP-26, U.S. EPA, Research Triangle Park, NC.

APPENDIX B

SUPPORTING METEOROLOGICAL MEASUREMENTS - ACOUSTIC SOUNDER AND SONIC ANEMOMETERS

SUPPORTING METEOROLOGICAL MEASUREMENTS - ACOUSTIC SOUNDERS AND SONIC ANEMOMETERS

EPA SHIS NO. 2

W.D. Neff
Wave Propagation Laboratory
Environmental Research Laboratories
National Oceanic and Atmospheric Administration

1. INTRODUCTION

In ~~addition to the WPL Lidar, the~~ Atmospheric Studies Program Area of the WPL provided a number of supporting boundary layer measurements for SHIS #2. These included two monostatic acoustic sounders, one located just upwind of the meteorological tower and one adjacent to the Hogback as shown in Figure B-1. A monostatic/ bistatic-Doppler sounder provided wind profiles and monostatic facsimile records 1.4 km upwind of the tower. A portable tethersonde system also provided wind and temperature profiles first near the Hogback, and during a portion of the experiment, near the Doppler site.

In addition, just prior to the SHIS #2 a preliminary version of a portable sonic anemometer system was assembled to provide supporting turbulence measurements. Two three-axis sonic anemometers were mounted on Tower A, one at 40 m, a second at 5 m. Electronics for two fast-response temperature sensors were also in place.

In the sections that follow we will describe these measurement systems, their operation during SHIS #2, current state of data reduction and some preliminary analysis and interpretation. In a closing section, we will outline some proposed improvements in these systems and their deployment in future experiments.

Sonic Data

SHIS #2 provided an opportunity to test a portable sonic anemometer data system. At the request of ERT, development of this system began in early September, 1982. Software was developed on an LSI-11, floppy-disc based microprocessor system. Raw data were recorded on a 9-track magnetic tape. Software processing in the field provided 20-min averaged data. While not fully completed and checked prior to SHIS #2, this system did provide mean winds, variances, and covariances in a coordinate system oriented with the sonic device. Post processing of the raw data tapes is being accomplished by the staff of the Boulder Atmospheric Observatory (BAO). By adapting this data for input to standard BAO software, a full range of analysis products can be made available including turbulence quantities in standard meteorological coordinates, in coordinates rotated along the mean wind, as well as spectra and cospectra. Addition of a hard-disc based, multi-tasking operating system to the field version of the LSI-11 system will eventually allow such products to be available in field settings.

As operated in this experiment, the sonic anemometer interface electronics provided both analog and digital outputs. The fast-response temperature sensor provides only analog data. Two versions of the data

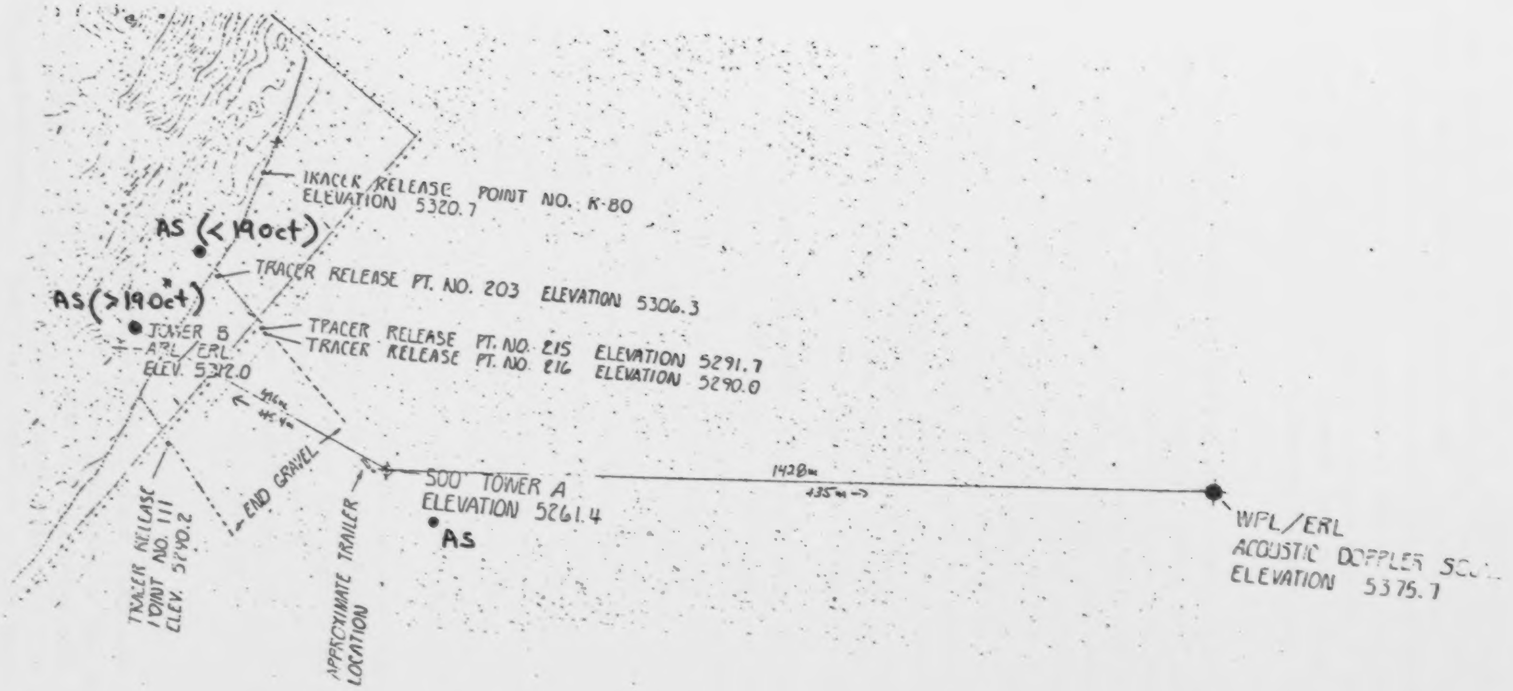
TRACER RELEASE POINT NO. K-80
ELEVATION 5320.7
AS (< 19Oct)
TRACER RELEASE PT. NO. 203 ELEVATION 5306.3
AS (> 19Oct)
TOWER B
ARL/ERL
ELEV. 5312.0
TRACER RELEASE PT. NO. 215 ELEVATION 5291.7
TRACER RELEASE PT. NO. 216 ELEVATION 5290.0
END GRAVEL
TRACER RELEASE
POINT NO. 111
ELEV. 5290.2
APPROXIMATE TRAILER
LOCATION
500' TOWER A
ELEVATION 5261.4
AS
1428m
435m
WPL/ERL
ACOUSTIC DOPPLER SO
ELEVATION 5375.7

Figure B-1. Location of the two monostatic acoustic sounders and the monostatic/bistatic Doppler sounder at Hogback Ridge.

acquisition program were developed to allow processing of these various data. The first version provided acquisition of 16-bit digital data directly from the sonic interface. The second provided 12-bit conversion of the analog outputs from the sonic interface. The limitations of a 12-bit A/D led to less resolution of both temperature and analog sonic data. Evaluation of spectra of temperature will provide some indication of the usefulness of these data. One may expect, however, that the data resolution should be better than that from conventional instrumentation such as propellor anemometers.

In actual operations, the sonic system performed reliably with two exceptions. Following the power outage of 8 October 1982, a number of computer system components were destroyed in addition to the ditigal sonic interface bus ICs. With spare cards from a backup computer system, the sonic system was operational again by 10 October. Because the replacement ICs for the sonic digital interface were not available until 15 October, the program was put into a purely analog mode, bypassing the digital interface. This provided reliable sonic-derived turbulence data for experiments 4 through 8. Inspection of w-data in the field and in the post-processing phase show that it is free of spurious noise except for glitches introduced by the radio transmitter located in the equipment trailer as shown in Figure B-2. In general, these radio-transmission glitches appear only in the bottom level of sonic data. Preliminary inspection indicates that these do not contribute significantly to sigma-w.

The installation of fast response temperature sensors proved more difficult. Early in the experiment a platinum wire temperature sensor was installed with the sonic on the lower boom. This sensor survived the entire experiment. However, its absolute calibration is off by a factor of two because of the mismatch between the differential output of the sensor and the single-sided input to the A/D. The upper sensor presented additional difficulties. Because the boom was not retractable, installation was accomplished by swinging from a rope supported at the top of the tower. With the fragility of the platinum wire sensors, repeated breakage occurred in this process. The decision was then made to record data from the ERT thermistor at 40 m. A scaling factor of 8°C/volt combined with the limited resolution of the 12-bit A/D provided a resolution of 0.04°C, a factor of 8 less than that for the platinum wire sensor.

As of 15 May 1983, preliminary hourly averaged values of wind and vertical velocity variance had been provided to ERT. In addition, one reformatted, scaled data tape had been submitted. Complete preprocessing is expected by the end of May. A number of BAO analysis routines have also been applied to the SHIS #2 sonic data. Some results from this preliminary analysis are described in Section 2 of this appendix.

Monostatic Data

Two monostatic sounders with high-resolution facsimile machines (0.30 m/hr; 150 m to 340 m vertical range displayed over 0.22 m) were operated throughout the experiment. One close to Tower A provided a characterization of the boundary layer near the tracer/smoke release point. The second, at the base of the Hogback, provided a characterization of the

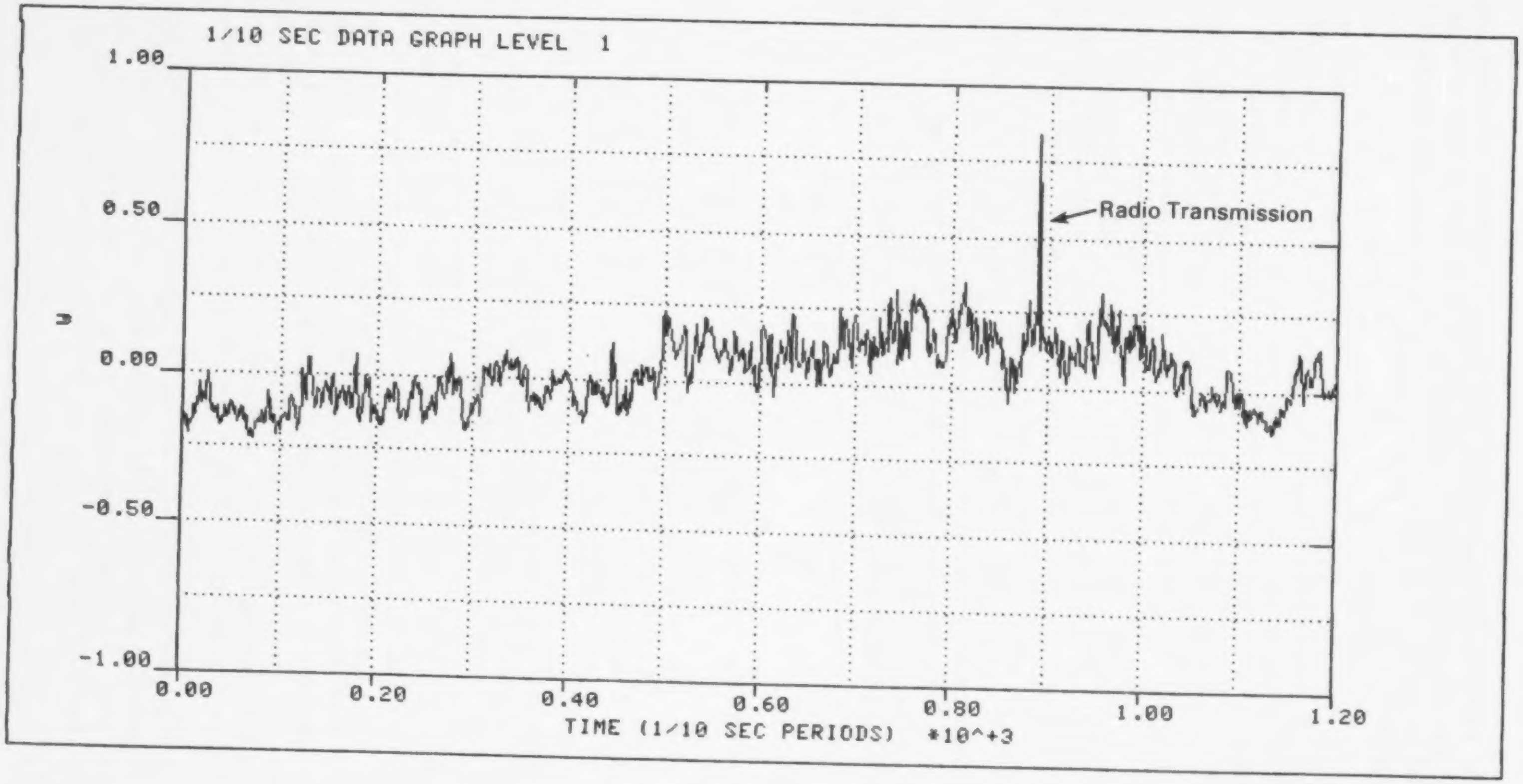

Figure B-2. Segment of vertical wind speed time-series data showing a radio transmission "glitch."

boundary layer flow as it approached the ridge. Prior to 19 October, the ridge-sounder was located directly opposite the Tower A access road. It was then moved 180 m south to avoid acoustic signal contamination from the noise of the oil-fog generator.

Facsimile recordings from monostatic acoustic sounders show time-height cross-sections of small-scale (0.20 m) temperature fluctuations as they move through an antenna beam of some 4° to 8° beamwidth. Such small-scale thermal structure is formed when turbulent motions mix parcels of different potential temperature. Examples include regions within temperature inversions where the vector wind shear is increased sufficiently to reduce the gradient Richardson number below a critical value, leading to the production of turbulence. More commonly, the shear layer induced by surface friction combined with radiative cooling of the surface usually produces a well-defined echo layer on acoustic sounder records. An example, showing both types of echo layers, appears in Figure B-3. In this case, a ground-based turbulent layer extends into the overlying inversion to a depth of about 40 m while elevated layers occur at heights extending up to 175 m. In general, the inversion is much more variable than shown in this example. Often, the height of the turbulent layers and the character of the turbulence change considerably over the course of an hour. Further discussion and examples of the interpretation of acoustic sounder data will be found in Section 2.

Doppler Data

The WPL bistatic Doppler sounder was located 1.4 km upwind of the experiment site near a power substation. This system, providing vertical profiles of the wind from 50 m to 250 m, was intended to characterize the approach flow and provide a general meteorology of the area. It operated in conjunction with a standard, medium resolution facsimile recorder (0.123 m/hr; 820 m maximum range). Figure B-4 shows a block diagram for this system including the layout of the bistatic transmitters and vertical receiver. Conventional wisdom has always suggested a bistatic arrangement to be preferable because of the increased forward scatter from velocity fluctuations that adds to the received signal strength and because the two components of the wind can be computed in a common volume. The commonly-noted drawbacks of such a system include the requirement for more open space to locate the antenna array and increased emission of noise into the environment. While such systems have increased signal-to-noise ratios, particularly under adiabatic conditions, the minimum range is somewhat greater than for monostatic systems. Also as we shall show below, with strong refraction (due to large wind shear or temperature inversions near the surface), displacement of the scattering volume and/or increased ground clutter can bias the Doppler shift from which the winds are computed.

From the results of SHIS #2, it would appear advisable to use a monostatic Doppler system for pure temperature inversion flow situations and where the scale of the flow is greater than the separation of the scattering volumes (that results from tilting two monostatic sounders in orthogonal directions).

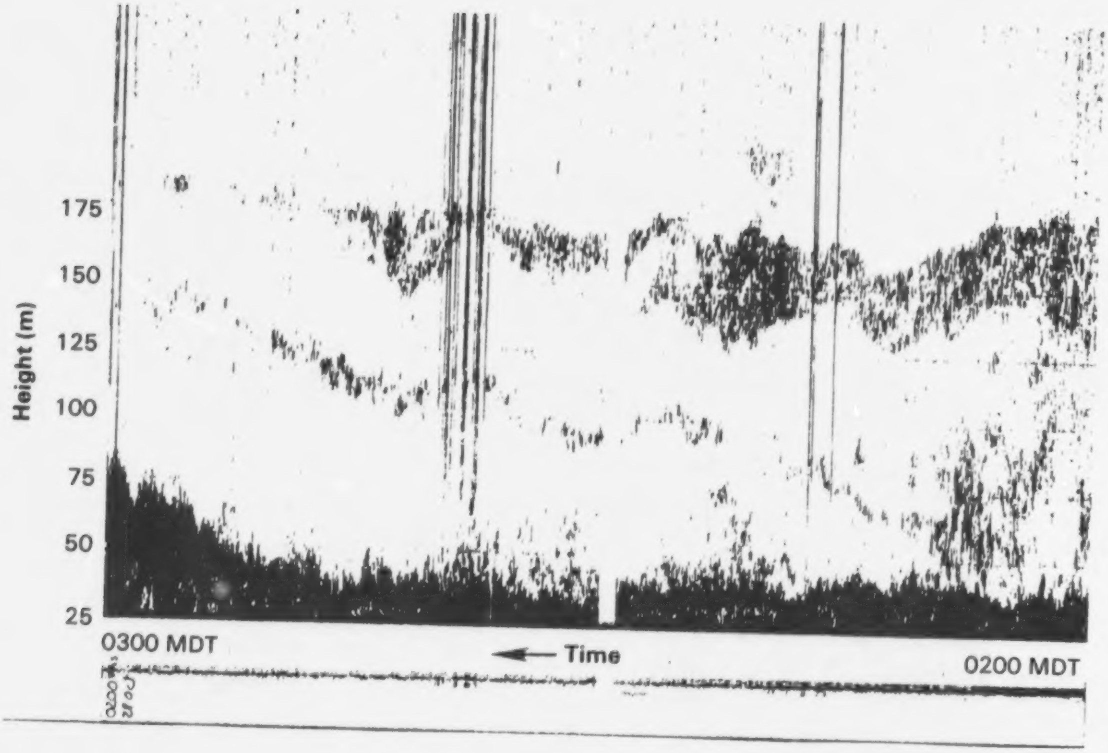

Figure B-3. Monostatic acoustic sounder facsimile record displaying a ground-based echo layer as well as elevated echo layers (10/29/83, 0200-0300 MDT).

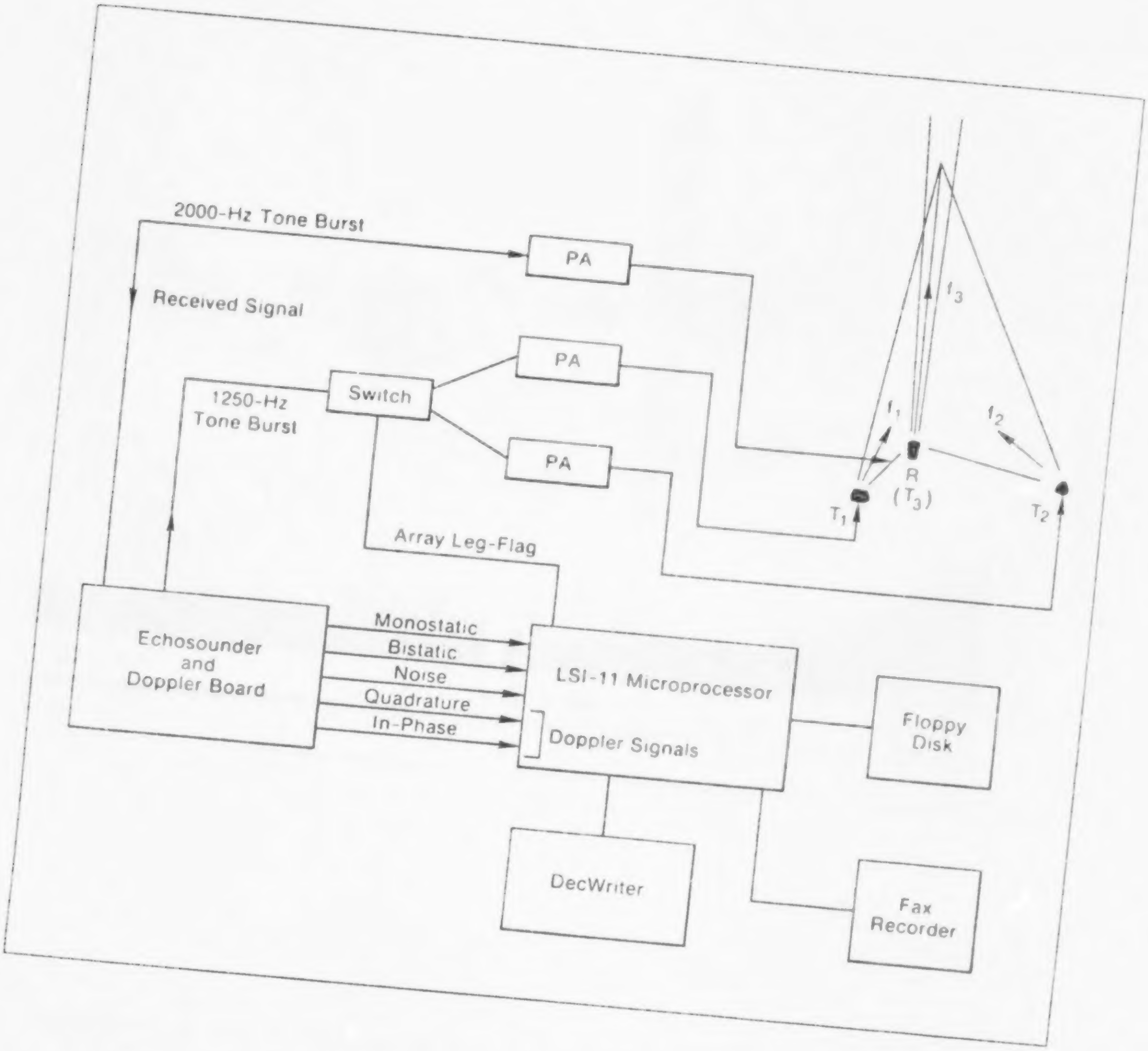
2000-Hz Tone Burst
PA
Received Signal
PA
Switch
1250-Hz
Tone Burst
PA
f_3
f_1
f_2
R
(T_3)
T_1
T_2
Array Leg-Flag
Echosounder
and
Doppler Board
Monostatic
Bistatic
Noise
Quadrature
In-Phase
LSI-11 Microprocessor
Doppler Signals
Floppy
Disk
DecWriter
Fax
Recorder

Figure B-4. Block diagram of the WPL bistatic Doppler sounder system.

Calibration and Data Quality Checks

Doppler sounders are best checked against fixed tower systems. In the field, basic program operation and parameter settings can be checked using a known frequency input. Calibration against a tethersonde is more difficult. Holding the balloon at a fixed level causes sidelobe reflections which introduce a zero Doppler shift, usually at the same height as the comparison. Using a single ascent (descent) of the balloon introduces the complications of comparing a 20-min time average with a snapshot wind profile. In addition, the motion of the balloon downwind or upwind can introduce a bias of as much as 1 m/s under stronger wind conditions.

To eliminate some of these problems, we sought comparison cases where the balloon ascended and descended in reasonable proximity to a 20-min Doppler averaging period. An example of such a comparison is shown in Figures B-5a and B-5b. In Figure B-5b, the two tethersonde profiles show a wind speed difference of about 1.5 m/s above 50 m. The reason for this is that the tetherline has a speed of about 0.5 to 1.0 m/s. At wind speeds of more than a few m/s the balloon starts moving downwind. As the angle to the surface decreases, the line speed subtracts from the wind speed. As the tethersonde descends, the effect is reversed. The net difference then between ascent and descent ranges from 1 to 2 m/s.

During several cases examined, the presence of a strong low-level jet resulted in anomalous Doppler shifts. Two possible causes have been identified. Both are associated with refraction of the bistatic acoustic beam by the wind shear and/or temperature gradient. This can, for example, result in a displacement of the scattering volume off the vertical axis of the receiving antenna making the Doppler shift reflect the vertical component of the wind more than the horizontal. The second possibility is that increased refraction near the ground results in increased ground clutter and hence a bias towards zero Doppler shift. These cases were evident only with a wind maximum below 40 m and appeared only to affect the range gates below 60 m. Following final quality assurance on these data, they will be submitted to the CTMD data base. These results do suggest the advisability of using monostatic Doppler geometrics for measuring winds near the surface under shallow drainage conditions.

```
ACOUSTIC DOPPLER DATA
 STARTING TIME
  10/20  6 0 MDT
               WIND                    DIRECTION (D)
INDEX  HEIGHT SPEED DIR
-----  ------ ----- ---    180      270       0      090      180
                            +********+********+********+********+
  22.....460   0.0   51     D                                   *
  21.....440   0.0   32     D                                   *
  20.....420   0.0   41     D                                   *
  19.....400   0.0   62     D                                   *
  18.....380   0.0  334     D                                   *
  17.....360   0.0   51     D                                   *
  16.....340   0.0   83     D                                   *
  15.....320   0.0   49     D                                   *
  14.....300   0.0   87     D                                   *
  13.....280   2.9   87     *    S                    D         *
  12.....260   0.0   88     D                                   *
  11.....240   2.4   86     *   S                     D         *
  10.....220   3.0   88     *     S                   D         *
   9.....200   3.6   95     *      S                   D        *
   8.....180   4.6   93     *        S                 D        *
   7.....160   5.7   91     *          S               D        *
   6.....140   4.8   88     *        S                D         *
   5.....120   5.8   81     *          S              D         *
   4.....100   6.0   79     *          S             D          *
   3..... 80   4.7  102     *        S                  D       *
   2..... 60   2.3  103     *   S                       D       *
   1..... 40   2.8   90     *    S                     D        *
                            +********+********+********+********+
                            0       5.0      10.0     15.0  18.0
   10/20   6: 0                        WINDSPEED (D)
```

Figure B-5a. Wind speed and direction profile measured by the bistatic Doppler sounder system (10/20/82, 0600-0620 MDT).

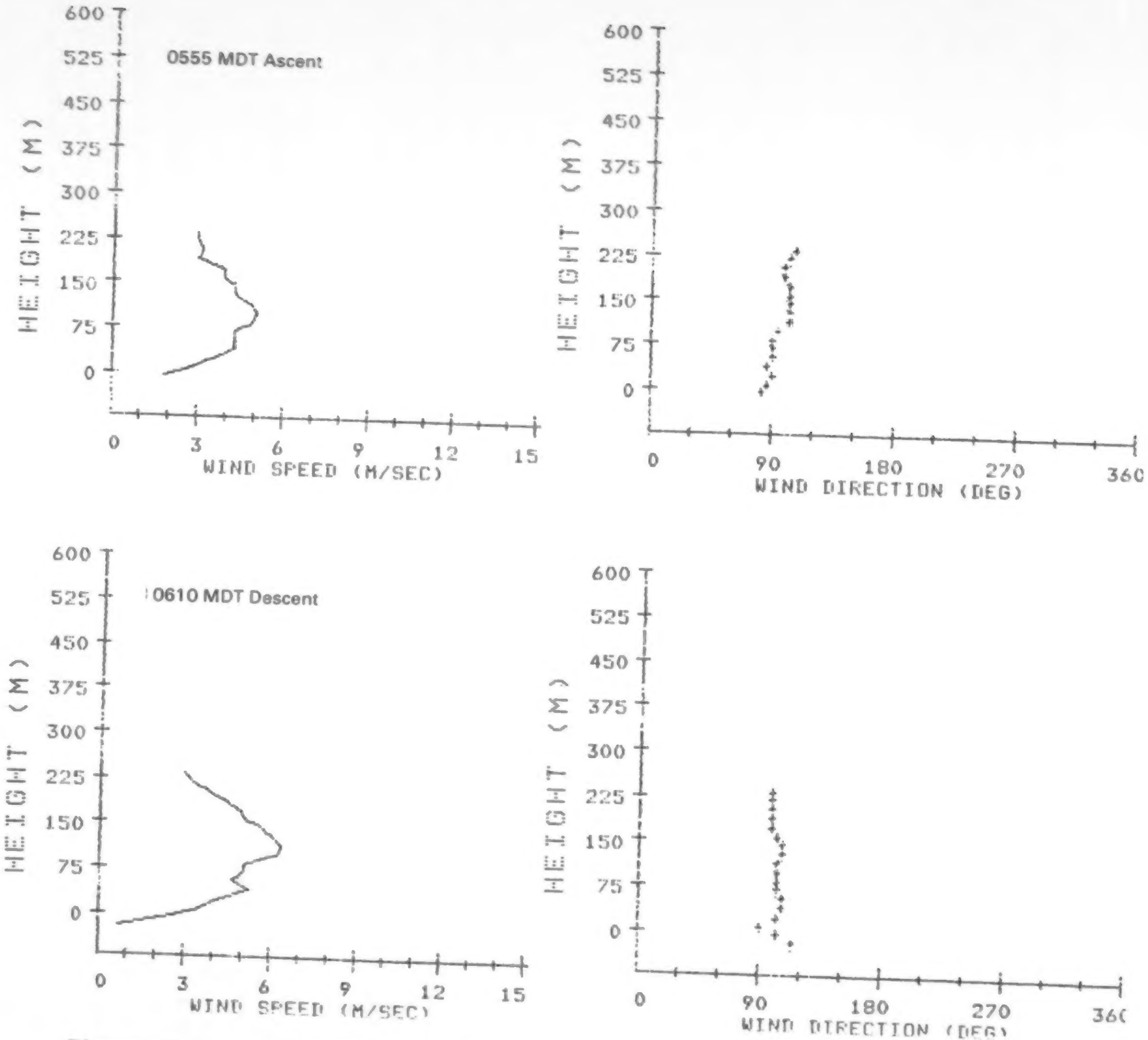

Figure B-5b. Wind speed and direction profiles measured by tethersonde (10/20/82; ascent 0555 MDT; descent 0610 MDT).

2. PRELIMINARY ANALYSIS

SHIS #2 provided a unique set of data from which to analyze winds and turbulence behavior in nocturnal, complex terrain flows. In particular, sonic anemometer data provide an accurate measure of turbulence down to very small scales. Monostatic sounders provide detailed flow visualizations that in general belie any expectation of a steady, simply-structured flow. The Doppler sounder together with supporting tower instrumentation provide an appraisal of the variability in the flow above the boundary layer.

Interpretation of Monostatic Data

1. Increasing shear above the surface-based inversion leads to dynamical instability. Such instabilities are easily identifiable from monostatic records and provide a measure of the vertical extent of large-eddy structure in the inversion. The growth of such instability regions seemed to be independent of the proximity to the Hogback. In fact, similar patterns were observed 1.4 km upwind at the Doppler site. From the Doppler wind data, increases in wind speed above the inversion of from 1 to 2 m/s were observed during these events.

As deduced from second-order closure modeling, turbulence depends inversely on the Richardson number. Since Ri in turn depends on the inverse square of the vector shear, small changes in the shear can translate into large increases in turbulence. From these data, it appears that mesoscale processes above the inversion can strongly affect turbulence within the inversion and boundary layer and hence the dispersion of the plume prior to impact on the Hogback.

2. The flow approaching the Hogback, like most nocturnal inversion flows, is characterized by intermittent turbulent layers and patches. For a given turbulence measurement, say using the 40-m sonic anemometer, the sounder record can provide a good indication of the vertical extent over which the measurement is valid and the variability of such regions in time. The data suggest that linear interpolation schemes are not in general reliable (again, the sounder record can indicate when such schemes might be valid). In addition, the sounder records show considerable variability on time scales that are a significant fraction of a typical averaging period of one hour. In such cases, the sounder record may suggest a more appropriate averaging period, not necessarily beginning on an even hour.

3. The sounder records, while showing many repetitive features in the approach flow, also revealed many short-term phenomena such as inversion height changes due to an apparent local horizontal convergence or divergence of the flow. In other circumstances such patterns have been associated with 10- to 20-min period internal waves.

Examples of Data from the Morning of 15 October

Figures B-6a and B-6b show two sequential half-hour segments of acoustic sounder records between 0500 and 0600 MDT on 15 October. Prior to 0500 MDT, the boundary layer, identified as the lowest echo layer on the facsimile recording, stayed below 50 m. It would oscillate above this level and would at times be perturbed by motions from above. During the early portion of the record shown in Figure B-6a, the flow appeared almost laminar at 40 m. (The absence of an echo on the sounder indicates either a laminar flow or one in which the potential temperature gradient is adiabatic. Adiabatic regions bounded by temperature inversions are not usually clear of echo: in such cases the decay time for the temperature spectrum is greater than the time required to transport some temperature variance $(\overline{w\theta^2})$ from the boundary). Figure B-7 shows the corresponding time series from the sonic anemometer at 40 m obtained over a 1-min section of this record. In this case, superimposed on a slow background oscillation are fluctuations on the order of 0.01 m/s. During this one hour period, the flow aloft increased in speed. This resulted in a thickening shear layer. Starting at a height of 70 m it rapidly expanded downward to meet the boundary layer below. At the same time, an increase in shear farther aloft expanded to fill a region up to 125 m. In this case Figure B-8 shows the effect on w (and therefore on sigma-w).

Evident in the sounder record are descending echo bands that are most noticeable between the surface and 80 m. These have, in previous research, been identified with Kelvin-Helmholz instability. The question then arises of the contributions of this large-eddy structure to sigma-w. This can be estimated from the log-log plot of frequency versus the product of frequency and power spectrum shown in Figure B-9. In this case, the product is almost an order of magnitude above the background spectrum, suggesting a significant contribution, but not an exclusive one. (A number of such cases will be analyzed with separate integrations over the wave and turbulence portion of the spectra). Almost evident in these records is the presence of an inertial subrange. Within the surface layer this tends to occur at frequencies greater than 1 Hz. In most cases analyzed thus far, the spectrum at periods greater than 10 s appear pink (freq. times the spectrum is flat).

A feature noted during the field exercise was the occurrence of positive heat fluxes in the 20-min averaged covariances. The cospectral analysis shown in Figure B-10 shows that these apparent positive fluxes result from low frequency motions. Generally, we have found that the flux is negative for frequencies above 0.01 Hz. In the particular case shown the flux for frequencies less than 0.01 Hz is positive. In part this may be due to a shallow, fluctuating downslope flow of cold air in the lowest 5 m. With a local terrain slope of 0.03 (based on the slope along the road), a 1 m/s drainage flow would produce a 0.03 m/s w. This negative w would then produce a positive correlation with the decrease in temperature.

Continuing Analysis

With acoustic sounder data (monostatic and Doppler), sonic anemometer turbulence information, and tethersonde data, analysis such as that described above will continue. It is expected that the analysis of the primary modeling cases will occur first followed by other cases of interest.

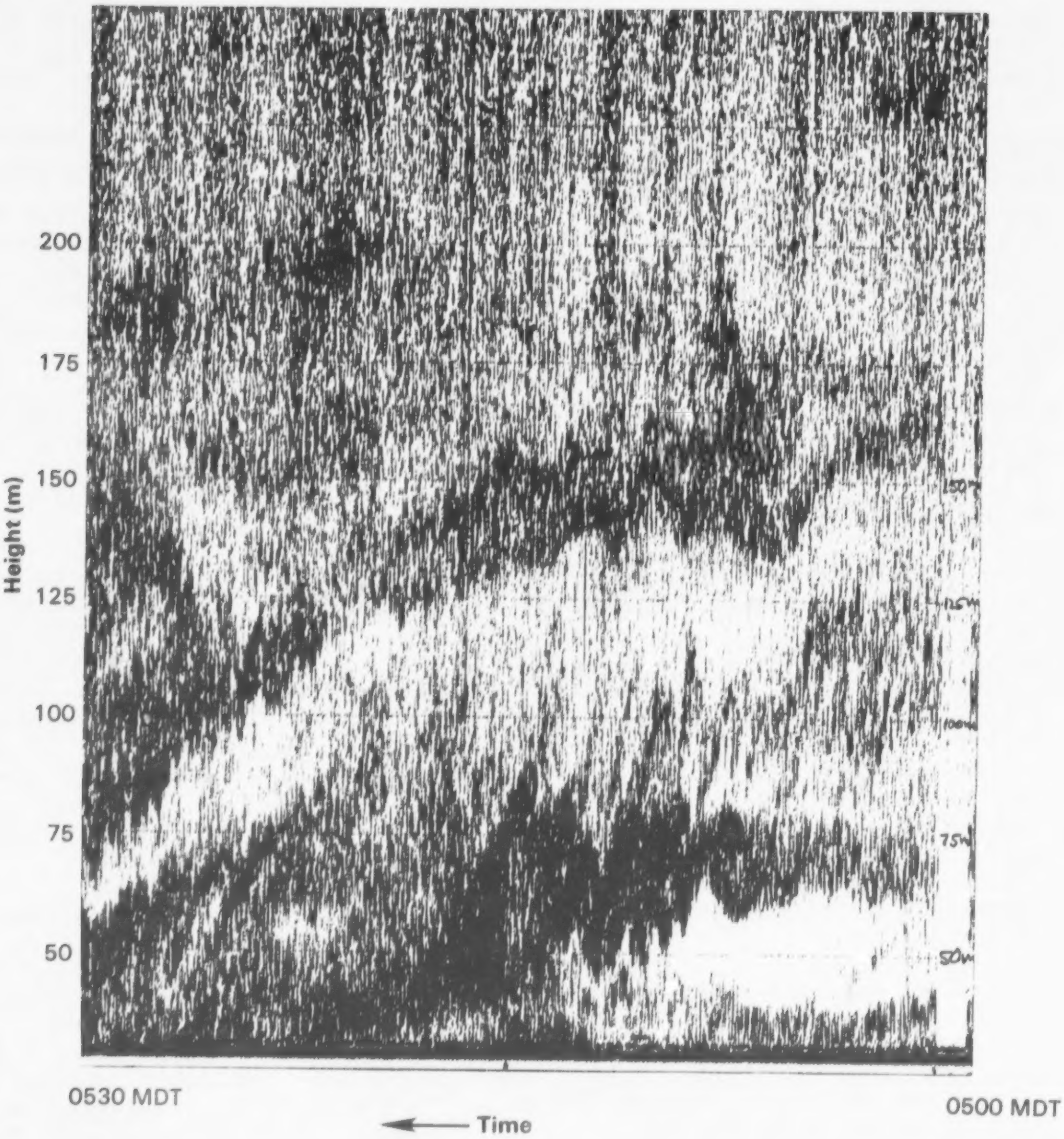

Figure B-6a. Acoustic sounder record (10/15/82, 0500-0530 MDT).

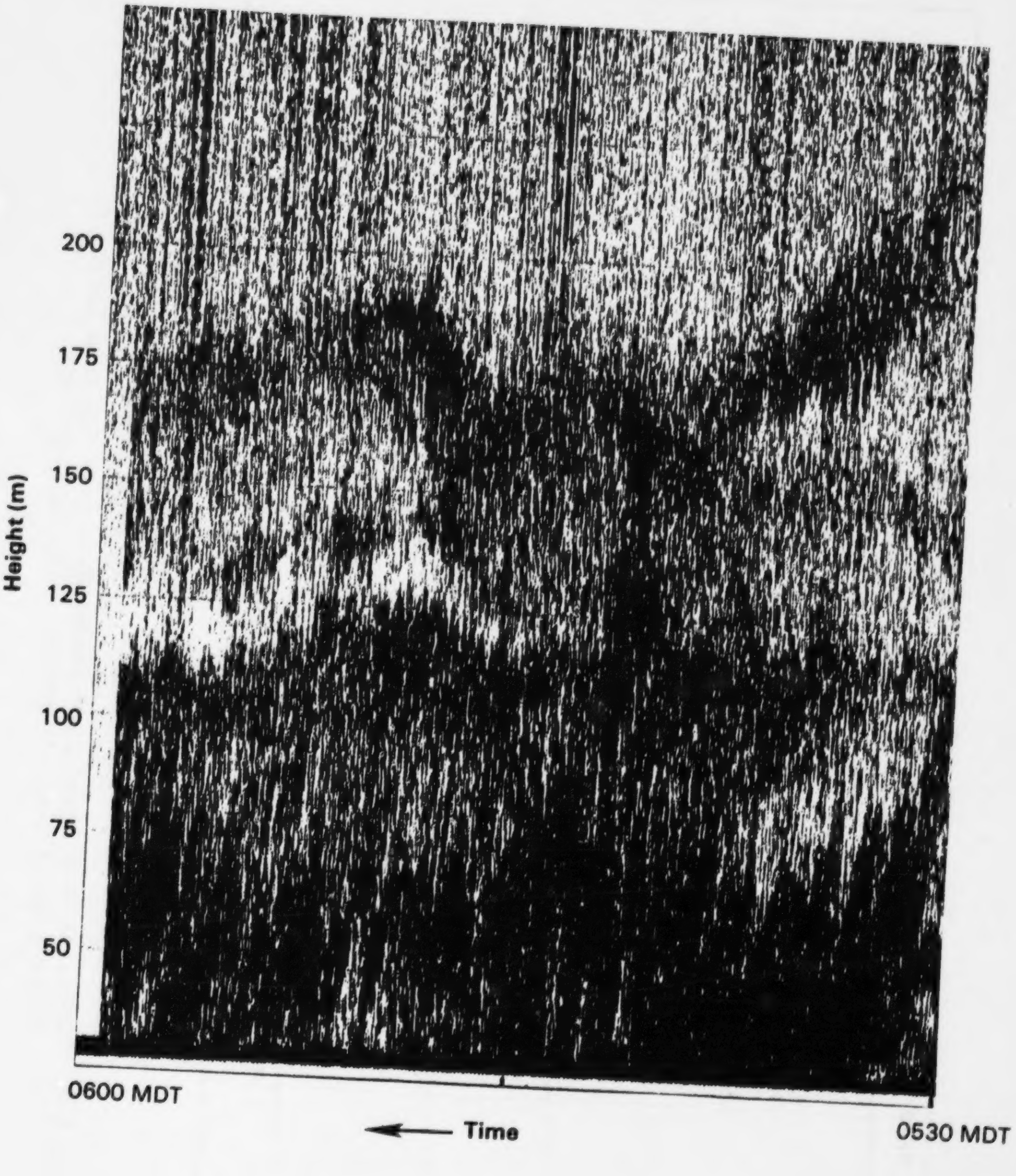

Figure B-6b. Acoustic sounder record (10/15/82, 0530-0600 MDT).

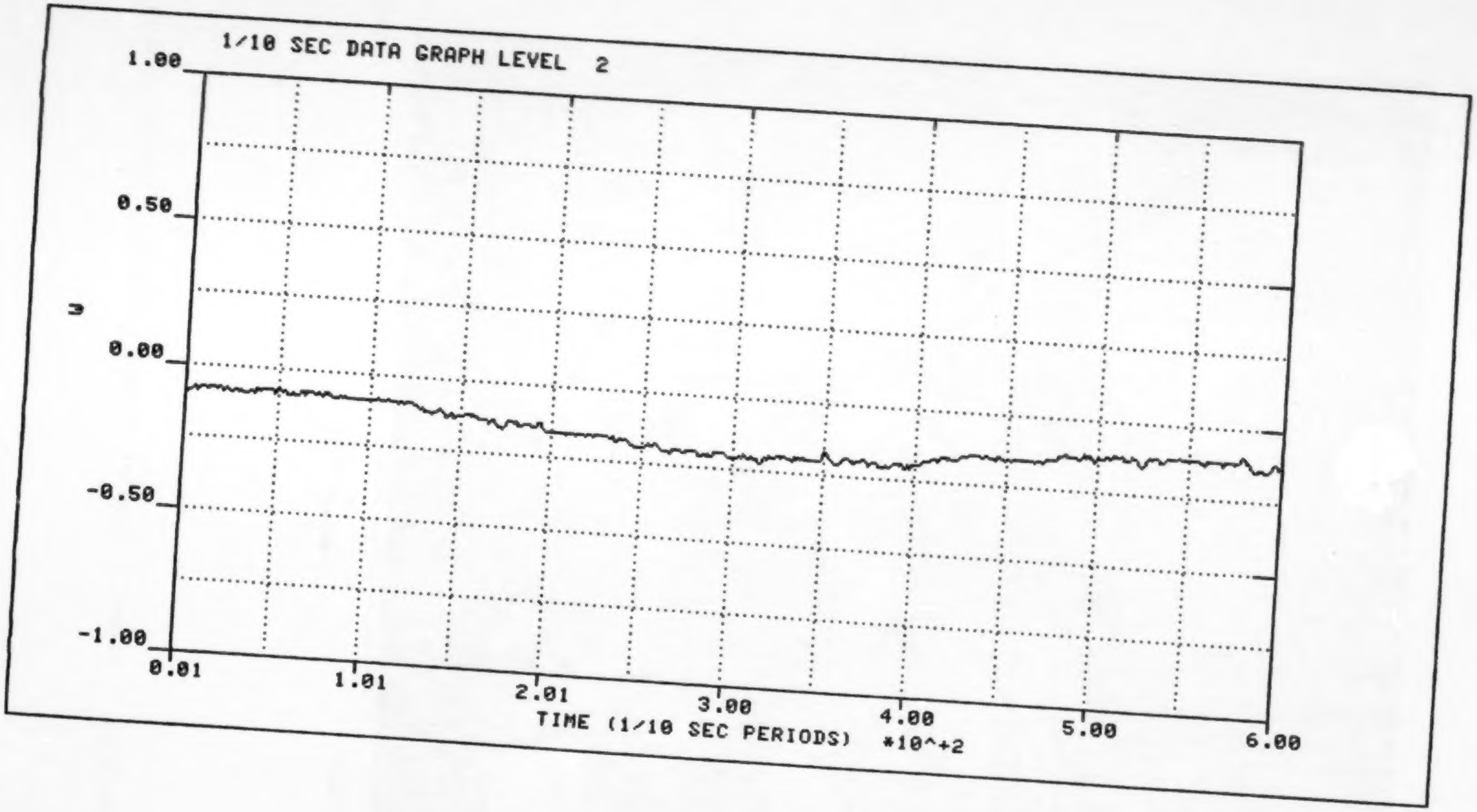

Figure B-7. Vertical wind speed time-series data from the 40-m level of Tower A for a 1-minute period (10/15/82, 0505 MDT).

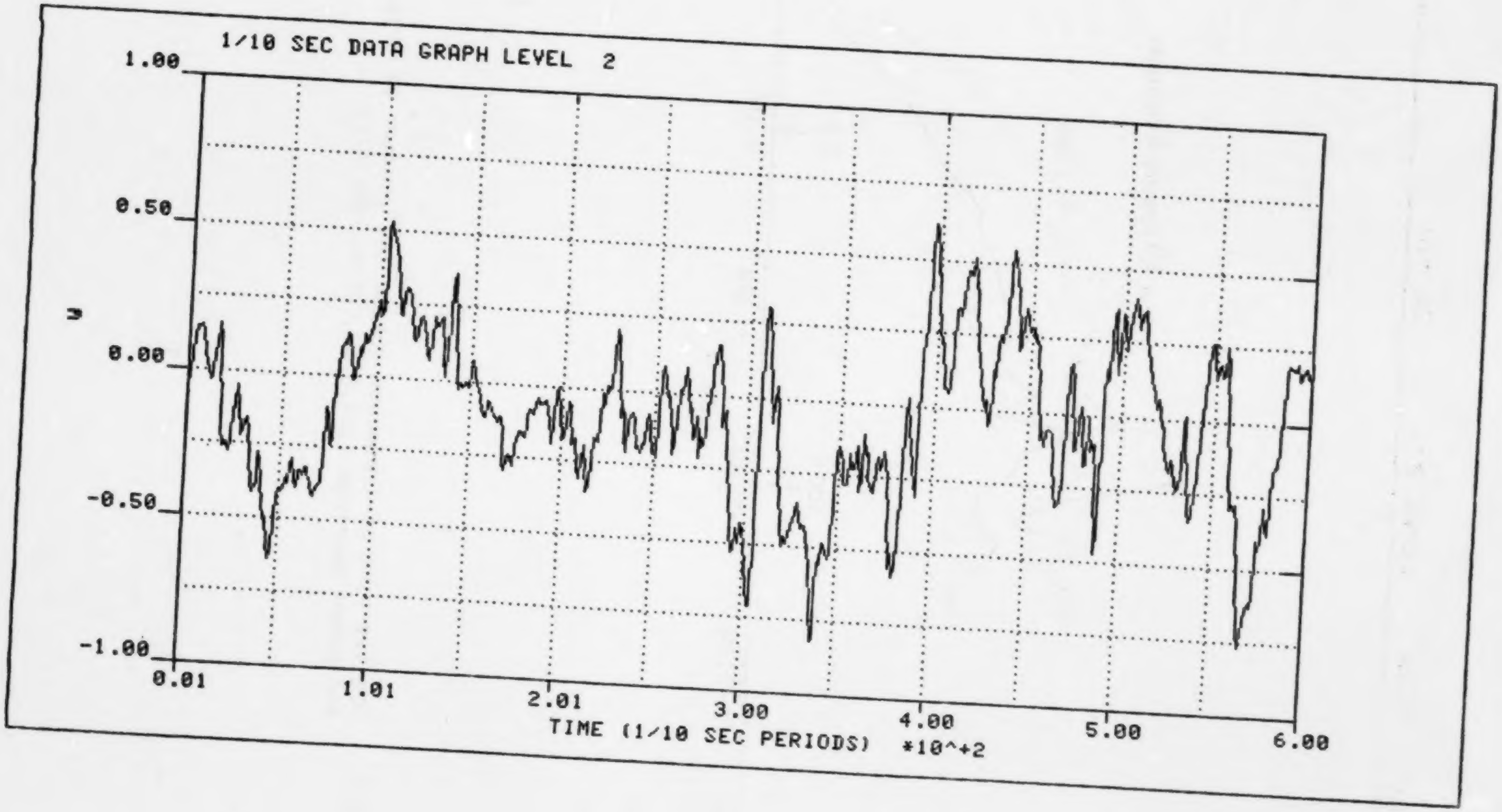

Figure B-8. Vertical wind speed time-series data from the 40-m level of Tower A for a 1-minute period (10/15/82, 0545 MDT).

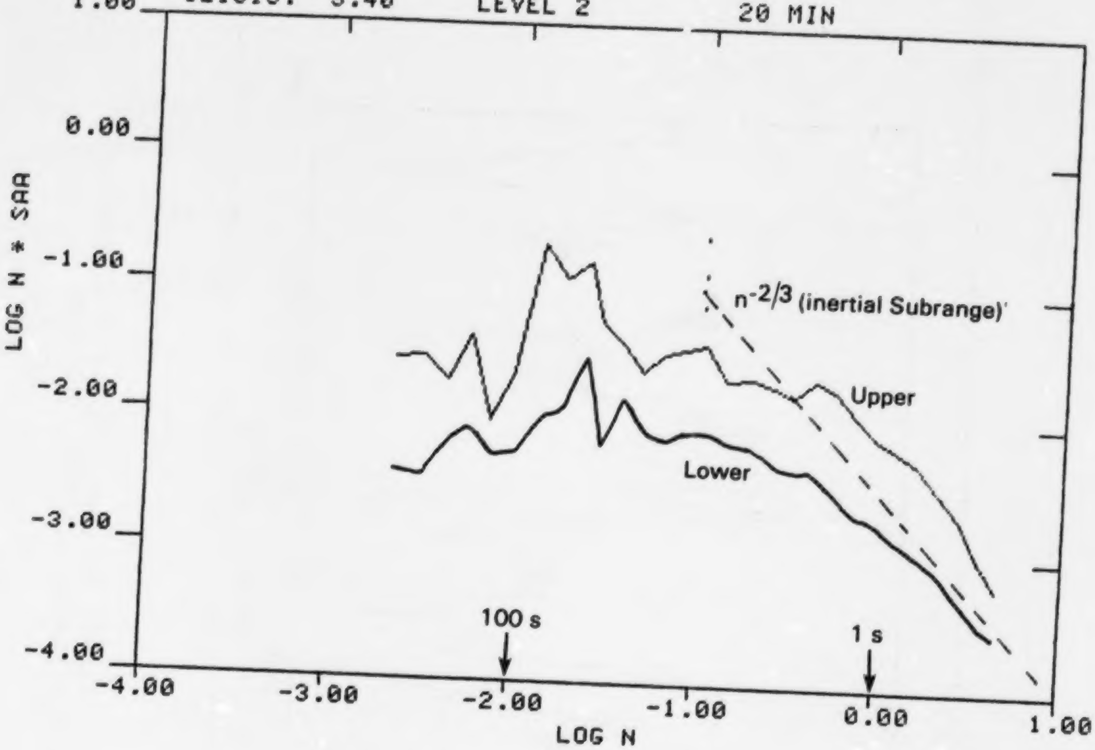

Figure B-9. Log-log plot of frequency versus the product of frequency and power spectrum (10/15/82, 0540-0600 MDT).

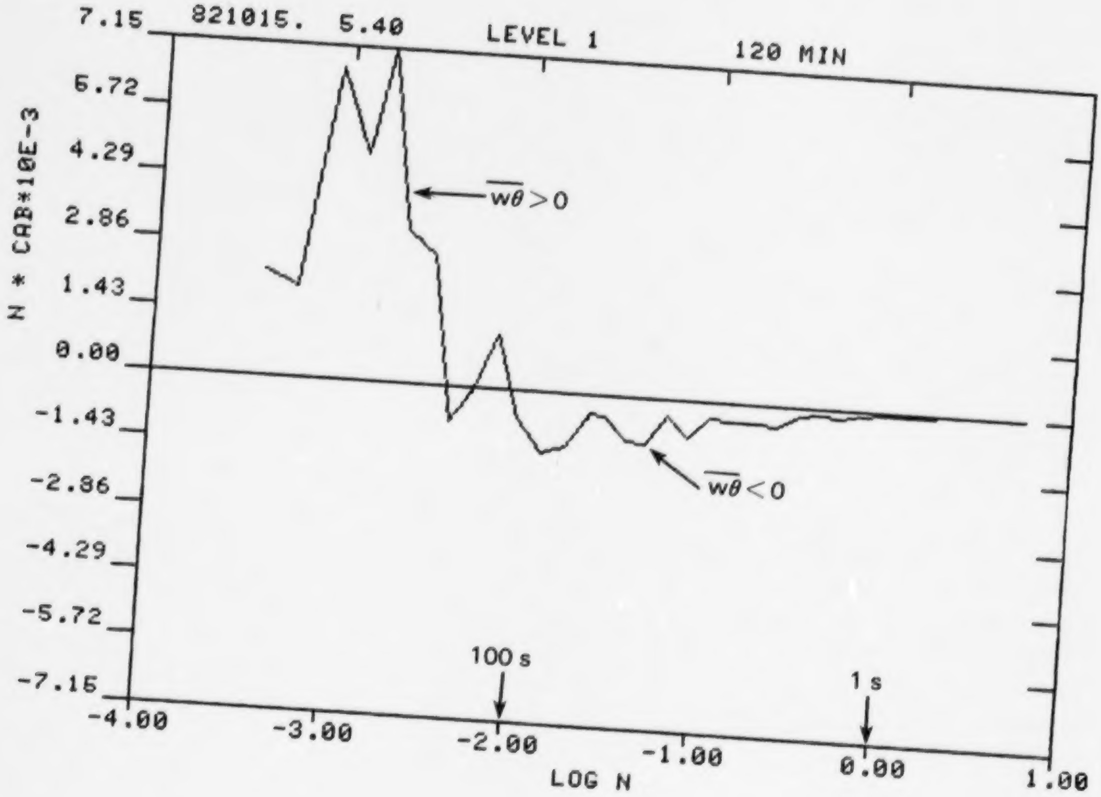

Figure B-10. Cospectral analysis of temperature and vertical wind speed fluctuations measured at 5 m showing that positive heat fluxes result from low frequency motions (10/15/82, 0540-0740 MDT).

☆USGPO: 1983 — 759-102/0789